

Site Specific Surface Chemistry of  
Prototypical Amino Acid, Peptide and  
DNA Base Groups on Si(111)7×7

by

Avishek Chatterjee

A thesis  
presented to the University of Waterloo  
in fulfillment of the  
thesis requirement for the degree of  
Doctor of Philosophy  
in  
Chemistry

Waterloo, Ontario, Canada, 2012

©Avishek Chatterjee 2012

## **AUTHOR'S DECLARATION**

I hereby declare that I am the sole author of this thesis. This is a true copy of the thesis, including any required final revisions, as accepted by my examiners.

I understand that my thesis may be made electronically available to the public.

## Abstract

The surface chemistry of glycine, glycyglycine, adenine and thymine on Si(111)7×7 are studied for the first time by X-ray photoelectron spectroscopy (XPS) and Scanning Tunneling Microscopy (STM) experimental techniques. The results are supported with the density functional theory based computations by elucidating equilibrium geometries of the adsorbate-substrate structures. In contrast to common carboxylic acids, glycine is found to adsorb on Si(111)7×7 dissociatively through cleavage of a N–H bond instead of O–H bond. Increasing the glycine film thickness reveals the existence of a transitional adlayer between the first adlayer and the zwitterionic multilayer. This transitional adlayer is estimated to be 1-2 adlayer thick and is characterized by the presence of intermolecular N··HO hydrogen bond. Density Functional Theory (DFT) calculations of glycine adsorption on Si(111)7×7 and Si(100)2×1 model surfaces illustrates that the formation of different surface adducts involving the –NH<sub>2</sub> and –COOH functional groups plays a vital role in determining the adsorbate structures on the 7×7 and 2×1 surfaces and therefore control the ultimate surface adproducts. The unique unidentate adsorption configuration of glycine on Si(111)7×7 through N–H dissociation, with the unreacted carboxyl group remaining free, has shown to be an effective way to capture other biomolecules such as glycyglycine, alanine, adenine and thymine on a glycine-functionalized Si(111)7×7 surface and through [O–H··N] hydrogen bonding. The captured molecules can be released simply by annealing. The glycine-functionalized Si(111) surface therefore provides a flexible platform for potential applications as selective molecular traps, chemical sensors, and biomolecular electronic components.

The STM study of glycine adsorption on Si(111)7×7 provides strong evidence for dissociative adsorption of glycine through N–H bond cleavage (and N–Si bond formation) as reported in X-ray photoemission study. In addition, STM images with higher glycine exposures shows that the second adlayer is mediated by vertical hydrogen bonding and that the horizontal hydrogen bonding between two N–H dissociated glycine adsorbates at two neighbouring adatom sites can be possible. Similar to glycine adsorption on Si(111)7×7 surface, the XPS investigation of glycyglycine on the Si(111)7×7 also reveals three growth stages; dissociative adsorption of glycyglycine in the first adlayer, a hydrogen bonded transitional adlayer and a ultimately the zwitterionic multilayer. In contrast to glycine, glycyglycine adsorbs in a bidentate fashion with the dissociation of N–H and O–H bonds in the first adlayer. The STM investigations support the evidence of dissociative adsorption of glycyglycine in a bidentate fashion on two adjacent Si adatoms across a dimer wall or an adatom-restatom pair as observed from the filled state images. The strong bidentate interactions of glycyglycine with the Si atoms also inhibit surface diffusion

of the adsorbed fragment, and the adsorption apparently follows random sequential adsorption statistics. The XPS and STM results of the glycylglycine adsorption on Si(111)7×7 can be corroborated with our DFT based computational study which suggests that the bidentate adproducts involving N–H and O–H dissociations are viable. In addition, the DFT results also predict that the free –CONH– and –COOH groups remaining on the respective bidentate adstructures could facilitate adsorption of the second adlayer through the formation of hydrogen bonding.

In sharp contrast to glycine and glycylglycine, the STM studies of adenine on Si(111)7×7 shows the evidence of molecular adsorption of adenine through dative bonding to the surface silicon atoms. The majority of the adsorbed adenine molecules are found to appear as dimer pairs at the initial adsorption stage, which are formed by hydrogen bonds. The experimental evidence of the formation of dative bonds between the substrate and adenine and the feasibility of the H-bond mediated dimers can also be supported by ab-initio DFT/B3LYP/6-31G++(d,p) calculations and X-ray photoemission data. As the exposure of adenine increases, the numbers of dimers as well as the unique self-organized adenine structures also increase. These dimers and self-assembled structures are found to be most prominent in the growth of adenine nanowires, most notably aligned along the Si dimer-wall or  $[\bar{1} 10]$  direction of the 7×7 unit cell. The self-aligned adenine dimer nanowires offer a natural template for catch-and-release biosensing, lithography, and molecular electronic applications. On the other hand, the STM study of another nucleobase thymine on Si(111)7×7 surfaces reveal the existence of three different kinds of adsorption products. When compared with the XPS and DFT based computational methods, it can be suggested that the three different adsorption products could correspond to 1,4 and 3,6 cycloaddition products and hydrogen bonded adcomplex respectively. The statistical analysis for three different exposures of Thy on the 7×7 surface further helps to assign the three different features observed in STM images to the 1,4 and 3,6 cycloaddition products as well as to the hydrogen bonded adcomplexes. The present work therefore illustrates the importance of the unique site specific surface chemistry of these four prototypical biomolecules on Si(111)7×7 which could be harnessed and used in the future biodevices by functionalizing the Si(111)7×7 surface with appropriate molecules such as glycine, glycylglycine, adenine or thymine.

## Acknowledgements

The activation energy barrier for the fulfillment of the thesis work was considerably huge when I first looked at my project in 2006. It required a lot of effort not only from my side but also from a lot of people without whom it would have been impossible for me to cross over the barrier.

I am indebted to my supervisor Prof. Kam Tong Leung as he gave me the opportunity to be a part of the Watlabs family and opened the door that lead to the fascinating world of science and technology in front of me. My journey since then was immensely enjoyable as well as adventurous. I enjoyed the beauty of scientific vision of logic and evidence based truth with the continuous flow of new challenges as I kept moving forward. Along with the intermittent successes, I have experienced the omnipresence of failures and disappointments which made me more focused and flexible as a person.

This thesis would not have been possible unless I mention my colleague Dr. Lei Zhang. I got an opportunity to work with him in couple of my projects and I have tried to learn from his systematic and analytical approach towards any unknown problem. It is an honour for me to get a chance to work with him as a coworker.

My supervisory committee guided me through all these years and I would to like thank Dr. Jean Duhamel, Dr. John Goddard and Dr. Dayan Ban for being my advisors.

It is a pleasure to thank our science and electronic shop people; Harmen Vander Heide, Peter Kessel, Jacek Szubra, Zhenwen Wang and Krunomir Dvorski for helping me every time I faced any technical problem. Their brilliance has always led me to come back to my experiments by solving problems I have encountered with.

I would also like to thank Dr. Jacob Fisher and Dr. Mike Chong for their invaluable suggestions and advices with my questions and problems.

I am truly thankful to my colleagues and group members, Samad bazargan, Helia Jalili, Debabrata Pradhan, Maryam Ebrahimi, Liyan Zhao, Nina Heinig, Nafiseh Moghimi, Marwa Abdellah, Jung Soo Kang, Bahareh Rahsepar, Joseph Palathinkal , Saurabh Srivastava and Anisur Rehman for their tremendous support and enthusiasm. I will remember those hours of discussions with my office mate Samad Bazargan, on various issues covering areas from science and technology, sports, politics, culture and arts.

My friends in Waterloo taught me a lot about life and I would never forget their contribution to the fulfilling of my thesis. My discussions with Kanwartej Singh Sra about various topics including research, philosophy and sports helped me learning new ideologies and gathering knowledge. I would also like to thank my close friend Deeparnab Chakrabarty for inspiring me to attain greater challenges and newer ideas. I will always remember my friends Shanee Raizada, Rajesh Tripathy, Puneet Dhaliwal, Kalikinker Mandal, Manu Hegde, Sarvagya Upadhyay, Anup Kumar Chalmalla, Sriram Sampath, Arjit Parihar, Parneet Singh Kohli and all others with whom I have spent my wonderful time in Waterloo.

I owe my deepest gratitude to my parents who have always been supportive to me and without their blessings I would not have achieved the goals that I have set for myself. I would like to thank my wife Aishwarya for her continuous support and love that helped me facing newer challenges.

I recognize that this research would not have been possible without the financial assistance of NSERC, University of Waterloo graduate Studies, Department of Chemistry at the University of Waterloo (Graduate Research Scholarships, Teaching Assistantships) and Waterloo Institute of Nanotechnology (WIN) Nanofellowship. I express my gratitude towards those funding agencies.

## **Dedication**

I dedicate this thesis to my parents Manas and Sumita Chatterjee for their love and endless support.

## Table of Contents

AUTHOR'S DECLARATION.....	ii
Abstract .....	iii
Acknowledgements.....	v
Dedication .....	vii
Table of Contents .....	viii
List of Figures .....	xi
List of Tables .....	xvii
Chapter 1 Introduction .....	1
1.1 Surface Chemistry of Silicon .....	1
1.2 Methodologies of surface sensitive techniques used for the experiments: .....	9
1.2.1 X-ray Photoelectron spectroscopy: .....	9
1.2.2 Scanning Tunneling Microscopy (STM) .....	13
1.3 Scope of Thesis: .....	18
Chapter 2 Experimental and Computational Details.....	19
2.1 X-ray Photoelectron Spectrometer .....	23
2.2 Variable Temperature Scanning Probe Microscope (VT-SPM): .....	25
2.3 Sample Cleaning and generation of 7×7 reconstructed surface: .....	30
2.4 Details of Computations: .....	30
Chapter 3 Glycine adsorption on Si(111)7×7 .....	34
3.1 Hydrogen-bond mediated transitional adlayer of glycine on Si(111)7×7 at room temperature .....	34
3.1.1 Introduction.....	34
3.1.2 Experimental Details.....	35
3.1.3 Results and Discussion.....	36
3.1.4 Summary .....	42
3.2 Computational surface chemistry of glycine on Si(111)7×7 and Si(100)2×1: Dissociative adsorption through adduct formation .....	43
3.2.1 Introduction.....	43
3.2.2 Results and Discussion.....	45
3.2.3 Summary .....	47
3.3 Hydrogen-Bond-Mediated Biomolecular Trapping: Reversible Catch-And-Release Process of Common Biomolecules on a Glycine-Functionalized Si(111)7×7 Surface .....	50

3.3.1 Introduction.....	50
3.3.2 Experimental Details.....	52
3.3.3 Results and Discussion.....	52
3.3.4 Summary.....	60
Chapter 4 Observation of vertical and horizontal hydrogen bonding formation in dissociative adsorption of glycine on Si(111)7×7 by Scanning Tunneling Microscopy .....	61
4.1 Introduction.....	61
4.2 Experimental Details.....	63
4.3 Results and Discussion .....	63
4.4 Summary .....	74
Chapter 5 Three-stage growth of glycine and glycyglycine nanofilms on Si(111)7×7 and their thermal evolution in ultrahigh vacuum condition: From chemisorbed adstructures to transitional adlayer to zwitterionic films .....	75
5.1 Introduction.....	75
5.2 Experimental Details.....	76
5.3 Results and Discussion .....	77
5.3.1 Computational chemistry of adsorption configurations .....	77
5.3.2 X-ray photoelectron spectroscopy of G and GG adsorption.....	79
5.4 Comparison of XPS results with the calculations .....	85
5.5 Summary .....	86
Chapter 6 Bidentate Surface Structures of Glycyglycine on Si(111)7×7 by High-Resolution Scanning Tunneling Microscopy: Site-specific Adsorption via N–H and O–H or Double N–H Dissociation .....	91
6.1 Introduction.....	91
6.2 Experimental & Computational Details .....	92
6.3 Results and Discussion .....	93
6.4 Summary .....	97
Chapter 7 Self-directed growth of aligned adenine dimer nanowires on Si(111)7×7: Direct imaging of formation of hydrogen-bond mediated dimers and clusters at room temperature by Scanning Tunneling Microscopy .....	101
7.1 Introduction.....	101
7.2 Experimental and Computational Details .....	103
7.3 Results and Discussion .....	104

7.4 Summary .....	117
Chapter 8 Surface [4+2] cycloaddition reaction of Thymine on Si(111)7×7 as observed by Scanning Tunneling Microscopy .....	118
8.1 Introduction.....	118
8.2 Experimental and Computational Details .....	120
8.3 Results and Discussion .....	121
8.4 Summary .....	130
Chapter 9 Conclusion and Future Work .....	131
Appendix A Ultrahigh Vacuum (UHV).....	137
Appendix B Tunneling through one dimensional rectangular potential barrier.....	138
Bibliography .....	140

## List of Figures

Figure 1-1 (a) STM empty state image and (b) filled state image of pristine Si(111)7×7 surface obtained with sample bias of +2 V and −2 V, respectively, all at tunneling current of 800 pA. (c) Schematic drawings of 7×7 unit cells for the STM images. The atoms in the unfaulted and faulted half unit cells are represented by lighter and darker spheres, respectively, in (c). (d) The DAS model for 7×7 unit cell with top and side view (lower panel) with the adatom-adatom, adatom-restatom, restatom-restatom and corner hole-adatom distances. (e) The layer by layer reconstruction of 7×7 unit cell, the topmost adatom layer to the lowest base layer stacked one above another. ....	6
Figure 1-2 Gas Phase equilibrium geometries of (a) glycine, (b) conformers of glycyglycine and the four DNA base groups: (c) adenine, thymine, guanine and cytosine. ....	9
Figure 1-3 Schematic diagram of the photoemission process from an atomic orbital by the impingement of X-rays. The incident X-ray photons expel a core electron from the solid, the kinetic energy of which depends on the binding energy of the electron and the work function of the solid material. ....	10
Figure 1-4 (a) schematic diagram of a typical XPS setup with X-ray source, sample, monochromator, electron analyser and detector. (b) The Omicron XPS system with the source, approximate position of sample (not visible in image), Rowland circle, analyser and the Channeltron detectors. ....	12
Figure 1-5 Schematic diagram of electron tunneling between a metal substrate and the sharp metallic tip. ....	13
Figure 1-6 Schematic diagram of tunneling conditions at different tip-sample bias polarities: (a) zero, (b) positive and (c) negative bias applied on the sample with respect to the tip. The sample and tip work functions are also shown as $\phi_S$ and $\phi_T$ in (a), (b) and (c).....	15
Figure 1-7 Schematic diagram of different modes of STM imaging. (a) Constant Current Imaging (CCI) mode with feedback loop turned on. (b) Constant Height Imaging (CHI) mode.....	17
Figure 2-1 (a) Omicron Molecular beam Epitaxy system. The Analysis chamber is equipped with a VT-SPM microscope and a monochromatic XPS spectrometer. The MBE1 chamber is uniquely designed for evaporating organic materials and is equipped with four different low temperature effusion cells and a mass spectrometer. MBE2 chamber is used for depositing metals and materials with high melting points (>1000° C) and has four different high temperature effusion cells. (b) and (c) the machine drawing showing the side and top view respectively. ....	21

Figure 2-2 Two different low temperature organic effusion cells. (a) OME effusion cell and (b) NTEZ effusion cell with quartz and PTFE crucibles. (c) The schematic diagram of different components of an effusion cell with crucible, conductor, heat reservoir, evaporant, thermocouple heaters and heat sink. ....	22
Figure 2-3 X-ray Photoelectron Spectrometer, including (a) the Sphera hemispherical analyser, an X-ray mirror assembly, X-ray source and manipulator. (b) Schematic diagram of the monochromator assembly showing the X-ray source, alignment drives, the crystal mirror housing on the Rowland circle along with the positions of the sample and of the X-ray anode. (c) XM 1000 MKII X-ray source with the aluminum coated anode, and the long and short filament cathodes. (d) Control electronics and the data acquisition computer.....	24
Figure 2-4 Omicron VT-SPM system. (a) SPM chamber with a camera, a wobblestick and the laser electronics for AFM operation. (b) VT-SPM microscope outside the chamber. (c) STM scanner stage with a STM tip, (d) STM data acquisition computer with control electronics. ...	26
Figure 2-5 (a) A home-built STM tip preparation setup with ring electrode, Teflon holder, W tip and NaOH lamellae. (b) Schematic diagram of the tip etching process. (c) Example of a bad tip with long taper and a pen like shape. (d) Example of a better tip with a shorter taper. ....	29
Figure 2-6 Top views (left) and side views (right) of different clusters for modeling selected parts of the Si surface: (a) $\text{Si}_{16}\text{H}_{18}$ cluster to represent the adatom-restatom pair, (b) $\text{Si}_{12}\text{H}_{12}$ to represent a single adatom-adatom pair across the unit cell. (c) $\text{Si}_{26}\text{H}_{24}$ to represent two adatom-adatom pairs across the dimer wall, all for the $\text{Si}(111)7\times 7$ surface, and (d) $\text{Si}_{15}\text{H}_{16}$ cluster to represent the double dimer cluster for the $\text{Si}(100)2\times 1$ surface.....	33
Figure 3-1 XPS spectra of the C 1s (right), N 1s (center), and O 1s regions (left) of glycine on $\text{Si}(111)7\times 7$ as a function of deposition time. Inset shows the optimized geometry of a N-bonded glycine adstructure coupled to a second glycine molecule through an XPS spectra of the C 1s (right), N 1s (center), and O 1s regions (left) of glycine on $\text{Si}(111)7\times 7$ as a function of deposition time. Inset shows the optimized geometry of a N-bonded glycine adstructure coupled to a second glycine molecule through an O–H...N hydrogen bond on a $\text{Si}_{16}\text{H}_{18}$ model surface, obtained by a DFT/B3LYP calculation with a 6-31++G(d,p) basis set. ....	37
Figure 3-2 Proposed (a) direct and (b) indirect proton-transfer mechanisms for the formation of N-bonded glycine (in the first adlayer) on an adatom-restatom model surface of $\text{Si}(111)7\times 7$ .....	41

Figure 3-3 Potential energy diagram, along with the optimized geometries and adsorption energies (in  $\text{kJ mol}^{-1}$ ) for different states, of glycine adsorption on model surfaces of (a) Si(111)7×7 and (b) Si(100)2×1. The more (less) probable pathway is shown as a solid (dashed line). ..... 48

Figure 3-4 Schematic diagram of the adsorption of glycine on a model Si(111)7×7 surface, with direct proton transfer (route a) and with intramolecular proton transfer (route b) from a Si←N adduct (II), leading to the final adsorption state (IV). ..... 49

Figure 3-5 N 1s spectra of Si(111)7×7 functionalized by a 15-s exposure of glycine (Gly) before (lowest trace) and after exposure to (a) 120 s of Gly, (b) 480 s of glycylglycine (GlyGly), (c) 720 s of alanine (Ala), (d) 10 s of adenine (Ade), and (e) 180 s of thymine (Thy), and upon annealing at (a-d) 120°C and (e) 95°C for 10 s. N 1s spectra for bare Si(111)7×7 after exposure to (b) 480 s of GlyGly and (d) 1260 s of Ade are marked as reference (Ref.). These spectra are compared with (f) the N 1s spectra of Si(111)7×7 functionalized by a 300-s exposure of GlyGly before and after 15 s of Gly exposure. .... 54

Figure 3-6 Equilibrium structures of (a, e) glycine (Gly), (b, f) glycylglycine (GlyGly), (c, g) alanine (Ala), and (d, h) adenine (Ade) H-bonded to Gly adsorbed on Si<sub>16</sub>H<sub>18</sub> (left column) and Si<sub>12</sub>H<sub>12</sub> (right column) model surfaces, all obtained by DFT/B3LYP GAUSSIAN03 calculations using a 6-31G++dp basis set..... 59

Figure 4-1 (a) STM empty state image and (b) filled state image of glycine adsorbed on Si(111)7×7 surface obtained with sample bias of +2 V and -2 V, respectively, all at tunneling current of 200 pA. (c) Schematic drawings (center column) of three 7×7 unit cells labeled A, B and C for the STM images, and height profiles (right column) along the lines L<sub>x</sub> (x= 1-6, 11-16) in the unfaulted half (marked by solid lines) and faulted half (marked by dashed lines). The atoms in the unfaulted and faulted half unit cells are represented by lighter and darker spheres, respectively, in (c) lower. The sites of interest are labeled by alphanumeric characters. The ovals in (c) upper mark the adatom-adatom pairs across the dimer wall that are affected by glycine adsorption. Inset in (c) shows the equilibrium geometry of a N-H dissociated glycine molecule adsorbed on a Si<sub>26</sub>H<sub>24</sub> cluster in a tilted configuration as obtained by DFT/B3LYP/6-31++G(d,p) calculation. .... 67

Figure 4-2 STM images taken at a sample bias of +2 V and tunneling current of 200 pA after glycine exposure of (a) 8 s, (b) 14 s, (c) 20 s, (d) 25 s and (e) 35 s; and (f) the corresponding total coverage (Cov) and the relative occupancies for center adatom (CA), corner adatom (AA),

faulted half (FH), unfaulted half (UH) sites, and for vertical doubles (VD) and horizontal doubles (HD). The ratios of AA to CA and UH to FH are shown on the right axis. ....	72
Figure 4-3 Equilibrium structures and the adsorption energies of glycine on (a1, a2) Si <sub>16</sub> H <sub>18</sub> and (b-e 1, b-e 2) Si <sub>26</sub> H <sub>24</sub> in (a-d1) the single and (a-d2, e1, e2) double configurations, with the configurations for (d1, d2, e1, e2) shown as top view, all obtained with DFT/B3LYP/6-31G++(d,p). STM images taken at a sample bias of +2 V and tunneling current of 200 pA attributed to the corresponding (a-d 3) single and (a-d 4, e3, e4) double configurations, with the respective line scans, L1-L10, given in (a-e 5). ....	73
Figure 5-1 Optimized geometries of adsorbate-substrate configurations (ASC) and their corresponding adsorption energies of glycine on a Si <sub>16</sub> H <sub>18</sub> cluster (a-d) and on a Si <sub>12</sub> H <sub>12</sub> cluster (e, f); and of glycyglycine on a Si <sub>16</sub> H <sub>18</sub> cluster (h-p) and on a Si <sub>12</sub> H <sub>12</sub> cluster (q-t). The optimized geometries of the H adsorbed on Si <sub>16</sub> H <sub>18</sub> and Si <sub>12</sub> H <sub>12</sub> clusters are shown in (g). The plausible ASCs consistent with the experimental results are marked by the tick symbols (☑). ....	88
Figure 5-2 Evolution of C 1s, N 1s and O 1s spectra of a glycine film deposited on Si(111)7×7 as a function of exposure time; and evolution of C 1s, N 1s and O 1s spectra of a thick as-grown glycine film as a function of annealing temperature. ....	89
Figure 5-3 Evolution of C 1s, N 1s and O 1s spectra of a glycyglycine film deposited on Si(111)7×7 as a function of exposure time; and evolution of C 1s, N 1s and O 1s spectra of a thick as-grown glycyglycine film as a function of annealing temperature. ....	90
Figure 6-1 (a) STM filled-state image and (b) empty-state image of glycyglycine adsorbed on a Si(111)7×7 surface obtained with a sample bias -2 V and +2 V, respectively, all at a constant tunnelling current of 150 pA. (c, d) Corresponding schematic diagrams depicting (A) an unreacted and (B) a reacted 7×7 unit cells, and (e, f) height profiles along the linescans L <sub>x</sub> (x= 1-4, 11-14) in the unfaulted half (marked by solid lines) and faulted half (marked by dashed lines). The atoms in the unfaulted and faulted half unit cells are represented by lighter and darker spheres, respectively, in (c). The sites of interest are labeled by alphanumeric characters. ....	98
Figure 6-2 (a) STM filled-state images taken at a sample bias of -2 V and a tunneling current of 150 pA, (b) the height profiles along the respective linescans, L1-L5, for bidentate adsorption of glycyglycine on the AA-AA, CA-CA and CA-AA and CA-RA sites, and the corresponding plausible equilibrium adstructures (with top and side views) and adsorption energies of	

glycylglycine on (c1-3)  $\text{Si}_{26}\text{H}_{24}$  and (c4)  $\text{Si}_{16}\text{H}_{18}$ , all obtained with DFT/B3LYP/6-31G++(d,p).  
..... 99

Figure 6-3 STM filled-state images taken at a sample bias of  $-2\text{ V}$  and a tunneling current of  $150\text{ pA}$  after glycylglycine exposure of (a)  $25\text{ s}$ , (b)  $30\text{ s}$ , (c)  $25\text{ s}$ , (d)  $40\text{ s}$  and (e)  $15\text{ s}$ ; and (f) the relative surface concentrations for bidentate adsorption at CA-RA, AA-AA, CA-CA, AA-RA and CA-AA sites and the total coverage and relative occupancies for total reacted CA and AA sites. 100

Figure 7-1 (a) Empty-state STM image ( $30\times 30\text{ nm}^2$ ) of adenine adsorbed  $\text{Si}(111)7\times 7$  obtained with a sample bias of  $+2\text{ V}$  and a tunneling current of  $150\text{ pA}$ ; (b) the empty-state image and (c) filled-state image (both  $5\times 5\text{ nm}^2$ ) of a selected  $7\times 7$  unit cell with a single adenine molecule adsorbed as marked by the square box in (a); (d) the height profiles along linescans L1 and L2 in (b) and (c) respectively; and (e) equilibrium adsorption geometries and their corresponding adsorption energies (in  $\text{kJ mol}^{-1}$ ) of a single adenine molecule datively bonded to a  $\text{Si}_{26}\text{H}_{24}$  cluster (with the Si adatoms marked by solid circles) through the N1, N3, N7 or N10 atom, as optimized by the DFT/B3LYP/6-31++G(d,p) method..... 106

Figure 7-2 Equilibrium geometries of the hydrogen-bonded adenine dimers involving different N atoms (a-f) and C atoms (g-i), obtained by the DFT/B3LYP/6-31++G(d,p) method with counterpoise energy corrections to the basis set superposition errors..... 108

Figure 7-3 (a) Empty-state STM image ( $30\times 30\text{ nm}^2$ ) of  $15\text{ s}$  exposure of adenine on  $\text{Si}(111)7\times 7$  recorded with a sample bias of  $+2\text{ V}$  and a tunneling current of  $150\text{ pA}$ ; (b) corresponding magnified STM images of selected adenine dimers including long dimer (LD), diagonal dimer (DD), side dimer (SD), and opposite dimer (OD) marked by open squares in (a) and (a, inset) the height profiles along linescans L2, L3 and L4 compared to that along L1; and (c) equilibrium geometries of adenine dimers datively bonded to the  $\text{Si}_{26}\text{H}_{24}$  cluster (with the adatoms marked by solid circles), as optimized by the DFT/B3LYP/6-31++G(d,p) method..... 112

Figure 7-4 (a) Empty-state STM image ( $30\times 30\text{ nm}^2$ ) of a  $15\text{ s}$  exposure of adenine on  $\text{Si}(111)7\times 7$  recorded with a sample bias of  $+2\text{ V}$  and a tunneling current of  $150\text{ pA}$ , and magnified views of H-bond mediated links between different dimers in (b) direct end-to-end (ETE), (c) offset ETE, (d)  $90^\circ$  zigzag (ZZ90), (e)  $60^\circ$  zigzag (ZZ60), (f) wide-angle turn (WAT), (g) right-angle turn (RAT) and (h) side-by-side (SBS) arrangements, with the arrows marking the direction of growth and the triangles outlining the half unit-cells..... 114

Figure 7-5 Empty-state STM images ( $50\times 50\text{ nm}^2$ ) of (a)  $6\text{ s}$ , (d)  $10\text{ s}$ , (b)  $15\text{ s}$ , and (c)  $25\text{ s}$  exposures of adenine on  $\text{Si}(111)7\times 7$  recorded with a sample bias of  $+2\text{ V}$  and a tunnelling current of  $150$

	pA, with (a), (b), and (c) shown with a magnified view ( $30 \times 30 \text{ nm}^2$ ); (e) Corresponding relative surface concentrations for singles (S), doubles (D), end-to-end (ETE), side-by side (SBS), and multiple dimers (MD), along with the total coverage (Coverage) and the percentage of brighter protrusions in S+D (marked by ovals and indicated as %B), all as a function of adenine exposure. ....	116
Figure 8-1	(a) STM empty-state image ( $24 \times 24 \text{ nm}^2$ ) for 15 s exposure of thymine on a Si(111) $7 \times 7$ surface obtained w a sample bias of +2 V at a tunneling current of 150 pA. Bright protrusions of three different intensities are marked as L (lower), M (medium) and H (higher). (b) Schematic drawings of the corresponding $7 \times 7$ unit cells for the selected part of the STM image, with the Si atoms of the half unit cells represented by lighter spheres while the sites with adspecies are indicated as darker spheres. (c) Height profiles along the linescans L1, L2, L3 and L4, corresponding to the unreacted Si adatoms, L, M and H protrusions, respectively. ....	123
Figure 8-2	STM filled-state image ( $16 \times 16 \text{ nm}^2$ ) for 10 s exposure of thymine on Si(111) $7 \times 7$ collected with a sample bias of -2 V at a tunneling current of 150 pA. The two different bright protrusions are labeled as B1 and B2 and are marked with triangular brackets. The height profiles along the lines L1, L2 and L3 corresponds to the unreacted Si adatoms, B1 and B2 features respectively are shown as inset. ....	124
Figure 8-3	Reaction scheme of [4+2] cycloaddition reaction of thymine on a model Si(111) $7 \times 7$ surface. Thymine first undergoes keto-enol tautomerism to form di-enol tautomer, which reacts with a Si adatom-restatom pair to produce 1,4-, 3,6- and 2,5-cycloaddition adspecies. ....	126
Figure 8-4	Equilibrium structures (with top and side views) and adsorption energies of thymine on a $\text{Si}_{16}\text{H}_{18}$ cluster, representing an adatom-restatom pair, resulting from (a) 1,4- (b) 3,6- and (c) 2,5-cycloaddition, and of their corresponding hydrogen-bonded complexes formed with an incoming thymine molecule. All the geometries are obtained with DFT/B3LYP/6-31G++(d,p) calculations. ....	127
Figure 8-5	STM images collected at a sample bias of +2 V and a tunneling current of 150 pA for thymine exposure of (a) 8 s, (b) 15 s, and (c) 25 s, all on Si(111) $7 \times 7$ ; and (d) the corresponding total coverage and the relative surface concentrations for L, M and H protrusion features. ....	129

## List of Tables

Table 2-1: Molecules in concern, their purity and melting points .....	20
Table 7-1: The combinations of dative bonded adenine N atoms, free hydrogen bonding configurations and the substrate modified dimer configurations.....	111

# Chapter 1

## Introduction

### 1.1 Surface Chemistry of Silicon

The application of surface chemistry goes back to early 19<sup>th</sup> century, when the platinum surface was first used as a catalyst to promote reactions between hydrogen and oxygen in 1823 by Dobereiner.<sup>1</sup> Since then surface chemistry has found numerous other applications and evolved as one of the most important fields in modern science and technology. The discovery of catalysis, electrochemistry and photography in the 19<sup>th</sup> century followed by the development of colloids and adsorption sciences in the early 20<sup>th</sup> century and the evolution of the polymer and biopolymer surfaces, nanoparticle science, optical surfaces and the microelectronics in the later 20<sup>th</sup> and early 21<sup>st</sup> century are the results of extensive research in surface chemistry of different substrates.<sup>1</sup> The rich diversity of surface properties and their importance in chemical and energy conversion technologies are two major aspects that brought the field of surface science to the center of attraction in the early 20<sup>th</sup> century. In the later 1950s, the emergence of solid state based electronic industry along with the development of ultrahigh vacuum (UHV) systems broadened the scope of surface chemistry. The use of UHV systems has two fold advantages, firstly, once the substrate surface is cleaned (i.e. the atoms of the top substrate layer have no immediate neighbours in the vertically upward direction), it can stay clean for a long time (~hours)[see appendix A]. This provides the researcher enough time to study the properties of the cleaned surfaces. Secondly, the availability of vacuum makes it possible to use electron and X-ray beams to probe the surfaces, which are often required in a surface-sensitive techniques. Generally, the substrate surface is cleaned by annealing in UHV to generate a fresh surface. This substrate annealing inside an UHV environment can be achieved by passing either a direct current through the substrate or by using indirect radiative heating with a hot tungsten filament (or an appropriate heater such as boron nitride) or electron beam bombardment from the backside of the substrate.

The rapid increase in the number of different surface characterization techniques, such as Auger Electron Spectroscopy (AES), Fourier Transform Infrared Spectroscopy (FTIR), X-ray Photoelectron Spectroscopy (XPS), Low Energy Electron Diffraction (LEED), to name a few, made it possible to study different phenomena such as adsorption, desorption, diffusion, growth and nucleation, as well as surface reactions on a molecular scale. The discovery of Scanning Tunneling Microscopy at the IBM laboratories by Binnig and Rohrer in the 1980s further revolutionized the field of surface science, because for the first

time it was possible to follow and manipulate atoms and molecules on different surface sites directly in a real space. Combination of STM with other chemical-specific techniques such as X-ray photoelectron spectroscopy (XPS) can provide a powerful toolset to study the unique site-specific surface chemistry of more complicated biomolecules on various semiconductor and metallic substrates.

The need for incorporating organic functions into existing semiconductor technologies has long been recognized to build molecular scale devices. The growth of organic molecules on a common semiconductor surface and their interactions therefore represents the first step in developing molecular devices.<sup>2,3</sup> Silicon, being one of the most important semiconductor materials, organic functionalization could significantly extend the present silicon-based device technology, especially when the device size has reached the nanoscale. Single-molecule detection and multi-species chemical sensing, molecular photonics and electronics, and DNA-based biomolecular computing are just some of the emerging applications of bio/organic functionalization. Organic functionalization of Si substrates has involved organic molecules, with nitrogen-containing functional groups (amines, amides) and oxygen-containing functional groups (carboxylic acids, alcohols) connected to an aliphatic backbone or an aromatic ring structure including benzene and their derivatives.<sup>4</sup> Several important molecules such as acetonitrile,<sup>5</sup> aniline,<sup>6</sup> benzenethiol,<sup>7</sup> ethanol<sup>8</sup> and formic acid<sup>9</sup> were found to adsorb via dissociative addition reaction, while trimethylamine<sup>10</sup> and N-methylpyrrolidine<sup>11</sup> by the formation of dative bonding, whereas acetylene,<sup>12</sup> benzaldehyde,<sup>13</sup> trans-2-butene,<sup>14</sup> and cis-2-butene<sup>14</sup> were found to adsorb via cycloaddition reaction with the Si(100)2×1 surface. Similarly, for Si(111)7×7 surface, the bio/organic molecules including methacrylic acid,<sup>15</sup> dimethylamine,<sup>16</sup> phenol,<sup>17</sup> pyrrole,<sup>18</sup> and methylhydrazine<sup>19</sup> found to adsorb via dissociative addition reaction, whereas geranyl acetone,<sup>20</sup> pyridine,<sup>21</sup> and trimethylamine<sup>10</sup> by the formation of dative bonding, and acetaldehyde,<sup>22</sup> acetonitrile,<sup>23</sup> cyclohexene,<sup>24</sup> ketene,<sup>25</sup> and N-methylpyrrole<sup>26</sup> via cycloaddition reaction.

Si(111) is one of the most important and well-studied surfaces among all other semiconductor surfaces. Clean Si(111) surface generally has two prominent reconstructions : 2×1 and 7×7. The 2×1 reconstruction can be generated by cleaving at or below room temperature, and is reported to be metastable and revert back to the more stable 7×7 reconstruction when annealed above 380°C.<sup>27</sup> The 7×7 reconstruction, on the other hand, is the most stable reconstruction of the (111) surface and is found to be stable up to ~850°C, above which it goes back to the 1×1 phase. Historically, the structure of the Si(111)7×7 surface has eluded scientists for a long time because of its inherent complexity. Since the first observation of the low energy electron diffraction (LEED) pattern of this surface by Schlier and

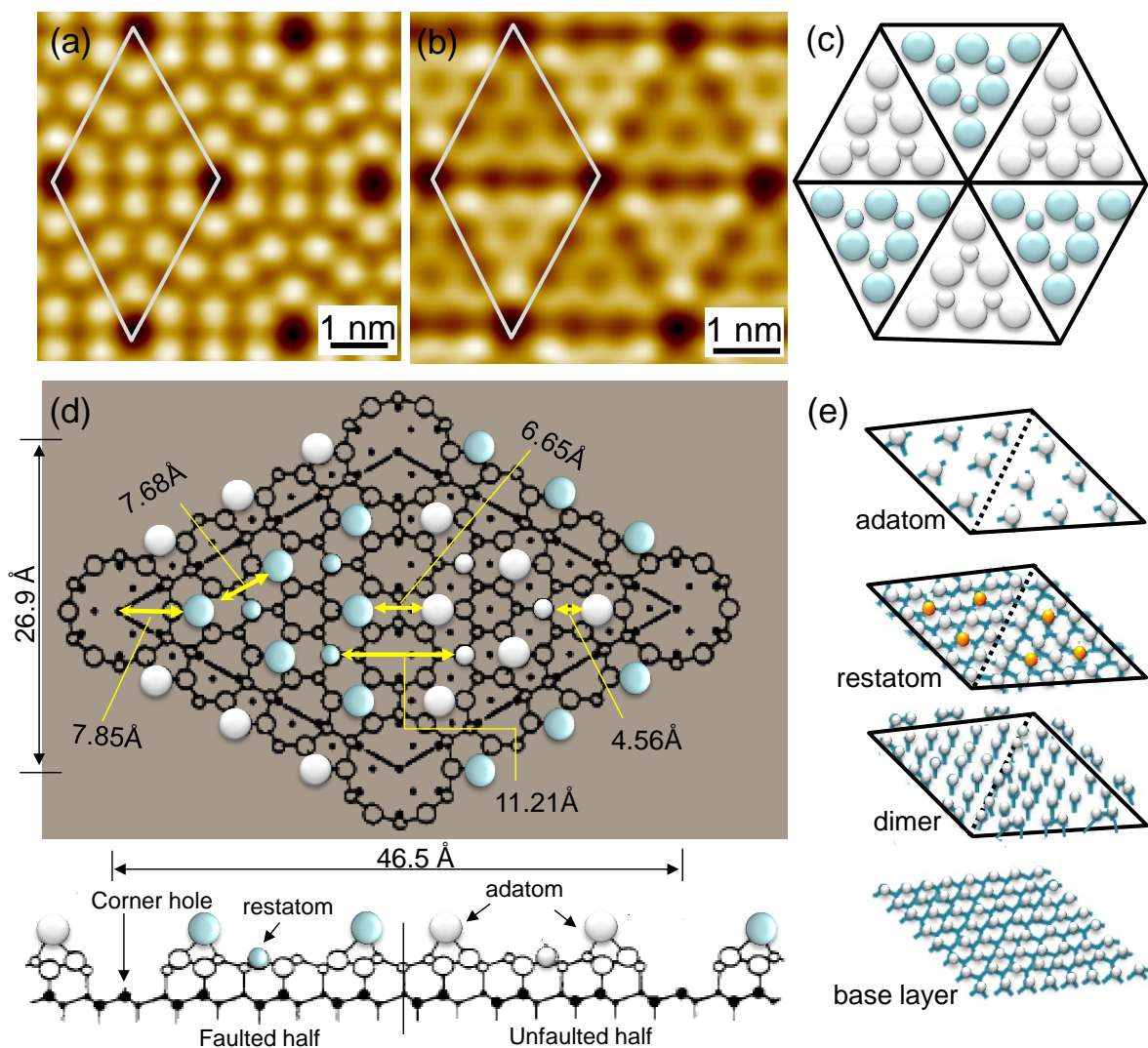
Farnsworth in 1959,<sup>28</sup> scientists all over the world have tried to understand and model the reconstruction. Among several groups who tried to model the surface without success, Chadi et al. gave a buckling distortion model with a theoretical comparison to the LEED data;<sup>29</sup> Lander et al. proposed a model array of 13 vacancies of local  $2 \times 2$  order in the  $7 \times 7$  unit cell with 49 surface sites;<sup>30</sup> while Harrison et al. later improved the Lander model by proposing an array of adatoms in its vacancy sites.<sup>31</sup> All the aforementioned models were not able to completely explain all the experimental results for Si(111) $7 \times 7$  reconstruction. In 1985, Takayanagi et al., based on his electron diffraction data, put forward a model that ultimately explains the nature of the  $7 \times 7$  reconstruction.<sup>32</sup> As the complexity of the  $7 \times 7$  reconstruction continued to baffle scientists, Binnig and Rohrer in 1983 published their first STM images of Si(111) $7 \times 7$  surface.<sup>33</sup> Based on the evidence provided by the real-space STM images of the  $7 \times 7$  reconstructed surface and the dimer-adatom-stacking-fault (DAS) model proposed by Takayanagi et al. in 1985, it was possible to account for the electron diffraction results and to understand the elusive nature of this reconstructed surface.

Figure 1-1a and 1-1b show typical STM image of the  $7 \times 7$  unit cell (marked by grey lines) obtained at +2 V and -2 V bias voltages respectively and a tunneling current of 800 pA at room temperature using a Omicron VT-SPM microscope in WATLab. This so-called empty-state and filled-state STM images reveal the positions and arrangement of the surface Si atoms in the unit cell. Figure 1-1c shows a corresponding schematic diagram of two  $7 \times 7$  unit cells, in which the bigger and smaller circles represent the positions of the Si atoms in the topmost (adatoms) and next top layers (restatoms) of the unit cell. The difference between the two half unit cells is clearly evident, with the protrusions in the faulted half unit cell (darker solid circles) reflecting a stacking fault being brighter than those in the unfaulted half unit cell (white solid circles). In the Dimer-Adatom-Stacking-Fault (DAS) model proposed by Takayanagi et al.,<sup>32</sup> the  $7 \times 7$  reconstruction is obtained from a layer-by-layer construction on a Si(111) $1 \times 1$  base layer that reduces the number of Si dangling bonds (unsaturated valencies of surface Si atoms) from 49 to 19 in each unit cell. As shown in Figure 1-1d, the 12 bigger solid circles (inside the unit cell marked as a diamond) represent the three-coordinated Si adatoms in the topmost layer, each with one dangling bond. The six smaller solid circles correspond to the Si restatoms in the second layer, known as the “restatom layer” also shown in Figure 1-1d and 1-1e. The third layer is the dimer layer (Figure 1-1d and 1-1e) consisting of three dimers on each side of the triangular half unit cell. The dimer layer saturates almost all the atoms sitting in the bulk layer below (base layer, Figure 1-1d), except for one Si atom known as the “corner hole” that carries one dangling bond. The dimer atoms in the dimer layer have two dangling bonds each, whereas the rest of the atoms above the dimer layer have also one dangling bond each. The

restatom layer sitting above the dimer layer satisfies the dangling bonds of the dimer layer, each of which saturates the dangling bonds of three underlying atoms. In order to satisfy all the dangling bonds of the dimer layer, the restatom layer in one of the triangular half unit cells gets rotated and generates the “stacking fault” in the  $7\times 7$  reconstruction. Therefore, the restatom layer occupies stacking fault sites in one half unit cell and normal or unfaulted sites in the other half unit cell. The geometric rearrangement of the Si atoms in the two half unit cells produces the differences in electronic structure of the half unit cells, which can be observed from the filled-state STM image where one half unit cell appears brighter than the other half (Figure 1-1a). The side view of these four layers is shown as in the lower panel of Figure 1-1d, and as a layer-by-layer reconstruction in Figure 1-1e. The formation of this layer-by-layer structure reduces the number of dangling bonds in a  $7\times 7$  unit cell from 49 to 19, corresponding to one on each of the 12 adatoms and 6 restatoms, plus 4 one-quarter dangling bond from each of the four corner holes.

Adatoms in the  $7\times 7$  unit cells may be considered as two general types. In particular, a corner adatom is located next to a corner hole, while a center adatom is located in between two corner adatoms (Figure 1-1d). Due to the reconstruction, the Si atoms inside a single  $7\times 7$  unit cell become nonequivalent in terms of electronic charge density, and they can be classified as three faulted corner adatoms, three faulted center adatoms, three faulted restatoms, three unfaulted corner adatoms, three unfaulted center adatoms and three unfaulted restatoms. The restatom and the corner hole get a formal charge of  $-1$  upon reconstruction, while each adatom has a formal charge of  $+7/12$ . Because a corner (*angulus* in Latin) adatom (AA) has only one neighbouring restatom (RA) while a center (*centrum* in Latin) adatom (CA) has two neighbouring RAs, almost twice the amount of charge transfer from CA to RA as that from AA to RA occurs, therefore causing the CA to have a larger formal charge than AA. The differences in the formal charges of CA ( $\sim +1$ ), AA ( $+7/12$ ) and RA ( $-1$ ) contribute to their site-specific reactivities. This is consistent with the STM image in Figure 1-1a that shows a brighter AA protrusion than CA, reflecting the corresponding higher electron density. The availability of both nucleophilic (RA) and electrophilic sites (AA, CA) makes the  $7\times 7$  surface particularly interesting towards various organic adsorbates with different functional groups. For small organic molecules such as glycine (with the  $\text{NH}_2$ -to-OH separation of  $3.7 \text{ \AA}$  for the most stable conformer in the isolated gaseous state), the neighbouring adatom-restatom pairs, i.e. CA-RA or AA-RA, with a separation of  $4.57 \text{ \AA}$  (Figure 1-1d) represent the most important reaction sites. This is because of their generally similar and therefore physically compatible dimensions. On the other hand, the considerably larger separations for a CA-CA pair across a dimer wall ( $6.65 \text{ \AA}$ ), a CA-CA or CA-AA pair within a half unit cell ( $7.68 \text{ \AA}$ ), and a CA-AA pair across a dimer wall ( $10.15 \text{ \AA}$ )

are more important for the larger adsorbates such as the DNA nucleobases (e.g., adenine) or peptides (e.g., glycylglycine).



**Figure 1-1** (a) STM empty state image and (b) filled state image of pristine Si(111)7×7 surface obtained with sample bias of +2 V and -2 V, respectively, all at tunneling current of 800 pA. (c) Schematic drawings of 7×7 unit cells for the STM images. The atoms in the unfaulted and faulted half unit cells are represented by lighter and darker spheres, respectively, in (c). (d) The DAS model for 7×7 unit cell with top and side view (lower panel) with the adatom-adatom, adatom-restatom, restatom-restatom and corner hole-adatom distances. (e) The layer by layer reconstruction of 7×7 unit cell, the topmost adatom layer to the lowest base layer stacked one above another.

Our group has studied the surface chemistry of a series of aliphatic bio/organic molecules, including di- and per-chloroethylenes,<sup>34</sup> dibromoethylene,<sup>35</sup> acrylic acid and propanoic acid,<sup>36</sup> allyl alcohol and allyl aldehyde,<sup>37</sup> and allylamine,<sup>38</sup> on Si(100)2×1, difluoroethylene,<sup>39</sup> and dichloroethylenes<sup>40</sup> on Si(111)7×7 surfaces. These studies revealed the wide varieties of interactions of the aliphatic organic molecules with the silicon surfaces, leading to reaction either via simple H-dissociation, addition or via cycloaddition with the surface Si atoms. In addition, our group also compare these results with those involving aromatic molecules, which are especially interesting because the aromatic ring backbone could interact with the surface through cycloaddition reactions as in benzene and toluene,<sup>41</sup> and through reactions with the heteroatom as in pyrrole, thiophene, and pyridine<sup>42</sup> on Si(100)2×1 and Si(111)7×7. Chlorobenzenes<sup>43</sup> and dihalogenated benzenes,<sup>44</sup> have been found to undergo dissociation reactions as the halogen (X= F, Cl and Br) atom gets adsorbed on a Si atom after dissociating from the aromatic backbone. All these past investigations by our group set the stage for studying more biologically important bifunctional or multifunctional organic molecules, with a special focus on the selectivities of the different benchmark organic functional groups towards the Si surface.

As the smallest building blocks of proteins and peptides, amino acids provide the basis to understand the larger biomolecular systems. A number of recent studies have been reported on the adsorption of amino acids on different surfaces. Among the ten naturally occurring amino acids that are produced by the human body, glycine (NH<sub>2</sub>CH<sub>2</sub>COOH) is structurally the simplest one, making it an excellent starting point to study specific interactions of the amino and carboxylic acid groups with the substrate bonding sites. The equilibrium geometry of a free glycine molecule (in the gas phase), as optimized by ab-initio calculations is shown in Figure 1-2a. Furthermore, glycine represents a unique class of bifunctional molecules, with an amino (–NH<sub>2</sub>) and a carboxylic acid (–COOH) groups, which allows it to function both as a base and an acid. The study of glycine on Si surfaces is therefore especially important, because not only both the base and acid groups coexist in a single molecule but also these functional groups can also be used to form hydrogen bonding adstructures. Appropriate coupling of these two functional groups to different surface sites offers surface selectivity for controlling the final adstructures. With one of the functional groups bonded to the surface and the other free to interact with incoming molecules, bifunctional molecules such as glycine are also important as linker molecules to form multilayer structures by hydrogen bonding for biodevice and molecular electronics applications.

Compared to glycine, glycyglycine is the simplest peptide and is made of two glycine residues by forming a –CONH– peptide bond. Figure1- 2b shows optimized geometries of a free glycyglycine

molecule in a straight chain conformer and two folded conformation forms as reported earlier in the literature.<sup>45</sup> Glycylglycine being the simplest peptide molecule, the interaction with the silicon surfaces would be interesting and should be studied along with that of glycine. The comparison of the growth mechanism of both the amino acid and its simplest peptide might provide information about the effect of dimension, peptide bond and termini functional groups of the adsorbate during adsorption process.

As the proteins are composed of smaller building blocks i.e. the amino acid molecules, DNA molecules in our body are also made of smaller building blocks known as DNA base or nucleobase groups. These DNA base groups are responsible for storing the genetic information of a living cell by forming selective hydrogen bonds with each other. Equilibrium geometries of the four DNA base molecules: adenine (Ade), guanine (Gua), thymine (Thy) and cytosine (Cyt) obtained by ab-initio calculations are shown in Figure 1-2c. Ade and Gua belong to the purine base group while Thy and Cyt belong to the Pyrimidine base groups. In a DNA molecule, Ade and Thy, and Gua and Cyt form selective hydrogen bonding with each other to produce the A-T and G-C base pairs, respectively, that are used to encrypt genetic information. Among the four base molecules, Ade is the only nucleobase molecule without any oxo group, which reduces the basicity of the amino purines and makes Ade more basic ( $pK_a = 4.2$ ) than Gua (3.3). Ade is also the most aromatic nucleobase as the aromaticity of the nucleobases decreases in the order: Ade > Gua > Cyt > Thy. Unlike the other three nucleobases, Ade also has only one functional group, i.e. the basic amino ( $-NH_2$ ) group, making it the only available linking point with other species if the ring N atoms are involved in anchoring the molecule to the surface. In contrast, Thy, being a pyrimidine base, has the lowest aromaticity among all the other DNA base groups. As reported earlier, Thy can undergo the keto-enol tautomerisation under suitable conditions, but in the gas phase it prefers the diketo form.<sup>46</sup> The study of Ade and Thy individually and together on the Si(111) surfaces can be interesting in terms of forming hydrogen bonded self-assembled structures. The self-assembled superstructures could be used in molecular electronics and future biodevices.

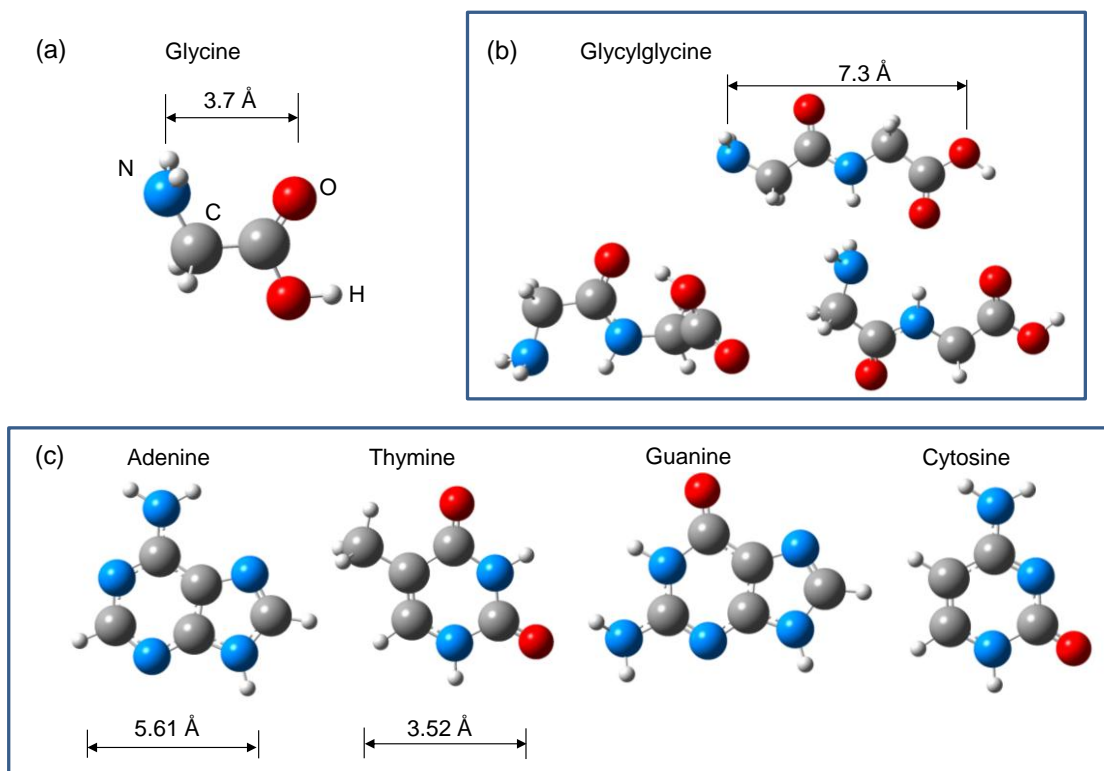


**Figure 1-2** Gas Phase equilibrium geometries of (a) glycine, (b) conformers of glycyglycine and the four DNA base groups: (c) adenine, thymine, guanine and cytosine.

## 1.2 Methodologies of surface sensitive techniques used for the experiments:

### 1.2.1 X-ray Photoelectron spectroscopy:

X-ray photoelectron spectroscopy (XPS) is based on the photoelectric effect, which was explained by Einstein in one of his famous papers in 1905.<sup>47</sup> Also known as electron spectroscopy for chemical analysis (ESCA), XPS has emerged as a very powerful tool for surface scientists because it can provide the electronic structure, composition and structural information of the probing substrate. This is an electron spectroscopic method in which an X-ray beam is used to eject electrons from the material. The kinetic energy,  $E_k$  of these photoelectrons is determined by the difference of the photon energy of the incident X-ray radiation ( $h\nu$ ), the sum of the work function of the solid ( $\phi$ ), and the binding energy  $E_b$  of the electron for solid (the Einstein equation):

$$E_k = h\nu - E_b - \phi \quad [\text{Equation 1}]$$

The most commonly employed X-ray sources are Mg ( $K\alpha$ ,  $h\nu = 1253.6$  eV) and Al ( $K\alpha$ ,  $h\nu = 1486.6$  eV). The photoemission process is shown schematically below in figure 1-3.

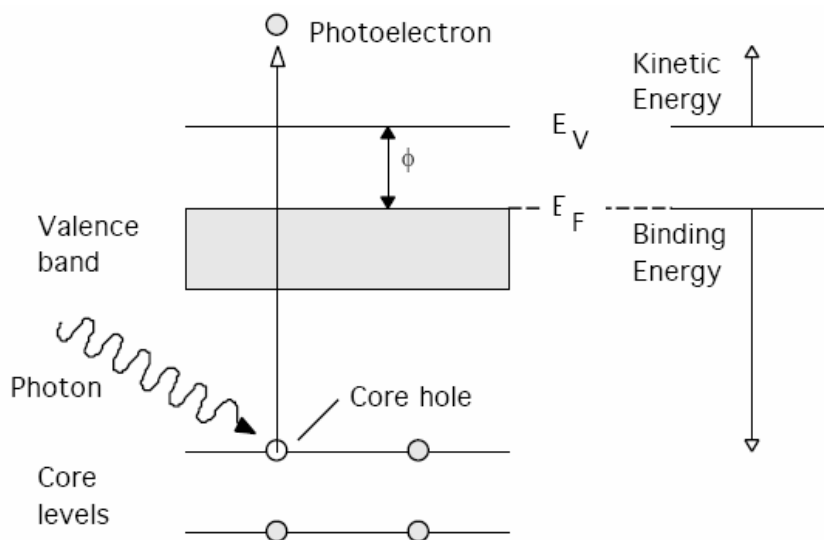


**Figure 1-3** Schematic diagram of the photoemission process from an atomic orbital by the impingement of X-rays. The incident X-ray photons expel a core electron from the solid, the kinetic energy of which depends on the binding energy of the electron and the work function of the solid material.

The kinetic energy distribution of the photoelectrons that are emitted from a solid surface carries its electronic structure information. No emission of the photoelectron is observed if the energy of the photon is less than the work function of the solid, i.e.  $h\nu < \phi$ . The binding energies of the electrons represent the strength of interaction between the electron and the nucleus and are dependent on the local chemical environments of the specific electron. Inner-shell electrons are tightly bound and localized to specific nuclei and are therefore specific to individual atoms within a molecule or an adsorbate.

Figure 1-4a shows a schematic diagram of typical XPS setup with the sample, X-ray source, monochromator, hemispherical electron analyser and the detector. The X-ray source generates the X-rays which are monochromated by using a monochromator. The monochromatized X-ray beam then impinges on the sample to produce photoelectrons which are collected with the hemispherical electron analyser and then detected for signal processing. Figure 1-4b shows our XPS setup integrated in the Omicron MBE system where the monochromatic X-ray source has a 500 mm Rowland circle and uses an Al anode. The X-ray source generates X-rays that are focused onto the sample by using the quartz-crystal mirror (part of the monochromator). The quartz crystal reflects and focuses the X-rays as a homogeneous beam and absorbs the unwanted radiation. The photoelectrons generated from the sample surface are collected by

electrostatic input lens and then are focused onto the entrance aperture of the electrostatic hemispherical deflection analyser. The analyser is composed of two concentric hemispheres; the inner and outer hemispheres are biased negative and positive with respect to the pass energy of the analyser. The analyser then disperses the electrons according to their energies across the exit plane to the Channeltron detectors.

Each and every element gives rise to a characteristic set of peaks in a typical XPS spectrum at binding energies determined by the photon energies and their respective kinetic energies. The appearance of peaks at particular binding energies therefore indicates the presence of a specific element in the sample under study. In addition, the intensity of the peaks gives us the concentration of an element within the XPS sampled region. Also to generate the atomic percentage values for a compound, each raw XPS signal should be divided by a relative sensitivity factor (RSF) for individual elements and should be normalized over all the elements detected. Furthermore, the exact binding energy of an electron in a solid depends not only on the electronic structure of the solid but also on the formal oxidation state of the atom and its local and physical environment. The changes of either the oxidation state or the local environment lead to shifts in the peak positions in the spectrum known as chemical shifts. The use of chemical shifts to differentiate between different oxidation states or the chemical environments is one of the great powers of XPS.<sup>48</sup>

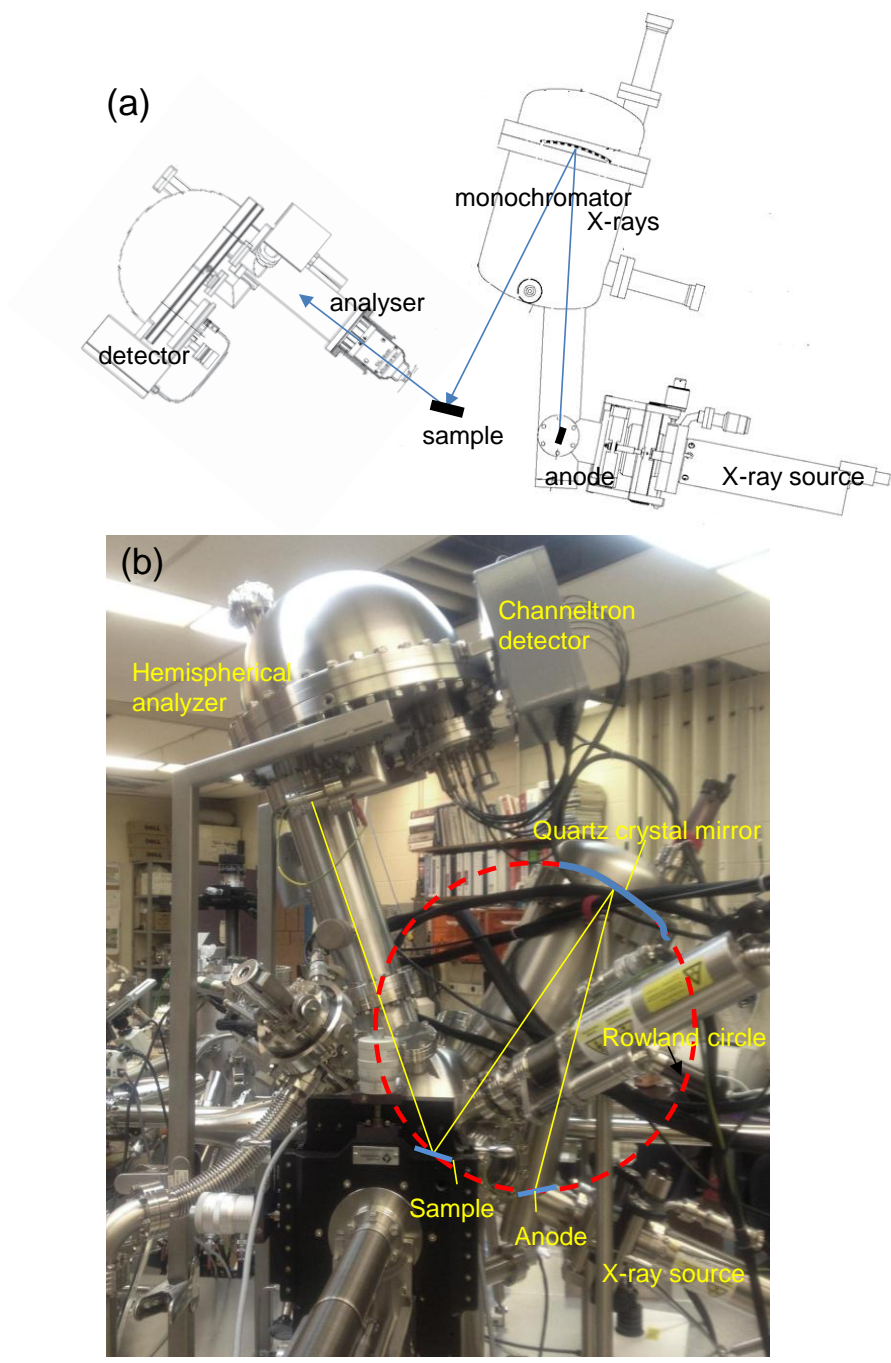


**Figure 1-4** (a) schematic diagram of a typical XPS setup with X-ray source, sample, monochromator, electron analyser and detector. (b) The Omicron XPS system with the source, approximate position of sample (not visible in image), Rowland circle, analyser and the Channeltron detectors.

### 1.2.2 Scanning Tunneling Microscopy (STM)

In early 1981, Gerd Binnig and Heinrich Rohrer while working on tunneling spectroscopy observed vacuum tunneling of electrons between a sharp tungsten tip and a platinum substrate in the IBM laboratories in Zurich. They realized that not only could they conduct local spectroscopy but also by adding a scanning feature they could even achieve topographic imaging. A new kind of microscopy was born, and it was later named as Scanning Tunneling Microscopy. The operating principle of STM could be described as a sharp tip (tungsten) scanning across the surface with a small gap maintained at a few angstroms between the tip and the surface and this gap can be controlled by the tunneling current flowing between them. Further evolution of the STM technique has later led to the invention of Atomic Force Microscopy and together they form the family of Scanning Probe Microscopies (SPM).

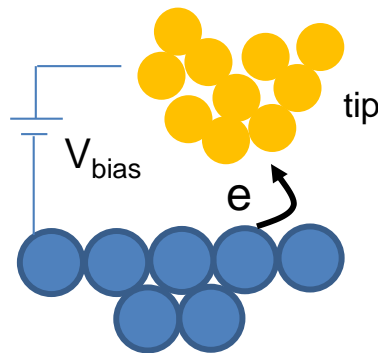


**Figure 1-5** Schematic diagram of electron tunneling between a metal substrate and the sharp metallic tip.

The tunneling effect is a quantum mechanical phenomenon and can only be explained by quantum mechanics. According to classical mechanics it is not possible for a particle to surmount a potential energy barrier which is higher than its total energy. But as a consequence of wave-particle duality of matter, in quantum mechanics an electron can tunnel through the barrier with a lower total energy. A simple but powerful example of one-dimensional rectangular potential barrier with height  $V_0$ , width  $d$ , can be used to show the tunneling mechanism. If an electron with energy  $E$  ( $E < V_0$ ) and mass  $m$  impinges on the potential barrier, by using the Schrodinger equations and the boundary conditions, the barrier transmission coefficient  $T$  and hence the tunneling current ( $i$ ) can be calculated. The tunneling current of this system can be found to vary exponentially with the barrier width ( $d$ ) as follows

$$i \propto \exp(-2\chi d) \quad [\text{Equation 2}]$$

Where  $\chi$  depends upon the barrier height ( $V_0 - E$ ) of the system; [see appendix B] it can be also observed that the tunneling current does not depend on the shape of the barrier. From the above equations it can be seen that the transmission probability and the tunneling current through a potential barrier decreases exponentially with the barrier thickness. The idea of electron tunneling through a junction is used to design a scanning tunneling microscope by bringing two electrodes (the sharp metal tip and the substrate surface) very close to each other and by applying a bias across the potential barrier. Depending on the polarity of the bias voltage, electrons from either the tip or the substrate can tunnel through the vacuum and flow towards the other electrode. Figure 1-5 shows a schematic diagram of the tunneling effect with a sharp tip staying very close to the substrate when a bias voltage is applied. The STM images are obtained by collecting the tunneling current while scanning the tip over the substrate surface at a fixed applied bias voltage between the tip and the surface.

A tunnel junction refers to the conductive junction formed between the sharp tungsten tip and a sample positioned at a very small separation. In order for an electron to tunnel either from the sample or from the tip, it has to overcome a potential barrier because of the vacuum between the sample and the tip.

During a STM experiment, a bias across the potential barrier is applied and thereby changing the tunneling junction. The potential can be applied to the junction in three ways as discussed below. Figure 1-6a represents the first case where no voltage is applied to the junction, and the sample and tip are in equilibrium by aligning their respective Fermi levels  $E_{FS}$  and  $E_{FT}$ , which results into zero net tunneling current. The second case shown in Figure 1-6b represents the situation when the sample is positively biased with respect to the tip. In this case, the electrons from the occupied states of the tip tunnel towards the unoccupied states of the sample states, which give rise to a tunneling current that flows from the sample to tip. Figure 1-6c represents the case where the sample is biased with a negative voltage with respect to the tip. The work functions for the sample and tip are also indicated in the figure by  $\phi_S$  and  $\phi_T$  respectively. Unlike the second case, now electrons from the occupied states of the sample flow to the unoccupied states of the tip, giving rise to a tunneling current that flows from the tip to the sample. From the tunneling current expression it can be observed that tunneling current ( $i$ ) depends exponentially on the tip-sample distance and hence the tunneling current between tip and sample is extremely sensitive to the tip-to-sample separation.

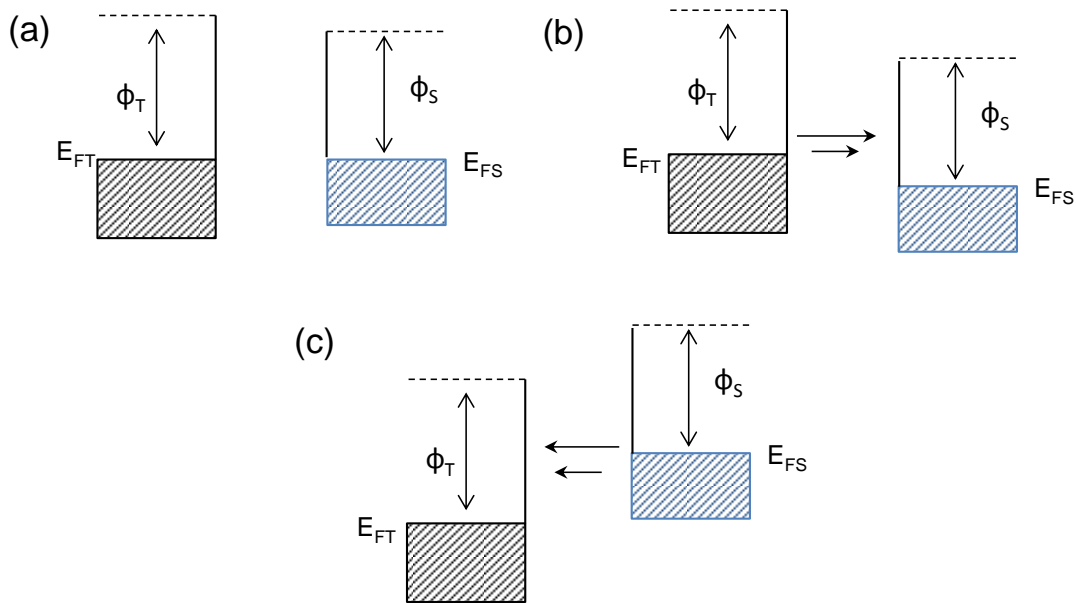


**Figure 1-6** Schematic diagram of tunneling conditions at different tip-sample bias polarities: (a) zero, (b) positive and (c) negative bias applied on the sample with respect to the tip. The sample and tip work functions are also shown as  $\phi_S$  and  $\phi_T$  in (a), (b) and (c).

In order to build an image using the tunneling concept, the tip has to move above the surface not just in the z direction but also along the x and y directions precisely. The control in the three-dimensional movement of the tip can be achieved by using piezoelectric devices coupled with feedback loop controls. Depending on the kind of information needed to be extracted, there exist various modes of operation in a STM. The most widely used modes are: (a) constant current imaging (CCI) and (b) constant height imaging (CHI) modes.

(a) Constant current imaging (CCI) mode:

The feedback loop in the STM electronics controls the height of the tip above the substrate surface during the scanning of the tip. In the CCI mode, this feedback loop is always kept on so that the tunneling current flowing between the sample and the tip is kept constant. The height (z axis) adjustment is performed by applying appropriate voltage to the z piezoelectric drive ( $V_z$ ), whereas the lateral tip position is controlled by voltages applied to the corresponding x and y piezoelectric drives i.e.  $V_x$  and  $V_y$ , respectively. The recorded signal  $V_z(V_x, V_y)$  can be translated to the topographic information  $z(x, y)$  from the sensitivities of the three piezoelectric drives. The contour map of  $z(x, y)$  so obtained therefore represents a constant current topography of the substrate surface. Figure 1-7a shows the schematic

diagram of the CCI mode where the tip is scanned across the substrate surface at a constant tunneling current with the feedback loop turned on all the time. The interpretation of a constant-current topograph is not trivial because it generally does not always represent the arrangement of atoms on the surface that determines  $z(x,y)$ . In order to interpret the constant current topograph, the tunneling junction of the tip and substrate surface should be modeled appropriately.

Tersoff and Hamman used the simplest possible model for the tip with a locally spherical symmetry and applied Bardeen's transfer Hamiltonian approach to STM.<sup>49</sup> Under the consideration of low temperature and low bias voltage, the tunneling current  $I$  between a tip and the sample surface can be shown as:<sup>49</sup>

$$I \propto n_S(E_F, r_0) \quad [\text{Equation 3}]$$

Where  $n_S(E_F, r_0)$  is the surface local density of states (LDOS) at the Fermi level  $E_F$  evaluated at the center of curvature  $r_0$  of the effective tip and corresponds to the charge density for the electronic states at  $E_F$ . The STM images at a low bias voltage in the CCI mode represent contour maps of constant LDOS at the  $E_F$  evaluated at the center of curvature of the effective tip, provided that the s-wave approximation for the tip is justified. Figure 1-7a shows the schematic diagram for the CCI mode where the tip is scanned over the surface with the feedback electronics turned on, to obtain constant current topograph and consequently measuring the surface local density of states.

(b) Constant height imaging (CHI) mode:

In the CHI mode, the feedback electronics is switched off completely and the tunneling current is recorded in accordance with the exponential dependence of the tunneling current on the tip-to-surface separation. The application of the CHI mode is limited to those surfaces that are atomically flat and this mode does not provide information about the vertical height ( $z$  scale). This information (vertical height) can be extracted if the absolute value of the local tunneling height is known as a function of location. Figure 1-7b shows a schematic diagram of the CHI mode with the feedback loop switched off and the tip scanning the surface at constant height. Figure 1-7b shows the schematic representation of the CHI mode where the tip scans over the surface at a constant height measuring the tunneling current at different points.

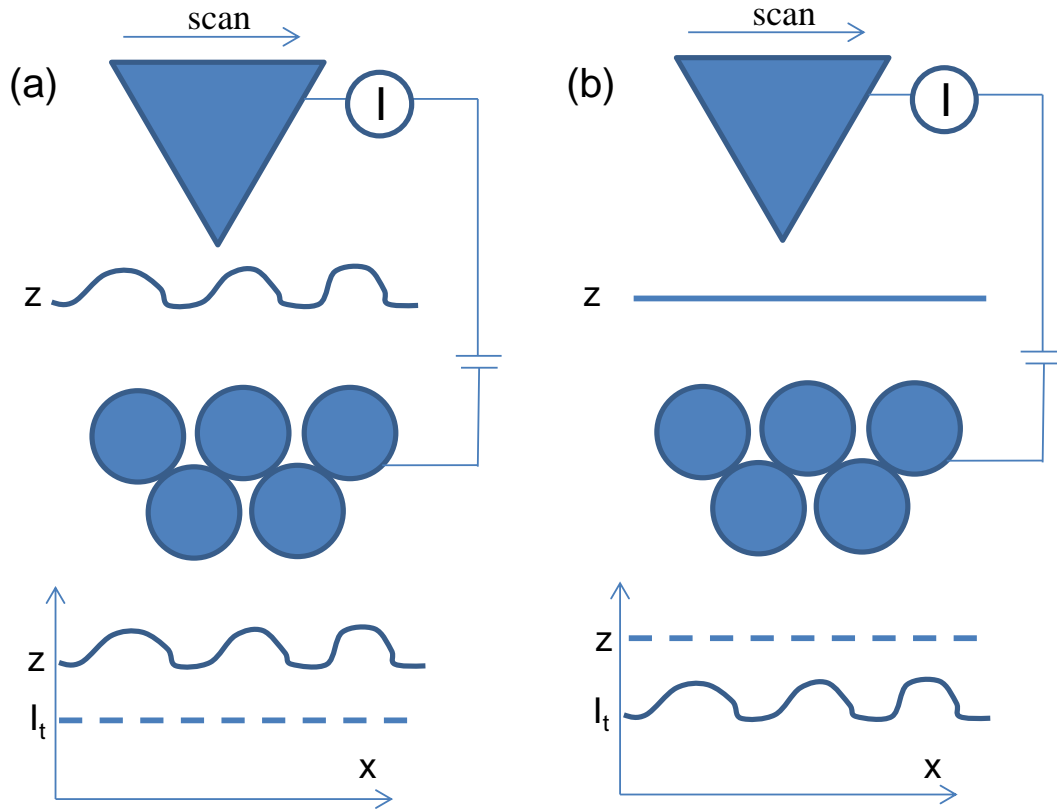


**Figure 1-7** Schematic diagram of different modes of STM imaging. (a) Constant Current Imaging (CCI) mode with feedback loop turned on. (b) Constant Height Imaging (CHI) mode.

### 1.3 Scope of Thesis:

The present work illustrates the importance of site specific chemistry of four benchmark biomolecules, glycine, glycyglycine, adenine and thymine on Si(111)7×7 surfaces. Chapter 1 describes the motivation and background for the present work along with brief literature review and methodologies of XPS and STM experimental techniques. Chapter 2 provides a brief description of the experimental setup used for the XPS and STM measurements, and computational details used for modelling the adsorption of these biomolecules on silicon surfaces. The experimental results, along with insights provided by our calculations, for the four benchmark biomolecules on Si(111)7×7 are given in the next six chapters. In particular, Chapter 3 reports the adsorption process of glycine on the Si(111)7×7 studied by XPS and DFT based computational methods. The growth evolution of dissociatively adsorbed glycine adlayer to the hydrogen bond mediated intermediate layer and ultimately to the zwitterionic thick films on Si(111)7×7 surface is followed by XPS and discussed in detail. The experimental results are substantiated by the DFT based computational methods which includes the details of the dissociative adsorption of glycine on the both Si(111)7×7 and Si(100)2×1 surfaces. The third chapter also indicates the application of the glycine functionalized Si(111)7×7 surface towards interacting with different kinds of biomolecules. This XPS investigation is followed by the STM study of the dissociation reaction of glycine with the 7×7 surface at very low exposure along with the DFT based calculations which is reported in the fourth chapter. After the detailed discussion on glycine adsorption in the third and fourth chapters, the fifth chapter describes the adsorption and thermal evolution of glycyglycine molecules with XPS and computational methods. Along with the glycyglycine, the thermal evolution of glycine is also reported in this chapter to compare the growth evolution for both the molecules. The site specific adsorption of glycyglycine molecules on Si(111)7×7 surface at very low exposures as observed by STM is presented in chapter 6. The surprising STM results for adenine that shows the unique self-organization of adenine molecules on the 7×7 surface are demonstrated in Chapter 7. Chapter 8 deals with the interesting case of thymine adsorption on the surface via cycloaddition reaction by STM and DFT based computational methods. Finally, the summary and future outlook of the present work are given in Chapter 9.

## Chapter 2

### Experimental and Computational Details

The experiments were performed in a five-chamber ultrahigh vacuum system (Omicron Nanotechnology Inc.), consisting of an analysis chamber for X-ray photoelectron spectroscopy (XPS) and scanning tunnelling microscopy (STM), two molecular beam epitaxy (MBE) systems for sample dosing of metals and organic materials, a fast-entry-lock (FEL) chamber for sample introduction, and a center transfer chamber connecting the other four chambers for sample transit and storage (Figure 2-1). The analysis chamber was equipped with an X-ray Photoelectron Spectrometer for chemical state analysis, and a variable-temperature scanning probe microscope (SPM) for atomic-resolution imaging STM experiments. The base pressure in the analysis chamber was generally lower/better than  $1 \times 10^{-10}$  mbar, while that in the MBE systems were better than  $5 \times 10^{-10}$  mbar after a fresh bake and normally in this range upon several dosing experiments. Single-side polished Si(111) chips ( $11 \times 2 \text{ mm}^2$ , 0.3 mm thick), with a resistivity of 0.005  $\Omega \text{ cm}$  (Virginia Semiconductor Inc.), were used as the substrates for all the experiments. The samples were introduced to the system through the FEL chamber and then moved through the transfer chamber to the analysis chamber. Sample transfers between the chambers were performed by using magnetic transfer rods.

The MBE1 chamber as shown in figure 2-1a-c is dedicated for deposition of biomolecular materials often in powder form, and is equipped with four specially designed water-cooled low-temperature effusion cells (Dr. Ebert MBE-Komponenten GmbH). Effusion cell OME1 and OME2 (figure 2-2a) are used for evaporating organic materials at a relatively low temperature range (15–350°C) whereas NTEZ1 and NTEZ2 as shown in figure 2-2b are used for evaporating materials at a higher temperature (80°–700°C). In order to follow the gas-phase molecular signature, the MBE1 chamber is also equipped with a 1-300 amu quadrupole mass spectrometer (SRS RGA 300). A solid biomaterial, preloaded in the respective effusion cell, was purified overnight by sublimation in vacuum, and appropriately outgassed for at least 30 minutes prior to exposure to the sample (the list of biomaterials is given in the table 2-1 below). The (powder) material inside the crucible of the effusion cell was heated uniformly along the entire length by a hot tantalum-wire filament as indicated in figure 2-2c. The temperature of the crucible was measured by using a thermocouple in direct contact with the crucible wall. All the effusion cells are each equipped with a water cooling shroud around the crucible to ensure homogeneous heating. The MBE chambers were each pumped by a turbomolecular pump, an ion pump and a titanium sublimation

pump. The chamber wall was lined inside with a cooling shroud that, when filled with liquid nitrogen, acted as an additional cryogenic pump. As a routine procedure, this cooling shroud was filled with liquid nitrogen before exposure of the biomaterials. The MBE2 chamber was identical to MBE1 except that it was equipped with two high-temperature effusion cells EFM (300-2000°C) and two WEZ cells (200-1300°C). MBE2 was dedicated for evaporation of metals (e.g. Fe, Ni, Cu, etc.) and high-temperature materials such as oxides, and was not used in the present work.

**Table 2-1: Molecules in concern, their purity and melting points**

Molecule	Purity	Supplier	Melting point
Glycine	98.5%	Sigma-Aldrich	182°C
Glycylglycine	99.5%	Sigma-Aldrich	220°C
Adenine	99%	Sigma-Aldrich	360-365°C
Thymine	99%	Sigma-Aldrich	~320°C

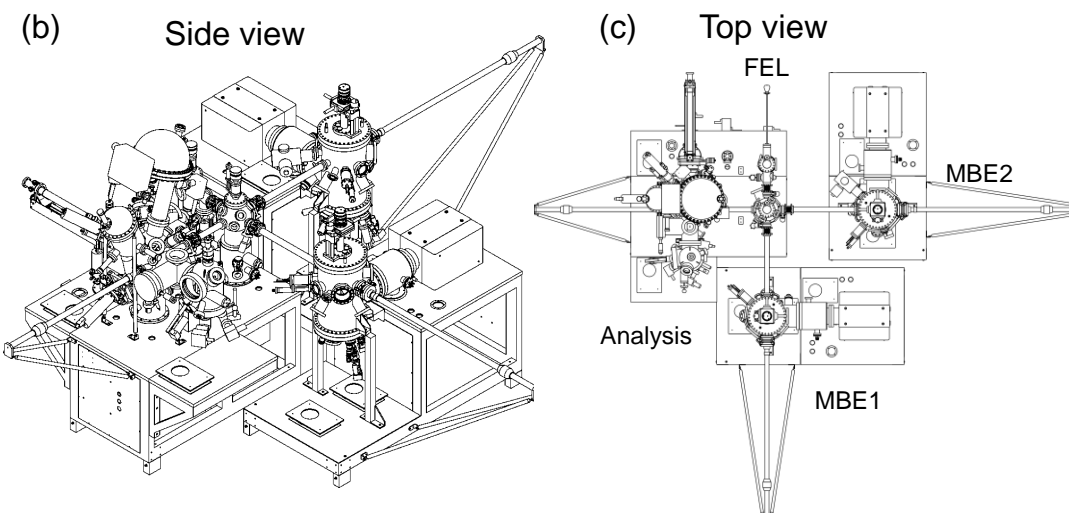
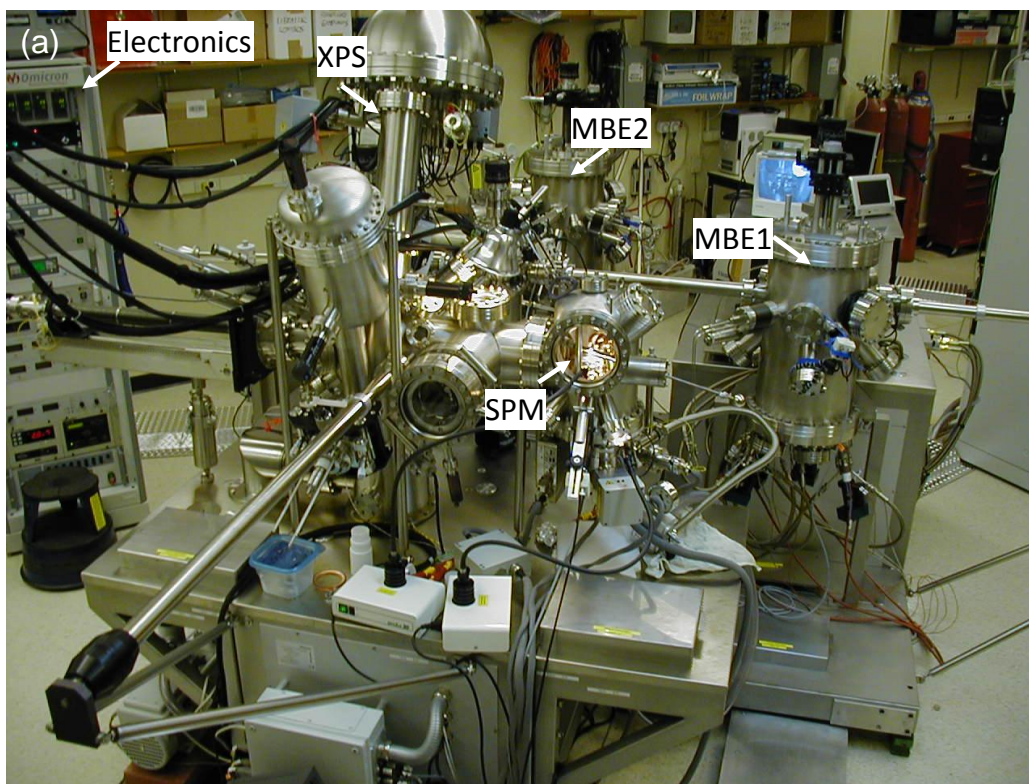


**Figure 2-1** (a) Omicron Molecular beam Epitaxy system. The Analysis chamber is equipped with a VT-SPM microscope and a monochromatic XPS spectrometer. The MBE1 chamber is uniquely designed for evaporating organic materials and is equipped with four different low temperature effusion cells and a mass spectrometer. MBE2 chamber is used for depositing metals and materials with high melting points ( $>1000^{\circ}\text{C}$ ) and has four different high temperature effusion cells. (b) and (c) the machine drawing showing the side and top view respectively.

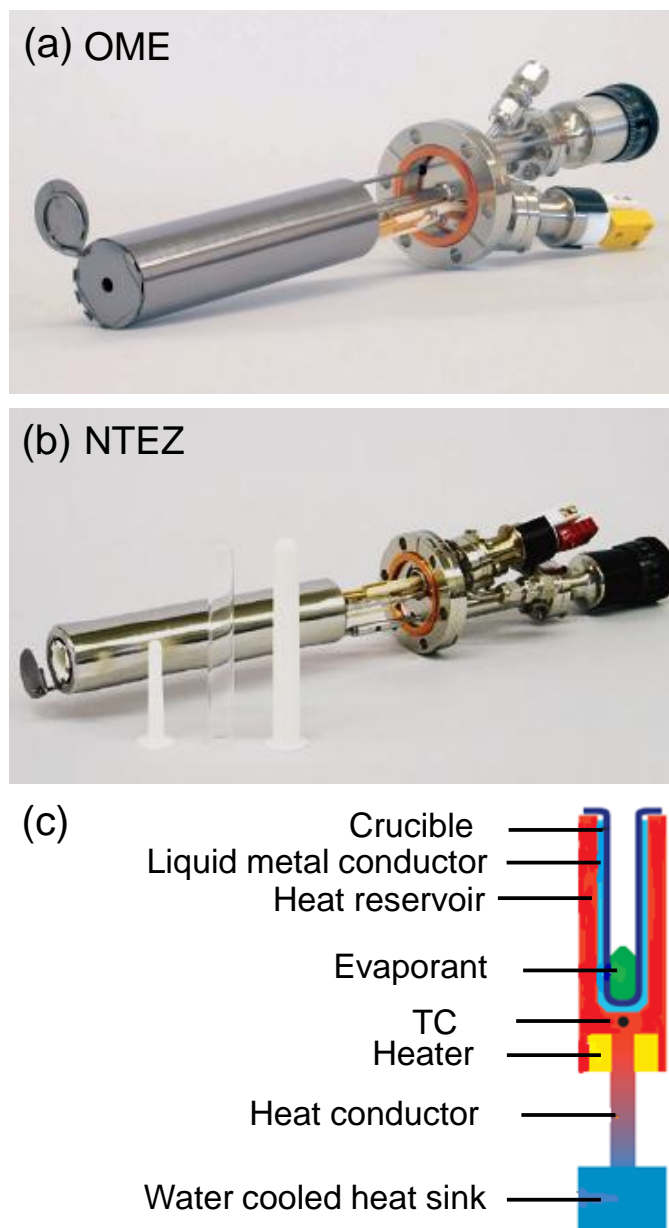


**Figure 2-2** Two different low temperature organic effusion cells. (a) OME effusion cell and (b) NTEZ effusion cell with quartz and PTFE crucibles. (c) The schematic diagram of different components of an effusion cell with crucible, conductor, heat reservoir, evaporant, thermocouple heaters and heat sink.

## 2.1 X-ray Photoelectron Spectrometer

The Analysis chamber is equipped with a SPHERA hemispherical electron analyzer, and a monochromatized Al  $K\alpha$  (photon energy = 1486.7 eV) X-ray source (XM 1000 MkII) for the XPS experiments. Figure 2-3a shows the different components of the XPS system that are installed in the Analysis chamber, along with a schematic diagram (Figure 2-3b) of the monochromator assembly with its three major components: X-ray source and manipulator, quartz-crystal mirror housing (monochromator), and position adjustment controls. The X-ray source has water-cooled aluminium-coated anode with two filaments (one short and one long) acting as the cathodes for focused and diffused operations respectively (Figure 2-3c). The short filament produces a high electron power density that gives rise to a bright X-ray emitting spot on the Al anode. It should be noted that the resulting photoemission signal from the sample is directly proportional to the brightness of the X-ray spot. On the other hand, the diffused source operates at a lower power density leading to a less focused X-ray spot on the sample. The maximum emission is 300 W at 15 kV for the shorter filament and 600 W at 15 kV for the longer filament, which are controlled by the X-ray source power supply. The monochromator exit leg and the Sphera analyser lens are installed at an angle which is in accordance with the fact that a high angle ( $\sim 80^\circ$ ) favours the collection of photoelectrons. The analyser can be operated in Constant Analyser Energy (CAE) mode or Constant Retard Ratio (CRR) mode. The input lens to the analyser collects the photoelectrons and focusses them to the entrance of the analyser. The input lens involves a double lens concept, where the first lens is responsible for the analysis area and angular acceptance and the second lens accelerates or retards the photoelectrons to the desired pass energy of the analyser. The seven channel electron multipliers (Channeltrons) are appropriately placed across the exit plane of the analyser to detect electrons with seven different transit energies simultaneously and thereby significantly enhancing the detection efficiency. A Channeltron typically multiplies a single electron by a factor of  $10^8$  times, resulting in an output current sufficiently large to be detectable by a preamplifier and ultimately the pulse counter electronics to generate an electron spectrum. The electronics control box for the XPS and the workstation used for data acquisition and analysis is shown in Figure 2-3d, and the X-ray control unit is fully software-controlled via an Ethernet interface with the data acquisition computer running a Windows XP operating system.

The binding energy scale of the X-ray photoelectron spectrometer can be calibrated by using the Ag  $3d_{5/2}$  peak at 368.3 eV, Au  $4f_{7/2}$  at 83.9 eV and Cu  $2p_{3/2}$  at 932.6 eV obtained with a pass energy 20 eV. The corresponding energy resolution of the instrument is also found to be 0.7 eV full width at half maximum for the Ag  $3d_{5/2}$  photoline (with a pass energy of 20 eV).

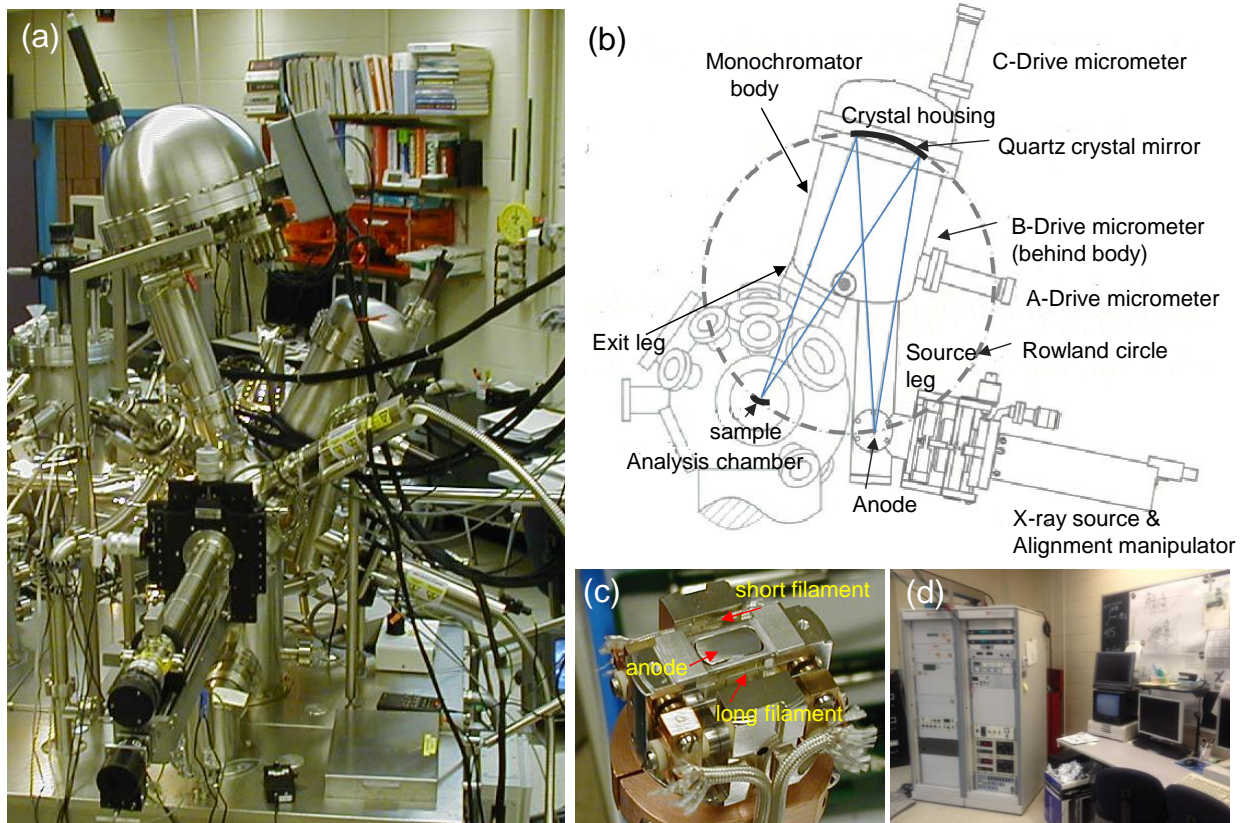


**Figure 2-3** X-ray Photoelectron Spectrometer, including (a) the Sphera hemispherical analyser, an X-ray mirror assembly, X-ray source and manipulator. (b) Schematic diagram of the monochromator assembly showing the X-ray source, alignment drives, the crystal mirror housing on the Rowland circle along with the positions of the sample and of the X-ray anode. (c) XM 1000 MKII X-ray source with the aluminum coated anode, and the long and short filament cathodes. (d) Control electronics and the data acquisition computer.

## 2.2 Variable Temperature Scanning Probe Microscope (VT-SPM):

Figure 2-4a shows the Omicron variable-temperature scanning probe microscope (VT-SPM) installed in the Analysis chamber, which is capable of both STM and AFM measurements. A more detailed view of the VT-SPM outside the chamber is shown in Figure 2-4b. The VT-SPM is designed to operate in a temperature range between  $-203^{\circ}$  and  $227^{\circ}\text{C}$  when combined with cooling and heating facilities. Sample heating in the microscope is achieved by an indirect radiative heating facility integrated into the sample stage whereas the sample cooling is achieved by using a continuous liquid helium flow cryostat. VT-SPM uses a unique vibration decoupling technique to provide effective noise reduction. The base plate is suspended by four springs (resonance frequency 2 Hz) and vibrations of the suspension system are prevented by using a non-periodic eddy current damping mechanism. To achieve this, the VT-SPM base plate is surrounded by a ring of copper plates seating in between the permanent magnets. The sample or tip transfer can be done by first blocking the spring suspension with the push-pull motion feedthrough (PPM, Figure 2-4b), and then the exchange by using a wobblestick (Figure 2-4a). The STM stage is then released and spring-loaded with the push-pull feedthrough. Figure 2-4c shows the scanner stage with a STM tip that can be moved vertically upward to reach the sample surface with the use of the piezo devices. The STM tip can be commanded to approach the surface with the help of a remote control box. After the STM tip reaches the tunneling position, experiments can be started by applying appropriate bias voltages and tunneling currents in the MATRIX control software (Figure 2-4d). A single tube scanner with a maximum scan range of  $10\ \mu\text{m} \times 10\ \mu\text{m}$  and z-travel of  $1.5\ \mu\text{m}$  can be used in the SPM microscope and a z resolution better than 0.1 nm can be achieved.

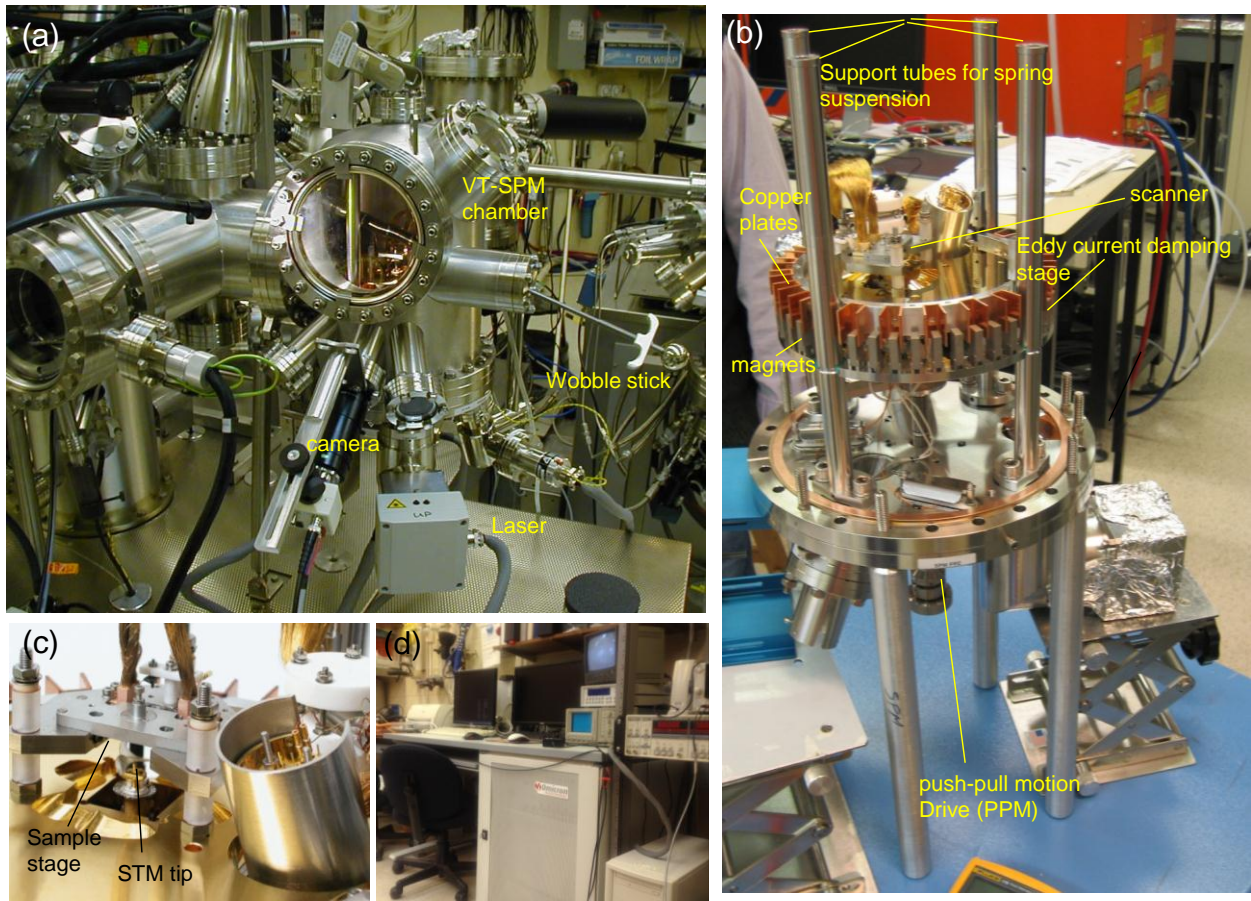


**Figure 2-4** Omicron VT-SPM system. (a) SPM chamber with a camera, a wobblestick and the laser electronics for AFM operation. (b) VT-SPM microscope outside the chamber. (c) STM scanner stage with a STM tip, (d) STM data acquisition computer with control electronics.

The material choice and the quality of the tip are important for obtaining high-resolution and reproducible STM images. During scanning, unwanted contact between the tip and the sample surface could occur. It is therefore necessary to choose a relatively hard material for the tip. Tungsten (W) tips have been widely used for most STM studies under UHV conditions. Molybdenum and iridium tips have also been used, while harder tips such as those fabricated from titanium carbide single crystals or ion-implanted diamond have been employed for specific applications.<sup>49</sup> STM studies under poor vacuum conditions or in air require a more inert material than W, such as platinum or gold, although these materials are soft and can be easily damaged as a result of accidental contact with the surface. In these cases, Pt-Ir alloys can be used instead.<sup>49</sup>

Different techniques to produce sharp STM tips have been reported in the literature.<sup>50,51,52</sup> One of the most effective techniques is the electrolytic etching process and it can be used to produce tips with a radius of curvature less than 10 nm. Klein et al. reported a lamellae drop-off technique to produce very sharp W tips, which uses electrolytic etching of a W wire in the lamellae of NaOH solution held in a ring electrode.<sup>53</sup> In our case, a modified version of Klein's technique is applied to prepare sharp W tips. Figure 2-5a shows our home-built electrolytic etching setup, with a Teflon holder for a ring electrode and a W wire (diameter 0.2-0.25mm). Freshly prepared 6 M NaOH solution is used as the etching solution. To obtain the ring electrode, a Cu wire is rolled against a circular object, e.g. a screwdriver, to give it a circular shape with a diameter not more than 7 mm. The Cu wire is cleaned with dilute hydrochloric acid and rinsed thoroughly with water before the etching process. Using our home-built Teflon holder, the ring electrode and a W wire (to be used as the STM tip) are mounted such that the W wire can be extended through the center of the ring electrode. The ring electrode with the W wire is then dipped in the 6 M NaOH solution and is withdrawn slowly so that a thin lamellae film of NaOH forms on the ring. The Cu wire and the W wire are connected as the reference and working electrodes, respectively, to an electrochemical station (CHI Instrument 660A). To minimize the strain on the thin W and Cu wires, metal clips were used. The W wire is then etched by using voltages 5-6 V and Amperometry method. The progress of the etching process is monitored closely as the etching of the W wire occurs at the perimeter of the W wire that is in the direct contact with the NaOH lamellae. At completion, the lower portion of the W wire, below the ring electrode, falls off, creating two sharp ends. As soon as the lower end begins to fall off, the etching should be stopped instantaneously to prevent the creation of a blunt tip. The upper portion of the W wire that is still hanging above the ring electrode can be checked with an optical microscope to assure that the tip so obtained has an ideal shape. After obtaining a sharp tip with a good shape it is cleaned by first dipping the tip in warm deionized water to dissolve all the excess NaOH

solution, and then followed by very carefully putting it under flowing water without putting too much stress on the tip edge for a few minutes. It has been observed that the STM tips with a relatively long taper produces a large region for mechanical resonance and results in the formation of an unstable tip. In order to obtain an STM tip with a shorter taper, the etching process is interrupted and the W wire along with the Teflon holder is inverted upside down and is restarted again.<sup>53</sup> This flipping step helps to produce W tips with a shorter taper, which proves to be more stable for STM experiments. A schematic diagram of the etching process is shown in Figure 2-5b. Figure 2-5c and 2-5d show, respectively, examples of a bad tip with longer taper and a better tip with shorter taper obtained by this etching technique.

The prepared STM tip is then clamped into a special STM tip holder and introduced in the UHV chamber. Before the STM experiment, the freshly prepared STM tip needs to be conditioned by applying successive voltage pulses (10 V) to flash away any oxides from the W tip surface.

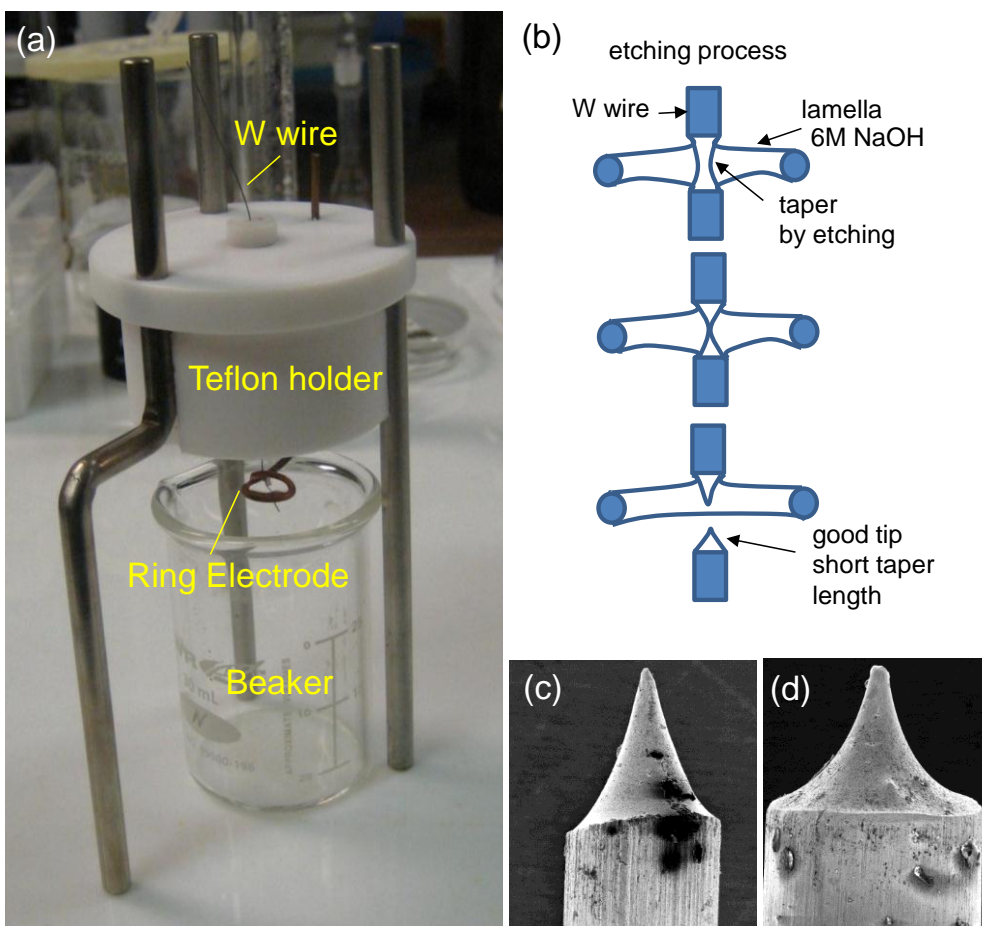


**Figure 2-5** (a) A home-built STM tip preparation setup with ring electrode, Teflon holder, W tip and NaOH lamellae. (b) Schematic diagram of the tip etching process. (c) Example of a bad tip with long taper and a pen like shape. (d) Example of a better tip with a shorter taper.

### **2.3 Sample Cleaning and generation of 7×7 reconstructed surface:**

Single-side polished Si(111) chips ( $11 \times 2 \text{ mm}^2$ , 0.3 mm thick), with a resistivity of  $0.005 \text{ } \Omega \text{ cm}$  (Virginia Semiconductor Inc.), have been used as the substrates for all the experiments. After cleaning the Si(111) sample with acetone and ethanol in an ultrasonic cleaner, the sample was introduced to the FEL chamber and transferred to the Analysis chamber via the transfer chamber using the appropriate magnetic transfer rods. The sample was further cleaned in vacuum first by outgassing at  $\sim 400^\circ\text{C}$  overnight and then followed by a flash-annealing procedure by passing a DC current directly through the sample to generate a contaminant-free  $7 \times 7$  reconstructed surface. The flash-annealing procedure involved annealing the outgassed sample rapidly to  $\sim 1200^\circ\text{C}$ , holding the sample at that temperature for  $\sim 5$  seconds, and then allowing the sample to cool rapidly to  $\sim 800^\circ\text{C}$  followed by slow cooling to room temperature at a rate of  $4\text{-}5^\circ\text{C/s}$ . This flash-annealing procedure was repeated several times until clean  $7 \times 7$  reconstructed Si(111) terraces with defect densities ( $< 1\%$ ) were observed in the STM images.

### **2.4 Details of Computations:**

The goal of computational surface science has always been to understand the basic principles that govern the physical and electronic structures of surfaces and the associated processes (such as surface reactions) that are different from that involving bulk matter. An example of the latter is the use of catalysts in various industrial processes. As modern experimental techniques, such as XPS and STM, provide specific knowledge about surface-related processes at the molecular level, computational techniques are being developed in a congruous fashion to explain the experimental observations and to provide better insights into the underlying phenomena and mechanisms.<sup>54</sup>

A wide range of surface processes can be modeled effectively with modern computational chemistry techniques. Classical and quantum mechanical methods are useful to explain such processes as dynamics of surface scattering, adsorption and desorption at surfaces. Electronic structure calculations for surface science problems are dominated by density functional theory (DFT) methods. DFT has been generally accepted as an invaluable tool in solid state physics when dealing with periodic structures. Many bulk properties have been accurately reproduced by DFT calculations in the Local Density Approximation (LDA), where the electron density is approximated to have the same value at every position in the system. DFT calculations have also proven to be invaluable for modelling chemical processes occurring on silicon and other semiconductor surfaces.<sup>55</sup> However, in cases such as those for molecules in which the electron density is typically far from spatially uniform, the LDA is not an appropriate approximation. The

Generalized Gradient Approximation (GGA) has been developed to explain the results not accountable by LDA. The most popular GGA exchange functional to date has been developed by Becke<sup>56</sup> and involves a single parameter, the value of which was optimized by fitting to the exactly known exchange energies of six noble gas atoms He through Rn.<sup>57</sup> On the other hand, Lee, Yang and Parr developed correlational functional commonly known as LYP that provides the full correlation energy of the system of interest. The LYP functional contains four empirical parameters fitted to the He atom and is the only functional that cancels the self-interaction error in an one-electron system.<sup>57</sup>

The complete specification of the exchange and correlation functional is expressed by connecting the two acronyms together in that order. For instance, BLYP calculation indicates that the calculation involves the Becke's exchange functional and Lee, Yang Parr's correlation functional.<sup>58</sup> B3LYP, BLYP, BP86, BPW91 are some of the more widely used GGA combinations in the literature to date. Initially developed to study vibrational absorption and circular dichroism, the B3LYP hybrid functional, consisting of Becke's three parameter exchange functional<sup>59</sup> and the Lee-Yan-Parr correlation functional,<sup>58</sup> has evolved as one of the most useful functionals for studying organic molecules in the gas phase and on surfaces of transition metals, semiconductors and oxides.<sup>60</sup>

As the adsorption and desorption processes of organic molecules depend on the individual surface sites, selected representative parts of a substrate surface can be considered and modeled by finite-size clusters focusing more on the specific surface site-molecule interactions. Higher level ab-initio computational methods can then be applied to gain insights into the interactions of different clusters with the adsorbate molecules.

Due to the complexity of the dimer-adatom-stacking-fault model structure of the Si(111)7×7 reconstructed surface, a Si<sub>16</sub>H<sub>18</sub> cluster is used in the present work to simulate one adatom-restatom pair of the 7×7 surface. The Si<sub>16</sub>H<sub>18</sub> cluster consists of one adatom (in the topmost layer) and one restatom (in the second top layer), with the pedestal atoms forming the third layer, and an additional fourth layer as the base layer to provide better rigidity to the cluster than the more commonly used Si<sub>9</sub>H<sub>12</sub> cluster. With the exception of the adatom and restatom, the Si atoms in the perimeter of the cluster are terminated with H atoms. Due to the presence of unsaturated dangling bonds on the adatom and restatom, we fix the adatom-to-restatom separation in the Si<sub>16</sub>H<sub>18</sub> cluster to 4.57 Å (as observed for the original adatom-restatom distance in a 7×7 unit cell) during geometry optimization, in order to avoid an unrealistic physical structure for the bare Si model surface. Once the optimized geometry of the bare Si<sub>16</sub>H<sub>18</sub> cluster

is obtained, subsequent geometry optimizations for the combined adsorbate-cluster system are performed without any geometrical constraint on the cluster.

As the adatom-restatom pair is represented by the  $\text{Si}_{16}\text{H}_{18}$  cluster (Figure 2-6a), a center adatom-center adatom pair of the  $7\times 7$  unit cell is represented by a  $\text{Si}_{12}\text{H}_{12}$  cluster<sup>61</sup> (Figure 2-6b) with the adatom-adatom distance constrained to 6.65 Å (as observed in the  $7\times 7$  unit cell). A bigger version of the  $\text{Si}_{12}\text{H}_{12}$  cluster is also constructed to represent a double adatom-adatom pair across the dimer wall. This  $\text{Si}_{26}\text{H}_{24}$  cluster (Figure 2-6c) allows more detailed study of the interactions between two adspecies on the two adatoms cluster.

In order to compare the adsorption process of glycine on  $\text{Si}(111)7\times 7$  with that on the  $\text{Si}(100)2\times 1$  surface, we have also considered a double-dimer cluster ( $\text{Si}_{15}\text{H}_{16}$ ) to represent dimers for the  $\text{Si}(100)2\times 1$  surface (Figure 2-6d). The  $\text{Si}_{15}\text{H}_{16}$  cluster has been reported to provide better results for the adsorption structures of a number of organic molecules than the single-dimer cluster ( $\text{Si}_9\text{H}_{12}$ ).<sup>62,63,64</sup> The use of the double-dimer cluster also facilitates the study of the dimer buckling effect and inter-dimer interactions, which cannot be realized in the single-dimer model. In order to build the  $\text{Si}_{15}\text{H}_{16}$  cluster, we start by fixing the positions of the Si atoms by using the appropriate crystallographic data for the bulk and the surface. Except for the double-dimer atoms, the Si atoms at the perimeter are terminated with H atoms. The structure is then fully optimized without applying any constraints to the Si cluster. This optimized Si cluster is subsequently used for determining the structure of the adsorbate, without any geometrical constraints on both the adsorbate and the Si cluster.

All the calculations in the present work study have been performed with Gaussian 03<sup>65</sup> and Gaussian 09<sup>66</sup> software. The calculations were run at a home-built computer cluster with eight Linux-based nodes, each of which with 8GB RAM and 4 cpu Pentium processing units. Apart from using the home-built cluster, the computations were also run on a supercomputer network system, SHARCNET (*Shared Hierarchical Academic Research Computing Network*). Both geometry optimizations and frequency calculations were performed by using five different split-valance basis sets, including 6-31G, 6-31G(d), 6-31G+(d), 6-31G+(d,p) and 6-31++(d,p), at the DFT level with B3LYP exchange and correlational functional. When employed with the DFT/B3LYP method, the 6-31G(d) basis set has been reported to provide better results, particularly for equilibrium structure and frequency calculations, for organic adsorbates, but at a lower computational cost, when compared to the larger basis sets, including 6-31G+(d), 6-31G++(d), 6-31G+(d,p) and 6-31G++(d,p). In addition, the adsorption energy ( $\Delta E$ ) for an adsorbate-substrate configuration (ASC) or adstructure is calculated as the difference between the total

energies of the optimized adstructure ( $E_{\text{adstructure}}$ ) and the sum of the total energies of adsorbate ( $E_{\text{adsorbate}}$ ) and the Si cluster ( $E_{\text{cluster}}$ ), i.e.  $\Delta E = E_{\text{adstructure}} - (E_{\text{adsorbate}} + E_{\text{cluster}})$ , using the same level of theory (DFT/B3LYP) and the same basis set [e.g. 6-31G(d)]. All the total energies are obtained without zero point energy corrections and no basis set superposition errors are made to  $\Delta E$  unless stated otherwise.

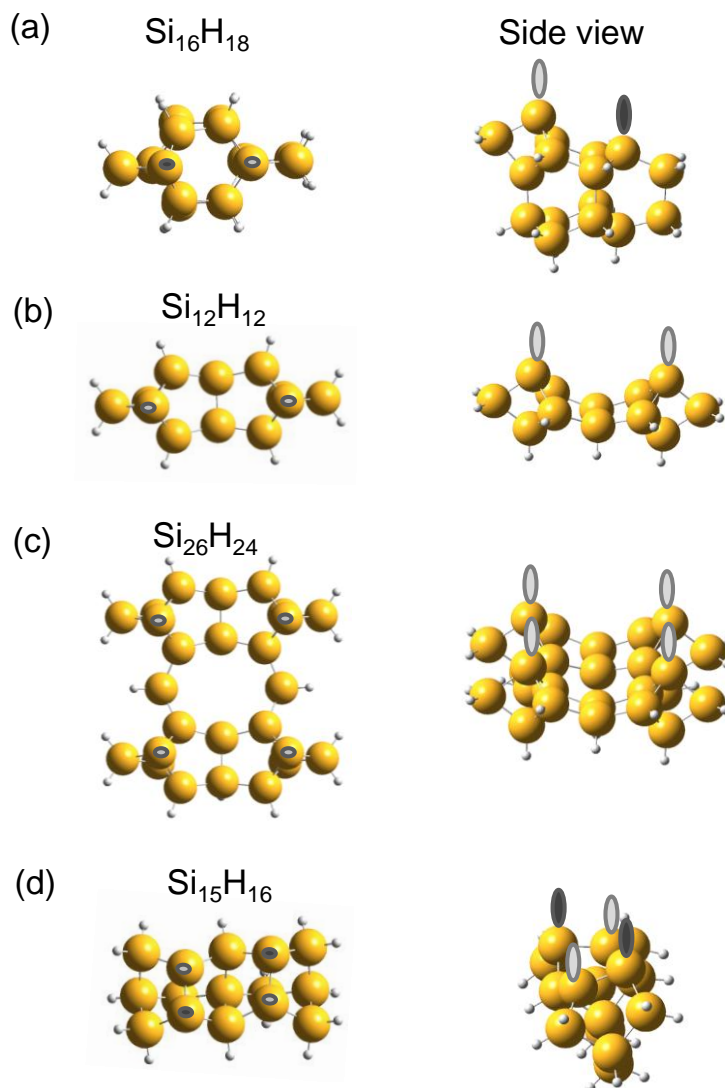


**Figure 2-6** Top views (left) and side views (right) of different clusters for modeling selected parts of the Si surface: (a)  $\text{Si}_{16}\text{H}_{18}$  cluster to represent the adatom-restatom pair, (b)  $\text{Si}_{12}\text{H}_{12}$  to represent a single adatom-adatom pair across the unit cell. (c)  $\text{Si}_{26}\text{H}_{24}$  to represent two adatom-adatom pairs across the dimer wall, all for the Si(111) $7\times 7$  surface, and (d)  $\text{Si}_{15}\text{H}_{16}$  cluster to represent the double dimer cluster for the Si(100) $2\times 1$  surface.

## Chapter 3

### Glycine adsorption on Si(111)7×7

#### 3.1 Hydrogen-bond mediated transitional adlayer of glycine on Si(111)7×7 at room temperature<sup>\* †</sup>

##### 3.1.1 Introduction

Thin films of amino acids evaporated in ultrahigh vacuum on well-defined solid surfaces have been studied extensively by a number of techniques, including X-ray photoelectron spectroscopy (XPS), scanning tunneling microscopy (STM), and thermal desorption spectrometry (TDS).<sup>67,68,69,70,71,72,73,74,75,76</sup> These studies focus specifically on interfacial bonding, conformation, thermal stability, self assembly and chirality of the amino acid films on various metal and oxide substrates. With the amino ( $-\text{NH}_2$ ) and carboxyl ( $-\text{COOH}$ ) groups in common, different amino acids ( $\text{NH}_2\text{CHR}\text{COOH}$ ) are identified by their unique side chains (R). As the building blocks of peptides and proteins, amino acids, and glycine in particular (with R being the H atom), are intensively studied to provide the fundamental reference information for more complicated proteins and peptides. It is well known that glycine exists as neutral molecules ( $\text{NH}_2\text{CH}_2\text{COOH}$ ) in the gas phase and as zwitterions ( $\text{NH}_3^+\text{CH}_2\text{COO}^-$ ) in solids and solutions, while deprotonated or anionic ( $\text{NH}_2\text{CH}_2\text{COO}^-$ ) and protonated or cationic ( $\text{NH}_3^+\text{CH}_2\text{COOH}$ ) forms are commonly found in solutions. When glycine is evaporated onto a substrate, the prevailing form is found to depend on the nature and temperature of the substrate and the film thickness. A thick (multilayer) glycine film always exists in the zwitterionic form regardless of the substrates, while the other forms could occur in thin films due to the interactions between glycine and the substrates that inhibit proton transfer among glycine molecules. Low substrate temperature or an inert substrate would therefore favour the formation of zwitterions even for thin films due to reduced interactions with the substrates. For example, glycine was found to adsorb in the zwitterionic form on Pt(111)<sup>67</sup> at low temperature ( $< 250$  K), and on Au(111) at room temperature (RT)<sup>68</sup>, but as the anionic form on Cu(110)<sup>69,70,71</sup> and Cu foil<sup>72</sup> at RT. For NiAl(110)<sup>73</sup> and  $\text{Al}_2\text{O}_3$ -film substrates,<sup>74</sup> glycine adsorbs in both the zwitterionic form at low temperature ( $< 250$  K) and anionic form at RT. Most of the earlier studies on glycine adsorption on

---

<sup>\*</sup> Reprinted with permission from [L. Zhang, A. Chatterjee, M. Ebrahimi, K. T. Leung, J. Chem. Phys, 130, 121103 (2009)]. Copyright [2009], American Institute of Physics.

<sup>†</sup> My specific contributions were research idea, XPS data collection (with Dr. Lei Zhang), data analysis and DFT calculations.

different substrates mainly focus on the thin-film (monolayer) and thick-film (multilayer) regimes. However, the transition from monolayer to multilayers is not well understood. This intermediate regime is especially important for investigating the chemical bonding involved in the evolution from the chemisorbed state to the zwitterionic form. Depending on the nature and temperature of the substrate, glycine could bond to the substrate in several ways: (a) through the N lone pair of the amino group,<sup>70</sup> (b) with the N atom after one N–H bond cleavage,<sup>76</sup> and (c) with one of the O atoms in unidentate coordination, or (d) with both O atoms in bidentate or bridging coordination after O–H bond cleavage.<sup>69,70,71,72,75</sup> In the present study, we report a detailed photoemission study of the growth evolution of glycine on Si(111)7×7 with focus on this intermediate regime. In addition to its obvious practical interest as a semiconductor surface, the 7×7 surface offers unique electronic and surface structures with directional dangling-bond sites<sup>32</sup> for understanding the fundamental interactions involved in organosilicon chemistry. We demonstrate, for the first time, the presence of a transitional adlayer between the interfacial (first) adlayer and the zwitterionic multilayer film. The N 1s spectra reveal that the interfacial adlayer bonds to the 7×7 surface through the N atom by N–H bond cleavage, while the transitional adlayer involves N···HO hydrogen bonding. The presence of hydrogen bonding in the transitional adlayer suggests its viability as a reversible platform for linking with other biomolecules by their hydrogen bonding interactions, thereby providing a versatile method for biofunctionalization of the Si surface.<sup>77</sup>

### 3.1.2 Experimental Details

The experimental procedure has been discussed in detail in the second chapter. Furthermore, glycine (with a normal melting point of 182°C) was deposited onto the Si substrates by thermal evaporation using a water-cooled effusion cell (designed specially for organic materials evaporation) in a separate sample preparation chamber. During evaporation, the temperature of the effusion cell was kept at 140°C, leading to a partial pressure of  $5.0 \times 10^{-9}$  Torr for the 30-amu mass fragment (corresponding to the base ion  $\text{NH}_2\text{CH}_2^+$  of glycine), as registered by a quadrupole mass spectrometer. In this study, glycine was deposited sequentially onto the Si substrate held at RT. The amount of glycine deposition was indicated by the total deposition time, which can be used to provide a measure of the relative film thickness. After each deposition, the Si 2p, O 1s, N 1s, and C 1s core-level spectra were measured with a pass energy of 20 eV, which gave an effective linewidth of 0.8 eV full width at half maximum (FWHM) for the Ag 3d<sub>5/2</sub> photoline at 368.3 eV. For each deposited glycine film, the energy scale was referenced to the Si 2p<sub>3/2</sub> photoline (99.3 eV) of the substrate. The spectra were fitted with Gaussian-Lorentzian lineshapes after appropriate background removal by using the CASA-XPS software.

### 3.1.3 Results and Discussion

Figure 3-1 shows the C 1s, N 1s and O 1s spectra of glycine films with different thickness as represented by the deposition time. For the lowest exposure of 10 s, the N 1s spectrum (center panel) exhibits a dominant feature at 399.1 eV attributed to N–Si bond, in good accord with the N 1s features at 398.8-399.4 eV found for dissociative adsorption of amines (e.g. hexylamine, N-methylpentylamine) via the N–H bond cleavage on Si(100)2×1 and Si(111)7×7 at RT.<sup>78,16,10,79</sup> Further deposition to 30 s leads to saturation of the feature at 399.1 eV and the emergence of a new feature at 401.4 eV, which gradually increases in intensity at 120-s deposition and becomes saturated at 240-s deposition with the saturation intensity about 1.5 times that of the feature at 399.1 eV. At the 480-s deposition, a new feature appears at 402.2 eV, with the intensities of both features at the lower binding energy remaining nearly unchanged, and it becomes the only prominent feature for 960 s and longer deposition times. The binding energy of this feature agrees with that of the protonated amino group (NH<sub>3</sub><sup>+</sup>).<sup>67,74,76,80</sup> Given that the corresponding binding energy of the O 1s spectrum for the 960-s deposition is found to be consistent with that of carboxylate (COO<sup>-</sup>) (see below), this glycine film exists predominantly in the zwitterionic form, as expected for glycine in the bulk state.

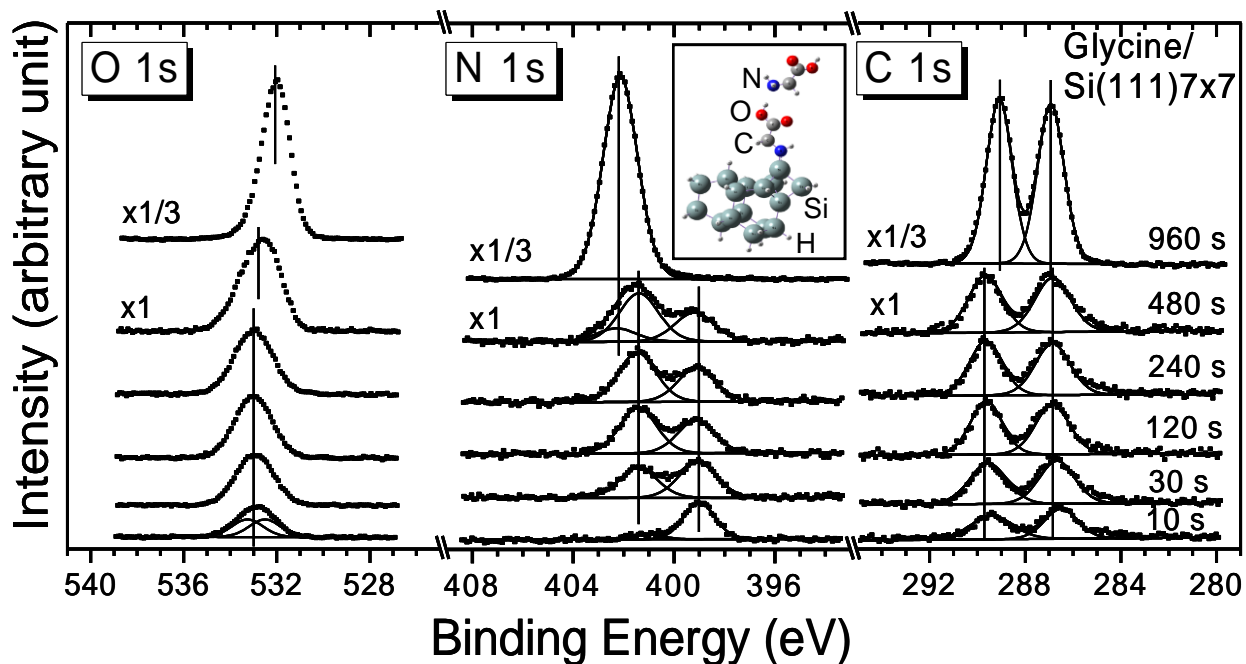
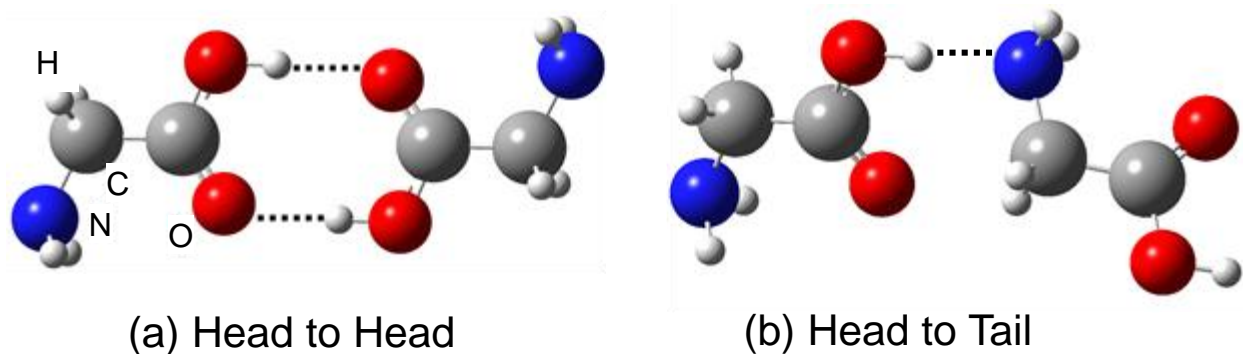


**Figure 3-1** XPS spectra of the C 1s (right), N 1s (center), and O 1s regions (left) of glycine on Si(111)7×7 as a function of deposition time. Inset shows the optimized geometry of a N-bonded glycine adstructure coupled to a second glycine molecule through an XPS spectra of the C 1s (right), N 1s (center), and O 1s regions (left) of glycine on Si(111)7×7 as a function of deposition time. Inset shows the optimized geometry of a N-bonded glycine adstructure coupled to a second glycine molecule through an O–H···N hydrogen bond on a Si<sub>16</sub>H<sub>18</sub> model surface, obtained by a DFT/B3LYP calculation with a 6-31++G(d,p) basis set.

The new N 1s feature observed at 401.4 eV has not been reported for glycine in the literature. In an early study by Clark et al.<sup>80</sup> on a series of glycine and their peptides (in powder form), the N 1s feature for a neutral amino group (–NH<sub>2</sub>) was found to be generally located at 400.4 eV, i.e. 1.8 eV lower than that for –NH<sub>3</sub><sup>+</sup> found in the zwitterions. The feature at 401.4 eV therefore corresponds to a new N species that is more positively charged than that in NH<sub>2</sub> but less so than that in NH<sub>3</sub><sup>+</sup>. Here it is reasonable to assume that the final state relaxation and screening effects are similar for different N species of the glycine film on Si(111)7×7.<sup>81</sup> We attribute this feature to N involved in the N···H–O hydrogen bonding with the carboxyl group of another glycine molecule. Similar N···H–O hydrogen bonding has been reported by O’Shea et al.<sup>82</sup> in the adsorption of isonicotinic acid (pyridine-4-carboxylic acid) on TiO<sub>2</sub>(110), where the N in the pyridine ring of one molecule forms a hydrogen bond with the carboxyl

group of another molecule in the layer above. The 1s binding energy of the N atom involved in the hydrogen bond (407.0 eV) is 1.7 eV higher than that without hydrogen bonding in isolated pyridine (405.3 eV). The larger N 1s core-level shift induced by hydrogen bonding for isonicotinic acid (1.7 eV) than that for glycine (1.0 eV)<sup>‡</sup> is due to their different N local chemical environments. Using DFT calculation, O’Shea et al. further illustrated that the strength of the hydrogen-bonding interaction (and therefore the core-level shift) could increase with increasing molecular cluster size due to a process known as cooperative hydrogen bonding.<sup>82</sup>

Owing to the directionality and selectivity, hydrogen bonding has also been used to account for self-assembly of small organic molecules on well-defined substrates as observed by STM, including, e.g., pairs and double rows of cysteine on Au(110),<sup>82,83</sup> L-methionine nanogratings on Ag(111),<sup>84</sup> 4-[*trans*-2-(pyrid-4-yl-vinyl)]benzoic acid (PVBA) chains on Ag(111),<sup>85</sup> and hexagonal network of melamine and perylene tetra-carboxylic di-imide on Ag/Si(111)-( $\sqrt{3}\times\sqrt{3}$ )R30°.<sup>86</sup> Intermolecular hydrogen bonding was also proposed to explain the “(3×2)pg” LEED pattern observed for glycinate on a Cu(110) surface.<sup>87</sup> Among neutral glycine molecules, hydrogen bonding can occur in two possible configurations shown in the following schemes: (a) a head-to-head configuration between the carboxyl groups to form double O–H···O hydrogen bonds as in cysteine pairs on Au(110);<sup>82</sup> and (b) a head-to-tail configuration between the carboxyl and amino groups (O–H···N or N–H···O) as in PVBA chains on Ag(111).<sup>85</sup>



We therefore assign the N 1s feature at 401.4 eV observed in this study to an O–H···N head-to tail hydrogen bonding configuration, which may form between the first adlayer (interfacial layer) and the second and possibly third adlayers (transitional layer). A “transitional region” has been noted in the earlier thermal desorption profiles of glycine films on Pt(111)<sup>80</sup> and Ni foil.<sup>88</sup> The N 1s spectral

<sup>‡</sup> This value was calculated by using the N 1s binding energy for the hydrogen bonding feature (401.4 eV) and that for neutral glycine molecules (400.4 eV) reported by Clark et al.<sup>17</sup>

evolution with the deposition time clearly reveals three different growth stages of glycine on Si(111)7×7: (1) formation of the covalently bonded interfacial layer; (2) development of the hydrogen-bonded transitional layer; and (3) continuous growth of the zwitterionic multilayer.

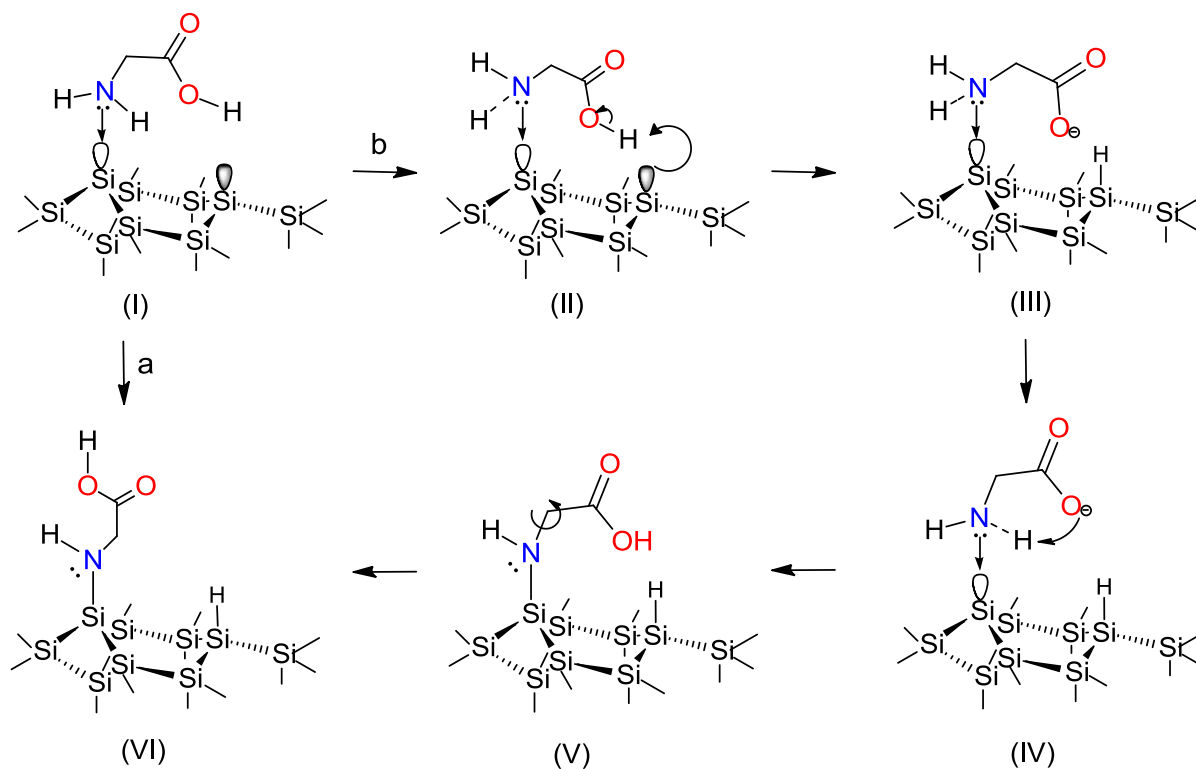
In the inset of Figure 3-1, we show a schematic diagram of the N-bonded glycine adstructure coupled to a second glycine molecule through an O–H···N head-to-tail hydrogen bond on a modeled Si surface. The electronic structure calculation was performed by using the GAUSSIAN 03 software. A Si<sub>16</sub>H<sub>18</sub> cluster<sup>89</sup> was used to represent the restatom–adatom sites at the faulted half of the Si(111)7×7 unit cell, after adopting the dimer-adatom-stacking fault model of Takayanagi et al.<sup>32</sup> All geometries including the Si<sub>16</sub>H<sub>18</sub> cluster and plausible glycine adstructures were optimized by using the DFT method with the B3LYP hybrid functional<sup>59,58</sup> and 6-31++G(d,p) basis set, and no imaginary frequencies were found in the corresponding frequency calculations. Evidently, bonding to the Si adatom is found to give a more stable equilibrium geometry than bonding to the restatom. The calculated bond length for the O–H···N hydrogen bond (1.89 Å) is found to be in general accord with that expected of a typical hydrogen bond (1.6–2.0 Å). Furthermore, the calculated N 1s orbital energy for the hydrogen-bonded glycine (419.5 eV), representing the transitional adlayer, is higher than that for the N-bonded glycine (418.5 eV), representing the interfacial layer. Within the limit of Koopmans' theorem,<sup>90</sup> this ordering of calculated orbital energies is in good accord with that of the corresponding observed N 1s binding energies, which provides further support for our spectral assignment of the N 1s features.

Figure 3-1 also shows the evolution of the corresponding O 1s spectra of the glycine film with increasing deposition time (left panel). Both the position (533.0 eV) and the width (1.9 eV FWHM) of the O 1s peak appear to be unchanged for deposition up to 240 s, indicating similar chemical environments of the O atoms in the interfacial and transitional layers. Given that a large O 1s chemical shift of 1.3 eV to the higher binding energy has been observed for formic acid from chemisorbed (formate in a unidentate configuration) to physisorbed states,<sup>91</sup> the single-peak O 1s feature therefore rules out the formation of O–Si covalent bonds in the interfacial layer. For the 10-s deposition, we fitted the corresponding O 1s spectrum (of the non-bonded carboxylic acid group) with two components of equal intensity and width at 532.5 eV and 533.3 eV, corresponding to the carbonyl O (C=O) and the hydroxyl O (OH), respectively. These binding energies are in good accord with those of carbonyl O (532.0 eV) and of hydroxyl O (533.3 eV) of mercaptopropionic acid bonded through the S end on Au(111).<sup>92</sup> The present assignment of the lower binding energy (532.5 eV) to carbonyl O is also in good agreement with that in acetaldehyde and acetone (532.7 eV),<sup>93</sup> and in PTCDA (532.4 eV).<sup>94</sup> For the 480-s deposition, the

corresponding O 1s peak becomes asymmetric and appears to be shifting to the lower binding energy side. Further deposition to 960 s leads to a much sharper O 1s peak (1.45 eV FWHM) and a lower binding energy position of 532.1 eV, which suggests that the O atoms in the multilayer film have a more homogeneous chemical environment and are more negatively charged. The observed binding energy position corresponds to that of carboxylate,<sup>67</sup> reflecting the zwitterionic nature of the multilayer film.

Figure 3-1 (right panel) shows that for deposition up to 480 s, the C 1s spectra reveal two well-defined peaks at 286.9 eV and 289.7 eV, corresponding to, respectively, methylene (>CH<sub>2</sub>) and carboxyl C,<sup>74</sup> with their intensity ratio (1:1) found to be in good accord with their stoichiometry. For the 960-s deposition, a notable shift of the carboxyl C 1s peak to the lower binding energy by 0.6 eV is found, while the location of the methylene C 1s peak remains unchanged. A similar binding energy shift in the corresponding O 1s has been discussed previously. These shifts found for the multilayer are consistent with the presence of a delocalized negative charge over the carboxylate group of the zwitterions, in contrast to the carboxyl group of the N-bonded adstructure (in the transitional and interfacial layers). The resulting energy separation between these two C 1s peaks found for the multilayer (2.2 eV) is in good accord with that for the glycine zwitterionic multilayers found on other substrates.<sup>67,70,74</sup> Conversely, the larger energy separation found for the shorter deposition time (2.8 eV) therefore confirms the non-zwitterionic nature of the interfacial and transitional layers.

The adsorption properties of glycine on Si(111)7×7 and Si(100)2×1 are found to be quite different. In particular, instead of the formation of O–Si bonds from O–H bond dissociation in glycine on Si(100)2×1 as observed by Lopez et al.<sup>75</sup> and calculated by Qu et al.,<sup>95</sup> formation of N–Si bonds as a result of N–H dissociative adsorption of glycine on Si(111)7×7 is found.



**Figure 3-2** Proposed (a) direct and (b) indirect proton-transfer mechanisms for the formation of N-bonded glycine (in the first adlayer) on an adatom-restatom model surface of Si(111)7×7.

As shown in Figure 3-2, based on the electrophilic-nucleophilic consideration,<sup>96,97</sup> the formation of a dative bond between the electron-deficient Si adatom and the N lone pair (Structure I) is more favourable than that between the adatom and the O lone pair. Hydrogen abstraction from a dative-bonded adduct can occur directly by an electron-rich Si restatom (pathway a) or indirectly via an intramolecular proton transfer (pathway b). Given that the separation between the N and O atoms in glycine (2.8 Å) is compatible with the adatom-restatom separation (4.6 Å),<sup>37</sup> the restatom can abstract a proton from the OH group (Structure II), producing a temporary negatively charged carboxylate species (Structure III), which would undergo an intramolecular proton transfer from the amino group (Structure IV) to produce Structure V and to Structure VI upon rotation around the C–N bond axis. Because the N–H bond distance (1.01 Å) is considerably shorter than the adatom-restatom separation (4.6 Å), the direct proton transfer (pathway a) is expected to be less favourable than the indirect pathway (pathway b) on the Si(111)7×7 surface. In the case of Si(100)2×1, the corresponding separation between the electron-rich up-atom and electron-deficient down-atom of the Si dimer (2.3 Å) is compatible with both the N–H (1.01

Å) and O–H bond lengths (0.91 Å) for direct H abstraction. Indeed, the DFT calculation of glycine on Si(100)2×1 by Qu et al.<sup>35</sup> showed that O–H bond dissociation has a lower activation barrier than the N–H bond dissociation, which leads to exclusive unidentate O bonded product. It should be noted that the bidentate adstructure of glycine through O–H and N–H dissociation on the two adatoms of the Si(111)7×7 proposed by Huang et al.<sup>10</sup> is not physically possible due to the large separation between the adatom and its nearest adatom neighbour (6.65 Å) compared to the O-to-N separation in glycine (2.8 Å).

### 3.1.4 Summary

We have studied the growth of glycine on Si(111)7×7 at room temperature in ultrahigh vacuum by X-ray photoelectron spectroscopy. Three N 1s features at 399.1, 401.4 and 402.2 eV emerge sequentially with increasing deposition time, which indicates three distinct stages in the growth process. Initially, glycine undergoes N–H dissociation to form a N-bonded adstructure at the surface, followed by the formation of a transitional layer (1-2 adlayer thick), which is characterized by the presence of the intermolecular O–H···N hydrogen bonding. Continued deposition gives rise to multilayers with glycine in the zwitterionic form. The evolution of the O 1s and C 1s features with the deposition time also supports this growth model. An intramolecular proton transfer mechanism has been proposed to account for the adsorption process through the amino group. The present observation of intermolecular N···H–O hydrogen bonding in amino acid, for the first time by XPS, has opened up a new way of detecting surface hydrogen bonds. Our preliminary study<sup>12</sup> further shows that the transitional layer can also be formed not only between the adsorbed glycine layer (the first adlayer) and other biomolecules with an amino group (e.g., glycylglycine, adenine) but also reversibly, potentially providing a facile way to change the surface reactivity and selectivity of the biomolecular functionalized Si surface.

## 3.2 Computational surface chemistry of glycine on Si(111)7×7 and Si(100)2×1: Dissociative adsorption through adduct formation<sup>§</sup>

### 3.2.1 Introduction

The two notable semiconductor surfaces, Si(111)7×7 and Si(100)2×1 offer unique bonding sites, each providing one and two directional dangling bonds, respectively, for interactions with approaching molecules. These fundamental differences account for the different chemical selectivities of these Si surfaces towards different adsorbates. Understanding the interactions between amino acid molecules and these Si surfaces is therefore technologically important for the development of future biodevices. As the simplest naturally occurring amino acid, glycine (NH<sub>2</sub>CH<sub>2</sub>COOH) also represents a unique type of bifunctional molecules, with an amino (–NH<sub>2</sub>) and a carboxylic acid (–COOH) groups. Appropriate coupling of these two functional groups to different surface sites offers surface selectivity for controlling the final adstructures. With one of the functional groups bonded to the surface and the other free to interact with incoming molecules, these bifunctional molecules can also be important as linker molecules to form multilayer structures by hydrogen bonding for biodevice and molecular electronics applications.<sup>98</sup>

To date, there are only four studies reported for glycine (and other amino acids) on Si(111)7×7 and Si(100)2×1 surfaces<sup>75,95,76,99</sup> and a recent computational work on Si(100)-c(4×2) surface.<sup>100</sup> The adsorption of glycine on Si(100)2×1 surface has been investigated by Lopez et al.<sup>75</sup> using high resolution electron energy loss spectroscopy (HREELS). The authors concluded that glycine adsorption mainly occurs via dissociation of the O–H bond of the carboxylic acid group and formation of O–Si bond, instead of dissociation of the N–H bond in the amino group and formation of N–Si bond. In a separate computational work, Qu et al.<sup>95</sup> later showed that on Si(100)2×1 the formation of O–Si bond is preferred over the formation of N–Si bond both thermodynamically (with the former producing a more negative adsorption energy than the latter) and kinetically (with N–H bond dissociation requiring more activation energy than O–H bond dissociation). This reaction has been proposed to go through an initial trapping step involving the formation of a datively bonded adduct. Qu et al. also showed that the adsorption energy of the Si←N adduct is much less than that of the Si←O adduct. This is not surprising in the formation of the initial adduct because the lone-pair electrons of the nitrogen atom in the amino group are more readily available for donation to a Lewis acid (e.g, a Si dangling-bond site) than that of the oxygen

---

<sup>§</sup> Reprinted with permission from [A. Chatterjee, L. Zhang, K. T. Leung, Chem. Phys. Lett., 508, 219 (2011)]. Copyright [2011], Elsevier B. V.

atom. Qu et al. further concluded that the lower O–H bond dissociation energy and the larger O–Si bond strength lead to 100% selectivity towards the formation of O–H dissociative product of glycine on Si(100)2×1.<sup>95</sup> For glycine adsorption on Si(111)7×7 surfaces, Huang et al.,<sup>76</sup> using HREELS and X-ray photoelectron spectroscopy (XPS), found that both the amino and carboxylic acid groups of glycine undergo reaction with the Si surface, and they concluded that these reactions lead to the formation of a bidentate adstructure that bridges two adatoms of the 7×7 unit cell. Realizing that the adatom-to-adatom separation (>6.65 Å) appears physically too large for simultaneous bidentate bonding through the –NH<sub>2</sub> and –OH termini of a glycine molecule (with a separation of 4.44 Å), we recently reexamined the adsorption process of glycine on Si(111)7×7 as a function of exposures with XPS.<sup>99</sup> We concluded that glycine adsorbs in a unidentate fashion to a single Si adatom by N–H bond dissociation of the amino group and formation of N–Si bond. The contrasting results obtained for the adsorption of glycine on the two different Si surfaces, i.e. Si(111)7×7 vs Si(100)2×1, demonstrate the remarkable differences in the chemical selectivities of the Si surfaces as dictated by their different local bonding structures.

The dimer-adatom-stacking-fault model for Si(111)7×7 reconstruction as proposed by Takayanagi et al.,<sup>32</sup> has been discussed in detail in the first chapter. Therefore it is known that the adatom-restatom pair (with the adatom-to-restatom separation of 4.57 Å) provides the most important reaction site, because the smaller organic molecules, including glycine, have similar dimensions.<sup>97</sup> Furthermore, the adatom is reported to have less electron occupancy than the restatom due to a small charge transfer from the adatom to the restatom, resulting in formal charges of +7/12 for the corner adatom and –1 for the restatom.<sup>101</sup> Consequently, the topmost layer of the Si(111)7×7 surface (with the adatoms) is more electrophilic in nature, in contrast to the nucleophilic next layer with the restatoms. Because a center adatom has two neighbouring restatoms, it has even less electron occupancy and is therefore more electrophilic than the corner adatom. The electrophilic adatoms should therefore be more reactive towards a nucleophilic functional group (e.g. –NH<sub>2</sub> of glycine) than the restatoms.

The Si(100)2×1 reconstruction, on the other hand, involves the formation of asymmetric buckled dimers on the surface. In this buckled dimer model for the Si(100)2×1 surface, one of the dangling bonds from each of two neighbouring atoms forms a strong  $\sigma$  bond with each other, while the remaining dangling bond combines with that of a neighbouring atom to form a weak  $\pi$  bond, creating a Si-Si dimer.<sup>38,102</sup> Due to the thermal motion at room temperature, the dimer is buckled with a dynamical tilt that causes an asymmetric electron distribution.<sup>103</sup> Charge transfer from the down-atom to the up-atom of the buckled dimer leads to the formation of an electrophilic-nucleophilic pair.<sup>38,104</sup> This structure of

nucleophilic top layer (of the up-atoms) followed by an electrophilic second layer (of the down-atoms) is in marked contrast to the case of Si(111)7×7 surface. The difference in their electronic environments leads to different surface reactions, resulting in their selectivities towards specific organic molecules with different functional groups.<sup>97,104</sup> In the present study, we use ab-initio calculations based on the Density Functional Theory (DFT) to demonstrate the importance of these basic chemistry concepts, particularly the formation of a viable adduct, in the adsorption of glycine on Si(111)7×7 and Si(100)2×1 surfaces.

### 3.2.2 Results and Discussion

Figure 3-3a shows the potential energy diagram along with the adsorption energies of glycine on the Si<sub>16</sub>H<sub>18</sub> cluster, and the respective optimized geometries of the adstructures. As the unreacted glycine molecule with the amino group oriented towards the Si adatom approaches the cluster, the N-to-Si separation is reduced. At a N-to-Si separation of 1.95 Å, a stable Si←N adduct state (II, with  $\Delta E = -107.5 \text{ kJ mol}^{-1}$ ) with respect to the unreacted state (I) can be obtained by appropriate geometry optimization. From this stable adduct state to the final N–H dissociative adsorption state (IV, with  $\Delta E = -237.9 \text{ kJ mol}^{-1}$ ), a transition state (III, with  $\Delta E = -78.3 \text{ kJ mol}^{-1}$ ) involving N–H bond dissociation can be observed at a N-to-Si separation of 1.83 Å. The corresponding N–H bond length in glycine is found to increase from 1.01 Å in the unreacted glycine molecule (I) to 1.05 Å in the adduct state (II) and to 1.31 Å in the transition state (III), which marks the onset of N–H bond dissociation. In the final N–H dissociative adsorption state (IV), the N-to-Si separation becomes the N–Si bond (1.70 Å). The evolution of increasing N–H bond length with decreasing N-to-Si separation illustrates the process of N–H bond dissociation and concomitant N–Si bond formation. The presence of the stable Si←N adduct (II), as an intermediate state trapped between the unreacted and the final product states, is therefore essential in the formation of the final adsorption state.

We have also studied the corresponding pathway leading to the O–H dissociative adstructure (V, with  $\Delta E = -268.6 \text{ kJ mol}^{-1}$ ). An extensive search in the potential energy surface for an analogous Si←O adduct that involves dative bonding from the O atom of –OH or >C=O group of glycine to the Si adatom has been conducted. No stable adduct state is found. It should be noted that the adstructure V is obtained by geometry optimization of the pre-dissociated NH<sub>2</sub>CH<sub>2</sub>COO· and H· fragments attached, respectively, to the Si adatom and restatom. Although  $\Delta E$  for the O–H dissociative adstructure appears more negative than that for N–H dissociative adstructure, the lack of a Si←O adduct indicates that such an adstructure cannot be realized. On the other hand, once the stable Si←N adduct is formed, the eventual proton

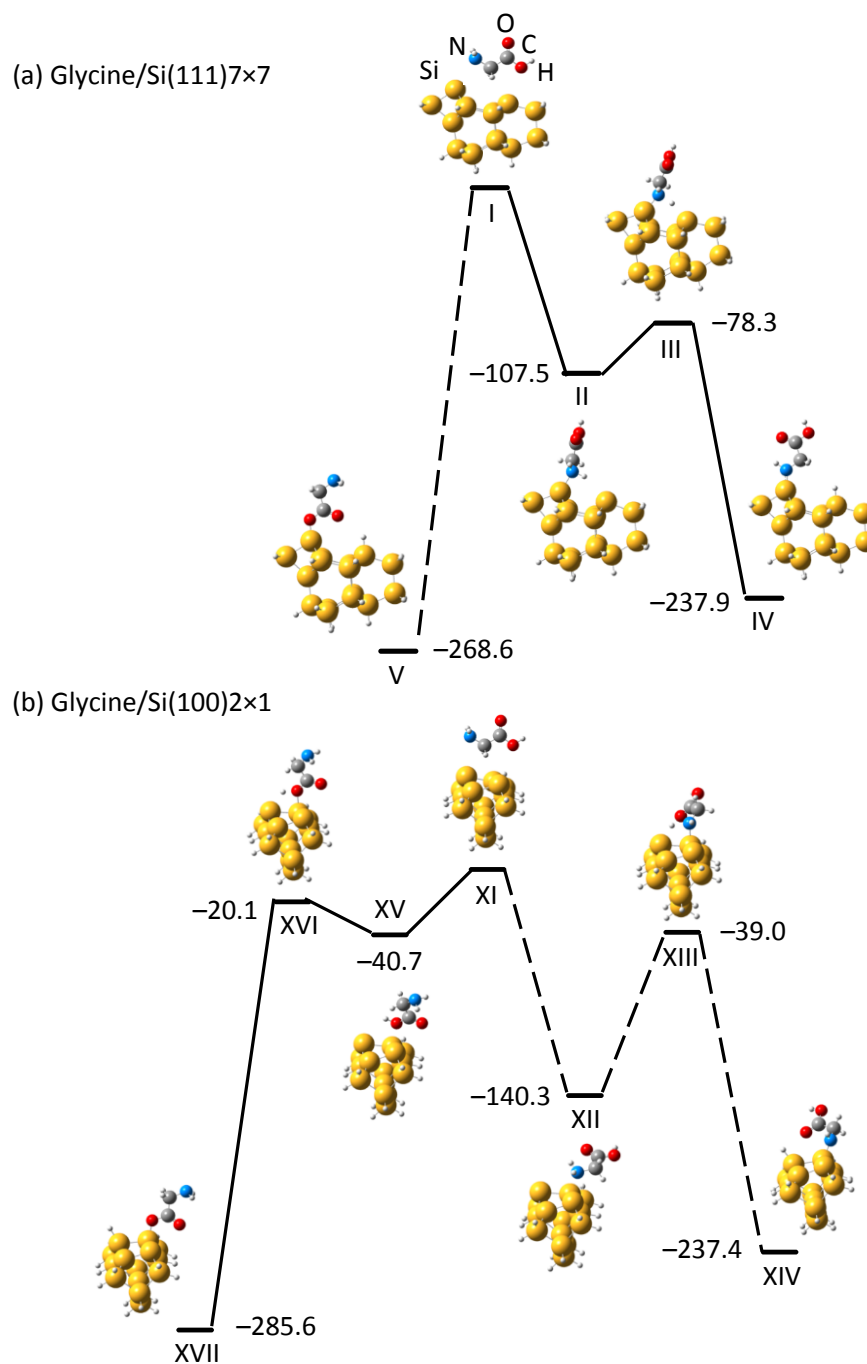
transfer to the restatom from the Si←N adduct could proceed directly through the transition state, as shown in Figure 3-4, route a. In addition, an indirect intramolecular pathway, as illustrated in Figure 3-4, route b, could also occur because the energy barrier for intramolecular proton transfer for the zwitterionic glycine has been found to be quite low (less than 2.09 kJ mol<sup>-1</sup>).<sup>105</sup> The initial formation of a stable Si←N adduct (Figure 3-4, II) is also essential for the subsequent proton snatching step from the –COOH group by the nucleophilic restatom (Figure 3-4, VI). This is possible because the molecule is sufficiently long to reach the restatom after anchoring to the adatom. This can lead to the formation of the carboxylate anion, with the N atom in the amino group remaining datively bonded to the Si adatom (Figure 3-4, VII), and the eventual proton transfer from the amino moiety to the Si restatom (Figure 3-4, VIII). The plausibility of an intramolecular proton transfer to the carboxylate oxygen from the tetravalently bonded amino N atom has been evaluated in the case of isolated or gas-phase zwitterionic glycine molecule.<sup>105</sup> This intramolecular proton transfer could lead to the formation of the final N–Si bonded adstructure in an unidentate geometry as observed experimentally in our recent work.<sup>99</sup>

Figure 3-3b shows the corresponding adsorption pathways of glycine on the model Si(100)2×1 surface involving N–H and O–H dissociation. Evidently, both the N–H and O–H dissociative pathways involve the formation of adduct states and transition states. In particular, as the N-to-Si separation decreases to 1.99 Å for the adduct state (XII, with  $\Delta E = -140.3$  kJ mol<sup>-1</sup>) and to 1.90 Å for the transition state (XIII, with  $\Delta E = -39.0$  kJ mol<sup>-1</sup>) and finally to 1.75 Å for the N–H dissociative adsorption state (XIV), the N–H bond length is found to increase concomitantly from 1.01 Å for the unreacted state (XI) to 1.03 Å for the adduct state (XII) and 1.41 Å for the transition state (XIII). Similarly, the O–H bond length increases from 0.98 Å for the unreacted state (XI) to 0.99 Å for the corresponding adduct state (XV, with  $\Delta E = -40.7$  kJ mol<sup>-1</sup>) and to 1.17 Å for the transition state (XVI, with  $\Delta E = -20.1$  kJ mol<sup>-1</sup>), as the O-to-Si separation decreases concomitantly to 2.05 Å (XV) and to 1.90 Å (XVI) and finally to 1.73 Å for the O–H dissociative adsorption state (XVII). As similarly observed for the Si(111)7×7 model surface (Figure 1a), the N–H dissociative adsorption state (XIV, with  $\Delta E = -237.4$  kJ mol<sup>-1</sup>) is found to be thermodynamically less stable than the O–H dissociative adsorption state (XVII, with  $\Delta E = -285.6$  kJ mol<sup>-1</sup>) for the Si(100)2×1 model surface. However, while a stable Si←O adduct cannot be obtained for the Si(111)7×7 model surface, the corresponding Si←N adduct (XII) is more stable than the Si←O adduct (XV) for the Si(100)2×1 model surface. Furthermore, the energy barrier between the Si←N adduct (XII) and the corresponding transition state (XIII), 101.3 kJ mol<sup>-1</sup>, is considerably larger than that between Si←O adduct (XV) and its transition state (XVI), 20.6 kJ mol<sup>-1</sup>. The smaller barrier found for the O–H

dissociative pathway compared to the N–H dissociative pathway therefore also favours the formation of the O–H dissociative product (XVII) over the N–H dissociative product (XIV) kinetically. The formation of the O–H dissociative product via Si←O adduct formation for the Si(100)2×1 model surface is consistent with the calculated results reported by Qu et al.<sup>95</sup>

### 3.2.3 Summary

In the present study, we calculate the potential energy diagrams and the adsorption energies of relevant adstructures of glycine on Si<sub>16</sub>H<sub>18</sub> and Si<sub>15</sub>H<sub>16</sub> used, respectively, as model Si(111)7×7 and Si(100)2×1 surfaces. Dissociative adsorption of glycine on the two surfaces proceeds via the formation of the surface adduct states followed by the respective transition states that lead to the final adsorption states. For the Si(111)7×7 model surface, the absence of a Si←O surface adduct leaves the formation of N–H dissociative product through the formation of the Si←N adduct as the only viable pathway. For the Si(100)2×1 model surface, the presence of the Si←O and Si←N surface adducts suggests that both O–H and N–H dissociative products are plausible. The considerably lower energy barrier to the respective transition state from the Si←O adduct than that from the Si←N adduct favours the formation of O–H dissociative adstructure. The present calculated result for the formation of N–H dissociative adstructure on the Si(111)7×7 surface is in good accord with the XPS data reported in our recent work,<sup>99</sup> while the formation of O–H dissociative adstructure is also found to be in good agreement with the calculated results of Qu et al.<sup>95</sup> and the experimental data of Lopez et al.<sup>75</sup> This study therefore illustrates that the nature of the surface adduct is vitally important in controlling the selectivities of Si(111)7×7 and Si(100)2×1 towards the dissociative adsorption of glycine.



**Figure 3-3** Potential energy diagram, along with the optimized geometries and adsorption energies (in  $\text{kJ mol}^{-1}$ ) for different states, of glycine adsorption on model surfaces of (a) Si(111)7×7 and (b) Si(100)2×1. The more (less) probable pathway is shown as a solid (dashed) line.

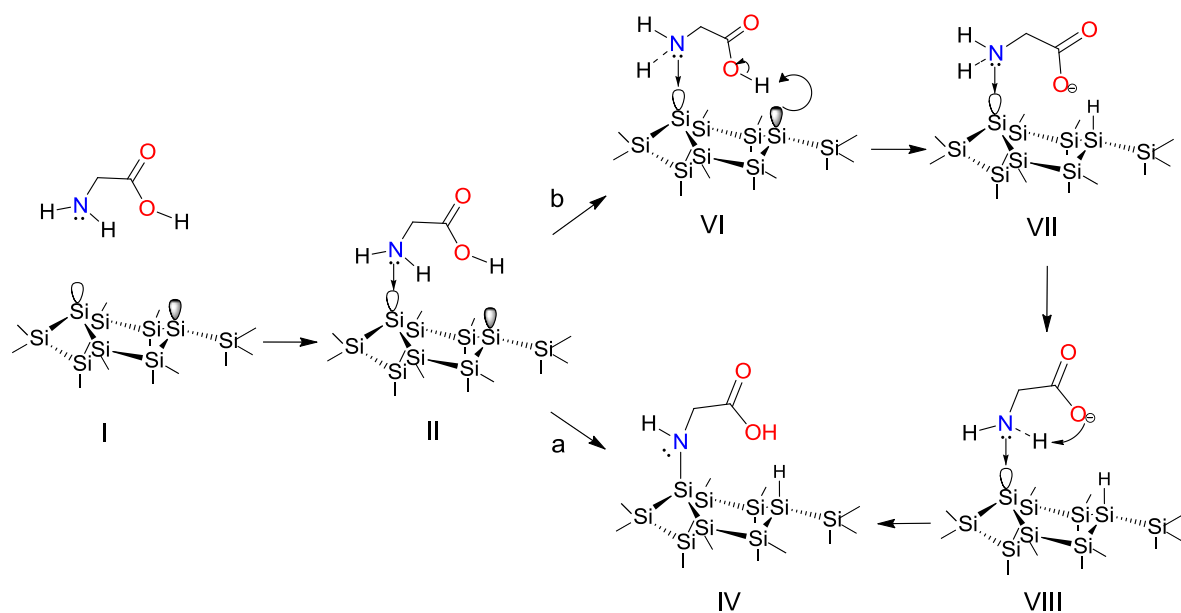


**Figure 3-4** Schematic diagram of the adsorption of glycine on a model Si(111)7×7 surface, with direct proton transfer (route a) and with intramolecular proton transfer (route b) from a Si←N adduct (II), leading to the final adsorption state (IV).

### 3.3 Hydrogen-Bond-Mediated Biomolecular Trapping: Reversible Catch-And-Release Process of Common Biomolecules on a Glycine-Functionalized Si(111)7×7 Surface\*\* ††

#### 3.3.1 Introduction

In the “bottom-up” approach of creating molecular nanostructures and devices, molecules are deposited and organized into various patterns either by interactions with specific sites on the substrate or by interactions with the molecules themselves (as in a self-assembly process). A well-ordered substrate surface, such as Si(111)7×7 or Si(100)2×1, has been shown to be sufficiently reactive to facilitate adsorption of organic molecules into ordered monolayers in registry with specific sites on the substrate through, e.g., [2+2] cycloaddition,<sup>106,107</sup> insertion reaction,<sup>34</sup> and other covalent bonding mechanisms.<sup>108</sup> On the other hand, adsorbate-adsorbate interaction, especially through hydrogen bonding, may lead to well-organized self-assembled monolayer on unreactive surfaces (e.g. Au, Ag).<sup>109,82,110,111,112,85</sup> Many well-ordered patterns observed with scanning tunneling microscopy (STM) have been interpreted in terms of H-bonding among neighboring molecular adsorbates. Owing to its selectivity and directionality, H-bonding could facilitate ordering of molecules with both H-bond donor and H-bond acceptor functional groups. In particular, the [O–H··O] H-bonding among the carboxyl groups has been reported to lead to honeycomb patterns of 1,3,5-benzenetricarboxylic acid on Ag(111),<sup>109</sup> pairing of cysteine on Au(110),<sup>82</sup> and domain-boundary rows of isonicotinic acid on Ag(111).<sup>110</sup> The [N–H··O] H-bonding results in hexamers of pyrrolidone on Au(111)<sup>111</sup> and trimers of uracil on Cu(111),<sup>112</sup> while the [O–H··N] H-bonding gives rise to twin chains of 4-[*trans*-2-(pyrid-4-yl-vinyl)]benzoic acid on Ag(111)<sup>85</sup> and a hexagonal superstructure of isonicotinic acid on Ag(111).<sup>110</sup> Although the observations of well-ordered STM patterns and the corresponding density functional theory (DFT) calculations generally support the existence of these H-bonds, X-ray photoelectron spectroscopy (XPS) and vibrational spectroscopy could offer more bond-specific information through the relevant peak shifts. For example, the N 1s binding energy of a H-bond acceptor (N) in the [O–H··N] H-bond is found to increase by more than 1 eV due to charge transfer from the N atom for isonicotinic acid,<sup>110,113</sup> diethanolamine,<sup>114</sup> ethylenediamine,<sup>115</sup> benzylic amide macrocycle,<sup>116</sup> and glycine.<sup>99</sup> In vibrational spectroscopy, a large decrease in the

---

\*\* Reproduced with permission from [J. Phys. Chem. Lett., 2010, 1(23), pp 3385-3390; DOI: 10.1021/jz101315m] Copyright ©2010 American Chemical Society

†† My specific contributions were research idea, XPS data collection (with Dr. Lei Zhang), data analysis and DFT calculations.

stretching frequency of the H-bond donor as a result of H-bond formation<sup>117</sup> has been reported for the self-assembly of 3-mercapto-N-pentadecylpropionamide on gold<sup>118</sup> and for a photo-switch consisting of bithienylethene-pyridine and carboxyl-tetrathiafluvalene.<sup>119</sup>

To date, H-bonding has mostly been employed to produce two-dimensional molecular nanostructures, and the use of H-bonding to develop nanostructures beyond the monolayer is uncommon. For three-dimensional growth involving a second or additional adlayer on top of the first adlayer, H-bonding can offer important advantages particularly in building a structurally flexible system. Unlike the weak, long-range, van der Waals interaction, a H-bond is selective and sufficiently strong to enable a molecule in the first adlayer to “catch” and assemble an incoming molecule into the second adlayer in a controllable fashion. On the other hand, unlike the strong covalent bond, the H-bond is sufficiently weak, making it easy to break and therefore enabling the first adlayer to “release” the captured molecules in the second adlayer by a simple stimulus such as mild heating. In effect, the adsorbates in the first adlayer serve as linker molecules that bind strongly to the substrate through covalent bonding at one end while “trapping” selective molecules (with compatible H-bonding groups) to form the second adlayer by H-bonding. By choosing appropriate molecules as the linkers for the first adlayer, the surface can be further functionalized in a reversible fashion with appropriate H-bond-compatible molecules.

We have found earlier in this chapter that deposition of glycine molecules on a Si(111)7×7 surface in ultrahigh vacuum leads to N–H dissociative adsorption of glycine and the formation of a deprotonated glycine adlayer through N–Si covalent bonding at the interface. We also observed that the formation of a second molecular glycine adlayer onto the interfacial (first) adlayer proceeds primarily by [O–H…N] H-bonding between the carboxyl group of the first-adlayer molecule and the amino group of a second-adlayer molecule.<sup>99</sup> An appropriately deposited glycine adlayer on Si(111)7×7 can therefore serve as a linker platform with its “dangling” carboxyl group available for trapping other molecules via H-bonding. In the present study, we demonstrate that such a platform can provide an effective “catch-and-release” mechanism for trapping a number of small biomolecules, including not just amino acids and peptides: glycine (Gly) and alanine (Ala), and glycyglycine (GlyGly), but also DNA base groups: adenine (Ade) but not thymine (Thy). Except for Thy, the respective N 1s XPS spectra collected after deposition and post-annealing of these biomolecules on the Gly/Si(111)7×7 surface clearly support that the present “catch and release” mechanism is mediated by interlayer H-bonding.

### 3.3.2 Experimental Details

Powders of Gly, GlyGly, Ala, Ade and Thy were loaded into effusion cells (designed for low-temperature evaporation of organic materials, MBE-Komponenten) and outgassed thoroughly overnight. The evaporation temperatures used for the deposition of Gly, GlyGly, Ala, Ade and Thy on the  $7\times 7$  substrate were 140, 175, 130, 133 and 108°C, respectively. The molecular identity of these biomolecules during deposition was confirmed by their cracking patterns obtained in-situ by using a quadrupole mass spectrometer.

By monitoring the saturation of the N 1s peak intensity for the N–Si feature, we first deposited a monolayer of Gly on a clean Si(111) $7\times 7$  substrate at room temperature (with a 15 s exposure).<sup>99</sup> Here, we define a monolayer of Gly as the coverage which corresponds to a saturated N 1s peak intensity for the N–Si feature. The resulting Gly/Si(111) $7\times 7$  surface was then used for subsequent deposition of Gly, GlyGly, Ala, Ade or Thy, and the follow-up desorption experiments. Mild sample annealing was achieved by passing a direct current ( $\sim 1$  A) through the sample for 10 s, with the approximate sample temperature monitored by using a nearby thermocouple. XPS measurement was made after each deposition and desorption experiments. The N 1s peak of the N–Si species for Gly/Si(111) $7\times 7$  was found to locate at 399.1 eV binding energy with the Si 2p<sub>3/2</sub> peak at 99.3 eV, in excellent accord with the literature values.<sup>120</sup> The spectra were fitted with Gaussian-Lorentzian lineshapes and a linear background by using the CASA-XPS software.

### 3.3.3 Results and Discussion

Figure 3-5 shows the N 1s XPS spectra of Gly, GlyGly, Ala, Ade and Thy on the Gly/Si(111) $7\times 7$  surface. We have also obtained XPS spectra of the C 1s and O 1s regions, and they offer supporting evidence for the adstructure evolution discussed below. For the Gly/Si(111) $7\times 7$  surface obtained by exposing 15 s of Gly to the  $7\times 7$  surface, the prominent N 1s peak at 399.1 eV can be attributed to N–Si species resulting from N–H dissociative adsorption of Gly on Si(111) $7\times 7$  (Figure 3-5a).<sup>99</sup> We have also shown in our recent work that the intensity of this peak is saturated at this exposure, indicating formation of the first Gly adlayer at the interface. Appropriately, we have therefore chosen a 15 s exposure of Gly on Si(111) $7\times 7$  as the functionalized platform for subsequent experiments. Further Gly exposure to 120 s results in a new peak at 401.4 eV, which corresponds to [O–H $\cdots$ N] H-bonding between the carboxyl group of Gly in the interfacial (first) adlayer and the amino group of newly deposited Gly in the second and subsequent adlayers.<sup>99</sup> Apparently, the interfacial Gly molecules (in the first adlayer) “catch” the

incoming Gly molecules by H-bonding. Because the intensity of the N 1s peak at 401.4 eV can be as large as 1.5 times that of the peak at 399.1 eV,<sup>99</sup> the observed H-bonding appears to occur beyond the adlayer H-bonded to the interfacial adlayer. After annealing at 120°C for 10 s, the H-bond feature at 401.4 eV is almost completely removed, indicating that nearly all the Gly molecules attached through [O–H···N] H-bonding have desorbed. The interfacial Gly molecules therefore “release” the H-bonded Gly in the second adlayer after only a mild anneal at 120°C. To test whether the Gly/Si(111) surface can be reused after the first “catch-and-release” cycle, we have repeated the Gly exposure (e.g., 45 s) to the post-annealed Gly/Si(111) surface and observed the reappearance of the H-bond feature at 401.4 eV, with little degradation of the functionalized platform. It is, however, crucial to make a judicious choice of the annealing temperature (i.e. the magnitude of current used in the direct current heating) that is sufficiently high to totally remove the H-bonded adlayers yet low enough to leave the interfacial adlayer intact (without dissociation). In this way, the functionalized platform can in principle be reused many times with the “reversible” catch-and-release process.

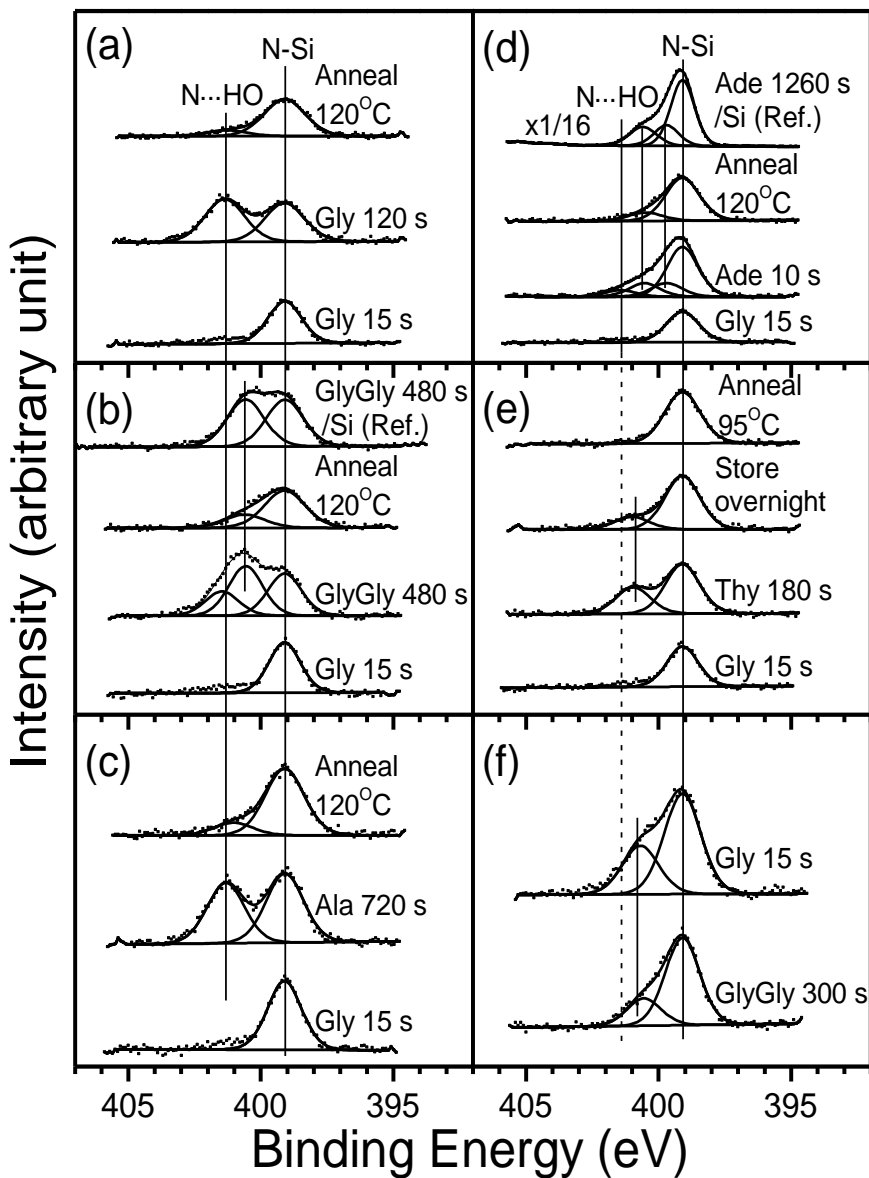


**Figure 3-5** N 1s spectra of Si(111)7×7 functionalized by a 15-s exposure of glycine (Gly) before (lowest trace) and after exposure to (a) 120 s of Gly, (b) 480 s of glycylglycine (GlyGly), (c) 720 s of alanine (Ala), (d) 10 s of adenine (Ade), and (e) 180 s of thymine (Thy), and upon annealing at (a-d) 120°C and (e) 95°C for 10 s. N 1s spectra for bare Si(111)7×7 after exposure to (b) 480 s of GlyGly and (d) 1260 s of Ade are marked as reference (Ref.). These spectra are compared with (f) the N 1s spectra of Si(111)7×7 functionalized by a 300-s exposure of GlyGly before and after 15 s of Gly exposure.

In order to test the generality of this catch-and-release approach, we repeat the deposition and desorption experiments on the Gly/Si(111)7×7 surface with different biomolecules. Figure 3-5b shows the N 1s spectrum of a 480 s exposure of GlyGly on the Gly/Si(111)7×7 surface. Evidently, in addition to the N–Si feature at 399.1 eV for Gly/Si(111)7×7, two new features at 401.4 and 400.6 eV are observed, and they can be attributed, respectively, to a [O–H···N] H-bonded adstructure as observed for the Gly case and to the amino or amide N not involved in bonding to the Gly/Si(111)7×7 surface. It should be noted that both the amino and amide [or C(O)NH] N atoms exhibit a similar N 1s binding energy at 400.6 eV.<sup>120</sup> Although it is not possible to identify from the N 1s spectrum alone which N atom in the GlyGly molecule is involved in the H-bonding, the amino N seems more likely, because the amino N is more basic than the amide N and the lone-pair electrons of the amino N are more geometrically accessible than those of the amide N. The intensities of these three N 1s features provide information on the extent to which the GlyGly adlayer attaches to the Gly interfacial adlayer by H-bonding. If all the deposited GlyGly molecules are H-bonded to the Gly molecules, the intensities of these three features should be equal to one another. However, the feature at 401.4 eV is found to be only about half as intense as the feature at 399.1 eV, which suggests that only half of the interfacial Gly molecules form the [O–H···N] H-bond with the GlyGly molecules. On the other hand, the feature at 400.6 eV appears slightly more intense than the interfacial N–Si feature, suggesting another GlyGly bonding arrangement with Gly that does not involve the [O–H···N] bonding. The ratio of GlyGly involved in the [O–H···N] H-bonding to those in the other bonding arrangement is about 2:1. For comparison, we show in Figure 3-5b the N 1s spectrum of a 480 s exposure of GlyGly directly onto a bare Si(111)7×7 substrate (i.e. without the 15 s exposure of Gly), in which no H-bonding feature (at 401.4 eV) is observed. GlyGly has been found to adsorb on the 7×7 surface in a bidentate configuration involving N–H dissociation of amino group and O–H dissociation of the carboxyl group or N–H dissociation of the amide group.<sup>120</sup> This demonstrates that it is the Gly molecules in the interfacial adlayer that “catch” the incoming GlyGly molecules with H-bonding. Furthermore, annealing the GlyGly adlayers at 120°C for 10 s also totally removes the feature at 401.4 eV, without affecting the N–Si bonding in the interfacial Gly adlayer, which suggests that the GlyGly molecules attached by H-bonding to the Gly adlayer are released after the anneal. The residual intensity at 400.6 eV after the mild annealing indicates that a small number of the GlyGly molecules remain attached to the Gly adlayer, which suggests that this other bonding mode is stronger than the H-bonding.

An Ala molecule has its  $C_{\alpha}$  atom bonded to a methyl group, replacing one of the two methylene H atoms (in a Gly molecule). Although the methyl group is generally non-reactive, it plays an important role in molecular assembly through the steric effect. Figure 3-5c shows that like Gly and GlyGly, the appearance of the N 1s feature at 401.4 eV upon 720-s exposure of Ala and its removal upon post-annealing at 120°C for 10 s on the Gly/Si(111)7×7 surface clearly support the [O–H··N] H-bond mediated catch-and-release mechanism. We note that higher exposures of Ala to the platform have not led to a greater N 1s intensity of the H-bond feature than the N–Si species, in contrast to that found for the Gly exposures to the platform. This suggests that the presence of the methyl group reduces the probability of forming the [O–H··N] H-bond between Ala and Gly molecules likely due to the steric effect.

In order to test the efficacy of this catch-and-release approach to trapping ring-like biomolecules, we repeat the above experiments for two common DNA base group molecules: Ade and Thy. An Ade molecule has a double-ring structure with three pyridinic, one pyrrolic and one amino N atoms, of which only the pyrrolic N atom is not expected to act as a H-bond acceptor to form a H-bond (with the carboxyl group of Gly serving as the H-bond donor). This is because of delocalization of the lone-pair electrons of the pyrrolic N in the aromatic ring. For amino N, the formation of the [O–H··N] H-bond with the Gly/Si(111)7×7 surface has been demonstrated above for chain-like biomolecules. For the pyridinic N, the formation of the [O–H··N] H-bond has also been reported on the basis of large N 1s binding energy shifts to the higher binding energy side.<sup>110,113,114,115,116</sup> Figure 3-5d compares the N 1s spectrum of a 10 s exposure of Ade to Gly/Si(111)7×7 with that of a thick Ade film (1260-s exposure) on pristine Si(111)7×7. The reference N 1s spectrum of the thick Ade film on the 7×7 surface exhibits three components at 399.1, 399.7 and 400.6 eV with an intensity ratio of 3:1:1, which can be assigned to the pyridinic, amino, and pyrrolic N atoms, respectively. The N 1s binding energy of the pyrrolic N is higher than that of the amino N due to the contribution of the lone-pair electrons of the pyrrolic N to the aromatic ring.<sup>121</sup> Both the pyridinic N and the N–Si species for the Gly/Si(111)7×7 interface essentially exhibit the same binding energy. For the N 1s spectrum of the 10 s exposure of Ade to the Gly/Si(111)7×7 surface, an additional weak component at 401.4 eV, attributable to a [O–H··N] H bonded species, is evident (in addition to the three components found in the reference spectrum). Interestingly, the intensity of this H-bond feature is estimated to be ~20% of that of the N–Si species in the Gly/Si(111)7×7 surface, which suggests that only one in five interfacial Gly molecules is involved in trapping an Ade molecule, possibly due to the relatively large size of an Ade molecule and the

availabilities of additional bonding configurations to Ade adsorption. The nature of the observed bonding features for Ade on Si(111)7×7 will be discussed in more detail elsewhere.<sup>122</sup> Annealing the Ade adlayers on Gly/Si(111)7×7 at 120°C for 10 s also removes the H-bonded N 1s feature at 401.4 eV, confirming similar release mechanism found for the chain-like molecules.

In a Thy molecule, two N atoms contribute their lone-pair electrons to the aromatic  $\pi$ -electron system, and they, unlike those in Gly, GlyGly, Ala and Ade, cannot form a [O–H··N] H-bond with an interfacial Gly molecule. This is verified by the absence of the H-bond feature at 401.4 eV in the N 1s spectrum for a 180-s exposure of Thy on the Gly/Si(111)7×7 surface, shown in Figure 3-5e. In addition to the N–Si feature at 399.1 eV, a new feature at 401.0 eV is also observed and found to correspond to that for a thick Thy film on bare Si(111)7×7 (400.9 eV, not shown) and on a Au foil (401.2 eV).<sup>123</sup> This N 1s feature is therefore assigned to the N atoms in Thy that are not directly involved in bonding to Gly/Si(111)7×7, which indicates the absence of [O–H··N] H-bonding. It is of interest to note that the intensity of this N 1s feature at 401.0 eV decreases by 75% over the 30-m measurement period of the XPS experiment (not shown). As illustrated in the N 1s spectrum for the sample with a 180-s exposure after storing in ultrahigh vacuum for an extended period (15 h) (Figure 1e), desorption of Thy could proceed even without X-ray irradiation until only a small amount of molecules (that are likely attached directly to the Gly adlayer) remains. The easy desorption of Thy with and without X-ray irradiation suggests the lack of strong bonding among Thy themselves and with the Gly/Si(111)7×7 surface. This N 1s feature at 401.0 eV can be completely removed by mild annealing at a lower temperature of 95°C for 10 s, confirming that the interactions between the Thy molecules adsorbed on Gly/Si(111)7×7 are weaker than the [O–H··N] H-bonding.

Finally, we examine whether a platform obtained by exposing 300 s of GlyGly to Si(111)7×7 could produce a similar trapping capability as the Gly/Si(111)7×7 surface. As shown in our recent work, GlyGly molecules in the interfacial (first) adlayer could bond to Si through amino and amide N atoms in a bidentate configuration, leaving the carboxyl end group free for further interaction with incoming molecules.<sup>120</sup> Figure 3-5f compares the N 1s spectra of GlyGly/Si(111)7×7 before and after a 15-s exposure of Gly. Evidently, no new feature attributable to the [O–H··N] H-bonding has been found near 401.4 eV after the Gly exposure, which suggests that the carboxyl groups of GlyGly in the interfacial adlayer are not suitable for forming H-bonding with the amino group of Gly. This is likely due to steric

hindrance and/or unfavorable bonding orientation or to the availability of other more preferable bonding route such as [N–H···O] H-bonding.<sup>120</sup>

In Figure 3-6, we summarize plausible H-bonding configurations as represented by calculated adsorption structures of Gly, GlyGly, Ala and Ade H-bonded to Gly adsorbed on two different sites of a model Si(111)7×7 surface. Details of these calculations will be given elsewhere.<sup>120</sup> Briefly, the equilibrium structures were optimized by using the Density Functional Theory method with the B3LYP hybrid functional<sup>124,59,58</sup> in the GAUSSIAN 03 software.<sup>65</sup> In accordance with the dimer-atom-stacking fault model of Takayanagi et al.,<sup>32</sup> we used a Si<sub>16</sub>H<sub>18</sub> cluster<sup>89</sup> to represent the adatom-restatom sites at the faulted half of the Si(111)7×7 unit cell, with the adatom-restatom distance fixed at 4.57 Å.<sup>97</sup> We also employed a Si<sub>12</sub>H<sub>12</sub> cluster<sup>61</sup> to represent the center adatom-adatom pair across the dimer wall, with the adatom-adatom distance constrained at 6.65 Å. Evidently, for the chain-like molecules, the bond length for the [O–H···N] H-bond is 1.65-1.69 Å while that for Ade is 1.90 Å. These bond lengths are in good accord with the expected value of a H-bond (generally between 1.6 Å to 2.7 Å), and they appear to be essentially identical for the adstructures at the adatom-restatom site (Figure 3-6, left) and the dimer wall site (Figure 3-6, right).

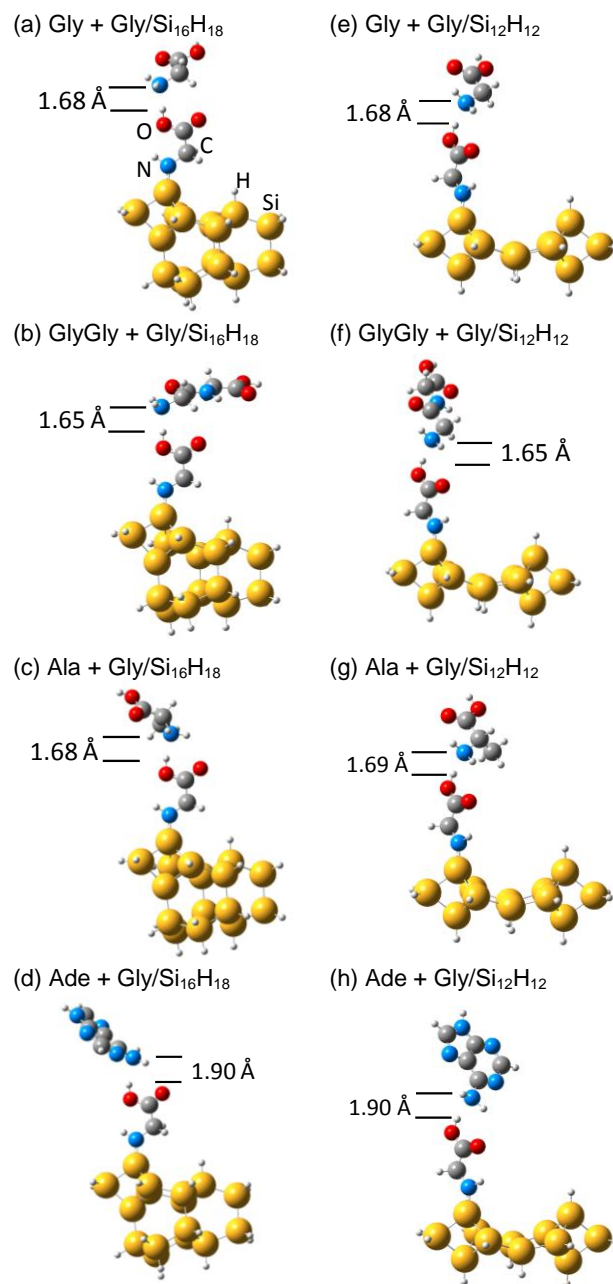


**Figure 3-6** Equilibrium structures of (a, e) glycine (Gly), (b, f) glycyglycine (GlyGly), (c, g) alanine (Ala), and (d, h) adenine (Ade) H-bonded to Gly adsorbed on Si<sub>16</sub>H<sub>18</sub> (left column) and Si<sub>12</sub>H<sub>12</sub> (right column) model surfaces, all obtained by DFT/B3LYP GAUSSIAN03 calculations using a 6-31G++dp basis set.

### 3.3.4 Summary

We have employed a Gly adlayer adsorbed to the Si(111)7×7 surface (through strong N–Si covalent bonding) to provide a functionalized platform for trapping biomolecules with appropriate N atoms to form [O–H···N] H-bonds with the free carboxyl groups of the deprotonated Gly molecules. This functionalized platform is found to be highly effective in capturing both chain-like (Gly, GlyGly, and Ala) and ring-like molecules (Ade). In a molecule such as Thy where appropriate H-bond acceptor is not available, no capture is observed. The capture efficiency appears to follow the decreasing order of Gly > Ala > GlyGly > Ade, which is mostly likely due to steric hindrance during the H-bond formation and the availability of N lone-pair electrons. The captured molecules can be easily released by breaking the H-bond with mild annealing at 120°C for 10 s. This “catch and release” process is verified by the appearance and disappearance of the [O–H···N] H-bond feature at 401.4 eV. In contrast, a GlyGly-functionalized surface is unable to capture Gly molecules due to the absence of the [O–H···N] H-bonding. The Gly-functionalized Si(111)7×7 surface can therefore be used as a versatile biomolecular trap in biosensing, molecular recognition, and/or other molecular electronics applications.

## Chapter 4

# Observation of vertical and horizontal hydrogen bonding formation in dissociative adsorption of glycine on Si(111)7×7 by Scanning Tunneling Microscopy

### 4.1 Introduction

There is a lot of interest in the interactions and surface chemistry of organic and biological molecules, including, e.g., amino acids, proteins, peptides, nucleosides, DNA and RNA, on a variety of metal<sup>125,126,127</sup> and semiconductor<sup>67,76,128</sup> substrates.<sup>129,130</sup> Understanding the nature of molecule-to-molecule and molecule-to-substrate interactions is very important for developing chemical sensors,<sup>131</sup> molecular devices,<sup>132,133</sup> biomolecular electronic components<sup>134,135</sup> and emerging nanotechnology applications.<sup>136</sup> Among the semiconductor substrates, Si(111)7×7 represents one of the most studied surfaces and offers a variety of bonding sites to approaching bio/organic adsorbates. Different organic molecules with different functional groups including acetic acid,<sup>137</sup> benzene,<sup>138</sup> pyrrole,<sup>18</sup> methanol,<sup>139</sup> butadiene,<sup>140</sup> dimethyl and trimethylamines,<sup>10</sup> and glycine,<sup>76,99</sup> on Si(111)7×7 have been found to undergo different types of reactions with the surface upon adsorption. For example, benzene<sup>138</sup> and butadiene<sup>140</sup> adsorb on the 7×7 surface through the cycloaddition reaction, while pyrrole<sup>18</sup> and methanol<sup>139</sup> undergo H dissociative adsorption. Furthermore, the carboxylic acids and the amines are especially interesting because their reaction mechanisms are quite different on the 7×7 surface. For carboxylic acids (e.g. acetic acid<sup>137</sup>), H dissociative adsorption is found to produce a conjugate base with the formation of O–Si bond, although its mechanism is far from well understood. For amines,<sup>10</sup> there has been evidence to support the formation of stable, datively bonded surface adducts by partially donating the lone pair electron density of the N atoms towards the Si atoms. One particularly interesting question is the relative reactivity of the carboxylic acid group and the amino group towards the 7×7 surface. The amino acids therefore offer such a unique testing ground because they are bifunctional molecules with both the acidic (carboxylic acid group) and basic (amino group) moieties.

To date, there are only five studies on glycine adsorption on Si(111)7×7 and Si(100)2×1. In particular, Lopez et al. studied glycine adsorption on Si(100)2×1 by high-resolution electron energy loss spectroscopy (HREELS) and reported a unidentate adstructure obtained by O–H dissociative adsorption and the formation of O–Si bond.<sup>75</sup> Later, Qu et al. showed in a computational study that O–Si bond

formation is preferred over N–Si bond formation on Si(100)2×1 both thermodynamically and kinetically.<sup>95</sup> For glycine adsorption on Si(111)7×7, Huang et al. studied multilayer growth by X-ray photoelectron spectroscopy (XPS) and HREELS.<sup>76</sup> They concluded that glycine adsorbs, via dissociation of both N–H and O–H bonds, in a bidentate configuration through the formation of N–Si and O–Si bonds with two Si adatoms. However, the glycine molecule with a NH<sub>2</sub>-to-OH separation of 3.7 Å appears to be physically much too small to realize the proposed bidentate structure that bridges across two adjacent adatoms, with a separation of 6.65 Å. In our recent XPS investigation of glycine on Si(111)7×7 as discussed in the third chapter,<sup>10</sup> we demonstrate that glycine adsorbs in a unidentate configuration through N–H dissociation with the carboxylic acid group remaining intact. With increasing exposure, we also observe the formation of a hydrogen-bonded intermediate layer and its evolution to zwitterionic multilayer. This observation is supported by our recent computational study, which shows that the formation of a Si←N adduct leads to unidentate N–H dissociative adproduct on a model Si(111)7×7 surface, in contrast to that found on a model Si(100)2×1 where Si←O adduct formation leads to unidentate O–H dissociative adproduct.<sup>141</sup> There are also rather limited studies of glycine on metal surfaces, all of which show evidence of hydrogen bonding. In particular, self-assembly of glycine on Cu{110} surfaces has been studied by Chen et al. using scanning tunneling microscopy (STM) to show the presence of hydrogen bonding between two different domains on the surface.<sup>127</sup> In a separate study, Nyberg et al. demonstrated the formation of hydrogen bonds between the deprotonated glycine molecules (in the form of glycinate) on a Cu(110) surface by X-ray absorption spectroscopy and near-edge X-ray absorption fine structure methods, along with theoretical simulations.<sup>87</sup>

The Si(111)7×7 surface offers a set of unique, directional bonding sites to approaching molecules.<sup>27</sup> As discussed in the first chapter, the 7×7 unit cell consists of 12 adatoms in the first layer, 6 restatoms in the second layer and the 1 corner hole in the third layer, which together give 19 dangling bonds.<sup>87</sup> Charge transfer from a restatom to an adatom results in a formal charge of +7/12 for the electrophilic adatom and –1 for the nucleophilic restatom.<sup>101,97</sup> Because a corner (*angulus* in Latin) adatom (AA) has only one neighbouring restatom (RA) while a center (*centrum* in Latin) adatom (CA) has two neighbouring RAs, almost twice the amount of charge transfer from CA to RA as that from AA to RA occurs, therefore causing the CA to have a larger formal charge than the AA. The differences in the formal charges of CA (~ +1), AA (+7/12) and RA (–1) contribute to their site-specific reactivities. The availability of both the nucleophilic and electrophilic sites makes the 7×7 surface particularly interesting towards various organic adsorbates with different functional groups. For small organic molecules such as glycine (with the NH<sub>2</sub>-

to-OH separation of 3.7 Å for the most stable conformer in the isolated gaseous state), the neighbouring adatom-restatom pairs (CA-RA or AA-RA, with a separation of 4.57 Å) represent the most important reaction sites. This is because of their generally similar and therefore physically compatible dimensions, in contrast to the considerably larger separations for CA-CA pair across the dimer wall (6.65 Å), CA-CA pair within a half unit cell (7.68 Å), CA-AA within a half unit cell (7.68 Å), and CA-AA across the dimer wall pairs (10.15 Å). For example, dissociative adsorption of pyrrole and amines on the CA and AA sites,<sup>138,140</sup> and cycloaddition reactions of thiophene and cyclohexadienes (1,3 and 1,4) on the adjacent adatom-restatom pairs<sup>142,24</sup> of Si(111)7×7 have been reported.

In the present study, we investigate the adsorption of glycine on the Si(111)7×7 surface at room temperature and report the first STM images of this fundamentally important system. Of particular interest are the interactions of the amino and carboxylic acid groups in glycine with different bonding sites (CA, AA, RA) on the 7×7 surface and their site-specific chemistry. The present results illustrate, for the first time, the importance of hydrogen bonding in a variety of adsorption configurations for the growth evolution of glycine on a semiconductor surface.

## 4.2 Experimental Details

The amount of glycine exposed to the 7×7 substrate was controlled by the exposure time with the effusion cell operating at 120°C and the deposition chamber pressure at  $1 \times 10^{-9}$  mbar.<sup>10</sup> The purity of glycine during its exposure to the 7×7 substrate was verified by collecting its mass spectrum in-situ with a quadrupole mass spectrometer (Stanford Research Systems RGA-300). After exposure, the sample was transferred back to the analysis chamber for STM imaging in constant current mode. During STM measurements, the pressure in the analysis chamber is always less than  $2 \times 10^{-10}$  mbar.

## 4.3 Results and Discussion

Figure 4-1a and 4-1b show the STM images of Si(111)7×7 after a 20 s exposure of glycine obtained with a tunneling current of 200 pA at a sample bias of +2 V and -2 V, corresponding to empty state imaging and filled state imaging, respectively. In Figure 4-1c, we show the corresponding schematic diagrams of three 7×7 unit cells (labeled A, B and C) with representative features attributable to glycine adsorption, and we identify specific CA, AA or RA sites with alphanumeric labels. The empty state image (Figure 4-1a) for cell A shows the local density of states (LDOS) of the unreacted or pristine 7×7 unit cell of the Si(111) surface, in which all the adatoms in both the faulted and unfaulted half unit cells exhibit similar intensities, as reflected also by the corresponding height profiles along the edges of the

half unit cells (line scans L1 and L2, Figure 4-1c upper). Unless stated otherwise, all the height profiles correspond to line scans starting from left to right of images. In the corresponding filled state image (Figure 4-1b), the six spheres representing the adatoms in the faulted half A (shaded spheres in Figure 4-1c lower) appear brighter than those in the unfaulted half A (unshaded spheres in Figure 4-1c lower). In the filled state image (Figure 4-1b), we can also identify the LDOS surrounded by three neighbouring adatoms as the restatoms (smaller circles in Figure 4-1c lower). The height profile along line scan L11 across the three adatoms in the faulted half shows the similarity of LDOS of these adatoms. The maximum height differential between L11 (for the faulted half) and its corresponding line scan L12 for the unfaulted half (Figure 4-1c lower) is found to be larger by 1 Å. In contrast, there is no difference in the maximum height differential between L1 and L2 (Figure 4-1c upper) in the empty state image. These observations are in excellent accord with earlier STM work for the pristine Si(111)7×7 surface.<sup>143</sup>

In the empty state image (Figure 4-1a), the faulted half unit cell B depicts a brighter oblong protrusion located closer to a dimer wall from the CA3a site (Figure 4-1c upper), which indicates the adsorption of a glycine moiety. The protrusion is particularly evident in the height profile along line scan L3, which shows a larger density than the corresponding unreacted sites along reference line scan L1. The presence of the adsorbed glycine moiety also appears to affect the LDOS of the CA4 site on the complementary (unfaulted) half unit cell B, as shown in the corresponding height profile along line scan L4. On the other hand, in the filled state image (Figure 4-1b), the reacted CA3a in the faulted half unit cell B appears to be nearly as bright as the unreacted CA1 in the faulted half unit cell A but with the centroid shifted towards the dimer wall. Interestingly, glycine adsorption at the CA3a site also depletes the LDOS at the CA4 site in the unfaulted half unit cell B across the dimer wall. These LDOS variations are clearly depicted in the height profiles along the respective line scans L13 and L14. In addition, there is no discernible density at the restatom RA3d site next to the reacted CA3a site, while the LDOS of the two adjacent adatoms AA3b and CA3c appear to increase. As reported earlier<sup>144,145</sup> and discussed further below, these LDOS changes are the signature of H adsorption at the restatom, which therefore indicates that glycine adsorption at CA3a produces a dissociated H atom that adsorbs at the RA3d site.

Our XPS study<sup>10</sup> as discussed in the third chapter, has shown that glycine adsorbs on Si(111)7×7 in a unidentate fashion by N–H dissociation with the formation of N–Si bond, and no evidence of bidentate adsorption is found. In particular, one adatom-restatom pair is involved in the reaction with glycine, with the N–H dissociative glycine fragment, –NHCH<sub>2</sub>COOH, and the dissociated H atom adsorbed onto the adatom and restatom, respectively. We have not considered the adsorption of the dissociated H atom on

another adatom because Lo et al. reported that H adsorption is energetically more favourable on the restatom than on the adatom.<sup>146</sup> Our model is consistent with the observed LDOS changes of the CA3a and RA3d pair in the filled state image (Figure 4-1b), in which H adsorption at RA3d, as reflected by the density depletion, causes an electron redistribution that increases the density of the two adjacent unreacted adatoms, AA3b and CA3c. Similar correlated bright-dark STM features as observed for the adatom-restatom pair in this study have also been reported in the literature.<sup>138,140,143,144,145</sup> For instance, in their combined STM-XPS study of adsorption of secondary and tertiary amines on Si(111)7×7,<sup>140</sup> Cao et al. observed correlated bright-dark features for dimethylamine but only bright protrusions for trimethylamine on Si(111)7×7. They concluded that the dark regions correspond to the adsorption of dissociated H atoms from dimethylamine on the restatoms next to the adsorbed dimethylamine moiety on the adatom, and the lack of dark regions in the STM image for the case of trimethylamine (which contains only methyl H atoms and therefore does not undergo H dissociation) supports the aforementioned assignment.

The LDOS of the center adatom across the dimer wall, CA4, from the reacted adatom CA3a is also found to be dramatically reduced in the filled state image (Figure 4-1c lower, L14) and narrower in the empty state image (Figure 4-1c upper, L4), when compared to those across the unreacted site CA2 (corresponding to L12 and L2 respectively). This indicates interactions between the adsorbed glycine fragment at CA3a and the adatom CA4. In our recent computational study using the Density Functional Theory calculations with a 6-31G++(d,p) basis set,<sup>95</sup> we consider only vertical unidentate adstructure at the adatom-restatom pair. Given the observed STM image (Figure 4-1b), we have now extended our calculations to include a near-horizontal unidentate adstructure tilted across the dimer wall, as modeled by a Si<sub>26</sub>H<sub>24</sub> cluster discussed below. The tilted adstructure for the N–H dissociated glycine molecule, shown as inset in Figure 4-1b, is believed to involve some form of “weak” dipole-dipole-like interaction between the “free” terminal –COOH group (with a negative partial charge) and the center adatom across the dimer wall (with a positive partial charge). Considering the difference in the clusters, the adstructure obtained on Si<sub>26</sub>H<sub>24</sub> is also found to have an adsorption energy (–348.1 kJ mol<sup>–1</sup>) more negative than that of the vertical unidentate adstructure obtained on Si<sub>16</sub>H<sub>18</sub> (–266.4 kJ mol<sup>–1</sup>), which confirms the feasibility of such a tilted adstructure. On the other hand, the formation of a stable bidentate adstructure bonded to two adatoms across the dimer wall cannot be realized with the present calculation, likely because the distance between two adatoms (6.65 Å) is too large for a glycine molecule (with the N-to-O separation of 3.70 Å) to form a bidentate product. Furthermore, if there were a bidentate configuration, the dissociated H atom from the –OH group would have adsorbed on one of the neighbouring restatoms in the complementary

half unit cell B. As all the restatoms in the unfaulted half unit cell B are clearly seen to be unaffected in the filled state image (Figure 4-1b), this would confirm the absence of the second dissociated H atom and therefore of the bidentate geometry. In addition, the orientation of the bright protrusion (e.g. CA3a) across the dimer wall (e.g. towards CA4) instead of towards the restatoms in the empty state image (Figure 4-1a) also allow us to rule out bidentate configuration across an adatom-restatom pair within the same half unit cell.

In addition to adsorption on the faulted half as illustrated in unit cell B, the empty state image for unit cell C shows other adsorption configurations (Figure 4-1a). In particular, the bright protrusions correspond to adsorption of a glycine molecule at a center adatom CA5a on the unfaulted half and of that at a corner adatom AA7a across the dimer wall on the faulted half (Figure 4-1a). Evidently, the oblong protrusion at CA5a extending toward CA6 and that at the AA7a extending to AA8 appear to be similar to that at CA3a extending to CA4 (in unit cell B). The height profile along L6 is also found to be similar to that along L3. However, the corresponding height profile along L5 appears different from that of L4 due to the presence of the adsorption at AA7a. The filled state image for unit cell C shows that the adsorption of the glycine moieties at CA5a and at AA7a evidently has caused H adsorption at the respective neighbouring restatoms RA5d and RA7d. The H adsorption is illustrated by the missing intensity at these restatom locations, RA5d and RA7d, and the concomitant increase in intensities of the neighbouring adatoms (AA5b and CA5c for RA5d, and CA7b and CA6 for RA7d). The higher intensity for AA5b is quite apparent in the height profile along line scan L16, when compared to L12 along the unreacted sites. The intensity increase at CA6 caused by H adsorption at RA7d due to electron redistribution also partially counters the intensity reduction at CA6 due to adsorption at CA5a (as similarly observed for the CA3a, CA4 pair in unit cell B). The near-normal intensity for CA6 therefore suggests a more vertically oriented glycine fragment adsorbed at the CA5a site, when compared to that at the CA3a site. This upright unidentate adsorption geometry, as also obtained by our DFT calculation, has been discussed in our earlier XPS study.<sup>10</sup> Furthermore, the adsorption at corner adatom AA7a has also caused intensity depletion at the corner adatom AA8 across the dimer wall, when compared to the unreacted corner adatoms of the same half unit cell. This is consistent with the presence of weak dipole-dipole-like interaction between the glycine fragment at AA7a and the adatom across the dimer wall (AA8), as proposed earlier as in the case of the CA3a, CA4 pair. In addition, the deep trough found in the height profile along line scan L15 can be attributed to both the H adsorption at RA7d and the glycine fragment adsorption at AA7a.

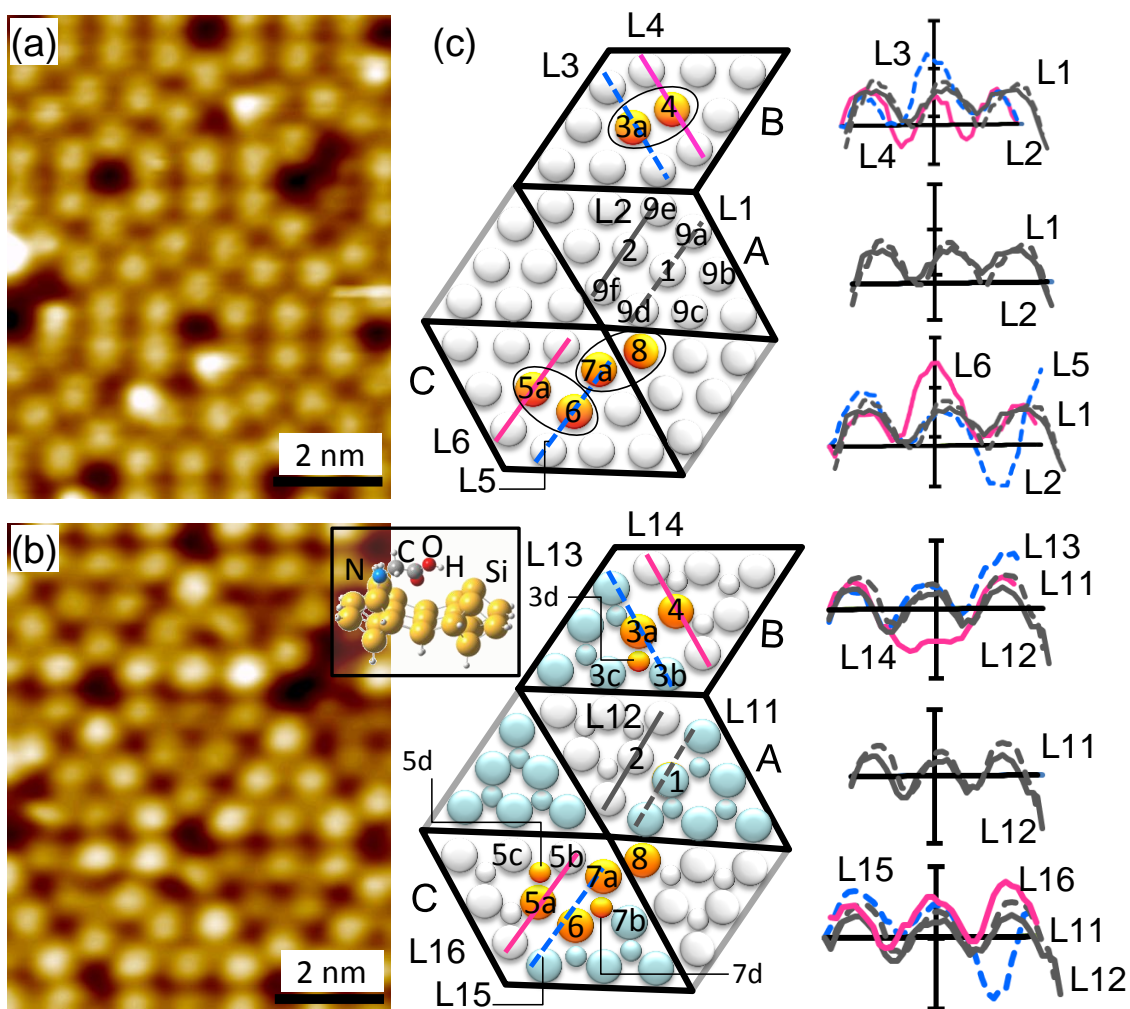


**Figure 4-1** (a) STM empty state image and (b) filled state image of glycine adsorbed on Si(111)7×7 surface obtained with sample bias of +2 V and −2 V, respectively, all at tunneling current of 200 pA. (c) Schematic drawings (center column) of three 7×7 unit cells labeled A, B and C for the STM images, and height profiles (right column) along the lines  $L_x$  ( $x = 1-6, 11-16$ ) in the unfaulted half (marked by solid lines) and faulted half (marked by dashed lines). The atoms in the unfaulted and faulted half unit cells are represented by lighter and darker spheres, respectively, in (c) lower. The sites of interest are labeled by alphanumeric characters. The ovals in (c) upper mark the adatom-adatom pairs across the dimer wall that are affected by glycine adsorption. Inset in (c) shows the equilibrium geometry of a N–H dissociated glycine molecule adsorbed on a  $\text{Si}_{26}\text{H}_{24}$  cluster in a tilted configuration as obtained by DFT/B3LYP/6-31++G(d,p) calculation.

In order to investigate the reactivity of different sites on Si(111)7×7 toward glycine, we show, in Figure 4-2, the empty state images, collected with a tunneling current of 200 pA at a sample bias of +2 V, for five different glycine exposures. As demonstrated in Figure 4-1, a protrusion in an empty state image can be used reliably to indicate a glycine fragment adsorbed on a surface site, in contrast to the more complex variation in filled state images. Using an image size of 50×50 nm<sup>2</sup> (with approximately 400 complete unit cells), as shown, e.g., for the 35 s exposure in Figure 4-2e, we determine the relative occupancies of the different sites (i.e. CA vs AA) and of the sites on the faulted and unfaulted half unit cells, as well as the total coverage (i.e. the fraction of the available sites that are occupied by glycine fragments). To obtain the relative occupancies of sites in the faulted and unfaulted half unit cells, we have also taken appropriate account of the corresponding filled state images (not shown). To better illustrate the adsorption features, we show, in Figure 4-2a-2d, only 17×17 nm<sup>2</sup> sections of the complete 50×50 nm<sup>2</sup> images (that we use for our statistical analysis). Not surprisingly, the total coverage of adsorbed glycine fragments is found to be increasing linearly with increasing exposure time in the early growth stage considered here (Figure 4-2f). In accord with dissociative adsorption of glycine on one of six adatoms in a half unit cell, for which the dissociated H atoms would occupy one of the three restatoms in the half unit cell, the maximum number of glycine adsorption in a half unit is therefore three, making the maximum possible total coverage to be 0.5 monolayer (where we define a monolayer coverage as the total number of Si adatom sites). Closer examination of the empty state and filled state images shows that the relative occupancy for the CA sites is higher than that of AA for each of the exposures (Figure 4-2f), in good accord with the fact that the CA sites are more electrophilic<sup>27</sup> and therefore more reactive to glycine than the AA sites. Furthermore, the relative occupancies of CA and of AA increase linearly with exposures, with the CA occupancy lying ~30% higher than the AA occupancy. In particular, the ratio between the relative occupancies for AA and CA is found to increase from 0.61 for the 8 s exposure to 0.66 for 20 s exposure and to 0.73 for 35 s exposure, which indicates that the rate of increase of adsorption on the AA sites increases faster than that on the CA sites with increasing exposure. The presence of a higher proportion of the unreacted AA sites than the unreacted CA sites is consistent with the earlier saturation of the CA sites before that of AA sites with increasing exposure. In addition, the majorities of the occupied CA sites (from a relative occupancy of 54% for 8 s to 50% for 35 s) and AA sites (from a relative occupancy of 26% for 8 s to 23% for 35 s) are found on the faulted half. This is consistent with the higher occupancy of sites on the faulted half than that on the unfaulted half, with the ratio between the relative occupancies for unfaulted half and faulted half found to increase from 0.21 for the 8 s exposure to 0.32 for 20 s exposure and to 0.49 for 35 s exposure. The observed earlier saturation of the faulted half sites than the unfaulted half sites with

increasing exposure is consistent with the higher reactivity of sites on the faulted half towards glycine. The CA (AA) sites on the faulted (unfaulted) half are therefore the most (least) reactive toward glycine adsorption.

The STM images in Figure 4-2 also reveal that while a predominant number of glycine molecules adsorbed individually (singles) appear as protrusions of similar size, some of the protrusions, marked by open squares in Figure 4-2, are discernibly larger (by at least 30% in diameter). As illustrated in Figure 4-3 below, these larger protrusions could be identified as an adsorbed glycine fragment vertically attached to a second glycine molecule by H-bonding (vertical doubles). Furthermore, glycine molecules also appear to adsorb in pairs in neighbouring sites, which could be the result of two adsorbed glycine fragments horizontally attached to each other by H-bonding (horizontal doubles). If we consider that the most probable adsorption were to occur at a center adatom site such as CA1 in Figure 4-1c upper (unit cell A), then a second glycine adsorption at CA2 (with a separation of 6.65 Å from CA1), at AA9a, CA9b, CA9c or AA9d (each with a separation of 7.68 Å from CA1), as well as at AA9e or AA9f (each with a separation of 10.15 Å from CA1) could form the horizontal doubles (marked as open eclipses in Figure 4-2). However, since the adsorption at CA1 would affect the LDOS at CA2, as discussed earlier, the second glycine adsorption on the other neighbouring sites would be more likely. As shown in Figure 4-2f, the relative occupancy (with respect to the total number of available sites) for the horizontal doubles (HD) is found to be consistently larger than that of the vertical doubles (VD). As the exposure time increases, both relative occupancies for VD and HD increase, with a higher increase in the VD occupancy at a higher exposure. These trends are consistent with the random statistical nature of molecular collisions with the surface in the adsorption process. It is also not surprising that the relative occupancies for HD and VD are considerably smaller than those of the singles during the initial stage of adsorption.

To understand the nature of the VD and HD adsorption mediated by H-bonding, we perform ab-initio calculations based on the Density Functional Theory (DFT) with a B3LYP hybrid functional<sup>59,58</sup> and a 631G++(d,p) basis set using the Gaussian 09 software.<sup>66</sup> To simulate the adsorption of a single glycine molecule on the 7×7 surface, we employ the Si<sub>16</sub>H<sub>18</sub> and Si<sub>26</sub>H<sub>24</sub> clusters to provide model surfaces for the adatom-restatom pair and the two adjacent adatom-adatom pairs across the dimer wall, respectively. In our earlier XPS study,<sup>10</sup> we have demonstrated that glycine undergoes initial N–H dissociative adsorption and formation of a transitional layer mediated by the [–H<sub>2</sub>N··HO(O)C–] H-bonds. The adsorption energies of the corresponding adsorbate-substrate configurations (ASCs) for “upright” single adsorption on the adatom-restatom pair (Figure 4-3a1, –266.4 kJ mol<sup>–1</sup>) and the double adatom-adatom pairs across

the dimer wall (Figure 4-3b1,  $-327.9 \text{ kJ mol}^{-1}$ ) are found to be in a similar energy range as the “tilted” single adsorption on the double adatom-adatom pairs across the dimer wall ( $-348.1 \text{ kJ mol}^{-1}$ , Figure 4-3c1), after consideration of the different clusters employed for modeling the different substrate sites. By adding a glycine molecule to the respective single ASCs in an appropriate fashion, we obtain the upright VD (Figures 4-3a2, 3b2) and tilted VD ASCs (Figure 4-3c2). The differences between the adsorption energies of upright and tilted VD ASCs and those of its corresponding singles plus a free glycine molecule give an estimate of the hydrogen bond energies, which are respectively  $-66.1 \text{ kJ mol}^{-1}$  (a2),  $-52.6 \text{ kJ mol}^{-1}$  (b2), and  $-19.79 \text{ kJ mol}^{-1}$  (c2). Interestingly, except for the tilted VD (c2), these values are found to be comparable to those calculated for  $[-\text{H}_2\text{N}\cdots\text{HO}(\text{O})\text{C}-]$  ( $-48.5 \text{ kJ mol}^{-1}$ ) and  $[-\text{C}(\text{OH})\text{O}\cdots\text{HO}(\text{O})\text{C}-]$  H-bonds ( $-67.6 \text{ kJ mol}^{-1}$ ) in free glycine molecules. For the tilted VD (c2), the weaker hydrogen bond strength is likely due to poor molecular alignment between the participating molecules.

Figures 4-3x3 and 3x4 (x=a-c) show typical STM images of these upright and tilted single and VD ASCs, respectively, with their corresponding height profiles along selected line scans shown in Figure 4-3x5 (x=a-c). In particular, as shown in Figure 4-3a5, the maximum height along L2 (200 pm) of the upright VD at the AA site (Figure 4-3a4) is nearly twice that along L1 (100 pm) of the upright single at the AA site (Figure 4-3a3). Similar height difference (Figure 4-3b5) is also observed along L4 for the upright VD at the CA site (200 pm, Figure 4-3b4), relative to that along L3 for the corresponding upright single (100 pm, Figure 4-3b3). The nearly twice height differences between the upright VD and their corresponding singles confirm the presence of the second glycine molecule H-bonded to their respective singles. For the tilted single at the CA site (Figure 4-3c3), the maximum height along L5 (80 pm, Figure 4-3c5) is discernibly less than that along L3 (100 pm, Figure 4-3b5) of the upright single at the CA site (Figure 4-3b3), which is consistent with the upright and tilted geometries in the respective ASCs. Similarly, the maximum height along L6 (180 pm, Figure 4-3c5) for the titled VD at the CA site (Figure 4-3c4) is also found to be smaller than that along L4 (200 pm, Figure 4-3b5) for the vertical VD at the CA site, which again is consistent with the proposed tilted VD ASC (Figure 4-3c2). The degree of tilt depends on the extent of the dipole-dipole interaction between the COOH terminus and the unreacted adatom across the dimer wall and could extend from vertical (no interaction) to near-horizontal (maximum interaction).

The STM image of two independent singles at a CA site and an adjacent AA site diagonally across the dimer wall (Figure 4-3d3) exhibits a height profile along the diagonal L7 with maximum height (80 pm)

similar to that of tilted single (Figure 4-3c3, L5). For the STM image of a typical HD (Figure 4-3d4), the height profile along the diagonal L8 (Figure 4-3d5) clearly shows similar maximum height as that of the two independent singles but with smaller separation between their peak maxima, which confirms the formation of H-bonding. Furthermore, the STM images of other HDs (Figure 4-3e3, 4-3e4) also exhibit similar height profiles along L9 and L10 (Figure 4-3e5) as that along L8 (Figure 4-3d5), which illustrates the variety of possible HD arrangement for different adjacent sites. Our DFT calculation shows an example of an ASC with two glycine fragments independently adsorbed at adatoms diagonally across the dimer wall, with different degrees of tilt (Figure 4-3d1). Our calculation also shows the formation of HD ASCs mediated by double H-bonding between two COOH termini from the glycine fragments adsorbed on adatoms diagonally across (Figure 4-3d2), on the same side of (Figure 4-3e1), and directly across the dimer wall (Figure 4-3e2).

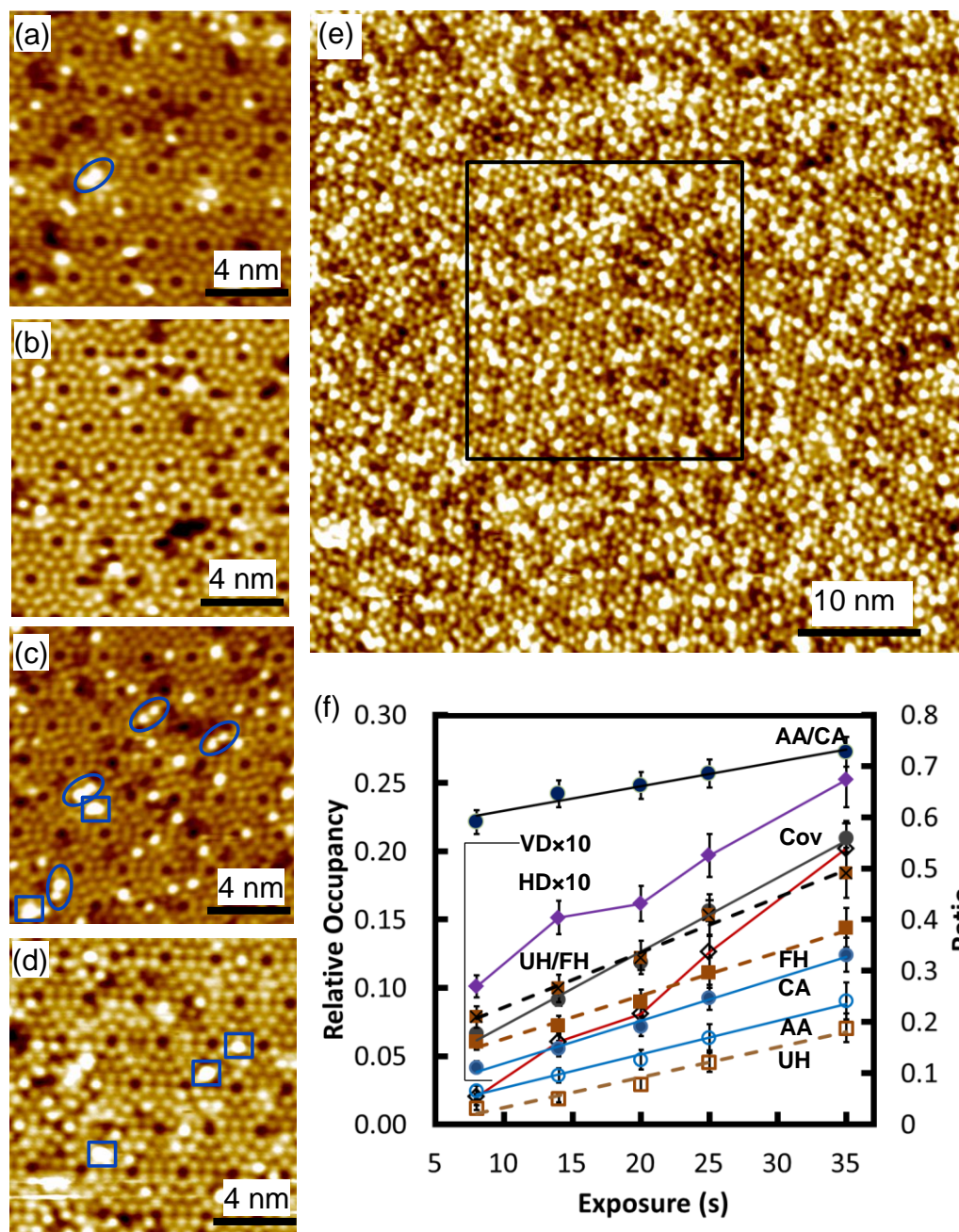


**Figure 4-2** STM images taken at a sample bias of +2 V and tunneling current of 200 pA after glycine exposure of (a) 8 s, (b) 14 s, (c) 20 s, (d) 25 s and (e) 35 s; and (f) the corresponding total coverage (Cov) and the relative occupancies for center adatom (CA), corner adatom (AA), faulted half (FH), unfaulted half (UH) sites, and for vertical doubles (VD) and horizontal doubles (HD). The ratios of AA to CA and UH to FH are shown on the right axis.

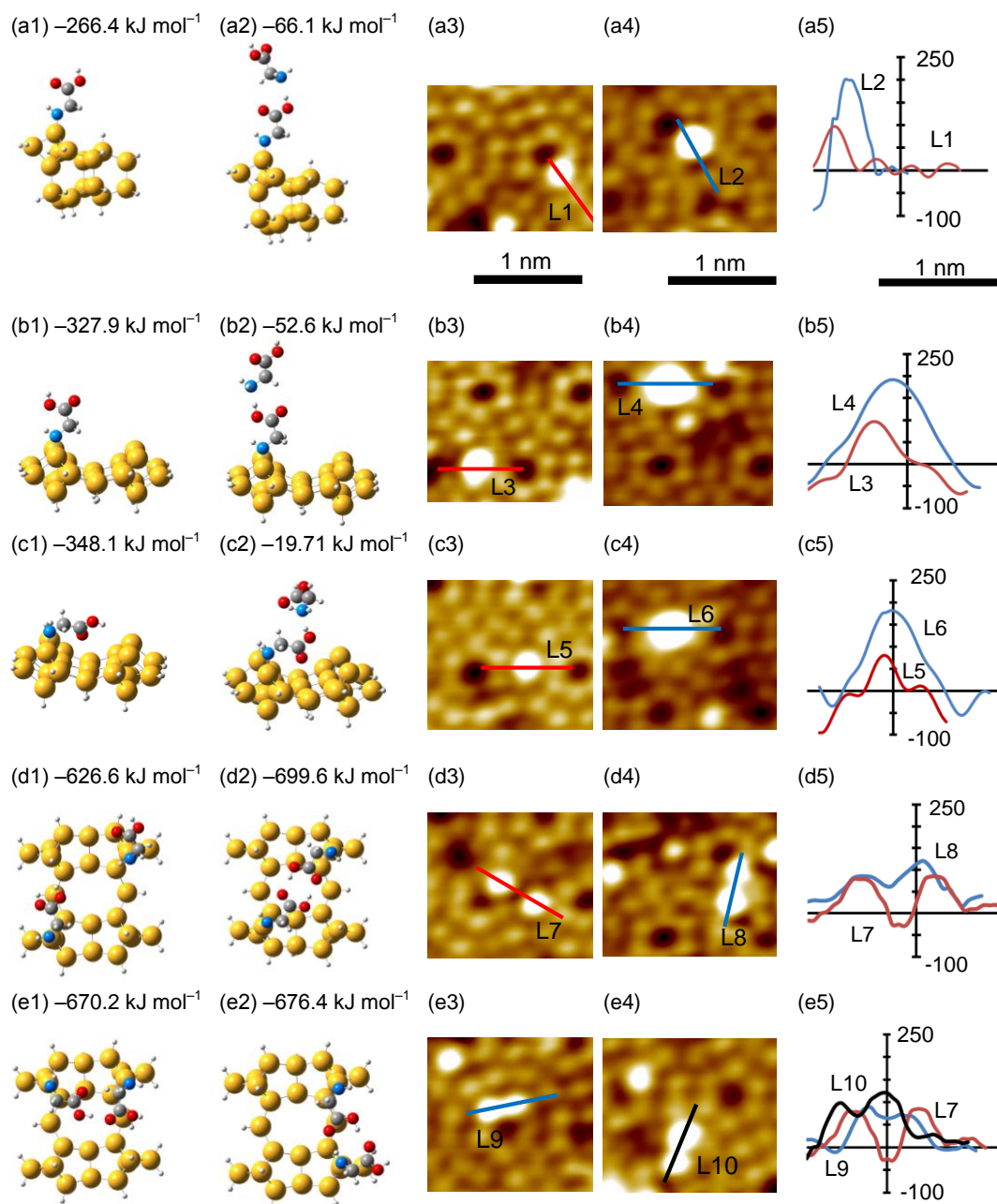


**Figure 4-3** Equilibrium structures and the adsorption energies of glycine on (a1, a2)  $\text{Si}_{16}\text{H}_{18}$  and (b-e 1, b-e 2)  $\text{Si}_{26}\text{H}_{24}$  in (a-d1) the single and (a-d2, e1, e2) double configurations, with the configurations for (d1, d2, e1, e2) shown as top view, all obtained with DFT/B3LYP/6-31G++(d,p). STM images taken at a sample bias of +2 V and tunneling current of 200 pA attributed to the corresponding (a-d 3) single and (a-d 4, e3, e4) double configurations, with the respective line scans, L1-L10, given in (a-e 5).

## 4.4 Summary

The early adsorption of glycine on Si(111)7×7 has been studied by STM. At the initial stage of adsorption (low exposure), we observe empty state and filled state images that correspond predominantly to individual (or single) H-dissociative adsorption of glycine at an adatom-restatom pair on the 7×7 surface. Of particular interest is the observation that the unidentate adsorption also affects the LDOS on the complementary adatom site (across the dimer wall), consequently reducing its occupancy. At a higher exposure, larger protrusions could be observed and identified by height profile analysis as an adsorbed glycine fragment vertically attached to a second glycine molecule by H-bonding. This is in good accord with our earlier XPS study that shows N–H dissociative adsorption of glycine and the formation of a transitional layer mediated by the  $[-\text{H}_2\text{N}\cdots\text{H}-\text{OC}(\text{O})-]$  H-bonding. Furthermore, adsorption in pairs in adjacent sites could also be found and attributed to two adsorbed glycine fragments horizontally attached to each other by H-bonding. The present study therefore demonstrates, for the first time, the presence of  $[-(\text{OH})\text{C}=\text{O}\cdots\text{H}-\text{OC}(\text{O})-]$  H-bonding in the formation of the interfacial (or first) adlayer. We also illustrate the plausibility of these single and H-bonding mediated vertical and horizontal double adsorption configurations by DFT/B3LYP calculations involving model surfaces of  $\text{Si}_{16}\text{H}_{18}$  and  $\text{Si}_{26}\text{H}_{24}$  clusters. Statistical analysis of STM images collected at different exposures further reveals that the apparent reactivity of individual sites towards glycine decreases in the following order: CA on the faulted half > AA on the faulted half > AA on the unfaulted half > CA on the unfaulted half. In the early stage of adsorption considered in the present study, the relative occupancies of these respective sites exhibit a linear trend, with the more reactive sites saturated faster than the less reactive ones. Furthermore, the relative occupancies for the horizontal doubles are notably larger than that of the vertical doubles, with the single significantly larger than the doubles in this early adsorption stage.

## Chapter 5

# Three-stage growth of glycine and glycyglycine nanofilms on Si(111)7×7 and their thermal evolution in ultrahigh vacuum condition: From chemisorbed adstructures to transitional adlayer to zwitterionic films<sup>‡‡ §§</sup>

### 5.1 Introduction

Film growth of simple amino acids (e.g. glycine, alanine, cysteine) on various well-ordered solid surfaces in ultrahigh vacuum has attracted a lot of attention because of their fundamental importance to understanding the interactions of larger biological materials (e.g. proteins and peptides) with solid surfaces. A number of amino acid molecules have been studied with scanning tunneling microscopy (STM) and found to form self-assembled monolayers or nanoarchitectures on surfaces.<sup>83,147,148,127</sup> For example, unidirectional molecular rows of cysteine were grown on Au(110)1×2 driven by an adsorbate-induced surface rearrangement<sup>83</sup> and electrostatic interactions between inter- and intra-row neighbouring zwitterions.<sup>147</sup> Nanogratings of L-methionine with tunable periodicity could be made on Ag(111) as a result of zwitterionic coupling.<sup>148</sup> The adsorption of glycine on Cu(110) was found to exhibit a sharp “p(3×2)g” LEED pattern, which was further resolved into a homochiral and a heterochiral domains by using STM.<sup>127</sup> However, despite the progress in these structural investigations, the film growth process of amino acids from the initial molecular adsorption to multilayer formation is not often well characterized, and the evolution mechanism of molecular structures and chemical bonding properties with increasing film thickness are not well understood.

As the simplest amino acid and peptide respectively, glycine (G) and glycyglycine (GG) are intensely studied as references for more complicated proteins and peptides. Both G and GG can exist in four different forms: the neutral form commonly present in gaseous state, the zwitterionic form found in solids and liquids, and the anionic and cationic forms typically stable in solutions.<sup>71</sup> However, when grown into films on metal and semiconductor substrates in ultrahigh vacuum, both G and GG may either exist in the non-zwitterionic forms or simply dissociate, depending on the nature of the substrates and/or the growth

---

<sup>‡‡</sup> Reprinted with permission from [L. Zhang, A. Chatterjee, K. T. Leung, *J. Phys. Chem. C.*, 115, 14155 (2011)]. Copyright [2011], American Chemical Society.

<sup>§§</sup> My specific contributions were research idea, XPS data collection (with Dr. Lei Zhang), data analysis and DFT calculations.

conditions.<sup>67,73,74,69,70,149,76,68,150,151,152,88</sup> The interactions between different functional groups of G and GG and specific surface sites of the substrate determine their respective forms in the film. A G molecule ( $\text{N}_a\text{H}_2\text{C}_{\alpha}\text{H}_2\text{C}_c\text{O}_n\text{O}_h\text{H}$ ) has two functional groups, amino ( $-\text{N}_a\text{H}_2$ ) and carboxylic acid groups ( $-\text{C}_c\text{O}_n\text{O}_h\text{H}$ ), attached to a methylene ( $>\text{C}_{\alpha}\text{H}_2$ ) unit, while a GG molecule ( $\text{N}_a\text{H}_2\text{C}_{\alpha 1}\text{H}_2\text{C}_p\text{O}_p\text{N}_p\text{HC}_{\alpha 2}\text{H}_2\text{C}_c\text{O}_n\text{O}_h\text{H}$ ) has an additional amide group ( $-\text{C}_p\text{O}_p\text{N}_p\text{H}-$ ) attached to a second methylene unit. In this notation, we have designated the amino and amide N's as  $\text{N}_a$  and  $\text{N}_p$  (a for amino and p for peptide-bond related), the methylene C's as  $\text{C}_{\alpha 1}$  and  $\text{C}_{\alpha 2}$ , and the amide C (involving the peptide bond) and carboxyl C as  $\text{C}_p$  and  $\text{C}_c$ , respectively, and the carbonyl O as  $\text{O}_p$  and  $\text{O}_n$  and hydroxyl O as  $\text{O}_h$ .

In the present study, we deposit G and GG on Si(111)7×7 in ultrahigh vacuum, and follow their film growth and subsequent thermal evolution by using X-ray photoelectron spectroscopy (XPS). The adstructures in the early growth stage have also been investigated with ab-initio calculations based on the Density Functional Theory (DFT) method. The present results reveal a similar three-stage growth process for both G and GG, with the initial dissociative adsorption followed by an intermediate transition stage involving H-bonding to the final formation of zwitterionic forms in the multilayer film. The thermal evolution of the thick G and GG films displays a reverse trend, with the zwitterionic multilayer and transitional adlayer desorbed sequentially and the interfacial adlayer less affected. The formation of hydrogen bonding during the film growth can be further exploited for the purpose of Si surface functionalization, for example, by deliberately choosing appropriate linker molecules that will covalently bond to the substrate while providing H-bonding to interact with other target molecules containing the appropriate (multi)functional groups. Given that a hydrogen bond is considerably weaker than a covalent bond yet stronger than a van der Waals bond, this type of hydrogen-bond capable linker molecules may provide a “catch-and-release” mechanism for novel bio-applications.<sup>77</sup>

## 5.2 Experimental Details

G (>98.5% purity, Sigma-Aldrich) and GG (>99.5% purity, Sigma-Aldrich), with normal melting points of 182°C and ~220°C, respectively, were evaporated from separate water-cooled effusion cells at 140°C and 170°C, respectively, onto the clean 7×7 surface held at room temperature in a separate preparation chamber (evacuated by a turbomolecular pump, an ion pump, a cryopump cooled by liquid nitrogen, and a titanium sublimation pump). The corresponding chamber pressure was  $1 \times 10^{-8}$  and  $3 \times 10^{-9}$  mbar during G and GG deposition, respectively. The nature of the G and GG vapours were confirmed by

recording their mass spectra [with their respective parent (base) ions of 75 amu (30 amu) and 132 amu (30 amu)]<sup>153</sup> with a quadrupole mass spectrometer. We used the deposition time to indicate the relative deposited amount. For submonolayer exposures, absolute coverage could in principle be determined from companion STM studies to be reported in our future work.<sup>154</sup> For higher exposures, it is possible to estimate the film thickness from the attenuation of the appropriate substrate photoemission signals, and the film thicknesses so obtained for the G and GG films with the largest exposures (960 s and 5400 s respectively) are 10 nm and 3 nm, respectively.<sup>48</sup> For the film growth experiments, G or GG was deposited sequentially on the same bare Si(111)7×7 substrate, with their corresponding Si 2p, O 1s, N 1s and C 1s core-level XPS spectra collected after each exposure. All spectra were fitted with mixed Gaussian-Lorentzian lineshapes (70% Gaussian and 30% Lorentzian) with a linear background removal by using the Casa-XPS software. For thick G and GG zwitterionic films, the FWHM for individual components in the C 1s, N 1s and O 1s spectra are 1.3, 1.5 and 1.5 eV, respectively. For thinner G and GG films where the molecules exist in a less homogeneous environment than thick films, the FWHM of the corresponding components are 0.2-0.3 eV larger. The binding energies are referenced to the Si 2p<sub>3/2</sub> (99.3 eV) of the bulk Si. For the thermal evolution experiments, an as-grown, thick G or GG film was annealed sequentially by resistive heating of the sample holder from 40°C up to 250°C, with the temperature monitored by a thermocouple located close to the sample holder. A relatively long soaking period (600 s) was used to ensure that the reported temperature corresponds to the thermally equilibrated sample due to the different locations between the sample and the thermocouple. The Si 2p, O 1s, N 1s and C 1s core-level spectra were recorded after each annealing.

## 5.3 Results and Discussion

### 5.3.1 Computational chemistry of adsorption configurations

Figure 5-1 shows the equilibrium geometries and the corresponding  $\Delta E$  values of possible ASCs for G and GG on the model Si<sub>16</sub>H<sub>18</sub> and Si<sub>12</sub>H<sub>12</sub> surfaces. For G on the Si<sub>16</sub>H<sub>18</sub> cluster, both bidentate and unidentate ASCs (Adsorption Structure Configuration) resulting from, respectively, double and single O<sub>h</sub>-H or N<sub>a</sub>-H dissociative adsorption have been considered. In particular, the [N<sub>a</sub>,O<sub>h</sub>]-bidentate ASC (corresponding to amino N<sub>a</sub> bonding to the Si adatom and carboxyl O<sub>h</sub> bonding to the restatom, Figure 5-1a) gives a more negative  $\Delta E$  (-459.5 kJ mol<sup>-1</sup>) than the [O<sub>h</sub>,N<sub>a</sub>]-bidentate ASC (corresponding to O<sub>h</sub> bonding to the Si adatom and N<sub>a</sub> bonding to the restatom, Figure 5-1b) (-451.1 kJ mol<sup>-1</sup>), which is consistent with the more basic character of the N<sub>a</sub> atom than O<sub>h</sub>. The O<sub>h</sub>-unidentate-A ASC

(corresponding to  $O_h$  bonding to the Si adatom, Figure 5-1c) has a more negative  $\Delta E$  ( $-268.6 \text{ kJ mol}^{-1}$ ) than the  $N_a$ -unidentate-A ASC (with  $N_a$  bonding to the Si adatom, Figure 5-1d) ( $-237.9 \text{ kJ mol}^{-1}$ ). It should be noted that we use suffixes A and R to indicate adsorption on adatom and restatom, respectively, in the present notation. Given that bonding to the more electrophilic Si adatom is found to give a more stable equilibrium geometry than bonding to the more nucleophilic restatom, we have not shown the corresponding unidentate ASCs for the restatom, which typically exhibit a higher  $\Delta E$  by  $12.5 \text{ kJ mol}^{-1}$  and  $4.5 \text{ kJ mol}^{-1}$  for the  $N_a$ -unidentate-R and the  $O_h$ -unidentate-R products respectively. For G on the  $Si_{12}H_{12}$  cluster, the corresponding unidentate ASCs follow a similar trend as those found on the  $Si_{16}H_{18}$  cluster, with the  $\Delta E$  for  $O_h$ -unidentate ASC (Figure 5-1e,  $-359.8 \text{ kJ mol}^{-1}$ ) being more negative than that of  $N_a$ -unidentate ASC (Figure 5-1f,  $-325.4 \text{ kJ mol}^{-1}$ ). Our calculation also shows that no stable bidentate ASC involving bridging both adatoms across the dimer wall could be obtained due to the large separation between the two adatoms ( $6.65 \text{ \AA}$ ) compared to the  $N_a$ -to-  $O_h$  distance in G ( $3.7 \text{ \AA}$ ).

It is important to recognise that the present calculation of adsorption energies only gives hints about the feasibility of formation of these ASCs from the thermodynamic perspective. Appropriate consideration of kinetic effects and the underlying formation mechanisms of these ACSs should be included in future work. For the purpose of the present study, we have also considered the formation of adducts of G on the model cluster, which are prerequisite to the formation of these ASCs. Our calculations showed that no stable adducts can be obtained for the O–H dissociative products, including  $[N_a, O_h]$ -bidentate,  $[O_h, N_a]$ -bidentate,  $O_h$ -unidentate-A and  $O_h$ -unidentate ASCs. More detailed discussion of the formation of these adducts is given elsewhere.<sup>141</sup> Despite the more negative  $\Delta E$ s found for these O–H dissociative products (Figure 5-1a-c, 5-1e), we conclude that the  $N_a$ -unidentate-A ASC (Figure 5-1d) and  $N_a$ -unidentate (Figure 5-1f) are the only plausible products for G on the respective  $Si_{16}H_{18}$  and  $Si_{12}H_{12}$  model surfaces.

The presence of the amide group ( $-C_pO_pN_pH-$ ) in GG provides additional bidentate and unidentate ASCs on the  $Si_{16}H_{18}$  cluster. Indeed, given that the  $N_a$ -to- $O_h$  distance in GG ( $7.31 \text{ \AA}$ ) is considerably larger than the adatom-to-restatom separation ( $4.57 \text{ \AA}$ ), bonding through the  $O_p$  and  $N_p$  atoms of the amide group is essential to the formation of bidentate ASCs. In particular,  $[N_p, O_h]$ -bidentate (Figure 5-1h),  $[N_p, N_a]$ -bidentate (Figure 5-1i), and  $[N_a, N_p]$ -bidentate ASCs (Figure 5-1j) on the adatom-restatom pair of the  $Si_{16}H_{18}$  surface arise from double  $N_p$ -H, and  $O_h$ -H or  $N_a$ -H dissociation and they provide two dissociated H atoms for Si–H bond formation. These bidentate ASCs give the most negative  $\Delta E$ s, with magnitude similar to those found for the corresponding bidentate ASCs of G. Additional  $[O_p, O_h]$ -bidentate ASC (Figure 5-1o) involves bonding of the amide  $O_p$  and  $O_h$ -H dissociative adsorption, giving

rise to one dissociated H atom for Si–H bond formation. The corresponding  $\Delta E$  is found to be notably less negative than those of the other bidentate ASCs and is more similar to those of the  $O_h$ -unidentate-A,R (Figures 5-1k, 5-1l),  $N_a$ -unidentate-A,R (Figures 5-1m, 5-1n), or  $N_p$ -unidentate-A ASC (Figure 5-1p), arising from a single  $O_h$ –H or  $N_a$ –H or  $N_p$ –H dissociation, respectively. Indeed, the small  $\Delta E$  difference ( $33.5 \text{ kJ mol}^{-1}$ ) found between  $[O_p, O_h]$ -bidentate ASC ( $-243.7 \text{ kJ mol}^{-1}$ ) and  $O_h$ -unidentate-R ASC ( $-277.2 \text{ kJ mol}^{-1}$ ) is consistent with the additional energy required for structural rearrangement as a result of the formation of the  $O_p$ –Si bond. The  $N_p$ -unidentate-A ASC arising from dissociative adsorption of GG through  $N_p$ –Si bond formation (Figure 5-1p) gives less negative  $\Delta E$  ( $-223.4 \text{ kJ mol}^{-1}$ ) than the  $N_a$ -unidentate-A ASC (Figure 5-1m,  $-245.7 \text{ kJ mol}^{-1}$ ) through  $N_a$ –Si bond formation. Finally, we also obtain other ASCs with higher  $\Delta E$ s (not shown), including  $N_p$ -unidentate-R ( $-193.1 \text{ kJ mol}^{-1}$ ),  $[N_a, O_p]$ -bidentate ( $-199.8 \text{ kJ mol}^{-1}$ ),  $[N_p, O_h]$ -bidentate ( $-198.3 \text{ kJ mol}^{-1}$ ) and  $O_p$ -unidentate-A ( $-84.1 \text{ kJ mol}^{-1}$ ). For GG on the  $Si_{12}H_{12}$  cluster, the longer  $N_a$ -to- $O_h$  distance ( $7.31 \text{ \AA}$ ) would enable a new  $[N_a, O_h]$ -bidentate ASC (Figure 5-1q) bridging across the two adatoms across the dimer wall. Not surprisingly, the  $\Delta E$  for this bidentate ASC ( $-742.9 \text{ kJ mol}^{-1}$ ) is calculated to be considerably more negative than those of the corresponding unidentate ASCs, including  $O_h$ -unidentate ( $-360.3 \text{ kJ mol}^{-1}$ , Figure 5-1r),  $N_a$ -unidentate ( $-325.4 \text{ kJ mol}^{-1}$ , Figure 5-1s), and  $N_p$ -unidentate ASCs ( $-314.0 \text{ kJ mol}^{-1}$ , Figure 5-1t).

As in the case of G on the  $Si_{16}H_{18}$  and  $Si_{12}H_{12}$  model surfaces, we also perform an exhaustive search for stable GG adducts as the precursors to the formation of the aforementioned ASCs.<sup>141</sup> These calculations show that stable adducts can be obtained for ASCs involving N–H dissociation and not O–H dissociation of GG on  $Si_{16}H_{18}$ , including  $[N_p, N_a]$ -bidentate (Figure 5-1i),  $[N_a, N_p]$ -bidentate (Figure 5-1j),  $N_a$ -unidentate-A (Figure 5-1m),  $N_a$ -unidentate-R (Figure 5-1n), and  $N_p$ -unidentate-A (Figure 5-1p). However, stable adduct can be found for  $[N_a, O_h]$ -bidentate (Figure 5-1q) but not  $O_h$ -unidentate (Figure 5-1r) on the  $Si_{12}H_{12}$  model surface. We therefore conclude that only ASCs involving N–H dissociation for GG are plausible, with the following relative stability trends based on their  $\Delta E$  values:  $[N_a, O_h]$ -bidentate ( $\Delta E = -742.9 \text{ kJ mol}^{-1}$ ) >  $N_a$ -unidentate ( $-325.4 \text{ kJ mol}^{-1}$ ) >  $N_p$ -unidentate ASCs ( $-314.0 \text{ kJ mol}^{-1}$ ) on  $Si_{12}H_{12}$ , and  $[N_p, N_a]$ -bidendate ( $-436.0 \text{ kJ mol}^{-1}$ ) >  $[N_a, N_p]$ -bidendate ( $-399.7 \text{ kJ mol}^{-1}$ ) >  $N_a$ -unidentate-A ( $-245.7 \text{ kJ mol}^{-1}$ ) >  $N_a$ -unidentate-R ( $-244.5 \text{ kJ mol}^{-1}$ ) >  $N_p$ -unidentate-A ASCs ( $-223.4 \text{ kJ mol}^{-1}$ ) on  $Si_{16}H_{18}$ .

### 5.3.2 X-ray photoelectron spectroscopy of G and GG adsorption

In the third chapter we have reported detailed XPS spectra of the C 1s, N 1s and O 1s regions of G as a function of exposure time, as also shown in Figure 5-2. Briefly, G is found to undergo  $N_a$ –H dissociative

adsorption on Si(111)7×7 upon the initial exposure, as shown by the presence of a prominent N 1s feature at 399.1 eV attributed to N–Si bond<sup>78,16,10</sup> at low exposure time < 480 s (Figure 5-2, centre).

Furthermore, the emergence of a new N 1s feature at 401.4 eV, assigned to N···H–O hydrogen bond, over the 30-480 s exposure range indicates the growth of a transitional adlayer mediated by H-bonding. This observation is consistent with our computational result, which shows that the plausible N<sub>a</sub>-unidentate-A ASC on Si<sub>16</sub>H<sub>18</sub> (Figure 5-1d) and N<sub>a</sub>-unidentate ASC on Si<sub>12</sub>H<sub>12</sub> (Figure 5-1f) both involve the formation of N–Si bond with the O–H bond intact. Further exposure for over 480 s gives rise to a third N 1s feature at 402.1 eV, which is characteristic of the protonated amino group (NH<sub>3</sub><sup>+</sup>) in the zwitterions.<sup>67,74,80</sup>

Based on the saturation intensity ratio of this new hydrogen bond-related N 1s feature at 401.4 eV to the N–Si feature at 399.1 eV (likely corresponding to adsorption of the first or interfacial adlayer), the transition adlayer is estimated to be ~1.5 times the interfacial adlayer. In the C 1s spectra (Figure 5-2, right), the two well-defined C 1s peaks at 286.9 eV and 289.7 eV at shorter exposure times (<960 s) can be assigned to, respectively, methylene (>CH<sub>2</sub>) bonded to N and carboxyl C,<sup>74,155</sup> with their intensity ratio close to unity, in good accord with their stoichiometry. For the 960 s exposure, the carboxyl C 1s peak is found to shift by 0.7 eV to a lower binding energy while the methylene C 1s position remains unchanged, which is consistent with the greater delocalization of the negative charge of the carboxylate group in the zwitterionic multilayer. Figure 5-2 also shows the evolution of the corresponding O 1s spectra of the G film with increasing deposition time (left panel). Below 480 s exposure, the O 1s peak at 533.0 eV is found to be discernibly broader (1.9 eV FWHM) than that at 531.9 eV (1.4 eV FWHM) for 960 s exposure, which can be assigned only to carboxylate O in the zwitterionic multilayer.<sup>80</sup> The broad feature is therefore due to multiple components, likely the carbonyl O (C=O) at 532.1-532.9 eV and the hydroxyl O (OH) component at 532.8-534.4 eV.<sup>156,157,158,159,160</sup> Given that the O 1s feature for Si–O bond is usually found at 532.2-532.8 eV,<sup>159,161</sup> the broad O 1s feature is not particularly useful to determine whether O–H dissociative adsorption could occur. For G adsorption, we could however rule out O–H dissociative adsorption from the N 1s spectrum in which no neutral N 1s feature at 400.6 eV is found.

In the present study, we further investigate the observed three-stage growth process by examining the thermal evolution of a thick G film (obtained after the 960-s exposure). Figure 5-2 also shows the spectral evolution of this G film after sequential annealing to 40°C, 70°C, 100°C, 200°C and 250°C, each for 600 s. After the 40°C anneal, the C 1s, N 1s and O 1s spectra remain unchanged in their spectral shapes and peak positions, but considerable intensity reductions (over 50%) are notable, which indicates partial desorption of the thick zwitterionic films after the 40°C anneal. The remaining zwitterions are

totally removed upon further annealing to 70°C, as indicated by the replacement of the characteristic N 1s feature at 402.1 eV by the N 1s features for N···H–O at 401.4 eV and for N–Si at 399.1 eV and by the shifts of both the O 1s feature (at 531.9 eV) and the carboxyl C 1s feature (at 289.0 eV) to higher binding energy. On the other hand, the hydrogen-bonded transitional adlayer and the covalently bonded interfacial adlayer are hardly affected by further heating at 70°C. However, continued annealing the sample to 100°C desorbs about half of the transitional adlayer, as indicated by nearly 50% intensity reduction of the H-bonded N 1s feature at 401.4 eV. The partial desorption of the transitional adlayer leads to a slight intensity increase of the interfacial (N–Si) N 1s feature at 399.1 eV. Annealing to 200°C almost completely removes the transitional adlayer. The residual N 1s intensity found near 401.0 eV could correspond to the remaining H-bonded N adspecies or thermally dissociated product (e.g. H<sub>2</sub>CN)<sup>67</sup> of the transitional and/or interfacial adlayer. An apparent shift of 0.7 eV in the O 1s feature to a lower binding energy (relative to that at 100°C) suggests the formation of O–Si bond. After the 250°C anneal, thermal dissociation takes place, as indicated by the more drastic intensity reduction of the two C 1s peaks than those of N 1s and O 1s peaks. Evidently, both the N–Si and O–Si covalent bonding are hardly affected by the anneal at 250°C. The thermal evolution of the thick G film therefore follows a reverse trend to the film growth.

Figure 5-3 shows the C 1s, N 1s and O 1s spectra of a GG film deposited on Si(111)7×7 as a function of exposure time. Evidently, the spectra for a thick film obtained with a 5400-s exposure of GG resemble those of GG powders (not shown),<sup>162</sup> consistent with the zwitterionic form in a thick GG film. The observed spectral similarity also verifies that GG does not dissociate significantly during thermal evaporation in the deposition process. In the zwitterionic form (N<sub>b</sub>H<sub>3</sub><sup>+</sup>C<sub>α1</sub>H<sub>2</sub>C<sub>p</sub>O<sub>p</sub>N<sub>p</sub>HC<sub>α2</sub>H<sub>2</sub>C<sub>c</sub>O<sub>n</sub>O<sub>h</sub><sup>-</sup>),<sup>\*\*\*</sup> there are two different types of N species: one in the protonated amino group (–N<sub>b</sub>H<sub>3</sub><sup>+</sup>), and the other in the amide group [–C<sub>p</sub>O<sub>p</sub>N<sub>p</sub>H–] containing the peptide bond, which give rise to the N 1s features at 402.2 eV and 400.6 eV, respectively (Figure 5-3, center). The observed binding energy positions for these spectral components are consistent with the published results for –NH<sub>3</sub><sup>+</sup> (402.0-402.5 eV),<sup>74, 162, 72, 163</sup> as found in G, and for amide in GG powders (400.4 eV)<sup>162</sup> and in thymine films (401.0, 401.2 eV).<sup>164, 123</sup> The corresponding energy separation between the N<sub>b</sub> 1s and N<sub>p</sub> 1s features (1.6 eV) in the zwitterions is found to be nearly the same as that between the N<sub>b</sub> 1s and N<sub>a</sub> 1s in the amino (–N<sub>a</sub>H<sub>2</sub>) group of the neutral molecular form (1.8 eV) as reported by Clark et al.<sup>80</sup> The N 1s feature of the amide group (N<sub>p</sub>) therefore nearly coincides with that of the neutral amino group (N<sub>a</sub>), which makes it difficult to differentiate these

---

\*\*\* The two oxygen atoms, O<sub>n</sub> and O<sub>h</sub>, in the carboxylate group of the zwitterion are equivalent.

two features in the present N 1s spectra. The corresponding C 1s spectrum for the 5400-s GG exposure (Figure 5-3, right) is evidently dominated by two strong features at 286.9 and 288.9 eV with similar intensities, corresponding to the methylene ( $C_{\alpha 1}$  and  $C_{\alpha 2}$ ) and to the carboxyl ( $C_c$ ) and carbonyl ( $C_p$ ) species, respectively, in good accord with those found for zwitterionic G films (Figure 5-2, right) and cysteine film.<sup>155</sup> The very sharp peak at 288.9 eV indicates a very small binding energy difference between the  $C_p$  and  $C_c$  species. The corresponding O 1s spectrum (Figure 5-3, left) can be well fitted with two components at 531.9 and 532.7 eV with an intensity ratio of 2:1, with the former attributed to the  $O_h$  in the deprotonated carboxyl group and the latter to the carbonyl  $O_p$ . These O 1s binding energies for GG are also in good agreement with those found in G.

The N 1s spectral evolution of GG with increasing exposure time (Figure 5-3, center) appears to be similar to that found for G (Figure 5-2, center). In particular, three features at 399.1 eV, 400.6 eV and 402.2 eV can be identified and assigned to N–Si,<sup>78,16,10</sup> amide  $N_p$  and/or neutral amino  $N_a$ , and protonated amino  $N_b$  species, respectively. In the initial growth stage (60 s exposure), the spectrum consists of a major component (N–Si) at 399.1 eV and a minor component (amide  $N_p$  and/or neutral amino  $N_a$ ) at 400.6 eV. With further exposure to 240 s, both features increase in intensity with the major feature at 399.1 eV becoming saturated, consistent with the emergence of an interfacial (first) adlayer through N–Si and O–Si bond formation. Because a GG molecule contains one amino  $N_a$  and one amide  $N_p$  atoms, the presence of a prominent feature at 399.1 eV at low exposure indicates that both the neutral amino and the amide N atoms simultaneously contribute to the N–Si bond formation at the interface. This is because if only one N (either amino or amide) atom is involved in the N–Si bonding while the other N remains unreacted, the N–Si component at 399.1 eV would have equal intensity as the unreacted (amino or amide) N component at 400.6 eV, which is clearly not observed in Figure 5-3 (center). From a structural point of view, the amino and amide N atoms, with a separation of 3.5 Å, are physically compatible to form covalent bonds with one Si adatom and its nearest restatom neighbour (separated by 4.57 Å) in a bidentate configuration on the Si(111)7×7 surface. This is consistent with our DFT calculation that shows the [ $N_p, N_a$ ]-bidentate ASC ( $-436.0 \text{ kJ mol}^{-1}$ , Figure 5-1i), and [ $N_a, N_p$ ]-bidendate ASCs ( $-399.7 \text{ kJ mol}^{-1}$ , Figure 5-1j) to be among the most stable ASCs. In addition, the minor feature at 400.6 eV at low exposure may be due to the unreacted amide  $N_p$  atom in the [ $N_a, O_h$ ]-bidentate ASC with the amino  $N_a$  atom and hydroxyl  $O_h$  atom bridging across the dimer wall (Figure 1q), which has the most negative adsorption energy ( $-742.9 \text{ kJ mol}^{-1}$ ). The continued growth of the  $N_a/N_p$  1s feature at 400.6 eV to a feature with almost equal intensity as the N–Si feature at 399.1 eV after 480 s of exposure indicates the

addition of GG adlayers in the neutral form. The  $N_a/N_p$  1s feature at 400.6 eV becomes a prominent feature after 840 s exposure, with a weak N 1s feature emerging at 402.2 eV, corresponding to the protonated amino group ( $-N_bH_3^+$ ) in the zwitterions. The emergence of the 402.2 eV feature at the 480-s exposure indicates the on-set of the GG zwitterionic film growth following the formation of a neutral GG transitional adlayer. From the intensities of the spectral features at 400.6 eV and 399.1 eV obtained at the 840-s exposure (completion of the transitional adlayer) and 240-s exposure (completion of the interfacial adlayer), we estimate the neutral GG transitional adlayer to have a similar thickness as the covalently-bonded interfacial adlayer. Like G, the growth of the GG transitional adlayer on the interfacial adlayer is mediated by hydrogen bonding, which is supported by the considerable thermal resistance of the transitional adlayer shown below. Further exposure to 5400 s causes continued increase in the intensities of both the  $N_b$  1s feature at 402.2 eV and the  $N_p$  1s feature at 400.6 eV, indicating the formation of a thick zwitterionic GG film. The N 1s spectra therefore reveal a three-stage, interfacial–transitional–multilayer growth of GG on Si(111)7×7 surface, similar to that found for G growth.

Figure 5-3 (right) also shows the spectral evolution of the C 1s features of the GG films with increasing exposure time. For exposures other than 5400 s, the C 1s spectra have been fitted with three components at 285.0, 286.6 and 289.6 eV and one component at a position that appears to change with exposure, i.e. 288.1 eV for 60 s, and 240 s, 288.4 eV for 480 s and 288.7 eV for 840 s. It has been seen that in the spectral evolution of the C 1s features of the G films (Figure 5-2, right), the position of the methylene C 1s feature is stable in the three growth stages of G at 286.9 eV, while the position of the carboxyl C 1s feature is also stable at 289.7 eV for the interfacial and transitional adlayers but shifts by 0.7 eV to a lower binding energy in the multilayer. This indicates that the methylene C 1s feature is hardly affected by the change of the G forms, whereas the carboxyl C 1s feature changes considerably when the carboxylic acid group (COOH) deprotonates to carboxylate (COO<sup>-</sup>), as a result of charge delocalization in the carboxylate. In a neutral GG molecule ( $N_aH_2C_{\alpha_1}H_2C_pO_pN_pHC_{\alpha_2}H_2C_cO_nO_nH$ ), there are two methylene  $C_{\alpha_1}$  and  $C_{\alpha_2}$ , one amide  $C_p$  and one carboxyl  $C_c$  atoms, the binding energies of which are expected to increase in the sequence of  $(C_{\alpha_1}, C_{\alpha_2}) < C_p < C_c$  from a simple consideration of the electronegativity of their nearest neighbours. Based on the magnitude and constancy of the binding energies of the fitted components, we therefore assign the features at 286.6 eV, 288.1–288.7 eV and 289.6 eV, respectively, to the two methylene  $C_{\alpha_1}$  and  $C_{\alpha_2}$  atoms, amide  $C_p$ , and carboxyl  $C_c$ . The gradual increase of the amide  $C_p$  1s binding energy with increasing exposure is in accord with the binding energy increase of the  $N_p$  1s from 399.1 eV for the interfacial adlayer to 400.6 eV for the transitional adlayer as a result of electron

delocalization in the peptide bond. In particular, the largely negatively charged  $N_p$  atoms at the interfacial adlayer lead to a correspondingly larger electron density in the  $C_p$  atoms and therefore a lower binding energy. The  $C_p$  1s binding energy (288.7 eV) for the 840-s exposure is in agreement with that (288.9 eV) of a peptide bond in thymine.<sup>123</sup> The intensity of the methylene C 1s feature is close to the sum of that of the carboxyl and amide C 1s features, in agreement with the C stoichiometry of GG. With further increase in exposure, formation of GG zwitterions, as in the case of G, gives rise to a considerable shift (0.7 eV) of the carboxyl  $C_c$  1s feature to the lower binding energy side and eventually merging with the amide  $C_p$  1s feature to form a sharp peak at 288.9 eV in the 5400-s thick film. Finally, the component at 285.0 eV is located at a 1.6 eV lower in binding energy than the methylene C and seems to be unrelated to GG. Because such a low binding energy could only result from formation of C–Si bond following C–H bond cleavage and that dissociation other than N–H or O–H bond upon GG adsorption is unlikely, we attribute this feature at 285.0 eV to residual hydrocarbon species likely arising from thermal evaporation of GG during the exposure process. A similar hydrocarbon residual peak at 285 eV has also been reported for thermally evaporated dipeptide and tripeptide films on Au(110)<sup>165</sup> and thick films of DNA base groups on H-terminated Si(111) under ultrahigh vacuum.<sup>166</sup> Figure 5-3 (left) also shows the corresponding O 1s spectra of the GG film with increasing deposition time. Like the G film, the O 1s spectra are dominated by a broad feature at 532.7 eV, with its width (2.0 eV FWHM) for exposures lower than 840 s discernibly larger than that for the 5400-s exposure (1.4 eV FWHM). We have previously assigned the O 1s feature for the 5400-s exposure to the deprotonated carboxylate  $O_n/O_h$  component (at 531.9 eV) and the carbonyl  $O_p$  components (at 532.7 eV) in the zwitterionic multilayer. The broad feature found at lower exposures can be due to a combination of carbonyl O at 532.1–532.9 eV and hydroxyl O component at 532.8–534.4 eV,<sup>156,157,158,159,160</sup> and is not very useful for revealing whether O–H dissociative adsorption could occur.

Thermal evolution of the thick GG film with the 5400-s exposure on Si(111)7×7 was studied by recording the C 1s, N 1s and O 1s spectra after sequentially annealing to 60, 100, 200 and 250°C, each for 600 s (Figure 5-3). After the 60°C anneal, the C 1s, N 1s and O 1s spectral profiles remain largely unchanged, except for a ~20% reduction in their intensities, which indicates desorption of a small amount of GG zwitterions. However, annealing at 100°C almost totally removes the GG zwitterions, as indicated by the dramatic near-complete reduction of the N 1s feature (of  $-N_bH_3^+$ ) at 402.2 eV (Figure 5-3, center). The resulting C 1s, N 1s and O 1s spectra appear similar to those of the film after 840-s exposure, which suggests that the transitional and interfacial adlayers remain stable to 100°C, in contrast to the G

transitional adlayers, half of which desorb at 100°C (Figure 5-2). Surprisingly, further annealing to 200°C does not appear to have a significant effect on the spectra, indicating that most of the transitional adlayer still remains intact at 200°C. This relatively high thermal stability of the transitional adlayer is consistent with the presence of additional H-bonding interactions in the GG transitional adlayer. The three functional groups in a GG molecule facilitate H-bonding formation among them. However, the absence of the N 1s feature at 401.4 eV suggests that the  $O_h-H\cdots N_a$  hydrogen bonding in the head-to-tail configuration does not occur, in contrast to that found in the G transitional adlayers. This may be due to an unfavourable orientation of the  $O_h-H$  moiety in the interfacial adlayer for hydrogen bonding with the incoming GG molecules and/or availability of other stronger hydrogen bonding. Instead,  $N_{a/p}-H\cdots O_n=C_c$  and  $N_{a/p}-H\cdots O_p=C_p$  H-bonding between an amino or amide group in the transitional adlayer and the carbonyl O in the interfacial adlayer, and/or  $O_h-H\cdots O_n=C_c$  and  $O_h-H\cdots O_p=C_p$  H-bonding between a hydroxyl O in the transitional adlayer and a carbonyl O in the interfacial adlayer may account for the relatively high thermal stability of the transitional adlayer. Indeed, extensive intermolecular amide-amide H-bonding has been reported to cause a higher onset temperature (by 125°C) of thermal desorption of amide-containing alkanethiol self-assembled monolayers on Au.<sup>167,168</sup> Unfortunately, the inherently large linewidths of the O 1s features do not allow definitive identification of the types of the H-bonds. After the 250°C anneal, the spectra become similar to those for the as-deposited film obtained after 480 s of exposure. Considerable reduction in the intensity of the  $N_a/N_p$  1s feature at 400.6 eV (Figure 5-3, center) is observed, which indicates that nearly half of the transitional adlayer has been removed. These annealing experiments show that the GG transitional adlayer is more strongly bonded than the G transitional adlayer, which almost completely desorbs at 200°C. Like the G film, the thermal evolution of the thick GG film also follows a similar reverse growth process.

#### 5.4 Comparison of XPS results with the calculations

Having presented both the plausible ASCs and XPS results, we are able to relate the most favourable ASCs, i.e. those having the most negative adsorption energies, to the XPS results of the interfacial adlayer, as represented by the 10-s G and 60-s GG films. The N 1s spectrum for the 10-s G film (Figure 5-2) clearly shows that the G molecule bonds to the Si(111)7×7 surface with covalent N-Si bonding after N-H bond cleavage. Although the corresponding  $N_a$ -unidentate-A configuration (Figure 5-1d) does not have the most negative adsorption energy, stable adduct that is prerequisite to the formation of ASCs can be obtained. In contrast, no stable adduct can be found for the O-H dissociative products. The dominance of the N-Si feature in the N 1s spectrum for the 60-s GG film (Figure 5-3) indicates that both

N atoms in the GG molecule bond to Si, which is consistent with the calculated  $[N_p, N_a]$ -bidentate (Figure 5-1i) and  $[N_a, N_p]$ -bidentate ASCs (Figure 5-1j), the adsorption energies of which are among the most negative ones on the  $Si_{16}H_{18}$  model surface. On the other hand, the clearly discernible N 1s feature at 400.6 eV for the 60-s GG film (Figure 5-3) can be attributed to the neutral  $N_p$  in the  $[N_a, O_h]$ -bidentate ASC (Figure 5-1q), which has the most negative adsorption energy on the  $Si_{12}H_{12}$  model surface.

## 5.5 Summary

We have investigated the growth of G and GG films on Si(111)7×7 at room temperature and their thermal evolution in ultrahigh vacuum by XPS. The equilibrium geometries and their corresponding adsorption energies of plausible adstructures for G and GG on an adatom-restatom pair (of a  $Si_{16}H_{18}$  cluster) and on a center-adatom-to-center-adatom pair (of a  $Si_{12}H_{12}$  cluster) were calculated by using the DFT/B3LYP method. From the spectral changes of the N 1s features with increasing exposure, three growth stages can be identified for G and GG films, and they correspond to the sequential formation of the covalently bonded interfacial adlayer, the hydrogen-bond-mediated transitional adlayer, and the zwitterionic multilayer. In the initial growth stage, G molecules adsorb on the 7×7 surface in a unidentate configuration by N–H bond dissociation, while GG molecules adsorb in bidentate configurations via bond dissociation of  $N_a$ –H and  $N_p$ –H bonds at an adatom-restatom site or of  $N_a$ –H and  $O_h$ –H bonds at a center-adatom-center-adatom dimer-wall site. Our XPS results are consistent with the three most stable, calculated  $[N_a, N_p]$ -,  $[N_p, N_a]$ -, and  $[N_a, O_h]$ -bidentate ASCs for a GG molecule. In the intermediate growth stage, formation of a transitional adlayer is proposed and it appears to be mediated by hydrogen bonding. For G, a head-to-tail  $N_a \cdots H - O_h$  hydrogen-bond configuration is supported by the presence of a new N 1s feature at 401.4 eV, i.e. an intermediate binding energy between those of  $N^0$  (400.6 eV) and  $N^{1+}$  (402.1 eV). On the other hand, the existence of hydrogen bonding for GG can be inferred from the relatively high thermal stability of the transitional adlayer (up to 200°C), as observed from the XPS spectral changes upon sequential annealing. The proposed transitional adlayers of G and GG are estimated to be one to two times as thick as their respective interfacial adlayers. In the final growth stage, G and GG grow continuously into multilayers in the zwitterionic form, consistent with it being their most stable solid forms. Thermal evolution studies of these as-grown thick G and GG films on Si(111)7×7 also reveal a reverse growth process, with the zwitterionic multilayer desorbed before the transitional adlayer, and the interfacial adlayer remaining unaffected at least to 200°C and 250°C respectively. The present study illustrates that hydrogen bonding plays a key role in the formation of the transitional adlayer in these important biomolecules. Given the intermediate bond strength of a hydrogen bond (between a

covalent bond and the long-range van der Waals interaction), the proposed hydrogen-bond mediated transitional adlayer offers new bonding flexibilities for building multifunctional biomolecular structures appropriate for biosensor and bioelectronic applications.

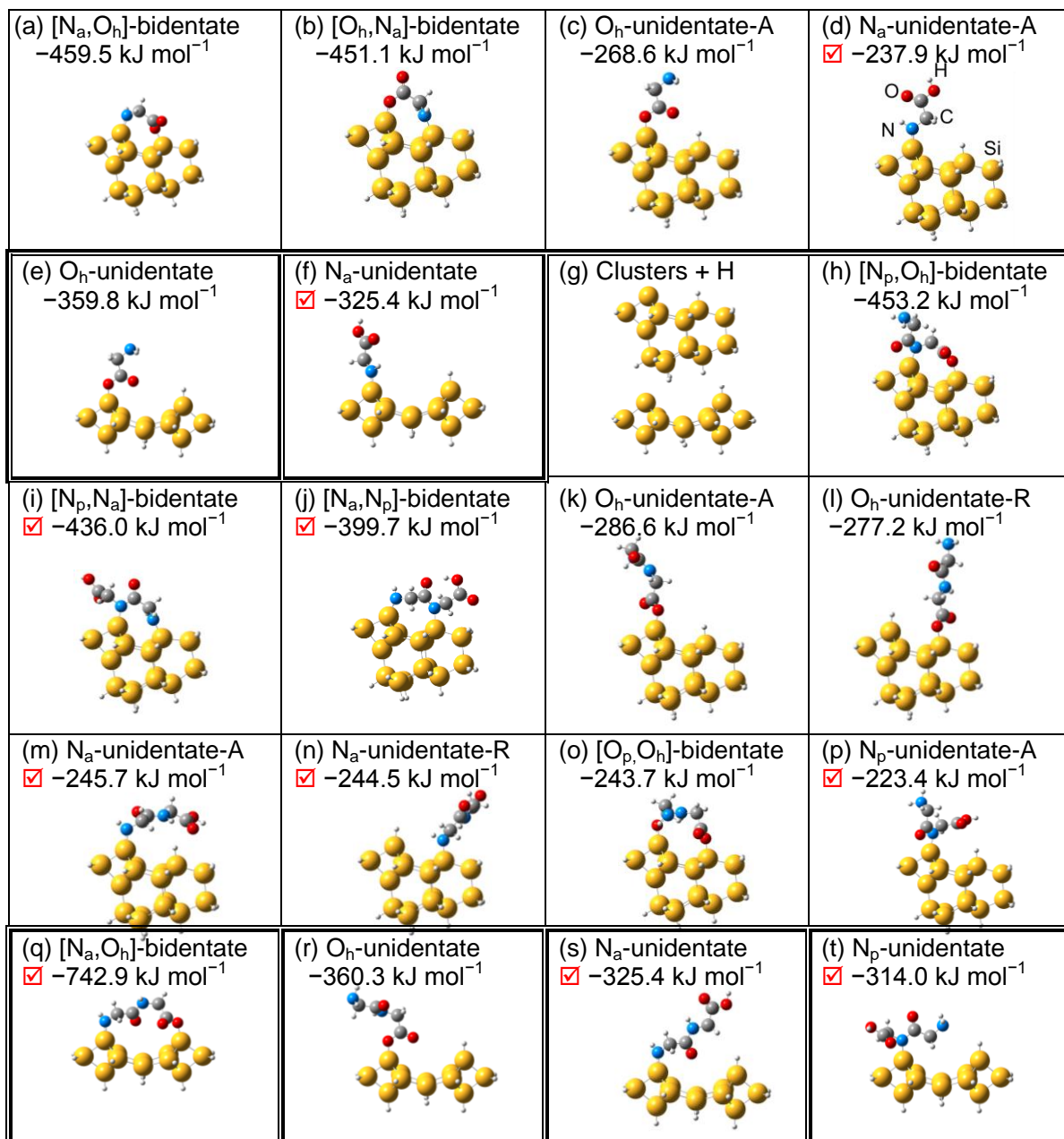


**Figure 5-1** Optimized geometries of adsorbate-substrate configurations (ASC) and their corresponding adsorption energies of glycine on a Si<sub>16</sub>H<sub>18</sub> cluster (a-d) and on a Si<sub>12</sub>H<sub>12</sub> cluster (e, f); and of glycylglycine on a Si<sub>16</sub>H<sub>18</sub> cluster (h-p) and on a Si<sub>12</sub>H<sub>12</sub> cluster (q-t). The optimized geometries of the H adsorbed on Si<sub>16</sub>H<sub>18</sub> and Si<sub>12</sub>H<sub>12</sub> clusters are shown in (g). The plausible ASCs consistent with the experimental results are marked by the tick symbols (☑).

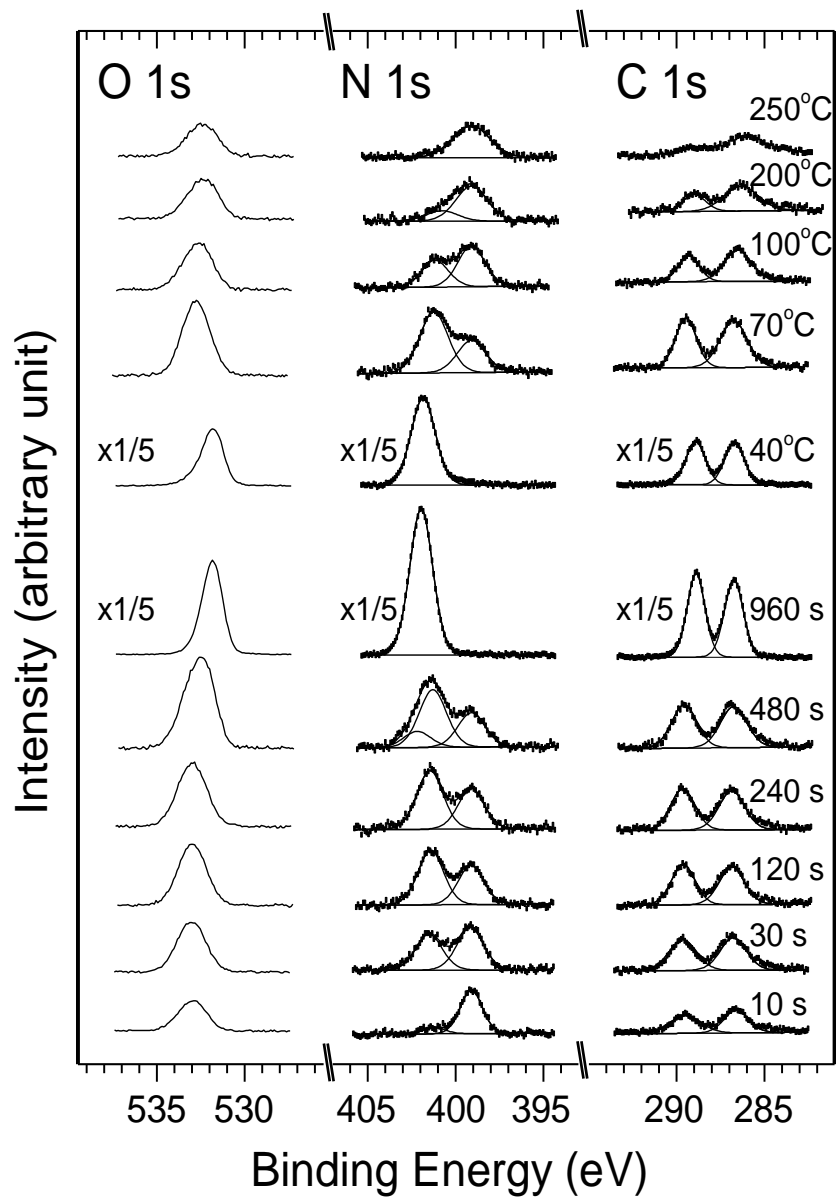


**Figure 5-2** Evolution of C 1s, N 1s and O 1s spectra of a glycine film deposited on Si(111)7×7 as a function of exposure time; and evolution of C 1s, N 1s and O 1s spectra of a thick as-grown glycine film as a function of annealing temperature.

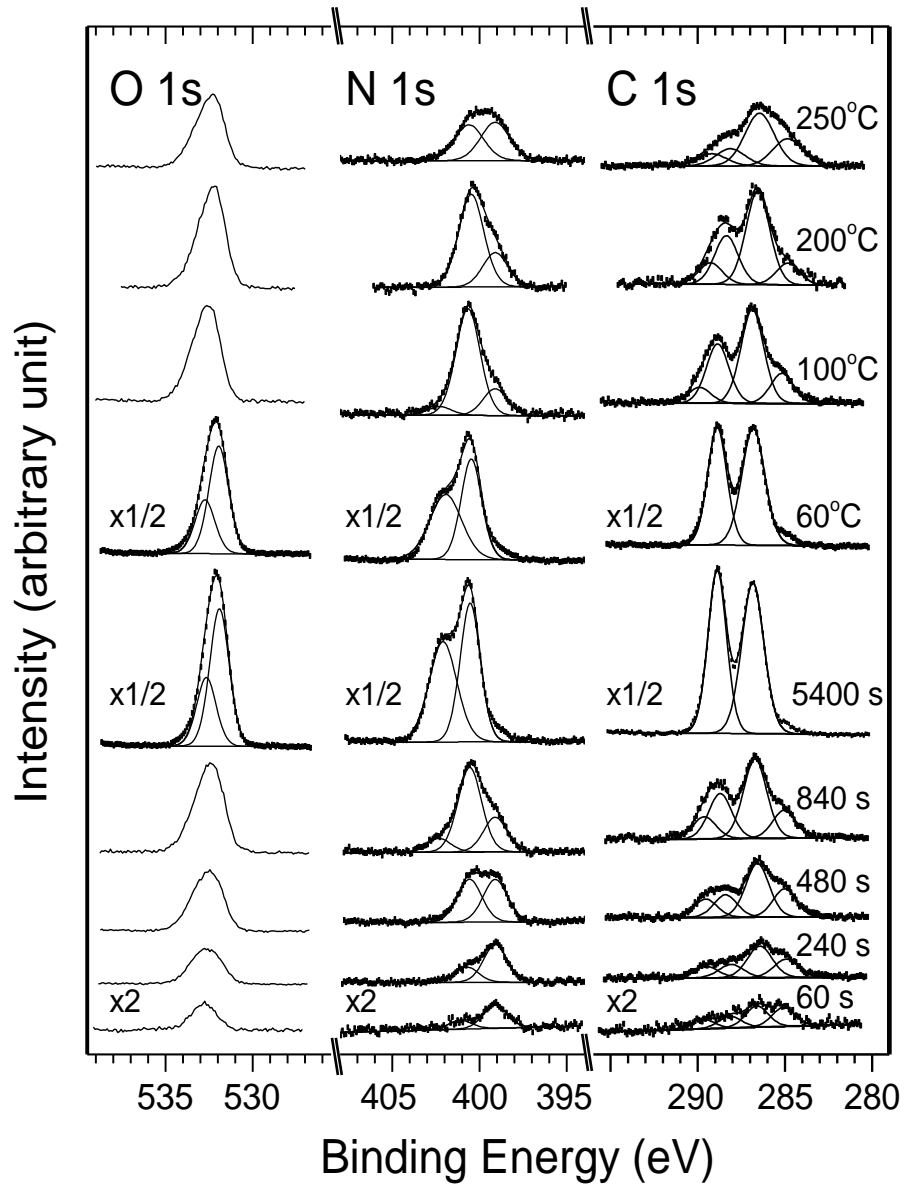


**Figure 5-3** Evolution of C 1s, N 1s and O 1s spectra of a glycylglycine film deposited on Si(111)7×7 as a function of exposure time; and evolution of C 1s, N 1s and O 1s spectra of a thick as-grown glycylglycine film as a function of annealing temperature.

## Chapter 6

# Bidentate Surface Structures of Glycylglycine on Si(111)7×7 by High-Resolution Scanning Tunneling Microscopy: Site-specific Adsorption via N–H and O–H or Double N–H Dissociation

### 6.1 Introduction

Organic functionalization of semiconductor surfaces has provided the impetus of incorporating biological molecules into existing electronic components for novel bioelectronic devices, biosensors, and nanotechnology applications.<sup>169,170,171,172,173</sup> Among the semiconductor materials, silicon continues to attract the most attention because Si single-crystal surfaces provide the singularly most important platform for fabricating microelectronic devices, often in ultrahigh vacuum conditions. Silicon single-crystal surfaces therefore offer the natural starting point for functional integration of biomolecules to improve performance and to add new functions, e.g. in molecular electronics and biosensing.<sup>133,4</sup> This type of biodevice development requires a better understanding of Si surface chemistry, particularly the surface reactions with prototypical biomolecules under ultrahigh vacuum conditions.

Si(111)7×7 and Si(100)2×1 represent two of the most fundamental (and most studied) semiconductor surfaces, and offer unique bonding sites, each with one and two directional dangling bonds (unsaturated valencies), respectively, for interactions with the approaching adsorbates. As also described in the earlier chapters, in the asymmetric buckled dimer model for the Si(100)2×1 surface, one of the dangling bonds from each of two neighbouring atoms forms a strong  $\sigma$  bond with each other, while the remaining dangling bond combines with that of a neighbouring atom to form a weak  $\pi$  bond, creating a Si-Si dimer.<sup>38,102</sup> Charge transfer from the down-atom to the up-atom of the buckled dimer leads to the formation of an electrophilic-nucleophilic pair.<sup>102,104</sup> This structure of nucleophilic top layer (of the up-atoms) followed by an electrophilic second layer (of the down-atoms) is in marked contrast to the case of Si(111)7×7 surface. In the dimer-adatom-stacking-fault model proposed by Takayanagi et al.,<sup>32</sup> has been discussed in the first chapter. The adatom-restatom pair (with the adatom-to-restatom separation of 4.57 Å) provides the most important reaction site for the smaller organic molecules with similar dimensions, including glycine.<sup>97</sup> Furthermore, the adatom is reported to have less electron occupancy than the restatom due to a small charge transfer from the adatom to the restatom, resulting in formal charges of  $\sim +1$  for the center adatom,  $+7/12$  for the corner adatom, and  $-1$  for the restatom.<sup>101</sup> Consequently, the

topmost layer of the Si(111)7×7 surface (with the adatoms) is more electrophilic in nature, in contrast to the nucleophilic next layer of the restatoms. Because a center adatom has two neighbouring restatoms, it has even less electron occupancy and is therefore more electrophilic than the corner adatom. The difference in their electronic environments leads to different surface reactions, resulting in their selectivities towards specific organic molecules with different functional groups.<sup>104,97</sup>

Biomolecules are generally complex in nature and some can be considered polymers of identical units (building blocks) or of combinations of different units. For example, a peptide is a polymer of amino acids, while a DNA molecule is a polymer of four nucleobases (adenine, guanine, cytosine and thymine) with sugar phosphate backbones. Glycylglycine (GG) is the simplest peptide consisting of two glycine residues connected by a single peptide bond. We have reported studies of the interactions of glycine with the Si(111)7×7 surface by X-ray photoelectron Spectroscopy (XPS)<sup>99</sup> and scanning tunneling microscopy (STM),<sup>154</sup> along with appropriate ab-initio calculations based on density functional theory (DFT) in the third and fourth chapters of this thesis respectively. We now extend this work to the interactions of GG with the 7×7 surface by STM, using our recent XPS/DFT results<sup>120</sup>, as also discussed in the fifth chapter of this thesis, to provide the local bonding information as the basis to infer the intriguing site-specific chemistry. In our recent XPS/DFT study, we show that the early growth stage of GG involves either N–H and O–H dissociation or double N–H dissociation. These surface dissociative adsorptions lead to bidentate adstructures with the formation of a N–Si and a O–Si bond or of double N–Si bonds, respectively.<sup>120</sup> Increasing the GG exposure on Si(111)7×7 surface leads to the introduction of a hydrogen bonded transitional adlayer which grows and ultimately promotes the formation of a GG zwitterionic (thick) film.<sup>120</sup> In the present study, we investigate the early growth stage of GG on the 7×7 surface by using high resolution STM, and determine the plausible bidentate adsorption configurations on different sites. In marked contrast to glycine adsorption where hydrogen bonding plays a pivotal role,<sup>99</sup> the strong bidentate adstructure-substrate interactions of GG with the 7×7 surface reduces the surface diffusion and the importance of hydrogen bonding among the adsorbates, and the adsorption essentially follows random sequential statistics.

## 6.2 Experimental & Computational Details

The STM images were recorded at room temperature in a constant current mode with the feedback loop on during measurement. During GG evaporation, the temperature of the effusion cell was kept at 170°C, with the chamber pressure rising to  $3\text{--}4 \times 10^{-9}$  mbar. The molecular nature of GG vapour was verified by the presence of the parent-ion and base-ion peaks at 132 and 30 amu, respectively, in its mass spectra

recorded with a quadrupole mass spectrometer before sample dosing.<sup>153</sup> Deposition time is used to indicate the relative exposure of GG, while the absolute coverage of GG can be obtained directly from the corresponding STM images.

### 6.3 Results and Discussion

Figure 6-1 shows the high-resolution filled-state and empty-state STM images of a 15 s GG exposure on Si(111)7×7 recorded with sample bias voltages of -2 V and +2 V, respectively, and a constant tunneling current of 200 pA. Schematic diagrams depicting an unreacted unit cell (A) and a reacted unit cell (B) for the respective images are shown in Figure 6-1c and 6-1d. Evidently, for the unreacted unit cell A, the filled-state image clearly shows the presence of the restatoms and discerns the faulted and unfaulted halves with the former being notably brighter than the latter (Figure 6-1a, 6-1c). The relative brightnesses of the faulted and unfaulted halves are also illustrated by the generally higher height profile of the adatoms along linescan L2 of the faulted half than that along L1 of the unfaulted half (Figure 6-1e). The height of the center adatom (CA) is found to be lower than that of the corner (*angulus* in Latin) adatoms (AA), which indicates that the local density of states (LDOS) of CA is lower than that of AA. This is consistent with the charge transfer from a CA to both of its neighbouring restatoms (RAs) being greater than the charge transfer from an AA to its only RA neighbour. On the other hand, the empty-state image for the unreacted unit cell (A) shows all adatoms with essentially the same brightness on both the faulted and unfaulted halves, which is also illustrated by the nearly overlapping height profiles along linescans L12 and L11, respectively. As the restatoms are not visible in the empty-state images, empty-state imaging is therefore less useful for probing dissociative adsorption that involves the restatoms, as shown for glycine<sup>154</sup> and the present case.

For the reacted unit cell B, the filled-state STM image (Figure 6-1a) shows a bright protrusion covering two adatoms (AA1a, AA3a) across the dimer wall, suggesting a bidentate adsorption arrangement involving both corner adatoms (AA-AA). The absence of intensities at the expected locations of the restatoms (RA1d, RA3d) suggests the presence of H atoms dissociated from a GG molecule, following the similar observation for glycine adsorption on the 7×7 surface.<sup>154</sup> Furthermore, H adsorption at the restatoms also cause brightness enhancement of the adjacent adatoms (CA1b, CA1c for RA1d, and CA3b, CA3c for RA3d). This brightness enhancement is quite apparent from the higher height profile along linescan L3 (L4) at the CA3c (CA1b) position relative to that along L1 (L2) at the corresponding CA position of the unreacted unit cell (Figure 6-1e). Our recent XPS and DFT study of GG adsorption on Si(111)7×7 has concluded that the GG molecule undergoes N-H and O-H or double N-H dissociations

to produce a bidentate adstructure. The two dissociated H atoms can land on the adjacent restatoms, causing dark depressions at the corresponding RA positions in the STM image, and terminate the Si dangling bonds with the formation of the Si–H bonds, which leads to the brighter appearance of the neighbouring unreacted adatoms as a result of the charge transfer from the reacted restatom. Given that the separation of N–H to C(O)N–H in GG (3.74 Å) is too small to bridge two adatoms across the dimer wall (6.65 Å), only N–H and O–H dissociation at the two termini could occur for this particular case. The corresponding empty-state image (Figure 6-1b) also shows a bright protrusion over AA11a and AA13a, which is also depicted by the more intense peaks at the respective AA locations along linescans L14 and L13 of the reacted unit cell when compared to those along L12 and L11 of the unreacted unit cell (Figure 6-1f).

In addition to the filled-state STM image shown in Figure 6-1, we also observe three other common patterns that correspond to other types of bidentate configurations of GG on the 7×7 surface for all the GG exposures employed in the present study. Figure 6-2 compares these four filled-state STM images recorded at –2 V bias voltage, along with their respective height profiles and possible ASCs (in both top and side views) obtained by DFT/6-31++G(d,p) calculations. In particular, Figure 6-2a1 shows another example of a bright protrusion over two corner adatoms across the dimer wall, with a separation of 6.65 Å, which corresponds to an AA-AA bidentate ASC (Figure 6-2c1) as in Figure 1. Similarly, Figure 6-2a2 shows a bright protrusion over two center adatoms across the dimer wall. The corresponding CA-CA bidentate ASC (Figure 6-2c2) could be approximated by the same bidentate ASC shown in Figure 6-2c1. The corresponding height profiles along linescans L1 and L2 show that both bidentate ASCs exhibit similar heights (100-110 pm) for the respective reacted adatoms. Furthermore, Figure 6-2a3 depicts a bright protrusion over a center adatom and a corner adatom on the same side of the dimer wall with a separation of 7.68 Å, which corresponds to a CA-AA bidentate ASC shown in Figure 6-2c3. Evidently, the NH<sub>2</sub> to COOH separation in a straight-chain GG conformer (6.08 Å) is compatible with the adatom-adatom separations for AA-AA, CA-CA and CA-AA bidentate configurations. Figure 6-2a4 shows two bright protrusions, each of which is located over an adatom-restatom pair corresponding to a CA-RA ASC with double N–H dissociations from the amine and peptide groups. The discernibly narrower widths of the height profiles along linescans L4 and L5 are consistent with the shorter CA-RA or AA-RA separation of 4.56 Å than the AA-AA or CA-CA and CA-AA separations. This CA-RA or AA-RA separation closely matches the shorter NH<sub>2</sub> to CONH distance in the GG molecule (3.74 Å). However, it is not possible to differentiate between the two different bidentate configurations: (XA–)NHCH<sub>2</sub>CON(–RA)CH<sub>2</sub>COOH and (RA–)NHCH<sub>2</sub>CON(–XA)CH<sub>2</sub>COOH (where XA = CA or AA) from our STM image

(Figure 6-2a4). Our present STM results are in good accord with our calculations reported in our recent work.<sup>120</sup> In particular, the bidentate ASCs involving N–H and O–H dissociations (with adsorption energies of  $-703.22 \text{ kJ mol}^{-1}$  for AA-AA or CA-CA and  $-700.20 \text{ kJ mol}^{-1}$  for CA-AA) and double N–H dissociations (with an adsorption energy of  $-436.0 \text{ kJ mol}^{-1}$  for CA-RA or AA-RA) are favoured thermodynamically. We could also rule out the less thermodynamically stable unidentate ASCs, because of the absence of any bright protrusion correlated with only one adjacent dark depression corresponding to a single dissociated H atom in any of the STM images examined in the present study.

Figure 6-3 shows the filled-state STM images collected over a  $50 \times 50 \text{ nm}^2$  area for five different exposures of GG (from 15 s to 40 s) on Si(111) $7 \times 7$ . For better illustration, we show selected  $20 \times 20 \text{ nm}^2$  areas for 4 of the 5 exposures. These images reveal that random distributions of the five bidentate configurations described in Figure 6-2, with no notable spatial correlation among the bidentate configurations. Figure 6-3f shows the corresponding relative surface concentrations of these five bidentate configurations as a function of GG exposure. The surface concentration for a particular bidentate configuration is obtained by counting its number of occurrences, and then dividing the resulting number by the total number of available adatom sites in the full  $50 \times 50 \text{ nm}^2$  STM image. A  $50 \times 50 \text{ nm}^2$  surface area contains approximately  $400 \ 7 \times 7$  unit cells with a total of 4800 Si adatoms and 2400 restatoms. Evidently, the surface concentrations of all five bidentate configurations appear to have rather similar increasing trend with increasing exposure. At the initial adsorption stage (15 s), the relative surface concentration of CA-RA bidentate configuration is found to be the highest among all the other bidentate configurations, representing almost 37 % of the total GG adsorption on the surface. This is followed by AA-AA (25%), CA-CA (17%), AA-RA (17%) and CA-AA bidentate configurations (4%). The relative surface concentrations of these bidentate configurations follow the essentially same ordering: CA-RA > AA-AA > CA-CA > AA-RA > CA-AA, with increasing exposure. Interestingly, the surface concentrations of AA-AA and CA-CA bidentate configurations appear to increase with a greater slope with respect to the exposure than the other bidentate configurations (CA-RA, AA-RA, CA-AA).

Upon N–H dissociative adsorption of GG on a CA site, the adstructure would undergo either an N–H dissociation to form a CA-RA bidentate configuration or an O–H dissociation to form a CA-CA bidentate configuration. The higher relative surface concentration observed for the CA-RA configuration than that of the CA-CA configuration therefore suggests that kinetic effects may play an important role in the adsorption of GG on Si(111) $7 \times 7$ . On the other hand, an N–H dissociative adsorption of GG on an AA site would also be followed by either an N–H dissociation to form an AA-RA bidentate or an O–H

dissociation to form an AA-AA bidentate configuration. However, unlike the CA site with 2 adjacent RA sites, an AA site is adjacent to just 1 RA site. The formation of an AA-AA bidentate configuration, requiring 1 RA site each across the dimer wall, is therefore more likely than an AA-RA bidentate configuration, requiring 1 RA site adjacent to the initial AA site plus 2 additional RA sites nearby. This accounts for the observation that AA-AA has a higher relative surface concentration than AA-RA. By the same token, CA-RA, with 2 adjacent RA sites, would have a higher relative surface concentration than AA-RA, with just 1 RA site. As the exposure increases resulting in more RA sites being occupied by the configurations, the growth of CA-RA (AA-RA) configuration, requiring 3 RA sites, becomes slower than that of CA-CA (AA-AA), requiring just 2 RA sites. Furthermore, the number of RA sites per unit cell is half of the total number of adatoms (CA+AA), the reduced availability of RA sites would have a larger effect on the growth of the CA-RA (AA-RA) than that of CA-CA (AA-AA). These effects contribute to the observed slower increase with increasing exposure for CA-RA than that for CA-CA. Finally, the CA-AA configuration has the lowest relative surface concentration over all the exposures, suggesting that the larger CA-to-AA separation (7.68 Å) is least favourable for bidentate adsorption, possibly due to steric effects.

We also show in Figure 6-3f the total CA and AA relative occupancies as well as the total coverage. The total CA (AA) site occupancy is given by the sum of the relative surface concentration of CA-RA (AA-RA) and that of CA-AA plus twice the relative surface concentration of CA-CA (AA-AA), while the total coverage (or total adatom occupancy) corresponds to the sum of CA and AA relative occupancies. Evidently, the higher total CA occupancy is nearly the same as the total AA occupancy over the entire exposure range. This indicates that there is minimal surface diffusion upon GG impact onto the surface and the adsorption appears to be purely statistical, despite the higher reactivity of CA than AA expected for other small organic molecules. The process of forming a bidentate configuration is therefore rapid, and the two resulting bonds are apparently strong enough to prevent surface diffusion of the adsorbate. In addition, the total coverage of GG is found to increase near-linearly from 3.4% for 15 s exposure to 7.5% for 40 s exposure. It is of interest to note that the total coverage of GG on Si(111)7×7 is considerably lower than that of glycine for similar exposure,<sup>154</sup> which suggests a lower sticking coefficient for GG than glycine on the 7×7 surface. Adsorption involving bidentate configurations on two Si sites for GG is statistically less favourable than the unidentate adsorption on a single Si site as in the glycine case, which could account for the difference in the amount of adsorption. Finally, the free –CONH– and –COOH groups remaining on the respective bidentate adstructures offer viable sites to facilitate adsorption of a second adlayer through the formation of hydrogen bonding. Such type of H-bond mediated growth

process particularly has been observed in our recent XPS work. However, in contrast to the unidentate adsorption structures of glycine, the geometries imposed by the bidentate adsorption structures are expected to be less flexible for such type of H-bonding formation.

## 6.4 Summary

The early adsorption process of glycylglycine on Si(111)7×7 at room temperature is studied by direct STM imaging and DFT calculations. The present study not only confirms our recent XPS results which suggest that adsorption of GG involves either N–H and O–H dissociation or double N–H dissociation, but also directly identifies five general types of site-specific bidentate bonding arrangements on the 7×7 surface. Using filled-state STM imaging, we are able to demonstrate that N–H and O–H dissociation occur on an adatom-adatom pair across or on the same side of a dimer wall while double N–H dissociation occur at an adatom-restatom pair. More importantly, our STM results show that both types of double dissociation on specific Si sites are equally probable. We further determine that the relative surface concentrations of these five bidentate configurations follow the ordering: CA-RA > AA-AA > CA-CA > AA-RA > CA-AA over the exposure range (up to 40 s) used in the present study. Our DFT calculations employing large Si<sub>26</sub>H<sub>24</sub> and Si<sub>16</sub>H<sub>18</sub> clusters as model surfaces further support that all five bidentate configurations are thermodynamically viable. In addition, the total relative occupancies of the CA and AA sites are found to be essentially the same. These observations point to the pure statistical nature of the adsorption process, suggesting that the bidentate interactions are sufficiently strong to prevent surface diffusion and the adsorption essentially occurs at the random points of molecular impact.

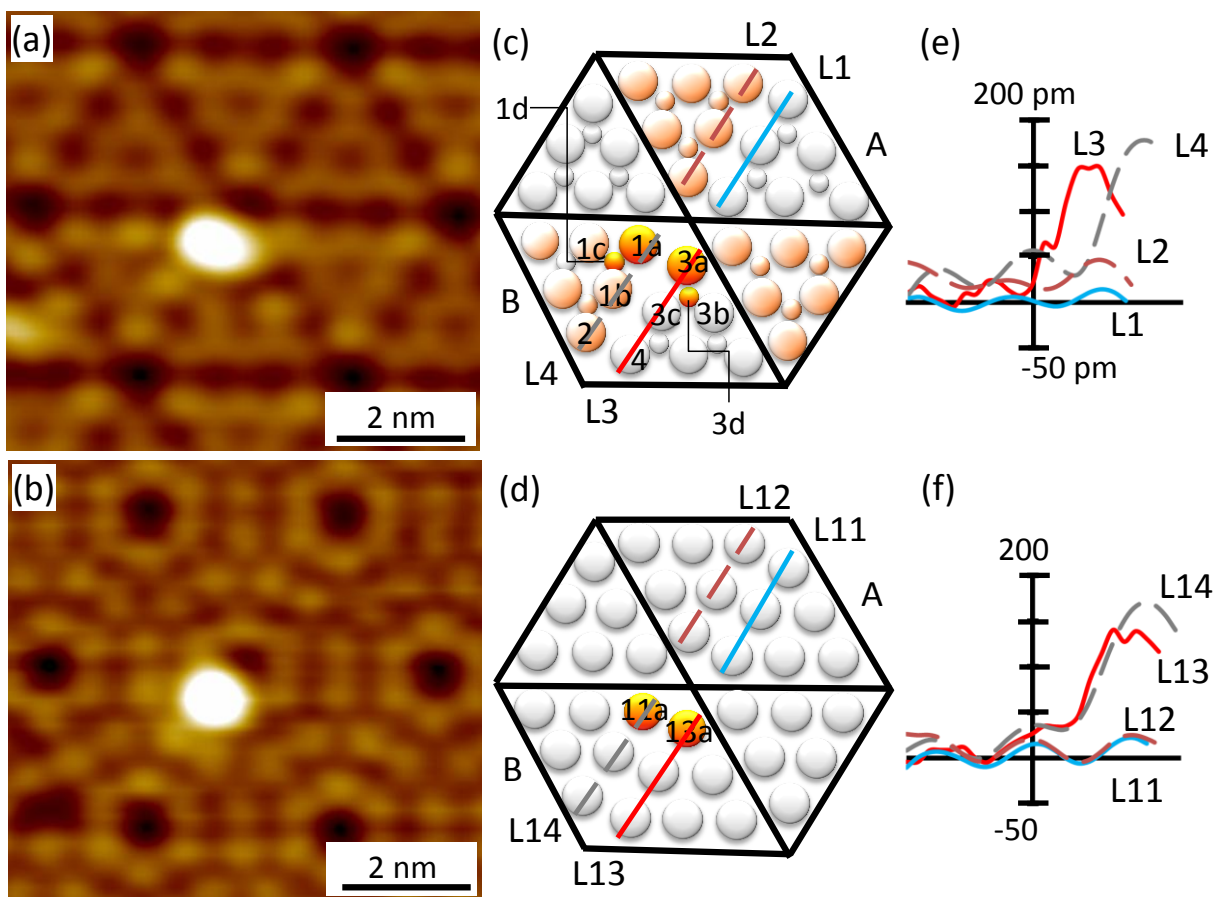


**Figure 6-1** (a) STM filled-state image and (b) empty-state image of glycylglycine adsorbed on a Si(111)7×7 surface obtained with a sample bias  $-2$  V and  $+2$  V, respectively, all at a constant tunnelling current of 150 pA. (c, d) Corresponding schematic diagrams depicting (A) an unreacted and (B) a reacted 7×7 unit cells, and (e, f) height profiles along the linescans  $L_x$  ( $x=1-4, 11-14$ ) in the unfaulted half (marked by solid lines) and faulted half (marked by dashed lines). The atoms in the unfaulted and faulted half unit cells are represented by lighter and darker spheres, respectively, in (c). The sites of interest are labeled by alphanumeric characters.

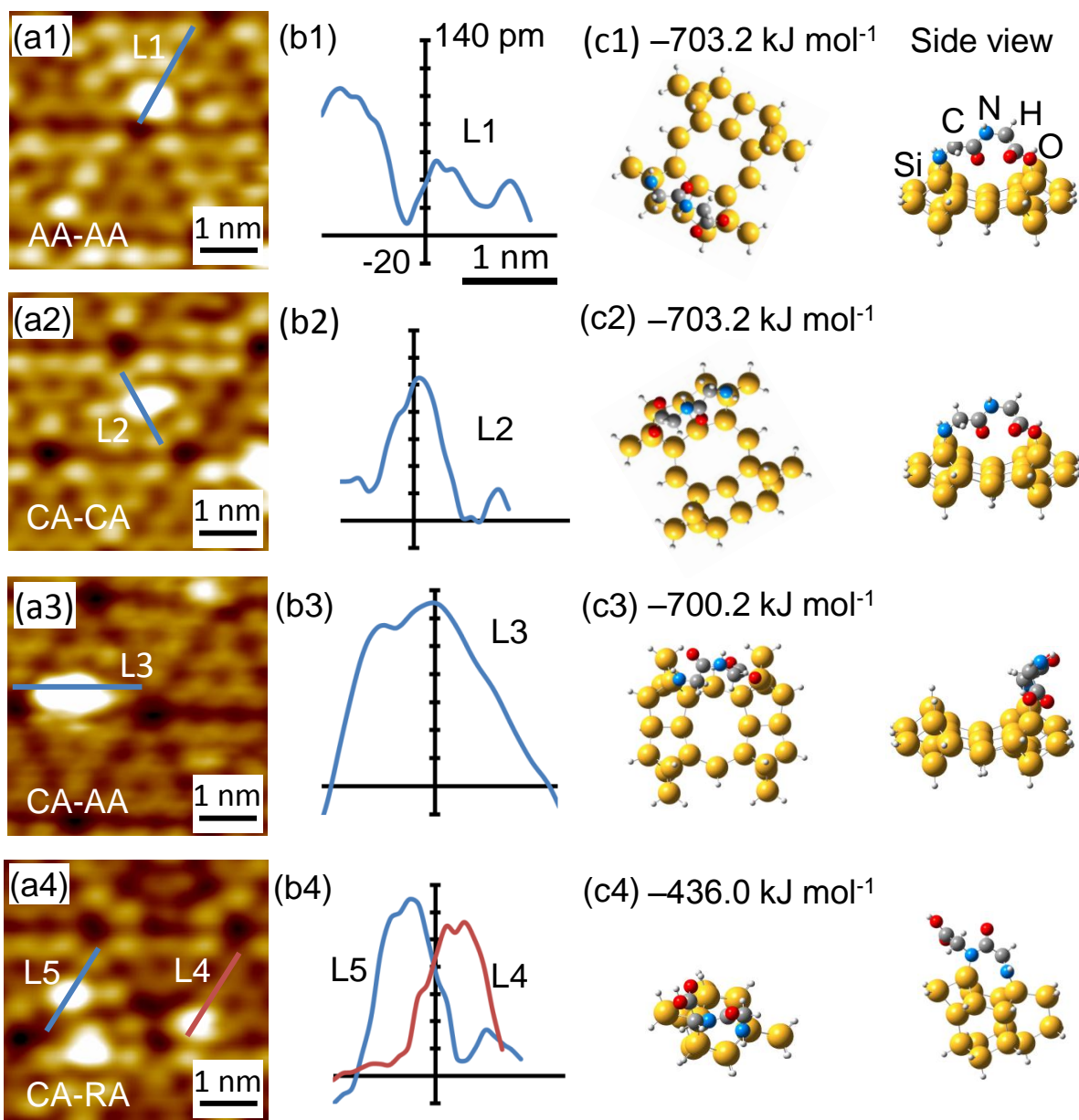


**Figure 6-2** (a) STM filled-state images taken at a sample bias of  $-2 \text{ V}$  and a tunneling current of  $150 \text{ pA}$ , (b) the height profiles along the respective linescans, L1-L5, for bidentate adsorption of glycylglycine on the AA-AA, CA-CA and CA-AA and CA-RA sites, and the corresponding plausible equilibrium adstructures (with top and side views) and adsorption energies of glycylglycine on (c1-3)  $\text{Si}_{26}\text{H}_{24}$  and (c4)  $\text{Si}_{16}\text{H}_{18}$ , all obtained with DFT/B3LYP/6-31G++(d,p).

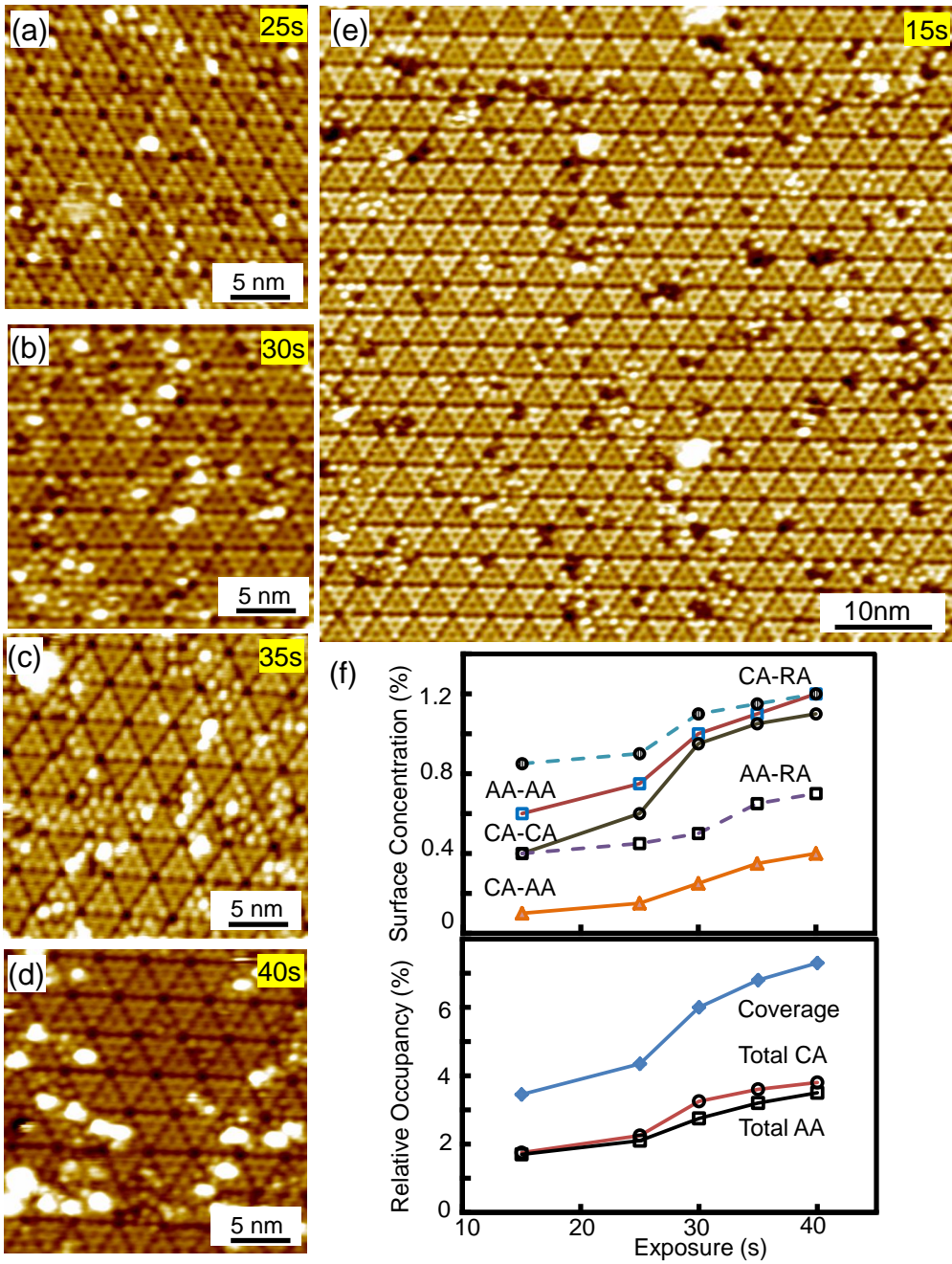


**Figure 6-3** STM filled-state images taken at a sample bias of  $-2$  V and a tunneling current of 150 pA after glycylglycine exposure of (a) 25 s, (b) 30 s, (c) 25 s, (d) 40 s and (e) 15 s; and (f) the relative surface concentrations for bidentate adsorption at CA-RA, AA-AA, CA-CA, AA-RA and CA-AA sites and the total coverage and relative occupancies for total reacted CA and AA sites.

## Chapter 7

# Self-directed growth of aligned adenine dimer nanowires on Si(111)7×7: Direct imaging of formation of hydrogen-bond mediated dimers and clusters at room temperature by Scanning Tunneling Microscopy

### 7.1 Introduction

Organic functionalization could significantly extend the present silicon-based device technology especially when the device size is now approaching the molecular scale. Single-molecule detection and multi-species chemical sensing, molecular photonics and electronics, and DNA-based biomolecular computing are just some of the emerging applications of bio/organic functionalization. To date, most of bio/organic functionalization of Si substrates have involved bifunctional and multifunctional organic molecules, with nitrogen-containing functional groups (amines, amides) and oxygen-containing functional groups (carboxylic acids, alcohols) connected to an aliphatic backbone or to an aromatic ring structure (including benzene and their derivatives).<sup>2</sup> In the case of aromatic molecules, the aromatic ring could interact with the surface through cycloaddition reactions as in benzene and toluene,<sup>41</sup> and through reactions with the heteroatom as in pyrrole, thiophene, and pyridine<sup>42</sup> on Si(100)2×1 and Si(111)7×7. The aromatic backbone can therefore serve as an anchor to the surface, making the derivatives of these aromatic molecules with one or more appropriate functional groups excellent linker molecules (e.g., chlorobenzenes<sup>43</sup> and dihalogenated benzenes).<sup>44</sup> While the interactions of multifunctional aliphatic molecules with the surface often involve covalent bonding, multifunctional heterocyclic aromatic molecules could also bind to the surface by dative bonding involving the heteroatom(s). The relatively moderate interaction as mediated by a dative bond not only preserves the molecular identity of the adsorbates but also facilitates their self-organization and initiation of film growth. This type of dative bonding therefore provides a different mechanism of anchoring the adsorbate to the surface, allowing all the functional groups on the ring backbone to interact with the surface, with each other (including, e.g., molecular folding), with other adsorbates (including self-organization) and with incoming species (acting as a linker molecule or undergoing biomolecular reactions).

Unlike metal surfaces, semiconductor surfaces offer directional bonds that are sufficiently strong to “trap” adsorbates at room temperature, eliminating the need to reduce the surface mobility of the

adsorbates at low temperature. As also discussed in the first chapter, the  $7\times 7$  reconstructed surface of Si(111) offers different types of dangling bond sites in the dimer-adatom-stacking fault model, with each unit cell consisting of 12 adatoms in the first layer, 6 restatoms in the second layer, and 1 corner-hole atom in the third layer.<sup>101,97</sup> The differences in the formal charges of a center adatom or CA ( $\sim +1$ ), a corner (Latin: *angulus*) adatom or AA ( $+7/12$ ) and a restatom or RA ( $-1$ ) contribute to their site-specific reactivities. On the other hand, the  $2\times 1$  reconstructed surface of Si(100) provides a lesser variety of dangling bond sites in the asymmetric dimer model, with each unit cell consisting of 1 up and 1 down atoms each with two dangling bonds.<sup>36</sup> In the present study, we focus on site-specific chemistry of the Si(111) $7\times 7$  surface that is generally considered less reactive than Si(100) $2\times 1$  but has a wider variety of bonding sites to accommodate different adsorbate structures.

To date, there has been a lot of recent STM studies on organic adsorbates on Si(111) $7\times 7$ , including formic acid,<sup>91</sup> methanol,<sup>139</sup> trimethylphosphine,<sup>174</sup> pyrrole,<sup>18</sup> thiophene,<sup>175</sup> tetracene,<sup>176</sup> naphthalene,<sup>177</sup> and glycine.<sup>154</sup> Unlike the other three nucleobases, Adenine (Ade) has only one functional group, i.e. the basic amino ( $-\text{NH}_2$ ) group, making it the only available linking point with other species if the ring N atoms are involved in anchoring to the surface. Among the four nucleobases, Ade also has the most number of ring N atoms capable of dative bonding (3). Of the three types of N atoms in Ade, there are three pyridinic N1, N3, N7 (H-bond acceptors), one pyrrolic N9 and one amino N10 (H-bond donors), all of which could form H bond(s) with complementary H-bond donors or acceptors in other Ade or nucleobases such as thymine. The higher electron densities at the pyridinic N atoms make these N atoms more likely to form dative bonding with the surface.

Despite their importance, the surface chemistry and early adsorption of Ade and indeed other nucleobase molecules on Si(111) $7\times 7$  has remained unknown. Only four studies on the adsorption of Ade and other nucleobases on Si(100) $2\times 1$  and Cu(111) and Cu(110) surfaces have been reported. In particular, adsorption of Ade on Si(100) $2\times 1$ <sup>178</sup> and of Ade and thymine together<sup>179</sup> have been studied by Kasaya et al. using STM and semiempirical molecular orbital calculations over 15 years ago. From their limited STM images at 0.02 ML (that do not reveal the Si dimer rows before exposure), they concluded the existence of dimers on the surface with strong interaction with the surface. Even with their companion semiempirical calculations, these rather low-quality STM images did not allow the authors to provide a clearer picture about the adsorption. Later, Furukawa et al. studied the adsorption of all four nucleobases on the Cu(111) surface at  $\sim 80$  K by STM and reported that except for the randomly oriented thymine, the other nucleobases form unique 2D structures on the surface.<sup>180</sup> Based on their molecular orbital

calculations involving H bonding of two identical nucleobase molecules, they suggested that H-bonding could direct the growth of the 2D structures. Adsorption of Ade on Cu(110) has also been studied by Chen et al. at selected coverages above 0.08 monolayer by low energy electron diffraction, STM, and electron energy loss spectroscopy, along with ab-initio calculations.<sup>125</sup> These authors concluded that Ade forms an ordered  $\begin{pmatrix} 1 & 2 \\ 6 & 0 \end{pmatrix}$  H-bonded structures after annealing an adenine-saturated surface at 430 K.

Recently, we have studied the adsorption and growth evolution of fundamental benchmark molecules of biological interest, including glycine (the simplest amino acid)<sup>99,154</sup> and glycyglycine (the simplest peptide)<sup>120</sup> by STM and X-ray photoelectron spectroscopy (XPS). Both glycine and glycyglycine are found to exhibit strong interactions with the dangling-bond sites of the  $7\times 7$  surface, preventing them from self-organization upon adsorption. In the present study, we investigate the adsorption of Ade on Si(111) $7\times 7$  for the first time by using STM and ab-initio calculations based on the Density Functional Theory (DFT). Our STM results show that Ade undergoes self-organization of dimers, quartets and higher-order superstructures along the Si dimer walls on the  $7\times 7$  surface. We also show that H-bonding plays a key role in the formation of these self-organized adsorbate structures. The site-specific information about the adsorption is in good accord with the local chemical-state information provided by our recent XPS study.<sup>122</sup>

## 7.2 Experimental and Computational Details

Ade (Adrich, 99 % purity, m.p. 360-365°C) was deposited onto the Si substrate by thermal evaporation from an effusion cell temperature of 110°C. The cracking patterns of Ade vapour were determined before and after deposition onto the Si substrate by a quadrupole mass spectrometer and they are found to be in good accord with that of Ade,<sup>153</sup> indicating that the Ade molecules remained intact in the gas phase upon evaporating at 110°C. All the STM images were collected with an electrochemically etched, atomically sharp W tip at room temperature in a constant current mode at 150 pA tunneling current and a bias voltage of +2 V (empty-state imaging) and of -2 V (filled-state imaging).

Planar molecules such as benzene and arenes, including the nucleobases, were found to have nonplanar ground-state geometries as predicted by the typical ab-initio methods (e.g., DFT, MP2, MP4) when combined with the standard Pople's basis sets. These inconsistencies could be explained in terms of intramolecular basis-set-superposition-errors as reported in the literature. For Ade, a similar approach has been adopted to deal with the problems of spurious imaginary frequencies found for the optimized

ground-state geometries with these methods (DFT, MP2) by counterpoise corrections. The counterpoise corrections could be calculated by considering the different components inside the Ade molecule, including the diatomic N–H and C=C components and the larger N=C–NH<sub>2</sub> and N=CH components with the unsaturated N atoms. We considered the latter larger components to be in high spin states as reported in the literature.<sup>181</sup>

### 7.3 Results and Discussion

Figure 7-1a shows a typical filled-state STM image for a 10 s exposure of Ade on Si(111)7×7. Each bright protrusion of the 30×30 nm<sup>2</sup> image represents an individual Ade molecule adsorbed on the surface. Evidently, approximately half of the bright protrusions appear individually on adatom sites (with a preference for center adatoms) while the other half appear in groups. A magnified filled-state image of an Ade molecule (single) adsorbed at a center adatom site on the faulted half of the 7×7 unit cell (Figure 7-1b) is found to be quite similar to the corresponding empty-state image (Figure 7-1c). In particular, the adsorbed Ade appears as bright protrusions in both images. The corresponding height profiles along linescans L1 and L2 (Figure 7-1d) show that the height above a neighbouring Si adatom for filled-state (220 pm) is larger than that for empty-state (150 pm), which could be due to a higher local density of states (LDOS) associated with the filled states of the adsorbed Ade. Evidently, both the filled-state and empty-state images show that the adsorption of Ade does not produce any correlated bright-dark features as found in the STM images for glycine adsorption,<sup>154</sup> which indicates the differences in the nature of their adsorption. In particular, glycine undergoes N–H dissociative adsorption through the formation of N–Si bond that leads to a bright protrusion in the STM image, while the formation of Si–H bond resulting from the dissociated H atom generates a corresponding dark depression in the nearest-neighbouring restatom site. The lack of correlated bright-dark features in the STM images for Ade adsorption therefore suggests that H dissociation does not occur in the adsorption process. This is in good accord with our recent XPS study that shows the formation of N→Si dative bonds for Ade adsorption on the 7×7 surface, as supported by the presence of the corresponding N 1s feature at 401.1 eV.<sup>122</sup>

Figure 7-1e shows four possible calculated adsorbate-substrate configurations (ASCs) of Ade adsorbed on the Si<sub>26</sub>H<sub>24</sub> model surface through the formation of dative bonding between different N atoms and a Si adatom, all optimized at the DFT/B3LYP/6-31++G(d,p) level. We identify the different adstructures as N<sub>n</sub> by the n-position of the N atom in Ade that forms the dative bond, along with their adsorption energies in Figure 7-1e. We could rule out dative bonding from the pyrrolic N (N9) because its lone-pair electrons are involved in the ring aromaticity. The ASC N3 with adsorption energy (–251.2 kJ mol<sup>–1</sup>) is

found to be comparable in stability to ASC N1 ( $-234.7 \text{ kJ mol}^{-1}$ ) and N7 ( $-227.7 \text{ kJ mol}^{-1}$ ). The ASC N10 ( $-184.9 \text{ kJ mol}^{-1}$ ) is less stable than the other three due to delocalization of electrons from the  $-\text{NH}_2$  group to the ring, which reduces the basicity of the amino group. On the other hand, the higher electron densities associated with the 1, 3 and 7 positions of the Ade ring give rise to the formation of more stable datively bonded products. In order to maximize the bonding between the N ring atoms and the Si adatom, ASC N3, N1 and N7 are found to have less tilted geometries (with the ring axis near perpendicular to the surface plane), in contrast to ASC N10 (involving the  $-\text{H}_2\text{N}\rightarrow\text{Si}$  dative bonding) with the ring axis nearly parallel to the surface plane. Figure 1a also shows that the single protrusions could appear with different sizes and degrees of brightness, which could be attributed to different extent of the molecular tilt with respect to the surface normal. This is consistent with the adsorption dynamics study of acetylene on Pd(111) reported by Dunphy et al.,<sup>182</sup> who observed that the relative size of the protrusion increases with the molecular tilt due to better overlap of the  $\pi$  orbital of acetylene with the STM tip. When the molecular axis of acetylene is perpendicular to the surface (zero tilt), the negative and positive lobes of its  $\pi$  orbitals cancel out the overlap with the (s) orbitals of the tip, resulting in dark depression in the STM image. The molecular tilt in molecules with  $\pi$  orbitals (such as Ade) could therefore give rise to single protrusions with different brightness and sizes.

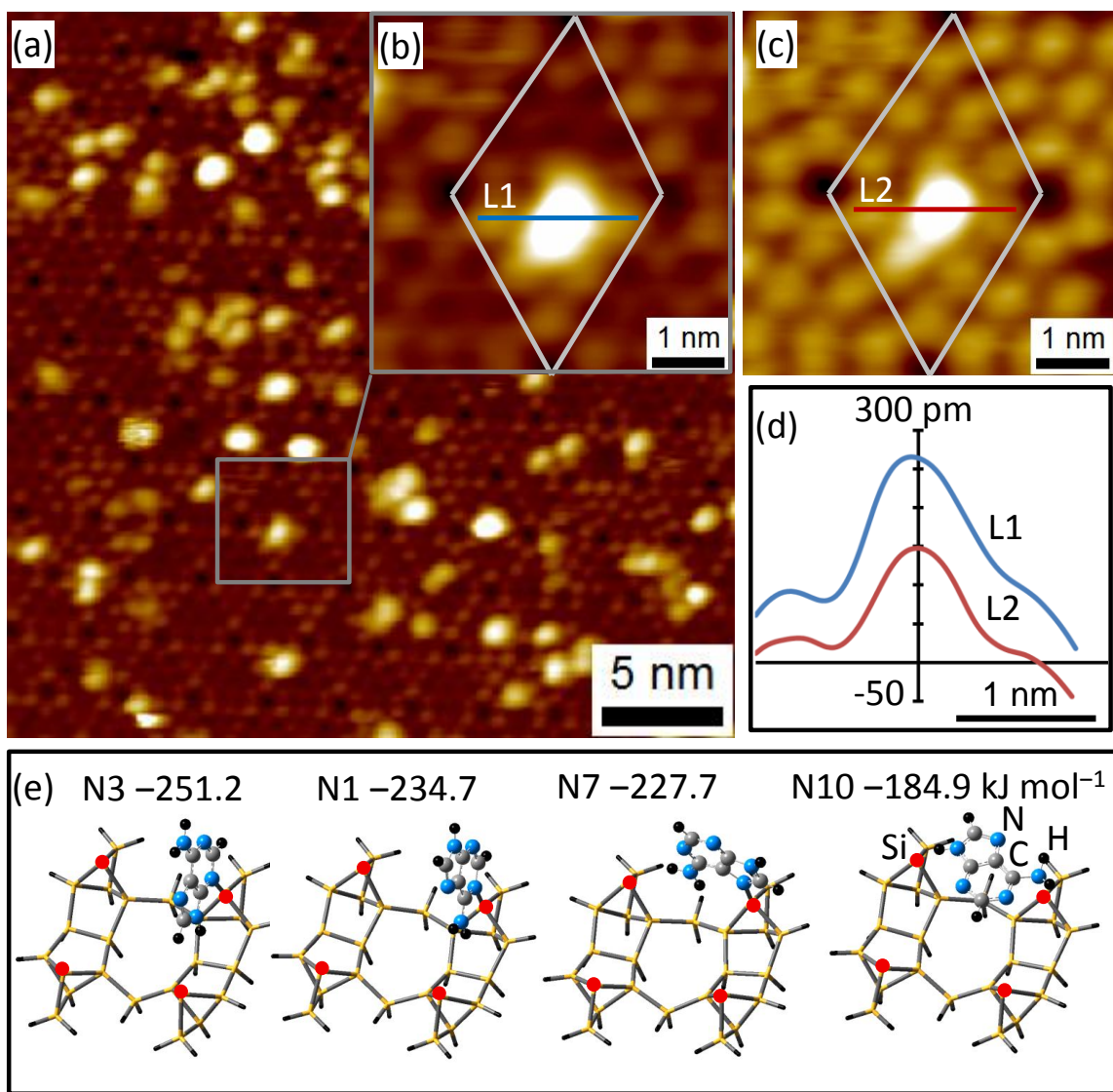
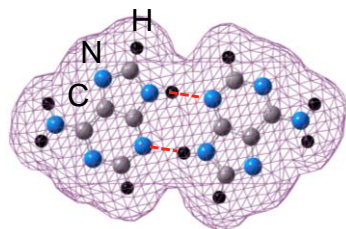


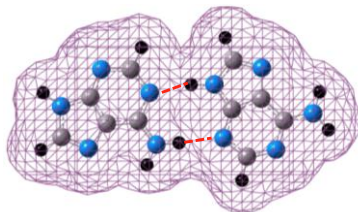
**Figure 7-1** (a) Empty-state STM image ( $30 \times 30 \text{ nm}^2$ ) of adenine adsorbed  $\text{Si}(111)7 \times 7$  obtained with a sample bias of +2V and a tunneling current of 150 pA; (b) the empty-state image and (c) filled-state image (both  $5 \times 5 \text{ nm}^2$ ) of a selected  $7 \times 7$  unit cell with a single adenine molecule adsorbed as marked by the square box in (a); (d) the height profiles along linescans L1 and L2 in (b) and (c) respectively; and (e) equilibrium adsorption geometries and their corresponding adsorption energies (in  $\text{kJ mol}^{-1}$ ) of a single adenine molecule datively bonded to a  $\text{Si}_{26}\text{H}_{24}$  cluster (with the Si adatoms marked by solid circles) through the N1, N3, N7 or N10 atom, as optimized by the DFT/B3LYP/6-31++G(d,p) method.

In addition to the singles, Figure 7-1 also reveals pairs of bright protrusions corresponding to dimers. To understand the formation of these dimers, we also performed DFT/B3LYP/6-31++G(d,p) calculations of “free” hydrogen-bonded Ade dimers. Figure 7-2 shows the possible hydrogen bonding arrangement among the pyridinic (N1, N3, N7), pyrrolic (N9) and amino groups (N10) in two isolated Ade molecules. Appropriate iso-density surface plots of the total electron densities of the dimers are also shown in order to illustrate their approximate shapes. The most stable H-bonded dimer A (Figure 7-2a) involves the N9–H···N3 and N3···H–N9 H-bonds, with the dimerization energy of  $-67.3 \text{ kJ mol}^{-1}$ . In this notation, we represent the H-bond between two different components in two Ade monomers by a triple dot (···), and we define the dimerization energy  $\Delta$  as the difference between the total energy of the H-bonded dimer, with counterpoise correction, and twice the total energy of a monomer. The next stable set of dimers involve N10–H···N3 and either N1···H–N9 (B1, with  $\Delta = -53.8 \text{ kJ mol}^{-1}$ , Figure 7-2b) or N7···H–N9 (B2, with  $\Delta = -49.5 \text{ kJ mol}^{-1}$ , Figure 7-2c). This is followed by the next group of dimers with H-bonds involving amino groups from both monomers: C1 with N10–H···N1 and N1···H–N10 ( $\Delta = -42.3 \text{ kJ mol}^{-1}$ , Figure 7-2d), C2 with N10–H···N1 and N7···H–N10 ( $\Delta = -39.8 \text{ kJ mol}^{-1}$ , Figure 7-2e) and C3 with N10–H···N7 and N7···H–N10 ( $\Delta = -36.3 \text{ kJ mol}^{-1}$ , Figure 7-2f). The stability of the dimers therefore appears to be inversely related to the number of H-bonds involving the amino group, with A (no amino group) > B1, B2 (one amino group) > C1, C2, C3 (two amino groups). The next least stable group of dimers involves one H-bond and one H-bond-like interaction between a N and a H–C groups, with D1 with N9–H···N7 and N3···H–C8 ( $\Delta = -35.9 \text{ kJ mol}^{-1}$ , Figure 7-2g) being more stable than D2 with N10–H···N1 and N7···H–C2 ( $\Delta = -18.9 \text{ kJ mol}^{-1}$ , Figure 7-2h). Finally, the least stable dimer E1 involves only H-bond-like interactions, with C8–H···N7 and N7···H–C8 ( $\Delta = -13.0 \text{ kJ mol}^{-1}$ , Figure 7-2i). It is of interest to note that of the more stable dimers involving only H-bonds (A, B1, B2, C1, C2, C3), it is more feasible to place two dimers end-to-end (with the long side of the dimer, i.e. along the H-bond direction, oriented back to back) rather than side-by-side (with the long side of the dimer oriented in parallel next to each other), because of the more ready availability of free N atoms at the ends of the dimers than on the sides. This type of inter-dimer interaction for such an end-to-end double dimer, usually with just a single inter-dimer H-bond, is expected to be weaker than the intra-dimer interaction within a single dimer with two H-bonds. While the dimer is a stable natural building block unit, a group of linear double or multiple dimers is expected to be a less stable unit.

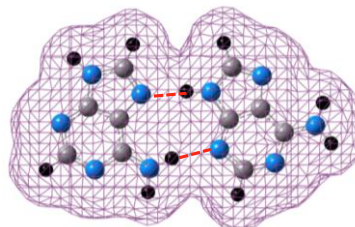
(a) A  $-67.3 \text{ kJ mol}^{-1}$



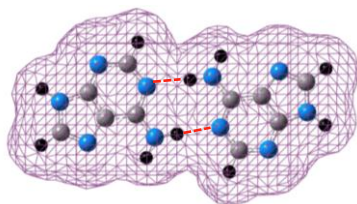
(b) B1  $-53.8 \text{ kJ mol}^{-1}$



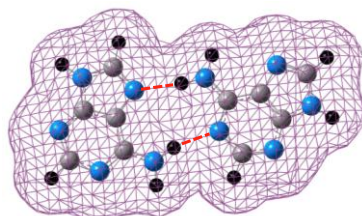
(c) B2  $-49.5 \text{ kJ mol}^{-1}$



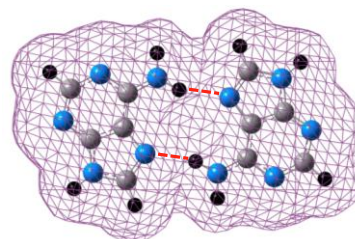
(d) C1  $-42.3 \text{ kJ mol}^{-1}$



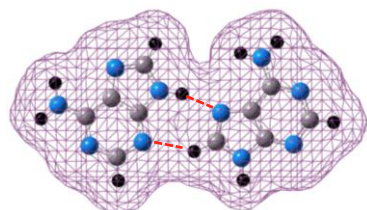
(e) C2  $-39.8 \text{ kJ mol}^{-1}$



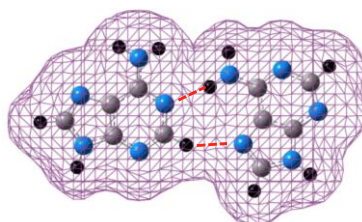
(f) C3  $-36.3 \text{ kJ mol}^{-1}$



(g) D1  $-35.9 \text{ kJ mol}^{-1}$



(h) D2  $-18.9 \text{ kJ mol}^{-1}$



(i) D3  $-13.0 \text{ kJ mol}^{-1}$

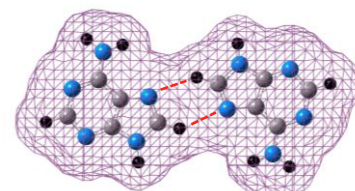


**Figure 7-2** Equilibrium geometries of the hydrogen-bonded adenine dimers involving different N atoms (a-f) and C atoms (g-i), obtained by the DFT/B3LYP/6-31++G(d,p) method with counterpoise energy corrections to the basis set superposition errors.

Given the similar appearances for Ade on Si(111)7×7 in both empty-state and filled-state imaging modes, as illustrated in Figure 7-1, it is more straightforward to use empty-state images for the analysis of Ade adsorption.<sup>49</sup> Figure 7-3a shows a 30×30 nm<sup>2</sup> empty-state image for a 15 s exposure of Ade on Si(111)7×7. Evidently, a higher exposure of Ade gives rise to a much larger proportion of dimers than monomers when compared to e.g. the 10 s exposure shown in Figure 7-1a. Closer examination reveals four types of dimers: long dimer (LD) with two Ade molecules adsorbed with a separation between 1.5 and 2 times the AA-to-CA distance (7.68 Å); diagonal dimer (DD) with two Ade molecules adsorbed at AA and CA diagonally across the dimer wall or at two CAs within a half unit cell; side dimer (SD) with both Ade molecules adsorbed at adjacent adatoms on the same side of the dimer wall; and opposite dimer (OD) with both Ade adsorbed at either AA and AA or CA and CA directly across the dimer wall (Figure 7-3b). As shown in Figure 7-3a, the intensity of the bright protrusions for dimers could also vary quite notably because of the different tilt orientation of the Ade molecules inside the dimer, with the brighter protrusions corresponding to Ade molecules lying closer to the surface plane (more tilt, second top panel). The corresponding height profiles (Figure 7-3a, inset) show that the double peaks along L2 are stronger and broader than those along L1. The intensities for the LD, SD and OD protrusions are usually found to be lower than the brightest DD protrusion (Figure 7-3b). Using the separation between the maxima of the height profiles along the appropriate linescans, we observe the separation follows the order LD (1.21 nm, along L1) > DD (1.15 nm, along L2) > SD (1.08 nm, along L3) > OD (1.05 nm, along L4), which is in good accord with the spatial separations between the respective surface atom pairs: diagonal AA-CA (1 nm) > same side AA-CA (0.7 nm) > opposite AA-AA or CA-CA (0.6 nm).

Figure 7-3c shows the plausible dimer ASCs of DD, SD and OD on the Si<sub>26</sub>H<sub>24</sub> cluster, with (N7, N7), (N1, N1) and (N1, N7) of the two Ade molecules forming the dative bonds with the appropriate adatom sites, respectively. We have not included calculations for LD ASCs because of the various possible configurations involving even larger clusters. The “single” ASC calculations shown in Figure 7-1e suggest that dative bonding involving N3, N1 or N7 of a single Ade molecule to an adatom site are more likely. Using a combination of any two of these three datively bonded singles, we could obtain possible “flat” dimer configurations as those shown in Figure 7-2 and these configurations are also summarized in Table 2. Interestingly, singles involving N1 and N7 dative bonding give rise to the more stable dimers (A, B1, B2), while dimers involving singles with N3 dative bonding are less stable. In order to achieve the possible dimer ASCs, the singles must undergo structural rearrangement from the “free” planar dimer configurations to appropriate substrate-modified non-planar dimer configurations so to achieve dative bonding of the participating singles to the adatoms and also to direct the singles into the DD, SD and OD

geometries. Based on the energies of the free dimer configurations (Figure 7-2), we only consider the three most stable free dimer configurations (A, B1, and B2) as candidates for the substrate-modified dimer configurations, as shown in Table 2. Evidently, except for SD involving N1+N1 dative bonded singles, all other DD, SD, and OD involving N1 and N7 dative bonding favour the modified A geometry. The resulted dimer ASCs could contain adsorbed Ade molecules with different tilts and twists as well as lateral positional rearrangement from one another, which could produce the different brighter protrusions for the corresponding dimers (Figure 7-3a, DD vs DD'). Furthermore, within an individual optimized dimer ASC, the Ade molecules are also found to exhibit different amounts of tilt and twist from each other, which is consistent with the observed different peak shapes and maxima in the height profiles (Figure 7-3a, inset). For example, one of the peaks along L2 (for DD) is found to have a larger maximum and a smaller width than the other peak. A modified A dimer ASC with different tilts in the individual Ade molecules (Figure 7-3c, top two panels) can therefore be used to account for two different DDs with different bright protrusions (Figure 7-3a, DD vs DD'). Similarly, a modified A or B2 dimer ASC could correspond to the observed OD arrangement, while a modified A or B1 dimer ASC could account for the SD arrangement (Figure 7-3b, bottom two panels).

**Table 7-1: The combinations of dative bonded adenine N atoms, free hydrogen bonding configurations and the substrate modified dimer configurations**

<b>N Positions of the Dative-bonded Monomers</b>	<b>“Free” Dimer Configurations</b>	<b>Substrate-modified Dimer Configurations</b>
N3+N3	C1 [N10–H...N1 and N1...H–N10] C2 [N10–H...N1 and N7...H–N10] C3 [N10–H...N7 and N7...H–N10]	(a)
N3+N1	B2 [N10–H...N3 and N7...H–N9] C3	(a)
N3+N7	B2, C1, C2	(a)
N1+N1	A [N9–H...N3 and N3...H–N9] B2 C3	Modified A for DD Modified B2 for SD Modified A, B2 for OD
N1+N7	A B1 [N10–H...N3 and N1...H–N9] B2	Modified A for DD Modified A for SD Modified A for OD
N7+N7	A, B1, C1	Modified A for DD Modified A, B1 for SD Modified A, B1 for OD

(a) Given the energies for the “free” dimer configurations, we only consider the top three most stable free dimer configurations (A, B1, and B2) for possible substrate-modified dimer configurations.

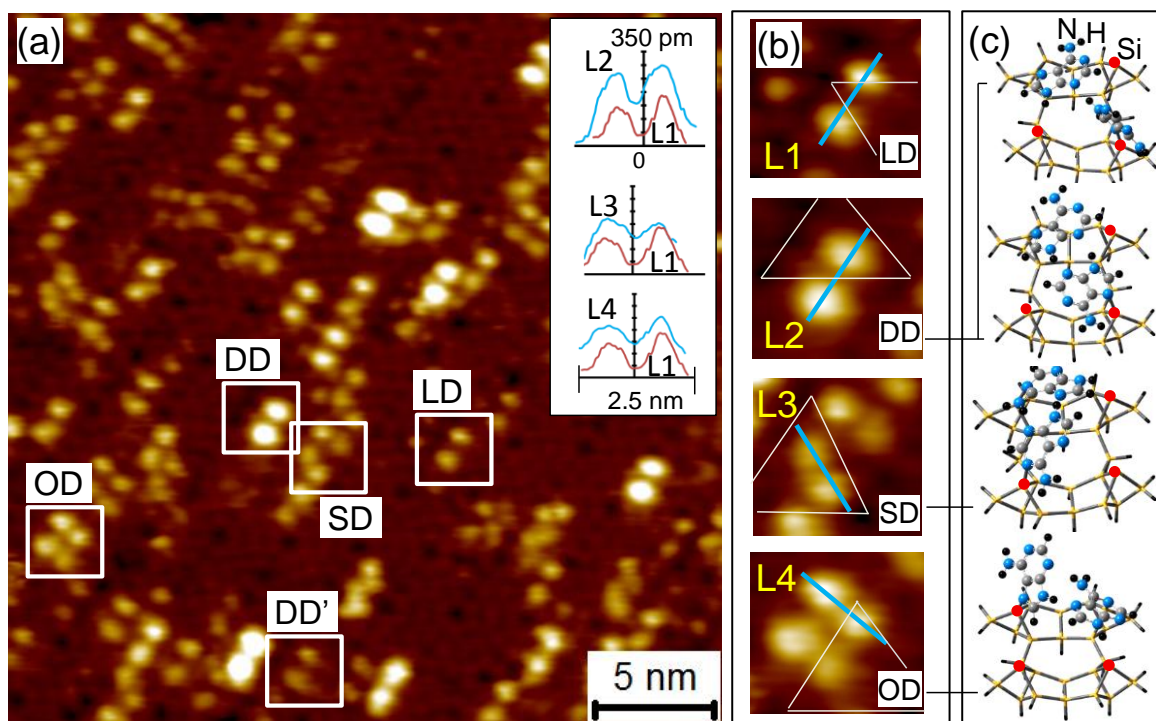


**Figure 7-3** (a) Empty-state STM image ( $30 \times 30 \text{ nm}^2$ ) of 15 s exposure of adenine on Si(111) $7 \times 7$  recorded with a sample bias of +2 V and a tunneling current of 150 pA; (b) corresponding magnified STM images of selected adenine dimers including long dimer (LD), diagonal dimer (DD), side dimer (SD), and opposite dimer (OD) marked by open squares in (a) and (a, inset) the height profiles along linescans L2, L3 and L4 compared to that along L1; and (c) equilibrium geometries of adenine dimers datively bonded to the  $\text{Si}_{26}\text{H}_{24}$  cluster (with the adatoms marked by solid circles), as optimized by the DFT/B3LYP/6-31++G(d,p) method.

In addition to the dimers found for the higher exposure of Ade on Si(111)7×7 surface, we observe apparent self-organization of these dimers into linear double dimers, quartets, linear chains, and other higher-order superstructures. To understand the general nature of this self-organization, we illustrate in Figure 7-4 the H-bond mediated “links” between individual dimer units found in the self-organization of these superstructures on the 7×7 template for a 15 s exposure of Ade. In particular, two dimers can be linked in an end-to-end (ETE) arrangement (i.e. along the long axis of the dimer marked by eclipse) near-linearly in two ways. Figure 7-4b shows a direct ETE configuration with one of the dimer protrusions being brighter than the other, which is likely due to different extents of the tilts in the two dimers. On the other hand, Figure 7-4c shows a slightly “offset” ETE configuration with equally bright protrusions for both dimers. The slight lateral offset is likely imposed by the H-bond alignment between two dimers with nearly equal amounts of tilts. Like the two ETE arrangements, the zigzag (ZZ) arrangements also involve one end of the dimer linked to another end of an adjacent dimer, except the link direction is no longer parallel to the long axis. For ZZ90 (Figure 7-4d), the angle between the link direction and the long axis is 90°, while this angle is 60° for ZZ60 (Figure 7-4e). For the ETE and ZZ arrangements, the growth direction of the second dimer (marked by dashed line arrow) is parallel to the long axis of the first dimer (marked by the dashed line in Figure 7-4), without and with lateral offset. In addition, the growth direction could also undergo a wide (obtuse) angle turn (WAT, Figure 7-4f), or a right-angle turn (RAT, Figure 7-4g). Furthermore, the growth direction could be perpendicular to the long axis of both dimers in a side-by-side (SBS) arrangement (Figure 7-4h). These seven link arrangements provide the basic mechanism for the observed chain-like growth. Of special interest is the remarkable alignment of the chains all along  $(-1\ 1\ 0)$  direction, indicating a strong surface template effect on the self-directed growth of these Ade dimers.

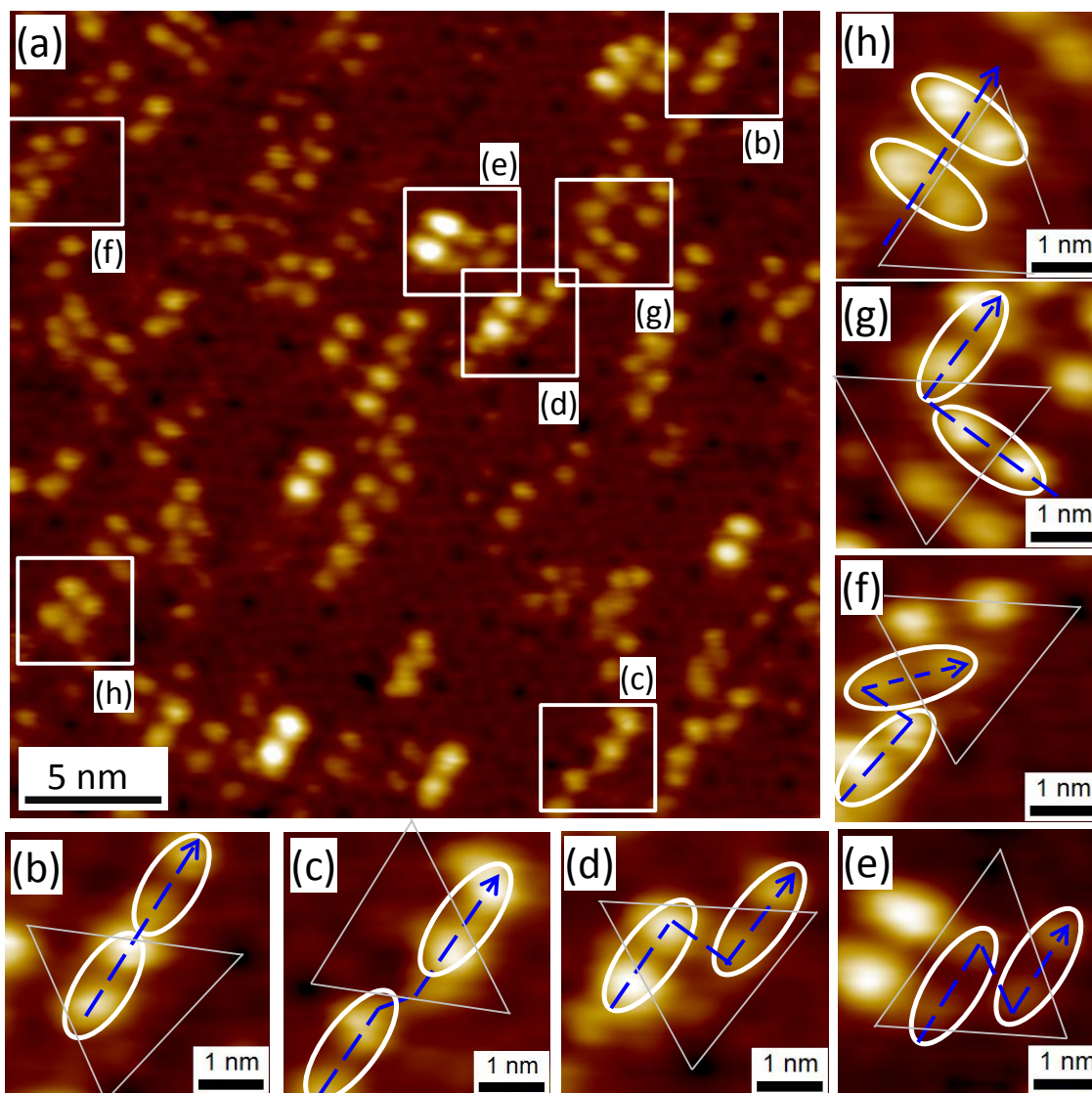


**Figure 7-4** (a) Empty-state STM image ( $30 \times 30 \text{ nm}^2$ ) of a 15 s exposure of adenine on  $\text{Si}(111)7 \times 7$  recorded with a sample bias of +2 V and a tunneling current of 150 pA, and magnified views of H-bond mediated links between different dimers in (b) direct end-to-end (ETE), (c) offset ETE, (d)  $90^\circ$  zigzag (ZZ90), (e)  $60^\circ$  zigzag (ZZ60), (f) wide-angle turn (WAT), (g) right-angle turn (RAT) and (h) side-by-side (SBS) arrangements, with the arrows marking the direction of growth and the triangles outlining the half unit-cells.

Figure 7-5 shows empty-state STM images for four Ade exposures on Si(111)7×7 during the early growth stage. Using the full 50×50 nm<sup>2</sup> images (of approximately 400 7×7 unit cells), we count the numbers of individual monomers or singles (S), dimers (D), selected double dimers such as ETE and SBS, and larger/longer dimer chains consisting of multiple dimers (MD), and their relative surface concentrations (i.e. the fractions of the available sites that are occupied by the respective Ade configurations) are presented in Figure 7-5e. Evidently, growth begins with just the S and D populations on the 7×7 surface for the 6 s exposure (Figure 7-5a), with the relative surface concentrations for S being higher than that for D (Figure 7-5e). As the exposure increases, the relative surface concentration for S decreases gradually while that for D increases (Figure 7-5e). For the 10 s exposure (Figure 7-5d), we also observe the emergence of double dimers and larger dimer chains, with their relative surface concentrations following the order: ETE > SBS > MD. The relative surface concentrations of ETE, SBS and MD all appear to increase as the exposure increases to 15 s and 25 s (Figure 7-5e). The increase in the ETE occupancy appears to slow while the increase in the SBS occupancy remains steady. This is consistent with the formation of double and multiple parallel chains becoming more prominent at a higher exposure. For exposures above 25 s (not shown), the 7×7 template is totally covered by Ade and accompanied with multilayer formation, which makes our statistical analysis difficult. In addition, with the exception of the very low exposure (i.e. 6 s), all other STM images for the higher exposures show remarkable alignment of the dimer chains along the [-11 0] direction. Even more interesting is that almost all the dimer chains are aligned along a particular direction, despite the three-fold symmetry of the 7×7 half unit cell. While the exact mechanism of this self-alignment is not clear, we hypothesize that inter-chain interactions play an important role in orienting the neighbouring dimers along a specific growth direction. Some of these inter-chain interactions are manifested in the H-bond mediated links shown in Figure 7-4. Moreover, most of the chains are limited to a maximum of 4-5 dimers (Figure 7-5c), likely because of the surface template effect of the 7×7 surface (in contrast to the more homogeneous metal surface) and of the tilted dimer bonding geometry that is less compatible with horizontal growth parallel to the surface. In Figure 7-5e, we also show the total coverage of Ade on the 7×7 surface, which evidently increases almost linearly up to 25 s exposure. The number of occupied adatoms on the faulted half of the 7×7 unit cell is found to be almost the same as that of the unfaulted half for the four exposures (not shown). Furthermore, the number of brighter protrusions (marked by ovals in Figure 7-5), with brightness similar to DD in Figure 7-3b, is found to decrease with increasing exposure. This is consistent with the geometry of dimers becoming less tilted (i.e. more vertical) at a higher exposure due to steric interactions.

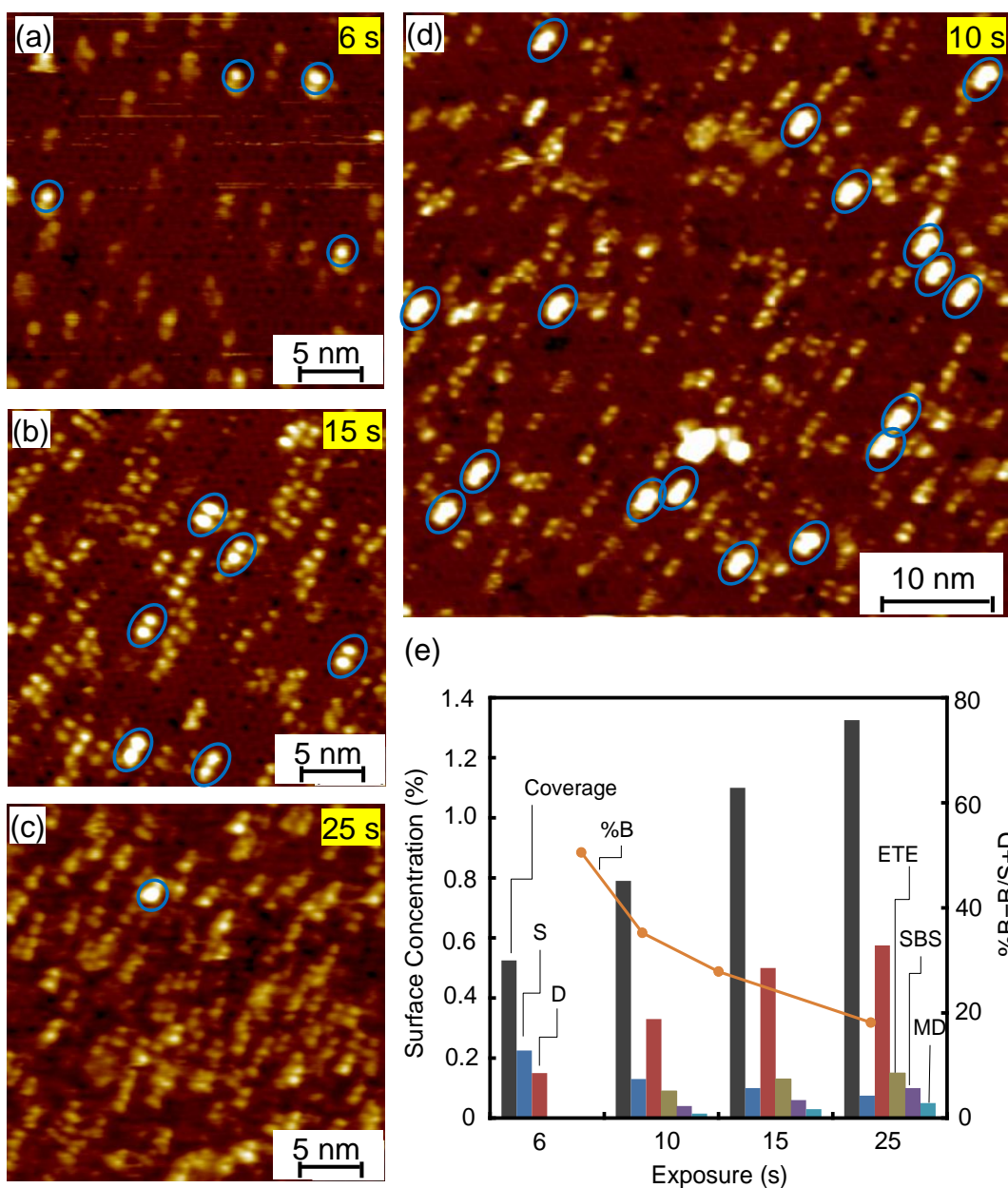


**Figure 7-5** Empty-state STM images ( $50 \times 50 \text{ nm}^2$ ) of (a) 6 s, (d) 10 s, (b) 15 s, and (c) 25 s exposures of adenine on Si (111) $7 \times 7$  recorded with a sample bias of +2 V and a tunnelling current of 150 pA, with (a), (b), and (c) shown with a magnified view ( $30 \times 30 \text{ nm}^2$ ); (e) Corresponding relative surface concentrations for singles (S), doubles (D), end-to-end (ETE), side-by side (SBS), and multiple dimers (MD), along with the total coverage (Coverage) and the percentage of brighter protrusions in S+D (marked by ovals and indicated as %B), all as a function of adenine exposure.

## 7.4 Summary

The early growth stage of Ade on Si (111)7×7 has been studied by STM. Both the empty-state and filled-state images show bright protrusions without any evidence of dissociation, which indicates molecular adsorption of Ade through dative bonding, in good accord with our recent XPS results. Variation in the brightness of the protrusions is observed and can be attributed to the extent of the molecular tilt with respect to the surface normal. Of particular interest is the unique site-specific information about the early adsorption of Ade on the 7×7 surface provided by the present study. In particular, above 6 s exposure, the observed protrusions predominantly appear as dimers, which indicates that hydrogen bonding interactions between Ade molecules play a prominent role in the initial adsorption and subsequent growth process. From the DFT/B3LYP/631++G(d,p) calculations for free H-bond mediated Ade dimers, we expect dimers involving N9–H···N3 and N3···H–N9 H-bonds (A in Figure 7-2), and N10–H···N3 and either N1···H–N9 (B1) or N7···H–N9 (B2) to provide the most stable dimer configurations on the surface. Our STM images obtained at a higher exposure further reveal the different adsorption arrangements of the Ade dimers with the Si adatoms on the 7×7 surface, including long dimers, diagonal dimers, side dimers and opposite dimers. Using a model surface based on the Si<sub>26</sub>H<sub>24</sub> cluster, we demonstrate the plausible adsorption substrate configurations of these adsorbed Ade dimers on adatoms across a Si dimer wall. At 15s Ade exposure, the dimers are found, for the first time, to self-organize into aligned superstructures, including straight, offset and zigzag chains, square quartets, double quartets, and other multiple dimer structures. We identify the common types of links in forming these dimer superstructures, including end-to-end (both direct and offset), 90° and 60° zigzags, wide-angle and right-angle turns, and side-by-side arrangements. The end-to-end growth is found to be the most prominent especially in the initial growth stage, which leads to the formation of dimer nanowires. At 25s exposure, dimer nanowires appear to grow side by side, remarkably all aligned in the same direction. While the exact mechanism of this self-aligned growth is unclear, we believe that inter-dimer hydrogen bonding interactions play an important role. The observed self-aligned growth of Ade on Si(111)7×7 promises potential applications in molecular electronics, lithography, and biomolecular sensing.

## Chapter 8

# Surface [4+2] cycloaddition reaction of Thymine on Si(111)7×7 as observed by Scanning Tunneling Microscopy

### 8.1 Introduction

Evolution in microelectronics and, more recently, nanotechnology has seen the spectacular surge in research in silicon-based chemistry, device fabrication and processing.<sup>2</sup> The concept of organic-to-silicon integration is being studied under various experimental conditions, particularly to test the suitability and efficiency for device fabrication.<sup>2,183</sup> At the same time, microelectronics continuously demands the use of increasingly smaller electronic components than those provided by the current state of the art. This has pushed the device size into the nanoscale, and indeed the use of molecules as electronic components has been proposed. In recent years, studies of appropriate candidates (molecules) for different molecular electronic applications have been intensified. The interactions of organic molecules with the silicon surfaces are driven by the functional groups of the adsorbates. A number of organic molecules have been studied on the Si surfaces. Simple hydrocarbons<sup>2</sup> with aliphatic chain backbones, alkenes, alkynes, and aromatic molecules without and with heteroatoms<sup>14</sup> have been investigated by a number of experimental methods, including X-ray photoelectron spectroscopy (XPS), Low Energy Electron Diffraction (LEED), High Resolution Electron Energy Loss Spectroscopy (HREELS) and Scanning Tunneling Microscopy (STM), and computational methods, such as Density Functional Theory (DFT), Moller-Plesset Perturbation (MP2) and semi-empirical techniques.<sup>2</sup> These studies generally demonstrate the nature and strength of interactions between the molecule and the Si substrate, as well as the mobility of the adsorbates and their response to heating, all of which are fundamentally important to device fabrication. Furthermore, appropriate organic molecules could provide unique functionalities that make them quintessential in forming complex and sophisticated biological materials, including proteins, DNA, peptides, and lipids. In particular, amino acids are the building blocks of proteins, while the four DNA base-group molecules are responsible for conserving the unique genetic codes by selective hydrogen bonding. In order to take advantage of the potentially novel functionalities of these biological molecules in a device, a better understanding of the nature of their interactions with a substrate surface is necessary. Using XPS, STM and DFT calculations, we have recently investigated the adsorption and in particular self-organization properties of adenine on the Si(111)7×7 surface. Of the four DNA base groups that are responsible for encrypted storage of genetic information in a DNA molecule, thymine (Thy) represents a

complementary partner to adenine. It is therefore of special interest to study both adenine and thymine and if possible their interactions between each other. As also discussed in the first chapter, Thy undergoes the keto-enol tautomerism under suitable conditions. But in the gas phase the diketo form instead of the di-enol form is found to be more stable as reported by the Rejnek et al.<sup>46</sup> Their theoretical study has shown that in the gas phase the di-keto form is  $\sim 60 \text{ kJ mol}^{-1}$  more stable than the di-enol form, while the stability of the enol forms are more prominent in aqueous solutions. So it can be observed from their work that with the increase of the polar medium (e.g. aqueous molecules) the enol forms of Thy can be more stable. It is well known that the Si(111)7 $\times$ 7 surface provides adsorption sites with different partial charges, while the adatom-restatom pair may be considered as a dipole, with partial charges of  $\sim +7/12$  and  $-1$  on the adatom and restatom respectively. This dipole arrangement of an adatom-restatom pair could induce a free Thy molecule to tautomerise into the di-enol form, which could then lead to the formation of cycloaddition products on the surface. This is indeed confirmed by our recent XPS and DFT study of Thy adsorption on Si(111)7 $\times$ 7.<sup>122</sup> In the present study, STM will be used to investigate the site-specific chemistry of Thy on Si(111)7 $\times$ 7.

Kasaya et al. studied the surface processes of adenine and thymine on Si(100)2 $\times$ 1 with STM and semiempirical calculations.<sup>184</sup> Their STM images showed the presence of bright protrusions and by comparing with calculations they assigned different protrusions to Thy and adenine molecules. Their semiempirical calculations further suggested that Thy adsorbs on the surface with its plane parallel to the Si surface almost 2.5 Å above the top Si layer. Their STM results showed that both adenine and Thy adsorb on the Si(100)2 $\times$ 1 surface in a flat-on configuration with their molecular plane parallel to the substrate surface, differing only in the shape and size of the protrusions in accordance with their calculations.<sup>184</sup> Recently, we have studied the growth of Thy on the Si(111)7 $\times$ 7 surface by XPS and reported that during the initial stages of growth, Thy undergoes [4+2] cycloaddition reaction with the Si surface atoms, producing bidentate adspecies. Furthermore, Thy is found to undergo surface-induced tautomerisation to form the di-enol tautomer, which leads to the formation of both the 3,6 (N3–Si and C6–Si) and 1,4 (N1–Si and C4–Si) cycloaddition products on the surface.<sup>122</sup> Apart from these two studies on Si surfaces, the only other surface study was the study of Thy interactions on Cu(111) surfaces by STM and semiempirical calculations.<sup>180</sup> The results showed that Thy forms cluster-like structures in a more randomly distributed manner than those of other three DNA nucleobases (adenine, guanine, cytosine), which suggested that the hydrogen bonds among Thy molecules are not as stable as the other DNA base molecules, thereby preventing self-assembled growth on the Cu(111) surface.<sup>180</sup>

To date, cycloaddition reactions for Thy on any surface has yet to be reported. The only work that described the interaction of Thy and Si(100)2×1 did not explain the chemistry between Thy and the 2×1 surface in detail as mentioned earlier.<sup>184</sup> The [2+2] cycloaddition reaction between two alkene molecules (as in the gas-phase) is symmetry-forbidden in the Frontier Molecular Orbital theory, but has been found to be quite facile between an alkene molecule and a Si(100)2×1 dimer.<sup>185</sup> In particular, simple alkenes such as cyclopentene<sup>186</sup> and more complex cyclooctadiene<sup>186</sup> have been reported to undergo [2+2] cycloaddition reaction with the Si(100)2×1 surface dimers. Unlike [2+2] cycloaddition, [4+2] cycloaddition is symmetry-allowed and has been found for 1,3 cyclohexadiene and 2,3-dimethyl-1,3-butadiene on Si(100)2×1 surfaces. In addition to the Si(100)2×1 surface, [4+2] cycloaddition reactions of aromatic molecules with Si(111)7×7 surfaces, including benzene,<sup>187,138,188</sup> thiophene<sup>175</sup> and pyridine<sup>21</sup> have been reported in the literature. It has been shown that these [4+2] cycloaddition reactions are more facile than those for the [2+2] cycloaddition on the 7×7 surface due to the presence of a larger strain on the latter than the former.

In the present study, the early adsorption process of Thy is investigated by STM and DFT calculations, in order to obtain better understanding of the initial growth and site-specific surface processes of Thy on Si(111)7×7.

## 8.2 Experimental and Computational Details

The pristine 7×7 surface was exposed to Thy (99% purity, Aldrich, with a melting point of ~320°C) by thermal evaporation at 95°C using a water-cooled low temperature effusion cell in a separate organic molecular beam epitaxy chamber, after appropriate outgassing of the effusion cell at 100°C for 48 hours. The molecular nature of Thy vapour was monitored in-situ by a quadrupole mass spectrometer installed in the deposition chamber and the cracking pattern of Thy vapour was found to be in accord with that reported in the literature.<sup>153</sup> All the STM images were obtained in the constant (tunneling) current mode at 150 pA with the feedback current loop turned on to produce constant current topographs. Home-made electrochemically etched W tips have been used for these STM experiments.

Planar molecules such as benzene and arenes (including the nucleobases) were found to have nonplanar ground-state geometries by using typical ab-initio methods (e.g., DFT, MP2, MP4) with the standard Pople's basis sets. These inconsistencies could be explained in terms of intramolecular BSSE deficiencies as reported in the literature by Asturiol et al.<sup>181</sup> The authors have developed a technique to deal with the problems of spurious imaginary frequencies found for the optimized ground-state

geometries of the DNA base groups with these methods (DFT, MP2) by counterpoise corrections. In particular, the counterpoise corrections for Thy could be calculated by considering different intramolecular components of the molecule, which led to the removal of the spurious ground-state imaginary frequency.<sup>181</sup>

### 8.3 Results and Discussion

Figure 8-1a shows a typical empty-state STM image, collected at +2 V sample bias with a 150 pA tunneling current, for a 15 s exposure of Thy on Si(111)7×7. Each bright protrusion of the 24×24 nm<sup>2</sup> image represents a single or a group of Thy molecules adsorbed on the Si(111)7×7 surface. Evidently, three different kinds of bright protrusions, with “lower” (L), “medium” (M) and “higher” (H) degrees of brightness have been identified. The Schematic diagrams of the 7×7 unit cells of the respective types of Thy adsorptions are also indicated in Figure 8-1b. The individual lighter spheres in the diagrams represent unreacted Si atoms whereas the darker (orange) spheres represent Si atoms with Thy adsorption. As illustrated in their corresponding height profiles along the respective linescans L2, L3 and L4 in Figure 8-1c, the L feature has the lowest height. Closer inspection of the L feature reveals that Thy adsorption has affected both the center adatom (CA) and an adjacent restatom (RA) simultaneously without involving other neighbouring Si atoms, which suggests that a Thy molecule is attached to the surface in a bidentate fashion. The maximum height difference between L2 and linescan L1 along the bare Si adatoms corresponds qualitatively to the “height” of the Thy adstructure on the CA-RA site. Our recent XPS study of Thy adsorption on Si(111)7×7 surface indicates that Thy undergoes [4+2] cycloaddition reaction to form a bidentate adproduct on the surface.<sup>122</sup> Given the molecular dimension of Thy to be 2.8 Å, bidentate adsorption of Thy across an adatom-restatom pair (with a separation of 4.57 Å) would be more physically compatible than that between two adatoms (with a separation of 6.65 Å). The M feature shown in Figure 8-1 is found to involve one corner adatom (AA) and an adjacent restatom. The corresponding height profile along linescan L3 indicates that the M feature has a greater height than that of the L feature. On the other hand, the even brighter H feature is found to be discernibly different from both the L and M protrusions. In particular, the corresponding height profile along linescan L4 reveals that not only the maximum height for H is greater than both the M and L protrusions but also the extent of the H protrusion is considerably larger, covering three adatoms (one AA and two CAs) and one restatom. Furthermore, the STM image exhibits no correlated dark-bright features, as observed for dissociative hydrogen adsorption of glycine on Si(111)7×7.<sup>154</sup> The absence of notable dark features for Thy adsorption therefore indicates that hydrogen dissociation does not occur during the adsorption process,

which is in good accord with our XPS results.<sup>122</sup> The three different types of protrusions, i.e. L, M and H, in the STM image therefore suggest the presence of three different Thy adsorption configurations on the Si(111)7×7 surface. Furthermore, all the protrusions appear to be randomly distributed, and there is therefore no apparent ordering or organization observed for the three types of protrusions. The relative surface densities of the three protrusions will be discussed in greater detail below.

Figure 8-2 shows a 16×16 nm<sup>2</sup> filled-state STM image, collected at –2 V sample bias with a 150 pA tunneling current, for a 10 s exposure of Thy on Si(111)7×7. The two different protrusions can easily be discerned in the image shown as “B1” and “B2” in Figure 8-2 and marked by triangles. The height profiles along the linescans L1, L2 and L3 corresponding to the unreacted Si atoms, B1 and B2 are shown in the inset of Figures 8-2 respectively. As found from the empty-state image, the position of the protrusion B1 in Figure 8-2 also confirms that Thy reacts simultaneously with the adatom-restatom pair. The height profile along the bigger protrusion B2 (L3) is compared with those along B1 (L2) and along the unreacted Si adatoms L1. The difference in height between the B1 and B2 protrusions is clearly evident. However, switching the bias voltage from empty-state to filled-state imaging modes evidently causes the STM tip to pick up unwanted moiety from the surface, which makes direct empty-state and filled-state imaging of the same scanning area extremely difficult. Direct correlation between the empty-state and filled-state images is therefore not possible in this case. Despite this challenge, the lack of correlated dark-bright features in the filled-state STM images that correspond to hydrogen dissociation as observed for the glycine adsorption<sup>154</sup> indicates that Thy does not undergo hydrogen dissociation reaction on the 7×7 surface.

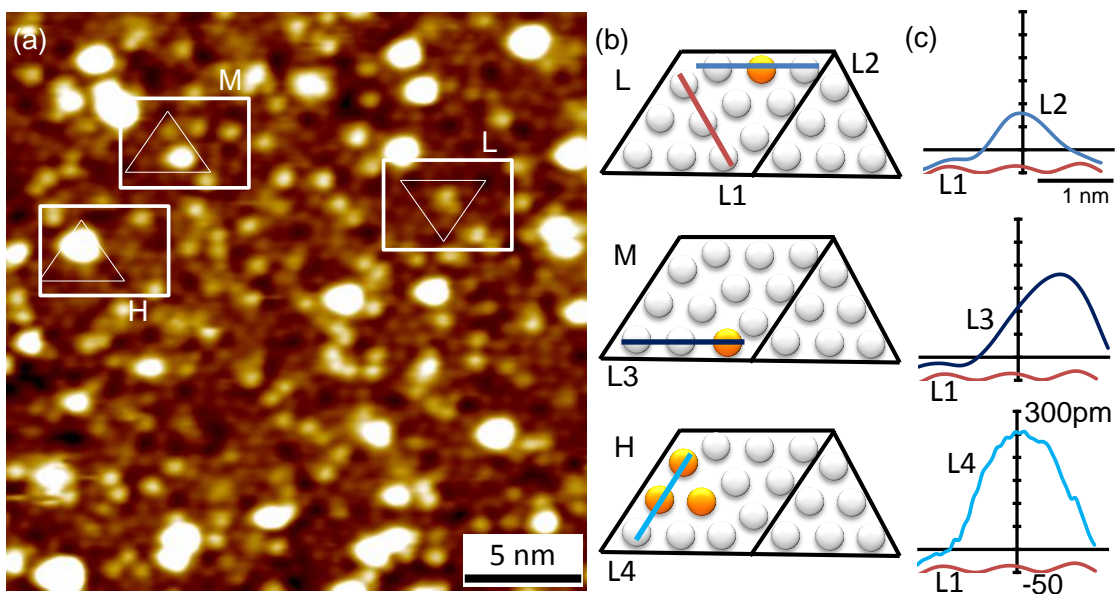


**Figure 8-1** (a) STM empty-state image ( $24 \times 24 \text{ nm}^2$ ) for 15 s exposure of thymine on a Si(111) $7 \times 7$  surface obtained w a sample bias of +2 V at a tunneling current of 150 pA. Bright protrusions of three different intensities are marked as L (lower), M (medium) and H (higher). (b) Schematic drawings of the corresponding  $7 \times 7$  unit cells for the selected part of the STM image, with the Si atoms of the half unit cells represented by lighter spheres while the sites with adspecies are indicated as darker spheres. (c) Height profiles along the linescans L1, L2, L3 and L4, corresponding to the unreacted Si adatoms, L, M and H protrusions, respectively.

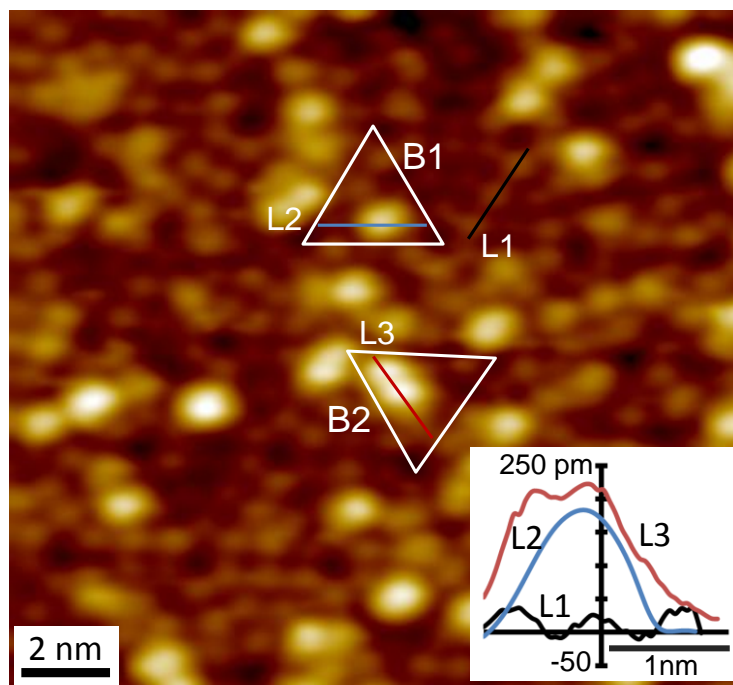


**Figure 8-2** STM filled-state image ( $16 \times 16 \text{ nm}^2$ ) for 10 s exposure of thymine on Si(111) $7 \times 7$  collected with a sample bias of  $-2 \text{ V}$  at a tunneling current of  $150 \text{ pA}$ . The two different bright protrusions are labeled as B1 and B2 and are marked with triangular brackets. The height profiles along the lines L1, L2 and L3 corresponds to the unreacted Si adatoms, B1 and B2 features respectively are shown as inset.

Figure 8-3 shows a plausible cycloaddition reaction pathway of Thy with a Si adatom-restatom pair. After tautomerization of Thy to the di-enol form, the di-enol tautomer then undergoes a [4+2] cycloaddition reaction with a Si adatom-restatom pair to form a bidentate 1,4-cycloaddition adproduct. Other cycloaddition reactions leading to the 3,6- and 2,5-cycloaddition adproducts could also be plausible. We have not considered [2+2] cycloaddition adproducts here because of the larger strain on the Thy molecule bridging an adatom-restatom pair. Indeed, no evidence of such [2+2] cycloaddition adproducts in the growth process of Thy on the 7×7 surface is found in our recent XPS study.<sup>122</sup>

The equilibrium geometries of Thy on a Si<sub>16</sub>H<sub>18</sub> cluster, representing an adatom-restatom pair of the 7×7 surface, obtained at the DFT/B3LYP level of calculation using 6-31++G(d,p) basis set are shown in Figure 8-4. Evidently, all three cycloaddition adproducts are found to have rather similar adsorption energies ( $\Delta E$ ), with 1,4- ( $\Delta E = -114.0 \text{ kJ mol}^{-1}$ ) being more stable than 3,6- ( $\Delta E = -111.5 \text{ kJ mol}^{-1}$ ) and 2,5-cycloaddition adproducts ( $\Delta E = -97.3 \text{ kJ mol}^{-1}$ ). Based on our recent XPS study of the Thy adsorption on Si(111)7×7, we conclude that only 1,4- and 3,6- cycloaddition, but not 2,5- cycloaddition, could exist on the 7×7 surface, and that almost 90% of the adproduct corresponds to the 1,4-cycloaddition adproduct.<sup>122</sup> Between the N1 and N3 atoms in the di-enol form of Thy, N1 is more nucleophilic because it has only one neighbouring –C–OH group when compared to N3 with two –C–OH groups. It is known that the higher nucleophilicity of diene (Thy, in this case) might influence the cycloaddition reaction rate and the stability of the final adproduct. Following the same argument, cycloaddition that leads to 1,4-cycloaddition adproduct should be more facile and stable than the one which leads to the 3,6-cycloaddition adproduct. In addition, as it can be seen from the 2,5-cycloaddition adproduct that the cycloaddition reaction involves the C5 atom that is next to a bulky –CH<sub>3</sub> group. The bulky substituents on the reaction site might cause steric effects that could reduce the overlap between the interacting orbitals from the reactants. The cycloaddition reaction leading to 2,5-cycloaddition adproduct therefore might not be facile, consistent with the smaller adsorption energy. We also calculate a hydrogen-bonded complex between an incoming thymine molecule and the respective cycloaddition adproducts. As shown in Figure 8- 4, the hydrogen-bonded adsorption complex for the 1,4-cycloaddition adproduct ( $\Delta E = -98.4 \text{ kJ mol}^{-1}$ ) is also found to be more stable than that for 3,6- ( $\Delta E = -82.0 \text{ kJ mol}^{-1}$ ) and than that for 2,5-cycloaddition adproduct ( $\Delta E = -74.0 \text{ kJ mol}^{-1}$ ). Both the 1,4-cycloaddition adproduct and the H-bonded Thy-adcomplex could be used to account for the different types of protrusions observed. Statistical analysis of these protrusions would allow us to calculate the concentrations of these adstructures as a function of exposure.

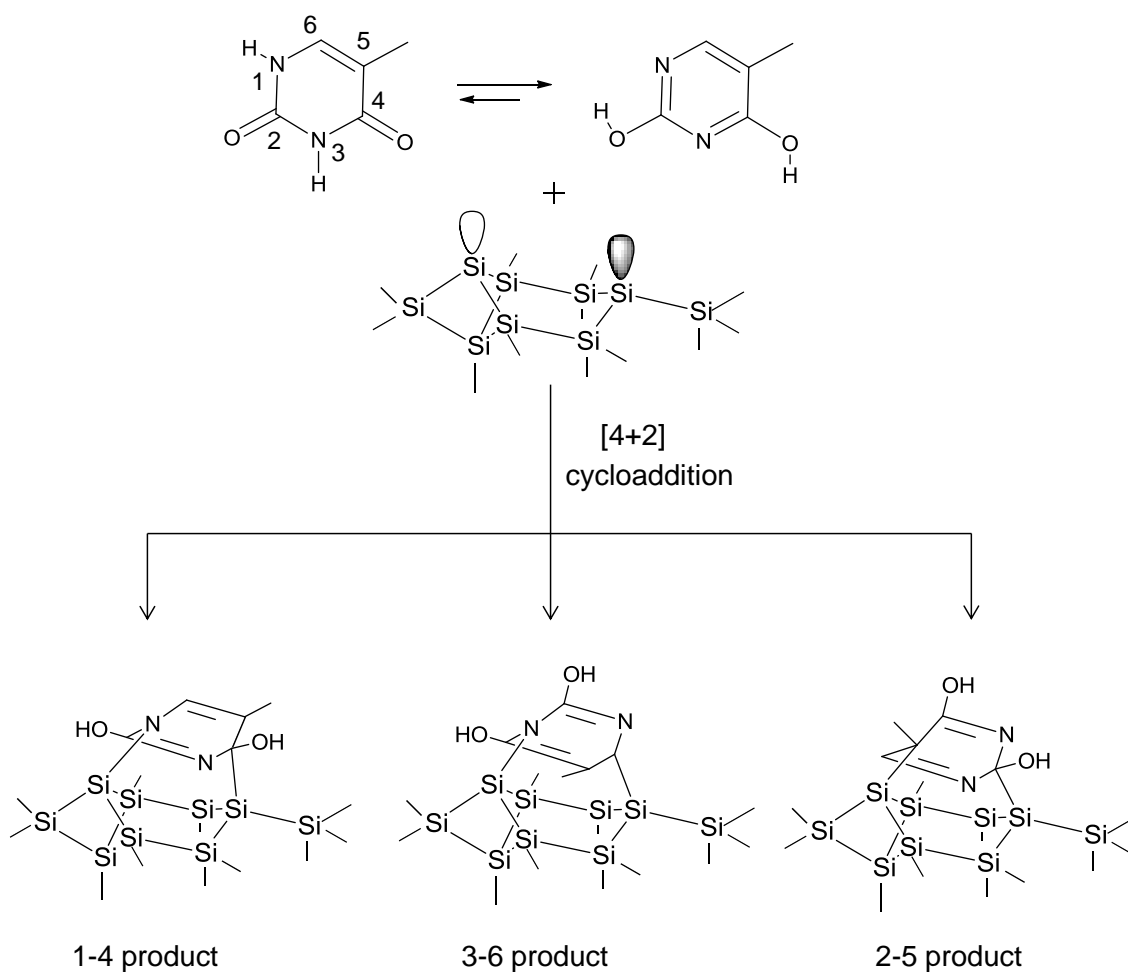
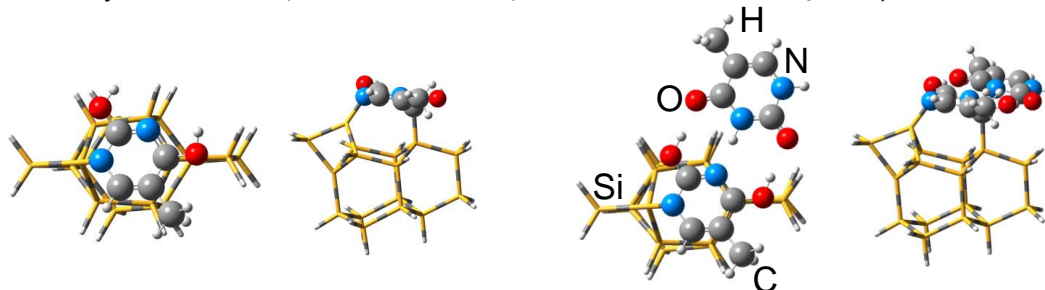
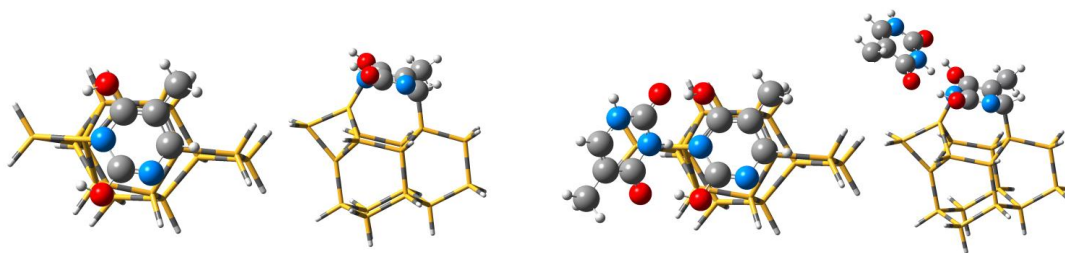


**Figure 8-3** Reaction scheme of [4+2] cycloaddition reaction of thymine on a model Si(111)7×7 surface. Thymine first undergoes keto-enol tautomerism to form di-enol tautomer, which reacts with a Si adatom-restatom pair to produce 1,4-, 3,6- and 2,5-cycloaddition adspecies.

(a) 1,4 Cycloaddition ( $-114.0 \text{ kJ mol}^{-1}$ ) H-Bonded adcomplex ( $-98.4 \text{ kJ mol}^{-1}$ )



(b) 3,6 Cycloaddition ( $-111.5 \text{ kJ mol}^{-1}$ ) H-Bonded adcomplex ( $-82.0 \text{ kJ mol}^{-1}$ )



(c) 2,5 Cycloaddition ( $-97.3 \text{ kJ mol}^{-1}$ ) H-Bonded adcomplex ( $-74.0 \text{ kJ mol}^{-1}$ )

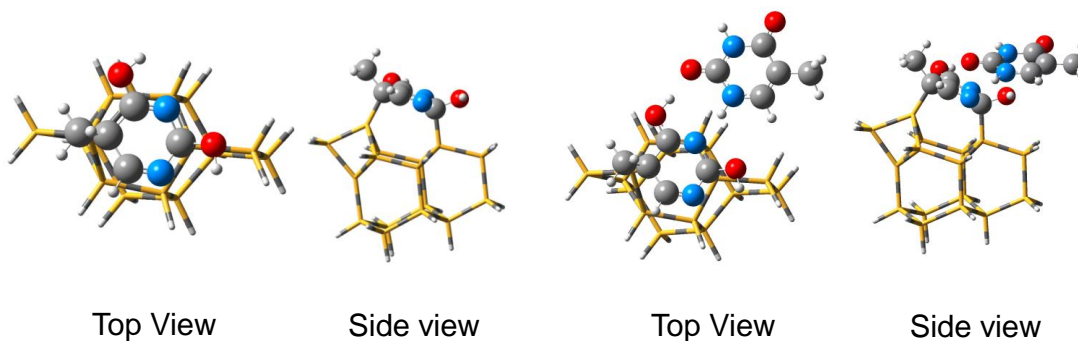


**Figure 8-4** Equilibrium structures (with top and side views) and adsorption energies of thymine on a  $\text{Si}_{16}\text{H}_{18}$  cluster, representing an adatom-restatom pair, resulting from (a) 1,4- (b) 3,6- and (c) 2,5-cycloaddition, and of their corresponding hydrogen-bonded complexes formed with an incoming thymine molecule. All the geometries are obtained with DFT/B3LYP/6-31G++(d,p) calculations.

Figure 8-5 shows part ( $30 \times 30 \text{ nm}^2$ ) of the empty-state STM images for three Thy exposures on Si(111) $7 \times 7$  during the early growth stage. Using the full  $50 \times 50 \text{ nm}^2$  images (of  $\sim 400 \text{ } 7 \times 7$  unit cells), we determine the relative surface concentrations of the L, M and H protrusions (i.e. the fractions of the available surface sites that are occupied by the respective Thy configurations) and the total coverage. Figure 8-5d shows that the relative surface concentrations for the L, M and H features as well as the total coverage all increase almost linearly with the exposure of Thy. With almost 80% of all the features, the relative surface concentration for L is found to be the highest, while the M and H features correspond to 16% and 4%, respectively, for the 8 s exposure. As the Thy exposure increases, the relative surface concentrations among the three types of protrusions remain essentially unchanged. In accord with the XPS results and the observed relative surface concentrations, we attribute the L and M features observed in the empty-state images to the 1,4- and 3,6-cycloaddition products respectively. The brighter H feature can be assigned to the hydrogen-bonded Thy adcomplex features as illustrated in Figure 8-4 and are marked by ovals in figure 8-5a-c. On the other hand, the B1 protrusions observed in filled-state images can be assigned to either 1,4 or 3,6 cycloaddition products. It might not be possible to distinguish between 1,4 and 3,6 products from the filled-state images but the larger B2 protrusions could be assigned to the hydrogen bonded adcomplex of Thy. At an evaporation temperature of  $95^\circ\text{C}$ , the total coverage of Thy is almost 5% for a 8 s exposure and 27% for a 25 s exposure. At higher exposures of Thy, the  $7 \times 7$  surface grid cannot be clearly distinguished, which makes it impossible to count the different configurations of Thy. Throughout the three Thy exposures, no noticeable physical correlations among the adsorbed Thy molecules can be discerned, likely because of the very strong molecule-substrate interactions exerted by double  $\sigma$  bonds in the cycloaddition products. Once the cycloaddition reaction occurs, individually adsorbed Thy molecules could no longer interact with the other neighbouring adsorbed Thy molecules. The strong adsorption behaviour observed for Thy on Si(111) $7 \times 7$  is therefore in marked contrast to Thy adsorption on the Au surface,<sup>190</sup> for which Thy molecules are found to interact weakly with the substrate and form self-organized structures. The considerably stronger substrate-molecule interaction observed in the present case prevents Thy molecules from migrating on the surface at room temperature and therefore no self-organized structures are formed.

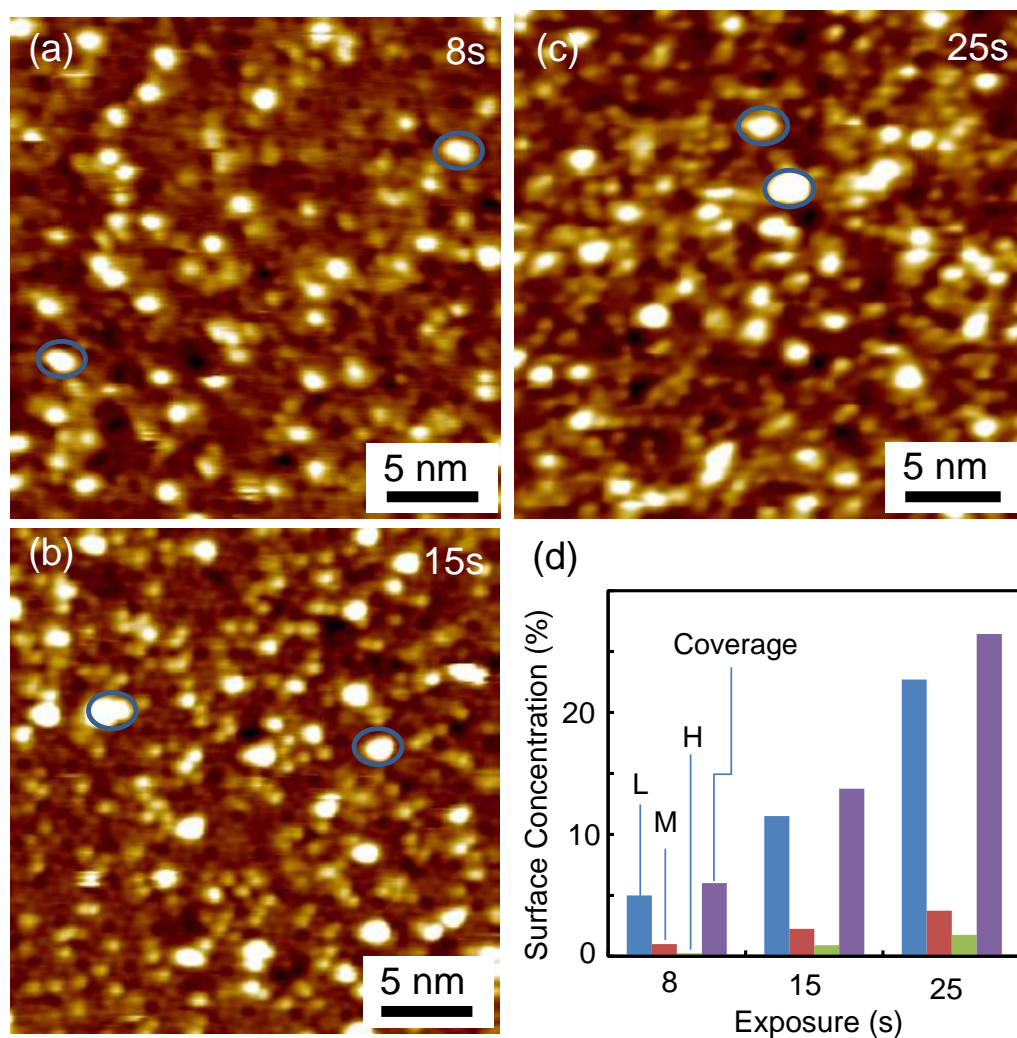


**Figure 8-5** STM images collected at a sample bias of +2 V and a tunneling current of 150 pA for thymine exposure of (a) 8 s, (b) 15 s, and (c) 25 s, all on Si(111)7×7; and (d) the corresponding total coverage and the relative surface concentrations for L, M and H protrusion features.

## 8.4 Summary

Site-specific chemistry of Thy on Si(111)7×7 has been studied by STM and DFT-based computational method. Both the empty-state and filled-state STM images reveal the presence of bright protrusions for the Thy molecules adsorbed on the surface. The lack of correlated dark-bright features, as observed for glycine adsorption on Si(111)7×7, indicates that Thy does not undergo hydrogen dissociation reaction on the surface. Further analysis of the empty-state images reveals three different types of bright protrusions L, M and H with L being the least bright and H being the brightest. From the positions and spatial extents of the L and M protrusions over the surface Si atoms in a 7×7 unit cell, we determine that the adsorbed Thy molecules react with the adatom-restatom pair simultaneously to form bidentate products. In particular, the H protrusions appear discernibly larger and involve two or more adatoms, which suggests different kinds of Thy adsorption on the surface. Furthermore, the filled-state image of Thy on the 7×7 surface clearly shows the involvement of the adatom-restatom pair for the L and M protrusions. The site-specific information about different reaction sites of the surface can be inferred from both imaging modes. We conclude that adatom-restatom pairs provide the preferred reaction sites for the incoming Thy molecules. Our recent XPS studies shows that Thy interacts with the 7×7 surface by cycloaddition reactions, leading to two different [4+2] cycloaddition products. The XPS results further suggest that Thy undergoes keto-enol tautomerism on the surface to form the di-enol tautomer, which then reacts with the adatom-restatom pairs to produce the respective cycloaddition products. Furthermore, our DFT/B3LYP/6-31++G(d,p) calculations show that the cycloaddition reactions between a di-enol Thy tautomer and an adatom-restatom pair can lead to the formation of three different cycloaddition products i.e. 1,4-, 3,6- and 2,5-cycloaddition adspecies, with the 1,4- being the most stable and 2,5-cycloaddition being the least stable. The 1,4- cycloaddition reaction may be more facile among all the three reactions from the nucleophilicity argument, whereas the steric factor may play an important role in the 2,5-cycloaddition reaction as it involves the bulky methyl group. Statistical analysis of the adsorbed Thy protrusions reveals that the L protrusions have the highest surface concentration (80%) with those for the M (16%) and H protrusions (4%) being considerably smaller. When compared with the XPS results, the L protrusions can be ascribed to the 1,4-cycloaddition products while the M protrusions to the 3,6 cycloaddition products. The H protrusions can be assigned to the hydrogen-bonded Thy molecules to the bidentate Thy adstructures, in good accord with our DFT/B3LYP/6-31++G(d,p) calculations.

## Chapter 9

### Conclusion and Future Work

The chemistry of benchmark biological molecules such as glycine, glycyglycine, adenine and thymine on a silicon surface is explored by using a combination of techniques including x-ray photoelectron spectroscopy, scanning tunneling microscopy, and DFT-based computation. In particular, the growth evolution of the simplest naturally occurring amino acid, glycine, on Si(111)7×7 at room temperature has been studied. Our XPS and STM results, together with our DFT calculations have revealed three distinct stages in the growth process. At the interfacial layer, glycine undergoes N–H dissociation rather than O–H dissociation and forms a N–Si bonded unidentate adstructure at the surface, followed by the formation of a hydrogen bond mediated transitional adlayer characterized by the intermolecular O–H···N hydrogen bonding. The hydrogen bonded transitional adlayer ultimately leads to the formation of glycine zwitterions in the multilayers, as the last stage of the growth process. Intermolecular N···H–O hydrogen bonding during the glycine adsorption process on Si(111)7×7 is observed for the first time by XPS, which also demonstrates a new way of detecting surface hydrogen bonds. Another striking feature of glycine adsorption observed in our experiments is the selectivity of the amino group (–NH<sub>2</sub>) in comparison to the carboxylic acid group (–COOH) towards reaction with the surface silicon atoms. The first adlayer is found to react with the 7×7 surface completely via the formation of N–Si bond, with no evidence of O–Si bond formation. The mechanism for the reaction of glycine and the Si adatom-restatom pair has also been investigated by the DFT calculations in order to gain insight into this kind of surface selectivity. It is found out that dissociative adsorption of glycine on the Si surfaces proceeds via the formation of the surface adduct-states followed by the respective transition states that lead to the final adsorption states. For the Si(111)7×7 surface, the absence of a Si←O surface adduct leaves the formation of N–H dissociative product through the formation of the Si←N adduct as the only viable pathway. On the other hand, it has been reported in the literature that for the Si(100)2×1 surface, the presence of the Si←O and Si←N surface adducts suggest that both O–H and N–H dissociative products are plausible. However, the considerably lower energy barrier to the respective transition state from the Si←O adduct than that from the Si←N adduct favours the formation of O–H dissociative product. Based on these computational results, we propose an intramolecular proton transfer mechanism to account for the adsorption process of glycine through the amino group in an unidentate geometry, with the acid group remaining free that is ultimately responsible for the formation of hydrogen bonds with the incoming

glycine molecules. The usefulness of such a glycine-functionalized Si(111)7×7 surface is tested by introducing different prototypical biomolecules onto the functionalized surface. The glycine adlayer adsorbed on Si(111)7×7 (through strong N–Si covalent bonding) provides a powerful platform for trapping biomolecules with appropriate N atoms to form [O–H…N] H-bonds with the free carboxyl groups of the deprotonated glycine molecule. Such a platform is found to be highly effective for providing reversible catch-and-release of other biomolecules such as adenine, glycyglycine, thymine and alanine through hydrogen bonding. The glycine-functionalized Si(111)7×7 surface can therefore be used as a versatile biomolecular trap in biosensing, molecular recognition, and/or other molecular electronics applications. The early adsorption of glycine on Si(111)7×7 has also been studied by STM and evidence of H-dissociative adsorption of glycine at an adatom-restatom pair on the 7×7 surface is obtained. STM images for higher exposures of glycine reveal the emergence of vertically and, for the first time, horizontally hydrogen-bonded glycine molecules on the surface. These observations are in good accord with our XPS results that show N–H dissociative adsorption of glycine and the formation of a transitional layer mediated by the [–H<sub>2</sub>N…H–OC(O)–] H-bonding. Statistical analysis of the STM images collected at several glycine exposures further shows that the Si center adatom sites on the faulted half unit cell are most populated and therefore most reactive towards glycine.

In comparison to glycine, the surface chemistry of the glycyglycine on Si(111)7×7 is found to be rather different at the interfacial adlayer. Our XPS and DFT results show that glycyglycine reacts with the Si surface via the formation of bidentate product, in marked contrast to the initial growth stage of glycine that involves an unidentate adsorption configuration. The bidentate geometries involving reactions of both the amino and peptide N atoms or of the terminal amino N and acidic O atoms are found to occur on the Si surface. The growth evolution of glycyglycine has been found to exhibit a similar trend as glycine. In particular, three growth stages can be identified with increasing exposure for the glycyglycine film, and they correspond to the sequential formation of the covalently bonded interfacial adlayer, the hydrogen-bond-mediated transitional adlayer, and the zwitterionic multilayer. Evidence of the intermediate hydrogen-bonded transitional adlayer for glycyglycine can be inferred from the relatively high thermal stability of the transitional adlayer (up to 200°C), as observed from the XPS spectral changes upon sequential annealing (whereas that for glycine can be detected from the N 1s XPS peak positions). Both the glycine and glycyglycine in the final growth stage grow continuously into multilayers in the zwitterionic form, consistent with it being their most stable solid forms. Thermal evolution studies of these as-grown thick glycine and glycyglycine films on Si(111)7×7 show that the

zwitterionic multilayer desorbs before the transitional adlayer, and the interfacial adlayer remains unaffected at least to 200°C and 250°C, respectively. Similar to glycine, the early adsorption process of glycyglycine on Si(111)7×7 at room temperature was also studied by direct STM imaging. The STM work not only confirms the XPS results that adsorption of glycyglycine involves either N–H and O–H dissociation or double N–H dissociation, but also directly identifies five general types of site-specific bidentate bonding arrangements on the 7×7 surface. It can also be observed that N–H and O–H dissociation (i.e. involving the N-terminal and O-terminal of the glycyglycine peptide) occur on an adatom-adatom pair across or on the same side of a dimer wall while double N–H dissociation occur at an adatom-restatom pair. More importantly, the STM results show that both types of double dissociation on specific Si sites are equally probable. In addition, the total relative occupancies of the center adatom and corner adatom sites are found to be essentially the same. These observations of the essentially statistical nature of the adsorption process suggest that the bidentate interactions are sufficiently strong to prevent surface diffusion and that the adsorption essentially occurs at the random points of molecular impact.

For comparison of site-specific surface chemistry of the simplest amino acid and its peptide, we also study the early growth stages of the adenine on Si (111)7×7 by STM. The bright protrusions as observed in the STM images indicate molecular adsorption of adenine through dative bonding to the surface Si atoms without any evidence of dissociation reaction. The formation of dative bonding has also been inferred from XPS measurements that are not included in this thesis. The variation in the brightness of the STM protrusions can be attributed to the extent of the molecular tilt with respect to the surface normal. STM also reveals that most of the adenine molecules on the surface appear as dimers interacting with each other through hydrogen bonding. These dimers are found to undergo self-organization into aligned superstructures, including straight, offset and zigzag chains, square quartets, double quartets, and other multiple dimer structures at higher exposures. Among the common types of links in forming these dimer superstructures, including end-to-end, 90° and 60° zigzags, wide-angle and right-angle turns, and side-by-side arrangements, the end-to-end growth appears to be the most prominent especially in the initial growth stage, which leads to the formation of dimer nanowires. The formation of these dimers indicates the remarkable ability of the adenine molecules to form self-organized structures on a semiconductor surface. The exact mechanism of the self-aligned growth of adenine is unclear; although we believe that inter-dimer hydrogen bonding interactions play an important role in forming the observed chains. In contrast to adenine, its complementary DNA base pair thymine is found to have completely different surface chemistry on Si(111)7×7. The XPS studies, though not included in the thesis, provide strong evidence for the formation of di-enol structure on the surface through keto- enol tautomerism of the

adsorbed thymine. These di-enol structures are found to react with the Si adatom-restatom pair through the [4+2] cycloaddition pathway producing the diene-type product. The early adsorption of thymine on Si(111)7×7 surface is also studied by STM and DFT calculations. The STM images clearly reveal the bright features occupying both an adatom and restatom sites simultaneously, which can be attributed to the [4+2] cycloaddition product. Both the XPS and DFT calculations have shown the presence of two different cycloaddition products on the surface, in good accord with the STM protrusions with different brightnesses. The relative surface concentrations of the two adsorption products, as inferred from the corresponding STM images, are found to be different for different exposures, with the 1,4-cycloaddition product being the most popular when compared to the 3,6-cycloaddition product. In addition, the presence of thymine molecules vertically attached to a thymine molecule through hydrogen bonding can also be observed in the STM images.

The present work focuses on the surface chemistry of adenine and thymine separately on Si(111)7×7. As extension of the present work, investigation of their interactions with each other on the silicon surfaces would be of great interest. Preliminary STM results involving simultaneous deposition of adenine and thymine on the 7×7 surface has been obtained. A more systematic study supported by XPS measurements and DFT calculations will be necessary to obtain better insight into this interesting coadsorption process of adenine and thymine. With the help of organic MBE technique, both DNA base groups can be evaporated from their respective effusion cells either simultaneously or sequentially. With the adsorption nature of adenine determined in the present work, the 7×7 surface can be exposed first with adenine for a preselected amount of time. This can then be followed by exposure of the predosed surface with thymine. Direct STM imaging would be useful for probing what happens to the thymine molecules when reacting with the adenine predosed Si surface, particularly with the wide variety of adenine superstructures supported on the 7×7 surface. The type of interactions can be compared with those obtained from the reverse sequence of exposing thymine first followed by adenine. Furthermore, simultaneous deposition of both DNA base groups may shed some light on the importance of gas-phase reactions between the two molecules and on the effects on different adsorption and diffusion kinetics on the resulting hybrid adsorption structures. These experiments can offer new insights into the nature of the “cooperative” adsorption and their interactions of adenine and thymine on the silicon surface. One of the important outcomes of this study would be to determine whether the two DNA base groups could form hydrogen bonded pairs on the 7×7 surface as found in an original DNA molecule. The other important question is whether the observed self-organized superstructures of adenine could be controlled or modified with the addition of its complementary DNA partner, thymine.

Furthermore, the adsorption of these four molecules on the Si surface can also be studied by ultrahigh vacuum Atomic Force Microscopy (AFM), which will provide much needed information on the “actual” topography or height profile of the adsorbate on the surface. This information will be useful to complement the local density of states information provided by the STM studies in the present work. The height profile of a particular adsorption configuration will be fundamental to our understanding of the growth evolution. As our Omicron VT-SPM has the option for AFM measurement, a systematic study of the four molecular systems is feasible. In addition, we can also extend our current computational techniques. While the current DFT calculations performed using the Gaussian 09 package are very useful to providing insights into the adsorption geometries and energies, they are rather limited in providing the information about the local density of states and for large periodic systems such as a surface or crystal lattice. These charge density calculations are better performed with the VASP (Vienna Ab initio Simulation Package), and they can provide important models for interpreting the STM images. In this case, the Si clusters, despite being the largest ever used as model surfaces for Si(111)7×7, will be replaced with an appropriate periodic Si lattice and the DFT method will be performed with appropriate plane wave basis sets.

To complete the present investigation involving prototypical DNA base molecules, XPS, STM and computational chemistry studies of the remaining two DNA base groups, i.e. Guanine and Cytosine should be of great interest. Similar to adenine guanine is a purine base and has a –C=O group attached to the aromatic ring. It would of great interest to find out whether guanine can form the dimer like superstructures on the Si(111)7×7 surface. The comparison of cytosine and thymine is also important as they are both pyrimidine bases and has carboxo groups attached to the ring and the experiments should performed to find out whether cytosine can also undergo cycloaddition reactions with an adatom-restatom pair. The knowledge of the nature of interactions of individual DNA base groups on the Si(111)7×7 surface can be used to further study the combined adsorption of all the four DNA base groups on the surface.

Furthermore, the adsorption of adenine on the Si surface has shown the formation of hydrogen bonded dimers, it would be interesting to find out what happens if substituted adenine derivatives are used. As adenine forms the most stable hydrogen bonded dimers through the N9–H hydrogen atom, substituting the N9 hydrogen with N9–CH<sub>3</sub> may affect the dimer formation on the surface and may be observed in the STM images. This experiment can also confirm that adenine while forming dative bonds with the surface Si atoms uses hydrogen associated to N9 atom is one of the hydrogen bond donors on the surface. The

N9–H can also be substituted with deuterium to test the isotope effect on the hydrogen bond formations of the adenine molecules on the surface. It has been reported that the hydrogen bonding efficiency gets reduced for couple of organic molecules in the literature and therefore would be of interest to study if this substitution has any effect on the dimer formation on the surface.

The present work shows that the Si(111) surface is remarkably flexible in providing a variety of adsorption sites and bonding arrangements with different types of biomolecules. In particular, glycine undergoes selective unidentate dissociation reaction, glycyglycine reacts in a bidentate bridging geometry through dissociation reaction, adenine forms datively bonded adduct, while thymine undergoes cycloaddition reaction with the surface Si atoms. The variety of chemical reactions observed in the present work and illustrated throughout this thesis for the four unique “benchmark”, biologically interesting molecules with the  $7\times 7$  surface is impressive, and they point to the reactivities of directional dangling bonds of different Si sites on the  $7\times 7$  reconstructed surface.

Furthermore, the combination of different surface-sensitive techniques, including both XPS and STM, along with detailed computational chemistry studies, provide complementary information that are crucial to the understanding of site-specific surface chemistry of these fascinating systems. For instance, while XPS and DFT studies of adenine offer the local chemical nature of the interactions with the surface, direct STM imaging provides the unique site-specific information. The present work therefore can be a perfect example for studying the surface chemistry of complicated biomolecules with a combination of complementary surface sensitive techniques which helped obtaining knowledge regarding the unique site-specific chemistry of the four important biomolecules on Si(111) $7\times 7$  surface.

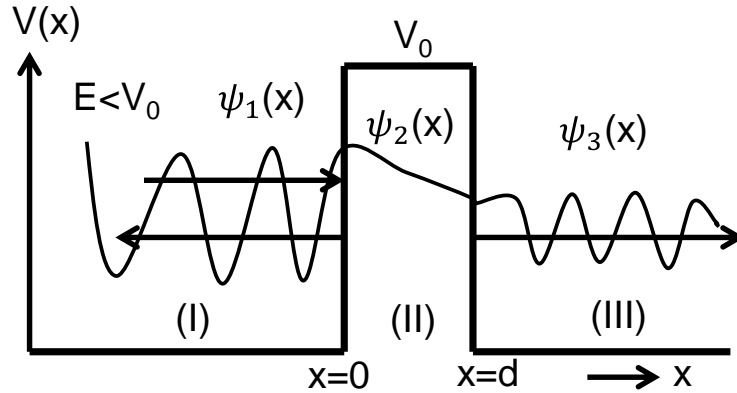
## Appendix A

### Ultrahigh Vacuum (UHV)

Ambient pressure is defined as the atmospheric pressure, i.e.  $1 \text{ atm} = 1.01 \times 10^5 \text{ Pa} = 1.01 \text{ bar} = 760 \text{ Torr}$ . It is quite impossible to keep a surface clean in this ambient condition because there are approximately  $10^{19}$  particles per cubic centimeter available to react with the surface all the time. There are roughly three different pressure ranges that can be obtained by using different types of vacuum pumps. The low vacuum regime from  $10^2$  to  $10^{-2}$  Torr can be obtained by using rotary vane pumps or dry diaphragm pumps. The high vacuum regime,  $10^{-2}$  to  $10^{-8}$  Torr can be obtained by using either diffusion pumps or turbomolecular pumps. The densities of gas molecules in the low and high vacuum range are  $10^{15}$  and  $10^9$  particles per cubic centimeter, which are quite an improvement over the ambient pressure. If the kinetic theory of gases is considered along with the assumption that every collision of the gas particles with the surface will result into adsorption (i.e. with a sticking coefficient of one), it can be shown that at  $10^{-6}$  Torr it takes just 1 second to cover the entire surface with one monolayer of gas particles. At  $10^{-8}$  Torr the time to contaminate the surface will be 100 seconds, which is still too short to be not practical for carrying out any measurement. The ultrahigh vacuum regime of  $10^{-2}$  Torr to  $10^{-11}$  Torr provides the best improvement, with the particle density of  $10^6$  per cubic centimeter, and it allows sufficient time ( $10^3$ – $10^5$  seconds) to carry out measurements on the surface before the surface gets contaminated. In order to reach this kind of vacuum, a combination of turbomolecular pump, ion pump and titanium sublimation pumps is necessary.

## Appendix B

### Tunneling through one dimensional rectangular potential barrier



Schrodinger equations for each region;

Region (I):

$$-\frac{\hbar^2}{2m} \frac{d^2\psi_1}{dx^2} = E\psi_1;$$

$$\text{or } \psi_1 = e^{ikx} + Ae^{-ikx}$$

$$\text{with } k^2 = \frac{2mE}{\hbar^2}$$

Region (II):

$$\frac{\hbar^2}{2m} \frac{d^2\psi_2}{dx^2} + V_0\psi_2 = E\psi_2$$

$$\psi_2 = B'e^{ik'x} + C'e^{-ik'x} = Be^{-\chi x} + Ce^{\chi x}; \text{ with } \chi^2 = -k'^2 = \frac{2m(V_0 - E)}{\hbar^2}$$

Region (III):

$$-\frac{\hbar^2}{2m} \frac{d^2\psi_3}{dx^2} = E\psi_3; \psi_3 = De^{ikx}$$

The barrier transmission coefficient (T), corresponding to the ratio of the transmitted current density  $j_t$  and the incident current density  $j_i$  which are given by

$$j_t = -\frac{i\hbar}{2m}(\psi_3^*(x)\frac{d\psi_3}{dx} - \psi_3(x)\frac{d\psi_3^*(x)}{dx}) = \frac{\hbar k}{m}|D|^2$$

$$\text{and } j_i = \frac{\hbar k}{m}$$

So the Transmission coefficient (T) will be given by,

$$T = \frac{j_t}{j_i} = |D|^2$$

One can obtain the simplified expression for the transmission coefficient,  $T \propto e^{-2\chi d}$ ; where “ $d$ ” is the barrier width and  $\chi^2 = [\frac{2m(V_0 - E)}{\hbar^2}]$  is the effective barrier height. The tunneling current “ $i$ ” is directly proportional to the transmission coefficient T, so one can ultimately write,

$$i \propto e^{-2\chi d}$$

i.e. the tunneling current varies exponentially with the barrier width.

## Bibliography

- (1) Somorjai, G. A.; Li, Y. *Introduction to Surface Chemistry & Catalysis*; Second.; John Wiley and Sons, 2010.
- (2) Leftwich, T.; Teplyakov, A. *Surf. Sci. Rep.* **2007**, *63*, 1-71.
- (3) Bent, S. F. *Surf. Sci.* **2002**, *500*, 879-903.
- (4) Leftwich, T.; Teplyakov, A. *Surf. Sci. Rep.* **2007**, *63*, 1-71.
- (5) Tao, F.; Wang, Z. H.; Qiao, Q. L.; Sim, W. S.; Xu, G. Q. *J. Chem. Phys.* **2001**, *115*, 8563.
- (6) Rummel, R. M.; Ziegler, C. *Surf. Sci.* **1998**, *418*, 303.
- (7) Coulter, S. K.; Schwartz, M. P.; Hamers, R. J. *J. Phys. Chem. B* **2001**, *105*, 3079.
- (8) Silvestrelli, P. L. *Surf. Sci.* **2004**, *552*, 17.
- (9) Tanaka, S.; Onchi, M.; Nishijima, M. *J. Chem. Phys.* **1989**, *91*, 2712.
- (10) Cao, X.; Hamers, R. J. *J. Am. Chem. Soc.* **2001**, *123*, 10988-96.
- (11) Wang, G. T.; Mui, C.; Tannaci, J. F.; Filler, M. A.; Musgrave, C. B.; Bent, S. F. *J. Phys. Chem. B* **2003**, *103*, 4982.
- (12) Liu, H. B.; Hamers, R. J. *Surf. Sci.* **1998**, *416*, 354.
- (13) Huang, H. G.; Zhang, Y. P.; Cai, Y. H.; Huang, J. Y.; Yong, K. S.; Xu, G. Q. *J. Chem. Phys.* **2005**, *123*, 104702-1.
- (14) Kiskinova, M.; Yates, J. T. *Surf. Sci.* **1995**, *325*, 1.
- (15) Huang, J. Y.; Shao, Y. X.; Huang, H. G.; Cai, Y. H.; Ning, Y. S.; Tang, H. H.; Liu, Q. P.; Alshahateet, S. F.; Sun, Y. M.; Xu, G. Q. *J. Phys. Chem. B* **2005**, *109*, 19831.
- (16) Cao, X.; Hamers, R. J. *Surf. Sci.* **2003**, *523*, 241-251.
- (17) Carborne, M.; Piancastelli, M. N.; Zanoni, R.; Comtet, G.; Dujardin, G.; Hellner, L. *Surf. Sci.* **1999**, *419*, 114.
- (18) Yuan, Z. L.; Chen, X. F.; Wang, Z. H.; Yong, K. S.; Cao, Y.; Xu, G. Q. *J. Chem. Phys.* **2003**, *119*, 10389.
- (19) Bu, Y.; Shinn, D. W.; Lin, M. C. *Surf. Sci.* **1992**, *276*, 184.

- (20) Carborne, M.; Comtet, G.; Dujardin, G.; Hellner, L.; Mayne, A. J. *J. Chem. Phys.* **2002**, *117*, 5012.
- (21) Tao, F.; Lai, Y.; Xu, G. Q. *Langmuir* **2004**, *20*, 366-368.
- (22) Bu, Y.; Breslin, J.; Lin, M. C. *J. Phys. Chem. B* **1997**, *101*, 1872.
- (23) Tao, F.; Chen, X. F.; Wang, Z. H.; Xu, G. Q. *J. Phys. Chem. B* **2002**, *106*, 3890.
- (24) Tao, F.; Wang, H. W.; Xu, G. Q. *Surf. Sci.* **2003**, *530*, 203-215.
- (25) Bu, Y.; Lin, M. C. *J. Chn. Chem. Soc.* **1995**, *42*, 309.
- (26) Tao, F.; Yuan, Z. L.; Chen, X. F.; Qiao, M. H.; Wang, Z. H.; Dai, Y. J.; Huang, H. G.; Cao, Y.; Xu, G. Q. *Phys. Rev. B* **2003**, *67*, 245406.
- (27) Waltenburg, H. N.; Yates, J. T. *Chem. Rev.* **1995**, *95*, 1589-1673.
- (28) Schlier, R. E.; Farnsworth, H. E. *J. Chem. Phys.* **1959**, *30*, 917.
- (29) Chadi, D. J.; Bauer, R. S.; Williams, R. H.; Hansson, G. V.; Bachrach, R. Z.; Mikkilson, J. C. jr *Phys. Rev. Lett.* **1980**, *44*, 799.
- (30) Lander, J. J.; Morrison, J. J. *App. Phys.* **1963**, *34*, 1403.
- (31) Harrison, W. A. *Surf. Sci.* **1976**, *55*, I.
- (32) S. Takahashi, M. Takahashi, Y. Tanishiro, K. T. *J. Vac. Sci. Technol. A* **1985**, *3*, 1502.
- (33) Binnig, G.; Rohrer, H.; Gerber, C.; Weibel, E. *Phys. Rev. Lett.* **1983**, *50*, 120.
- (34) Zhou, X. J.; Li, Q.; Leung, K. T. *J. Phys. Chem. B* **2006**, *110*, 5602-10.
- (35) Zhou, X. J.; Li, Q.; He, Z. .; Yang, X.; Leung, K. T. *Surf. Sci.* **2003**, *543*, L668-L674.
- (36) Ebrahimi, M.; Chong, J. M.; Leung, K. T. *J. Phys. Chem. C* **2010**, *114*, 2947-2957.
- (37) Ebrahimi, M.; Leung, K. T. *Surf. Sci.* **2009**, *603*, 1203-1211.
- (38) Radi, A.; Ebrahimi, M.; Leung, K. T. *Surf. Sci.* **2010**, *604*, 1073-1081.
- (39) He, Z.; Leung, K. T. *J. Phys. Chem. B* **2005**, *109*, 14971-8.
- (40) He, Z.; Li, Q.; Leung, K. T. *Surf. Sci.* **2006**, *600*, 514-526.
- (41) Li, Q.; Leung, K. T. *Surf. Sci.* **2001**, *479*, 69-82.

- (42) Li, Q.; Leung, K. T. *Surf. Sci.* **2003**, *541*, 113-127.
- (43) Zhou, X. J.; Leung, K. T. *J. Phys. Chem. B* **2006**, *110*, 9601-7.
- (44) Zhou, X. J.; Leung, K. T. *Surf. Sci.* **2006**, *600*, 3285-3296.
- (45) Gil, A.; Bertran, J.; Sodupe, M. *J. Chem. Phys.* **2006**, *124*, 154306.
- (46) Rejnek, J.; Hanus, M.; Kabelác, M.; Ryjáček, F.; Hobza, P. *Phys. Chem. Chem. Phys.* **2005**, *7*, 2006-17.
- (47) Einstein, A. *Annalen der Physik* **1905**, *17*, 132.
- (48) Briggs, D.; Seah, M. P. *Practical surface analysis: Volume I- Auger and X-ray Photoelectron Spectroscopy*; 2nd ed.; Wiley, Toronto, 1990.
- (49) Wiesendanger, R. *Scanning Probe Microscopy and Spectroscopy: methods and application*; Cambridge University Press, 1994; pp. 144-45.
- (50) Biegelsen, D. K. *App. Phys. Lett.* **1987**, *50*, 696.
- (51) Fotino, M. *Rev. Sci. Instrum.* **1993**, *64*, 159.
- (52) Song, J. P. *Rev. Sci. Instrum.* **1993**, *64*, 900.
- (53) Klein, M.; Schwitzgebel, G. *Rev. Sci. Instrum.* **1997**, *68*, 3099.
- (54) Gross, A. *Theoretical Surface science*; springer, 2009; p. 342.
- (55) Steckel, J. A.; Jordan, K. D. *Computational Materials chemistry: Methods and Applications* **2004**, 246-265.
- (56) Becke, A. D. *Phys. Rev.* **1988**, *38*, 3098.
- (57) Cramer, C. J. *Essentials of Computational Chemistry*; John Wiley and Sons, 2002; p. 247.
- (58) C. Lee, W. Yang, R. G. P. *Phys. Rev. B* **1988**, *37*, 785.
- (59) Becke, A. D. *J. Chem. Phys.* **1993**, *98*, 5648.
- (60) Tirado-Rives, J.; Jorgensen, W. L. *J. Chem. Theory Comput.* **2008**, *4*, 297-306.
- (61) Lee, H. S.; Choi, C. H. *Theor. Chem. Account* **2007**, *120*, 79-83.
- (62) Felici, R.; Robinson, I. K.; Ottaviani, C.; Imperatori, P.; Eng, P.; Perfetti, P. *Surf. Sci.* **1997**, *375*, 55-62.

- (63) Lu, X.; Xu, X.; Wang, N.; Zhang, Q.; Lin, M. C. *J. Phys. Chem. B* **2001**, 10069-10075.
- (64) Ebrahimi, M.; Fernando Rios, J.; Leung, K. T. *J. Phys. Chem. C* **2009**, 113, 281-289.
- (65) M. J. Frisch and G. W. Trucks and H. B. Schlegel and G. E. Scuseria and M. A. Robb and J. R. Cheeseman and G. Scalmani and V. Barone and B. Mennucci and G. A. Petersson and H. Nakatsuji and M. Caricato and X. Li and H. P. Hratchian and A. F. Izmaylov and , J. A. and J. E. P. and F. O. and M. B. and J. J. H. and E. B. and K. N. K. and V. N. S. and R. K. and J. N. and K. R. and A. R. and J. C. B. and S. S. I. and J. T. and M. C. and Gaussian 03 **2003**, Gaussian Inc. Wallington CT 2003.
- (66) M. J. Frisch and G. W. Trucks and H. B. Schlegel and G. E. Scuseria and M. A. Robb and J. R. Cheeseman and G. Scalmani and V. Barone and B. Mennucci and G. A. Petersson and H. Nakatsuji and M. Caricato and X. Li and H. P. Hratchian and A. F. Izmaylov and , J. A. and J. E. P. and F. O. and M. B. and J. J. H. and E. B. and K. N. K. and V. N. S. and R. K. and J. N. and K. R. and A. R. and J. C. B. and S. S. I. and J. T. and M. C. and Gaussian 09 **2009**, Gaussian Inc. Wallingford CT 2009.
- (67) Lofgren, P.; Krozer, A.; Lausmaa, J.; Kasemo, B. *Surf. Sci.* **1997**, 370, 277-292.
- (68) Zhao, X.; Rodriguez, J. *Surf. Sci.* **2006**, 600, 2113-2121.
- (69) Barlow, S. M.; Kitching, K. J.; Haq, S.; Richardson, N. V. *Surf. Sci.* **1998**, 401, 322-335.
- (70) Hasselstrom, J.; Karis, O.; Weinelt, M.; Wassdahl, N.; Nilsson, A.; Nyberg, M.; Pettersson, L. G. M.; Samant, M. G.; Stohr, J. *Surf. Sci.* **1998**, 407, 221-236.
- (71) Nyberg, M.; Hasselström, J.; Karis, O.; Wassdahl, N.; Weinelt, M.; Nilsson, A.; Pettersson, L. G. M. *J. Chem. Phys.* **2000**, 112, 5420.
- (72) Uvdal, K.; Bodo, P.; Ihs, A.; Liedberg, B.; Salaneck, W. R. *J. Colloid Interface. Sci.* **1990**, 140, 207-216.
- (73) Tzvetkov, G.; Ramsey, M. G.; Netzer, F. P. *Surf. Sci.* **2003**, 526, 383-393.
- (74) Tzvetkov, G.; Koller, G.; Zubavichus, Y.; Fuchs, O.; Casu, M. B.; Heske, C.; Umbach, E.; Grunze, M.; Ramsey, M. G.; Netzer, F. P. *Langmuir* **2004**, 20, 10551-9.
- (75) Lopez, A.; Heller, T.; Bitzer, T.; Richardson, N. V. *Chem. Phys.* **2002**, 277, 1-8.
- (76) Huang, J. Y.; Ning, Y. S.; Yong, K. S.; Cai, Y. H.; Tang, H. H.; Shao, Y. X.; Alshahateet, S. F.; Sun, Y. M.; Xu, G. Q. *Langmuir* **2007**, 23, 6218-26.
- (77) Zhang, L.; Chatterjee, A.; Leung, K. T. *J. Phys. Chem. Lett.* **2010**, 1, 3385-3390.
- (78) Cao, X.; Hamers, R. J. *J. Vac. Sci. Technol. B* **2002**, 20, 1614.

- (79) Cao, X.; Coulter, S. K.; Ellison, M. D.; Liu, H.; Liu, J.; Hamers, R. J. *J. Phys. Chem. B* **2001**, *105*, 3759-3768.
- (80) Clark, D. T.; Peeling, J.; Colling, L. *Biochim. Biophys. Acta* **1976**, *453*, 533-545.
- (81) Martensson, N.; Nilsson, A. *Journal of Electron Spectroscopy and Related Phenomena* **1995**, *75*, 209-223.
- (82) Kühnle, A.; Linderoth, T. R.; Hammer, B.; Besenbacher, F. *Nature* **2002**, *415*, 891-3.
- (83) Kühnle, a.; Molina, L.; Linderoth, T.; Hammer, B.; Besenbacher, F. *Phys. Rev. Lett.* **2004**, *93*, 1-4.
- (84) Schiffrin, A.; Riemann, A.; Auwärter, W.; Pennec, Y.; Weber-Bargioni, A.; Cvetko, D.; Cossaro, A.; Morgante, A.; Barth, J. V. *PNAS* **2007**, *104*, 5279-84.
- (85) Barth, J.; Weckesser, J.; Cai, C.; Günter, P.; Bürgi, L.; Jeandupeux, O.; Kern, K. *Angew. Chem. Int. Ed.* **2000**, *39*, 1230-1234.
- (86) Theobald, J. a; Oxtoby, N. S.; Phillips, M. a; Champness, N. R.; Beton, P. H. *Nature* **2003**, *424*, 1029-31.
- (87) Nyberg, M.; Odelius, M.; Nilsson, A.; Pettersson, L. G. M. *J. Chem. Phys.* **2003**, *119*, 12577.
- (88) Holtkamp, D.; Jirikowsky, M.; Kempken, M.; Benninghoven, A. *J. Vac. Sci. Technol. A* **1985**, *3*, 1394-1397.
- (89) Bournel, F.; Carniato, S.; Dufour, G.; Gallet, J.-J.; Ilakovac, V.; Rangan, S.; Rochet, F.; Sirotti, F. *Phys. Rev. B* **2006**, *73*, 1-13.
- (90) Koopmans, T. C. *Physica (Amsterdam)* **1933**, *1*, 104.
- (91) Huang, J. Y.; Huang, H. G.; Lin, k Y.; Liu, Q. P.; Sun, Y. M.; Xu, G. Q. *Surf. Sci.* **2004**, *549*, 255-264.
- (92) Whelan, C.; Ghijsen, J.; Pireaux, J.; Maex, K. *Thin Solid Films* **2004**, *464-465*, 388-392.
- (93) Armstrong, J. L.; White, J. M.; Langell, M. *J. Vac. Sci. Technol. A* **2000**, *15*, 1146-1154.
- (94) Soubiron, T.; Vaurette, F.; Nys, J.; Grandidier, B.; Wallart, X.; Stievenard, D. *Surf. Sci.* **2005**, *581*, 178-188.
- (95) Qu, Y.; Wang, Y.; J, W. Li.; Han, K.-L. *Surf. Sci.* **2004**, *569*, 12-22.
- (96) Mui, C.; Han, J. H.; Wang, G. T.; Musgrave, C. B.; Bent, S. F. *J. Am. Chem. Soc.* **2002**, *124*, 4027-4038.

- (97) Tao, F.; Xu, G. Q. *Acc. Chem. Res.* **2004**, *37*, 882-93.
- (98) Rakshit, T.; Liang, G.-C.; Ghosh, A. W.; Datta, S. *Nano Lett.* **2004**, *4*, 1803-1807.
- (99) Zhang, L.; Chatterjee, A.; Ebrahimi, M.; Leung, K. T. *J. Chem. Phys.* **2009**, *130*, 121103.
- (100) Luo, X.; Qian, G.; Sagui, C.; Roland, C. J. *Phys. Chem. C* **2008**, *112*, 2640-2648.
- (101) Northrup, J. E. *Phys. Rev. Lett.* **1986**, *57*, 154-157.
- (102) Yoshinobu, J. *Prog. Surf. Sci.* **2004**, *77*, 37-70.
- (103) Li, J.; Qu, Y.-Q.; Han, K.-L.; He, G.-Z. *Surf. Sci.* **2005**, *586*, 45-55.
- (104) Filler, M. a.; Bent, S. F. *Prog. Surf. Sci.* **2003**, *73*, 1-56.
- (105) Tse, Y.-C.; Newton, M. D.; Vishveshwara, S.; Pople, J. A. *J. Am. Chem. Soc.* **1978**, *100*, 4329-4331.
- (106) Hamers, R. J.; Hovis, J. S.; Lee, S.; Liu, H.; Shan, J. *J. Phys. Chem. B* **1997**, *101*, 1489.
- (107) Hovis, J. S.; Liu, H.; Hamers, R. J. *Surf. Sci.* **1998**, *404*, 1-7.
- (108) Guisinger, N. P.; Elder, S. P.; Yoder, N. L.; Hersam, M. C. *Nanotechnology* **2007**, *18*, 044011.
- (109) Payer, D.; Comisso, A.; Dmitriev, A.; Strunskus, T.; Lin, N.; Wöll, C.; Devita, A.; Barth, J. V.; Kern, K. *Chem. Eur. J* **2007**, *13*, 3900-6.
- (110) Li, H.; Xu, B.; Evans, D.; Reutt-robey, J. E. *J. Phys. Chem. C* **2007**, *111*, 2102-2106.
- (111) Xie, Z. X.; Charlier, J.; Cousty, J. *Surf. Sci.* **2000**, *448*, 201-211.
- (112) Nakagawa, T.; Tanaka, H.; Kawai, T. *Surf. Sci.* **1997**, *370*, L144.
- (113) Shea, J. N. O.; Schnadt, J.; Bru, P. A.; Hillesheimer, H.; Wang, C.; Luo, Y.; Hans, A. *J. Phys. Chem. B* **2001**, *105*, 2-5.
- (114) Abel, M.-L.; Rattana, A.; Watts, J. F. *Langmuir* **2000**, *16*, 6510-6518.
- (115) Smith, J. L.; Herman, R. G.; Terenna, C. R.; Galler, M. R.; Klier, K. *J. Phys. Chem. A* **2004**, *108*, 39-46.
- (116) Cecchet, F.; Rudolf, P.; Groningen, N.-ag; Rapino, S.; Margotti, M.; Paolucci, F.; Baggerman, J.; Brouwer, A. M.; Kay, E. R.; Wong, J. K. Y.; Leigh, D. A. *J. Phys. Chem. B* **2004**, 15192-15199.

- (117) Schramm, U.; Reisen, G.; Prins, L. J.; Reinhoudt, D. N.; Timmerman, P. *Angew. Chem. Int. Ed.* **2001**, *40*, 2382.
- (118) Clegg, R. S.; Hutchison, J. E. *Langmuir* **1996**, *12*, 5239.
- (119) Feng, Y.; Zhang, Q.; Tan, W.; Zhang, D.; Tu, Y.; Ågren, H.; Tian, H. *Chem. Phys. Lett.* **2008**, *455*, 256-260.
- (120) Zhang, L.; Chatterjee, A.; Leung, K. T. *Journal of Physical Chemistry C* **2011**, accepted & in press.
- (121) Plekan, O.; Feyer, V.; Richter, R.; Coreno, M.; Simone, M. de; Prince, K. C.; Trofimov, A. B.; Gromov, E. V.; Zaytseva, I. L.; Schirmer, J. *Chem. Phys.* **2008**, *347*, 360-375.
- (122) Zhang, L.; Chatterjee, A.; Leung, K. T. *To be published*.
- (123) Haug, A.; Schweizer, S.; Latteyer, F.; Casu, M. B.; Peisert, H.; Ochsenfeld, C.; Chassé, T. *Chem. Phys. Chem* **2008**, *9*, 740-7.
- (124) Kohn, W.; Sham, L. *J. Phys. Rev* **1965**, *140*, A1133.
- (125) Chen, Q.; Frankel, D. J.; Richardson, N. V. *Langmuir* **2002**, *18*, 3219-3225.
- (126) Frankel, D. J.; Chen, Q.; Richardson, N. V. *J. Chem. Phys.* **2006**, *124*, 204704.
- (127) Chen, Q.; Frankel, D. J.; Richardson, N. V. *Surf. Sci.* **2002**, *497*, 37-46.
- (128) Strother, T.; Cai, W.; Zhao, X.; Hamers, R. J.; Smith, L. M. *J. Am. Chem. Soc.* **2000**, *122*, 1205-1209.
- (129) Oliveira Brett, A. M.; Chiorcea, A.-M. *Langmuir* **2003**, *19*, 3830-3839.
- (130) Gray, J. J. *Curr. Opin. Struc. Biol.* **2004**, *14*, 110-5.
- (131) Seker, F.; Meeker, K.; Kuech, T. F.; Ellis, a B. *Chem. Rev* **2000**, *100*, 2505-36.
- (132) Ashkenasy, G.; Cahen, D.; Cohen, R.; Shanzer, A. *Acc. Chem. Res.* **2002**, *35*, 121-128.
- (133) Wolkow, R. A. *Annu. Rev. Phys. Chem.* **1999**, *50*, 413.
- (134) Vilan, a; Shanzer, a; Cahen, D. *Nature* **2000**, *404*, 166-8.
- (135) Heath, J. R. *Annu. Rev. Mater. Res.* **2009**, *39*, 1-23.
- (136) Hamley, I. W. *Angew. Chem. Int. Ed.* **2003**, *115*, 1730-1752.

- (137) Venugopal, V.; Chatterjee, A.; Ebrahimi, M.; He, Z. H.; Leung, K. T. *J. Chem. Phys.* **2010**, *132*, 174702.
- (138) Kawasaki, T.; Sakai, D.; Kishimoto, H.; Akbar, A. A.; Ogawa, T.; Oshima, C. *Surf. Interface anal.* **2001**, *31*, 126-130.
- (139) Tanaka, K.-I.; Xie, Z.-X. *J. Chem. Phys.* **2005**, *122*, 54706.
- (140) Baik, J.; Kim, M.; Park, C.-Y.; Kim, Y.; Ahn, J. R.; An, K.-S. *J. Am. Chem. Soc.* **2006**, *128*, 8370-1.
- (141) Chatterjee, A.; Zhang, L.; Leung, K. T. *Chem. Phys. Lett.* **2011**, *508*, 219-223.
- (142) Cao, Y.; Yong, K. S.; Wang, Z. H.; Deng, J. F.; Lai, Y. H.; Xu, G. Q. *J. Chem. Phys.* **2001**, *115*, 3287.
- (143) Feenstra, R. M. *Surf. Sci.* **1994**, *299-300*, 965-979.
- (144) Lo, R.-L.; Ho, M.-S.; Hwang, I.-S.; Tsong, T. *Phys. Rev. B* **1998**, *58*, 9867-9875.
- (145) Boland, J. *Surf. Sci.* **1991**, *244*, 1-14.
- (146) Lo, R.-L.; Hwang, I.-S.; Ho, M.-S.; Tsong, T. *Phys. Rev. Lett.* **1998**, *80*, 5584-5587.
- (147) Cossaro, A.; Terreni, S.; Cavalleri, O.; Prato, M.; Cvetko, D.; Morgante, A.; Floreano, L.; Canepa, M. *Langmuir* **2006**, *22*, 11193-8.
- (148) Schiffrin, A.; Riemann, A.; Auwärter, W.; Penec, Y.; Weber-Bargioni, A.; Cvetko, D.; Cossaro, A.; Morgante, A.; Barth, J. V. *PNAS* **2007**, *104*, 5279-84.
- (149) Feyer, V.; Plekan, O.; Tsud, N.; Lyamayev, V.; Prince, K. C.; Carravetta, V. *J. Phys. Chem. C* **2010**, *114*, 10922-10931.
- (150) Gao, F.; Li, Z.; Wang, Y.; Burkholder, L.; Tysoe, W. T. *J. Phys. Chem. C* **2007**, *111*, 9981-9991.
- (151) Wu, C. R.; Nilsson, J. O.; Salaneck, W. R. *Phys. Scr.* **1987**, *35*, 586.
- (152) Lange, W.; Jirikowsky, M.; Benninghoven, A. *Surf. Sci.* **1984**, *136*, 419-436.
- (153) <http://webbook.nist.gov/chemistry> *NIST Chemistry WebBook*.
- (154) Chatterjee, A.; Zhang, L.; Leung, K. T. *To be published*.
- (155) Gonella, G.; Terreni, S.; Cvetko, D.; Cossaro, A.; Mattera, L.; Cavalleri, O.; Rolandi, R.; Morgante, A.; Floreano, L.; Canepa, M. *J. Phys. Chem. B* **2005**, *109*, 18003-9.

- (156) Briggs, D.; Beamson, G. *Anal. Chem.* **1993**, *65*, 1517-1523.
- (157) Lopez, G. P.; Castner, D. G.; Ratner, B. D. *Surf. Interface anal.* **1991**, *17*, 267.
- (158) Buchwalter, L. P.; Czornyj, G. *J. Vac. Sci. Technol. A* **1990**, *8*, 781-784.
- (159) Tang, H. H.; Cai, Y. H.; Ning, Y. S.; Lai, Y. H.; Xu, G. Q. *Surf. Sci.* **2007**, *601*, 3293-3302.
- (160) Huang, J. Y.; Shao, Y. X.; Huang, H. G.; Cai, Y. H.; Ning, Y. S.; Tang, H. H.; Liu, Q. P.; Alshahateet, S. F.; Sun, Y. M.; Xu, G. Q. *J. Phys. Chem. B* **2005**, *109*, 19831-8.
- (161) Tang, H. H.; Dai, Y. J.; Shao, Y. X.; Ning, Y. S.; Huang, J. Y.; Lai, Y. H.; Peng, B.; Huang, W.; Xu, G. Q. *Surf. Sci.* **2008**, *602*, 2647-2657.
- (162) Chatterjee, A.; Zhao, L.; Zhang, L.; Pradhan, D.; Zhou, X.; Leung, K. T. *J. Chem. Phys.* **2008**, *129*, 105104.
- (163) Iucci, G.; Battocchio, C.; Dettin, M.; Gambaretto, R.; Dibello, C.; Borgatti, F.; Carravetta, V.; Monti, S.; Polzonetti, G. *Surf. Sci.* **2007**, *601*, 3843-3849.
- (164) Petrovykh, D. Y.; Kimura-Suda, H.; Whitman, L. J.; Tarlov, M. J. *J. Am. Chem. Soc.* **2003**, *125*, 5219-26.
- (165) Vallée, A.; Humblot, V.; Méthivier, C.; Pradier, C.-M. *J. Phys. Chem. C* **2009**, *113*, 9336-9344.
- (166) Seifert, S.; Gavrilu, G. N.; Zahn, D. R. T.; Braun, W. *Surf. Sci.* **2007**, *601*, 2291-2296.
- (167) Clegg, R. S.; Reed, S. M.; Hutchison, J. E. *J. Am. Chem. Soc.* **1998**, *120*, 2486-2487.
- (168) Lewis, P. A.; Smith, R. K.; Kelly, K. F.; Bumm, L. A.; Reed, S. M.; Clegg, R. S.; Gunderson, J. D.; Hutchison, J. E.; Weiss, P. S. *J. Phys. Chem. B* **2001**, *105*, 10630-10636.
- (169) Hamers, R. J. *Annu. Rev. Anal. Chem.* **2008**, *1*, 707-36.
- (170) Allara, D. L. *Biosens. Bioelectron.* **1995**, *10*, 771-783.
- (171) Mirkin, C. A.; Ratner, M. A. *Annu. Rev. Phys. Chem.* **1992**, *43*, 719.
- (172) Aviram, A.; Ratner, M. A. *Chem. Phys. Lett.* **1974**, *29*, 277.
- (173) Bergveld, P. *Sensors And Actuators A* **1996**, *56*, 65-73.
- (174) Shimomura, M.; Sanada, N.; Fukuda, Y.; Moller, P. *Surf. Sci.* **1995**, *341*, L1061-L1064.
- (175) Cao, Y.; Yong, K. S.; Wang, Z. H.; Deng, J. F.; Lai, Y. H.; Xu, G. Q. *J. Chem. Phys.* **2001**, *115*, 3287.

- (176) Yong, K. S.; Zhang, Y. P.; Yang, S.-W.; Wu, P.; Xu, G. Q. *J. Phys. Chem. A* **2007**, *111*, 12266-74.
- (177) Yong, K.; Zhang, Y.; Yang, S.; Xu, G. *Surf. Sci.* **2008**, *602*, 1921-1927.
- (178) H. Tabata, T. Kawai, M. K. *Surf. Sci.* **1995**, *342*, 215.
- (179) T. kawai, H. Tabata, M. K. *Surf. Sci.* **1996**, *357-358*, 195-201.
- (180) Furukawa, M.; Tanaka, H.; Kawai, T. *J. Chem. Phys.* **2001**, *115*, 3419.
- (181) Asturiol, D.; Duran, M.; Salvador, P. *J. Chem. Theory Comput.* **2009**, *5*, 2574-2581.
- (182) Dunphy, J.; Rose, M.; Behler, S.; Ogletree, D.; Salmeron, M.; Sautet, P. *Phys. Rev. B* **1998**, *57*, R12705-R12708.
- (183) Yates, J. T. *Science* **1998**, *279*, 335-336.
- (184) H.Tabata, T. Kawai, M. K. *Surf. Sci.* **1996**, *357-358*, 195-201.
- (185) Hamers, R. J.; Coulter, S. K.; Ellison, M. D.; Hovis, J. S.; Padowitz, D. F.; Schwartz, M. P.; Greenlief, C. M.; Russell, J. N. *Acc. Chem. Res.* **2000**, *33*, 617-24.
- (186) Hovis, J. S.; Liu, H.; Hamers, R. J. *Appl. Phys. A* **1998**, *66*, S553-557.
- (187) Cao, Y.; Wei, X. M.; Chin, W. S.; Lai, Y.; Deng, J. F.; Bernasek, S. L.; Xu, G. Q. *J. Phys. Chem. B* **1999**, *103*, 5698-5702.
- (188) Horn, S. a.; Patitsas, S. N. *Surf. Sci.* **2008**, *602*, 630-637.
- (189) Lu, X.; Wang, X.; Yuan, Q.; Zhang, Q. *J. Am. Chem. Soc.* **2003**, *125*, 7923-7929.
- (190) Xu, W.; Kelly, R. E. a; Otero, R.; Schöck, M.; Laegsgaard, E.; Stensgaard, I.; Kantorovich, L. N.; Besenbacher, F. *Small* **2007**, *3*, 2011-4.